Growth and Characterization of Polycrystalline Rare-Earth Iron Garnet Films and Heterostructures

By

Jackson J. Bauer

B.S., Chemical Engineering
University of Nebraska-Lincoln, 2017

Submitted to the Department of Materials Science and Engineering in Partial Fulfillment of the Requirements for the Degree of

DOCTOR OF PHILOSOPHY IN MATERIALS SCIENCE AND ENGINEERING

AT THE

MASSACHUSETTS INSTITUTE OF TECHNOLOGY

JUNE 2021

Author _____
Department of Materials Science and Engineering
May 11, 2021

Certified by _____
Caroline A. Ross
Professor of Materials Science and Engineering, Associate Department Head
Thesis Supervisor

Accepted by _____
Frances M. Ross
Chair, Department Committee on Graduate Studies

Growth and Characterization of Polycrystalline Rare-Earth Iron Garnet Films and Heterostructures

By

Jackson J. Bauer

Submitted to the Department of Materials Science and Engineering on May 11, 2021 in Partial Fulfillment of the Requirements for the Degree of Doctor of Philosophy in Materials Science and Engineering

Abstract

Spintronics is a fast-developing field which makes use of the two spin states of the electron, and has the potential for more efficient, robust, and faster microelectronic devices. Thin films of rare-earth iron garnets, a class of insulating ferrimagnetic oxides, are particularly well suited to this application as the anisotropy, magnetization, magnetostriction, and damping can be easily controlled through selection of rare-earth ion and substrate. Previous work on garnets has focused on epitaxial single-crystal films grown on garnet substrates, which are expensive and not of commercial importance. Thus, it is of interest to grow nanometer scale thin films of garnets as polycrystalline layers on non-garnet substrates with perpendicular magnetic anisotropy.

In this thesis, the growth of polycrystalline thin films of rare-earth iron garnets with controllable anisotropy and spin transport properties comparable to single crystal films is reported. Perpendicular magnetic anisotropy, which is essential for efficient manipulation of the magnetization through spin-orbit torque injection from an adjacent conductive layer, is achieved via control of the magnetoelastic anisotropy from thermal expansion mismatch between the film and substrate for europium iron garnet/quartz and dysprosium iron garnet/silicon. Heterostructures with a platinum overlayer allow investigation of the spin Hall magnetoresistance, which indicates a high degree of spin transparency at the interface. Next, a novel heterostructure is developed that allows for the growth of ultra-thin (< 10 nm) polycrystalline garnet films through the use of a nonmagnetic seed layer and diffusion barrier. The magnetic proximity effect in heavy metals is also investigated across the magnetic compensation temperature of dysprosium iron garnet, demonstrating exchange coupling behavior different from that of metallic magnets and validating the importance of a sharp, contamination free interface in these materials. Finally, a molecular field coefficients model is modified to account for non-ideal stoichiometry and site occupancy in the garnet crystal structure. The model is used to explain discrepancies between the bulk and thin film magnetic compensation temperatures. The work demonstrated here outlines the potential for integration of magnetic insulators into next-generation spintronic devices.

Thesis Supervisor: Caroline A. Ross
Title: Toyota Professor of Materials Science and Engineering, Associate Department Head

Acknowledgements

The work in this thesis would not have been possible without my support network of mentors, colleagues, and family. I would like to take this opportunity to express my gratitude for all of the guidance and encouragement I have received over the last four years.

First, my advisor Professor Caroline Ross for giving me the opportunity to join her group. I have enjoyed unyielding support and guidance that has been instrumental in my development as a scientist and engineer. Her work ethic, insight into research problems, and invaluable advice have been a great inspiration to me, allowing me to complete all of the work in this thesis. I would also like to thank my committee members, Professor Geoffrey Beach and Professor Jennifer Rupp for their time and helpful suggestions regarding the direction of the research and interpretation of results.

Being a member of the Ross group has been an excellent experience. I would like to thank my friends and colleagues for their training, guidance, collaboration, fruitful discussions, and for taking the time to enjoy this experience together: Ethan Rosenberg, Takian Fakhrul, Shuai Ning, Astera Tang, Yabin Fan, Bharat Khurana, and all other members of the Ross group. Dr. Corey Fucetola and Julia Hollingsworth also deserve thanks for being instrumental in making sure the laboratory equipment and the day-to-day life in the group functioned smoothly. The last year has been complicated by the shift to the virtual world, but the transition has been eased by the camaraderie amongst our group, for which I am very grateful.

MIT has a phenomenal group of staff that underpins so much of the research done here. I would especially like to thank Dr. Charlie Settens for his knowledge in all types of x-ray characterization, his friendship, and his eternally positive outlook. David Bono can be counted on to fix nearly any electronic device, and his expertise in fixing equipment, especially with the VSM, was always a learning experience. I would also like to thank Alan Schwartzman for his assistance with scanned probe microscopy measurements.

I would also like to extend thanks to our collaborators at the University of Minnesota, Dr. Subhajit Kundu and Professor K. Andre Mkhoyan. Your expertise in electron microscopy allowed us invaluable insights into the structure of our films. I would also like to thank Dr. Patrick Quarterman, Dr. Alexander Grutter, and Dr. Julie Borchers at the NIST Center for Neutron Research for their many hours of data collection and analysis.

Next, I would like to thank my parents, Mark and Jane, and my brother, Joshua. Your patience, humor, and care were crucial to my motivation and wellbeing. Finally, I would like to thank my wife, Sammie. Your love, understanding, and patience helped me to stay grounded and balanced these past four years. This would not have been possible without your help.

This work would not have been possible without the support of the NSF-MRSEC program under DMR-1419807, the NSF, DARPA, and SMART, an nCORE center of the SRC.

Table of Contents

List of Figures

Figure 8.8: Plot of compensation temperature vs. RE:Fe ratio for TbIG. The ratio of octahedral:tetrahedral Fe is constant. For higher RE:Fe, more vacancies are introduced onto the Fe sublattices, in the ratio 2:3 (oct:tet). A fraction of the octahedral vacancies are occupied by excess Tb as antisite defects. The horizontal and vertical dashed lines correspond to the experimental T_{Comp} and RE:Fe, respectively.

List of Tables

1. Introduction

1.1 Motivation

1.1.1 Increasing Compute Demand

Computers and networks underpin nearly every aspect of the global economy and daily life. From daily communications, self-driving cars, the internet of things, and the development of artificial intelligence technologies, the demand for increased computational power and bandwidth is increasing at a nearly exponential rate, compounded by the expansion of internet access to more people than ever before[1]. The power of modern computational tools has also advanced the state-of-the-art in nearly every scientific and medical field, as high-throughput models allow exploration of new materials and treatments faster than possible experimentally.

However, all of this computational demand has a hefty cost. Data centers, through which nearly all internet traffic passes, accounted for nearly 2% of the total United States energy demand in 2014 and nearly 1% globally in 2019[1,2]. This figure does not account for the energy consumption in the billions of local devices such as personal computers and workstations. Clearly, the continued increase in usage leads to a tremendous energy demand and carbon footprint. To reduce the environmental impact of these activities, most of the work has focused on improving the existing technology. Advancements in server efficiency through standby power reduction and architectural innovations have reduced the electrical demand for a given task by a factor of 4 since 2010[3]. This has mitigated the increase in demand, but the limits of the conventional complementary metal oxide semiconductor (CMOS) technologies, which underpin the vast majority of integrated circuits, are closer than ever before.

1.1.2 New Materials and Technologies for Greater Energy Efficiency in Computing

To push the envelope on computational power and efficiency, it is necessary to explore new technological paradigms. Consider one aspect of modern computers: dynamic random-access memory (DRAM). DRAM serves as a sort of short-term memory for central processing units (CPUs), providing a rapid access to data that is too big to be stored in the processor cache or data that is not immediately needed. The data is stored in bits on the DRAM that consist of 1 transistor and 1 capacitor. However, capacitors are *volatile*; a voltage must be constantly applied, or the signal decays and the information is lost. Thus, DRAM is constantly drawing energy, even when the data is just being stored. In contrast, hard disk drives (HDD), which typically serve as long-term storage, keep information in tiny magnetic bits. These magnetic bits are small grains of a magnetic material, magnetized in or out of the plane, with each direction corresponding to a 0 or 1. Magnetic materials are *nonvolatile*, that is the state is retained when the mechanism used to set the state is removed. However, the speed of HDD technology is orders of magnitude slower than the CPU, necessitating the use of high speed intermediate DRAM.

Much effort has been made into the development of magnetic random-access memory (MRAM), which attempts to combine the best aspects of these two technologies. MRAM stores information in a 1 transistor – 1 magnetic tunnel junction (MTJ) geometry, analogous to DRAM[4]. However, the state of the MTJ is retained after it is written and the write current is removed, resulting in increased efficiency over conventional DRAM.

MRAM is part of a larger exciting field known as spintronics, which makes use of the two intrinsic spin states of the electron. The ability to use and manipulate the spin of the electron allows

potentially twice the information to be conveyed compared to an unpolarized electric current[5]. Spintronics has the capacity to not only increase the processing speed but to also lower the energy consumption of integrated circuits. Beyond MRAM, exciting research is being done on long-term data storage and spin-based logic devices[6,7].

1.1.3 Rare-Earth Iron Garnets as a Spintronics Platform

Most of the research on spintronics has focused on metallic magnets. However, recent advancements in the field have enabled the development of spintronic devices based on insulating magnetic oxides with properties that exceed that of metallic magnets[8]. Insulating magnets are capable of transporting a pure electron spin current, in which spin information propagates as a wave through the material, but no electronic motion takes place as the material is not conductive. Spin currents are extremely efficient as there is no electrical resistance or Joule heating in the magnetic layer (reducing both electrical and cooling demand), and the energy loss is only through dissipative magnetic damping mechanisms in the material. Additionally, magnetic insulators are capable of much faster magnetization dynamics than their metallic counterparts, into the terahertz regime.

In particular, the rare-earth iron garnets (REIG) are a promising class of materials for highly efficient spintronic devices. The choice of rare-earth ion(s) in the garnet structure allows for simple tuning of the saturation magnetization, magnetic damping, magnetic anisotropy, and many other properties of the material. This allows optimization of this class of materials for specific applications. REIG can be grown as thin film materials by a variety of physical vapor deposition techniques, and then integrated with metal films to form heterostructures or be patterned into

devices. This unique combination of tunability, stability, and compatibility with other materials pushes garnets to the forefront of spintronics research.

1.2 Organization of Thesis

In this thesis, we explore the development and integration of polycrystalline rare-earth iron garnet films with controllable magnetic anisotropy. The potential for use as spintronic devices, the development of ultra-thin films, and the capacity for integration with existing CMOS technologies is explored. We then explore how the magnetic proximity effect, a problem of fundamental physical interest with implications on spin transport, behaves in this system compared to metallic systems.

Chapter 2 provides a background on magnetism, the garnet structure and its properties, the magnetic proximity effect, and spintronics.

Chapter 3 discusses the experimental growth and characterization methods used in the thesis.

Chapter 4 reports the development of perpendicularly magnetized polycrystalline garnet films on non-garnet substrates and the spin transport properties of polycrystalline garnet/Pt heterostructures.

Chapter 5 extends the work on perpendicularly magnetized polycrystalline garnet films to silicon substrates. Exceptionally large grain sizes in dysprosium iron garnet and excellent spin transport is reported in this material for the first time.

Chapter 6 explores the behavior of the magnetic proximity effect in dysprosium iron garnet/heavy metal heterostructures above and below the magnetic compensation temperature. A different behavior and mechanism of the magnetic proximity effect compared to metallic systems is reported.

Chapter 7 details the growth of ultra-thin polycrystalline garnet films for the first time, necessary for efficient current-induced switching, through the use a of a novel heterostructure.

Chapter 8 reviews the molecular field coefficient model of magnetization in the garnet system. Extensions to the model incorporating off-stoichiometry, anti-site defects, vacancies, and non-ideal valence states with comparison to experimental data are discussed.

Chapter 9 summarizes the work reported in the thesis along with a discussion of future directions for this research.

2. Background

2.1 Magnetism

2.1.1 General

Magnetism is a fundamental physics phenomena that is universally known, but the explanation for why it occurs lies in quantum mechanics, with an accurate framework for its existence not emerging until the twentieth century[9]. Only four elements are magnetic at room temperature, iron, cobalt, nickel, and gadolinium, with ruthenium recently demonstrated to be ferromagnetic at room temperature under certain conditions[10].

The explanation for the existence of ferromagnetism centers around the behavior of a pair of spins, such as a pair of electrons which each have a spin of 1/2. Werner Heisenberg was the first to develop the mathematics to explain the existence of ferromagnetism, with the formulation becoming known as the Heisenberg Hamiltonian:

$$\widehat{H} = -\sum_{ij} J_{ij} \boldsymbol{S}_i \cdot \boldsymbol{S}_j \tag{2.1}$$

Where J_{ij} is the exchange constant between the i^{th} and j^{th} spins in a material, S_i and S_j[11,12]. Paul Dirac arrived at similar formulation, later the same year[13]. The Pauli exclusion principle requires that no two electrons may be in the same quantum state, so that either the spin or spatial part of the electron wavefunction must be antisymmetric, while the other is symmetric[14]. J_{ij} is the difference in energy between the electrons having symmetric spatial state/antisymmetric singlet spin state (S = -½ + ½ = 0) and the electrons having an antisymmetric spatial state/symmetric triplet spin state (S = ½ + ½ = 1). For J > 0, the triplet state is favored, and for J < 0 the singlet state is favored. The exact type of exchange depends on the materials system, but this simple equation can be used to explain the existence of magnetism.

There are several main types of exchange that occur in magnetic materials. First, consider the case of the ferromagnetic transition metals: iron, nickel, and cobalt. The simplest explanation of the magnetism in metals is through the rigid band model, which originated as an attempt to explain the famed Slater-Pauling curve, which shows the trend in magnetization across the *3d* transition metals[9]. The rigid-band model (see figure 2.1) asserts that there is a splitting in the band structure for the *3d* orbitals as a means of free energy minimization, resulting in one polarization being fuller than the other and resulting in a net magnetic moment. While this does not accurately reflect the complex band structures of materials, it is an adequate explanation for many phenomena.

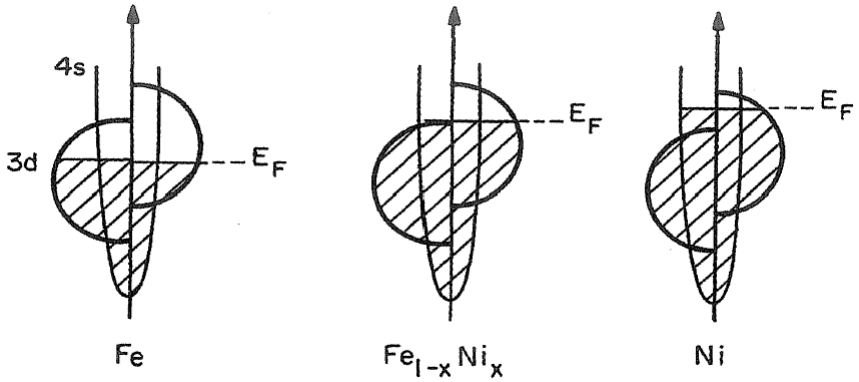

Figure 2.1: Rigid band model for Fe, Ni, and an FeNi alloy. The splitting of the 3d orbitals are shown. From ref. 18. Used with permission.

Rare-earth elements have a fundamentally different form of exchange coupling, as the electrons responsible for the magnetism are buried in the *4f* orbitals, well below the $5d^16s^2$ conduction electrons in the valence shell. RKKY coupling (named for Ruderman, Kittel, Kasuya, and Yosida) describes how the inner *4f* electrons polarize these conduction electrons, and the sign and magnitude of this polarization oscillates with distance from the atomic nucleus[15–17]. This exchange is relatively weak but is the dominant form of exchange coupling in rare-earth metals and dilute magnetic semiconductors.

Oxides are the focus of this work, and the explanation of magnetism in magnetic oxides requires a third major type of exchange coupling. Consider the case of MnO, which has the rock-salt type structure and is an antiferromagnet[12]. Mn has one unpaired electron and oxygen has two, and these four electrons must be distributed across three atoms when examining the coupling between two Mn atoms (Mn-O-Mn). This is shown schematically in figure 2.2. If the Mn atoms are coupled ferromagnetically, there is only one possible state (the ground state), and the excited states are forbidden by the Pauli exclusion principle. In contrast, if the Mn atoms are coupled antiferromagnetically, then there are two possible excited states, allowing the kinetic energy of the electrons to be reduced by delocalizing over the three total states. For this reason, almost all magnetic oxides are antiferromagnetic, with the only ferromagnetic exceptions being CrO_2 and EuO[18]. However, there is another broad class of magnetic materials, ferrimagnets, of which many are oxides. These ferrimagnetic oxides include perovskites, orthoferrites, spinels, and rare-earth iron garnets.

Having a background in the origins of magnetism, a discussion of the types of magnetic materials is now necessary. There are three classes of materials that exhibit some degree of permanence in their magnetic state in the absence of an external field: ferromagnets, antiferromagnets, and ferrimagnets. The first type is ferromagnets, in which there is only one magnetic sublattice present. The most common examples are the transition metals Fe, Ni, and Co.

Antiferromagnets are different in that they do not have a magnetic moment, or a very weak one depending on the antiferromagnetic ordering. In most cases, there are two identical magnetic sublattices that are antiferromagnetically coupled, resulting in a cancellation of the net moment.

Louis Néel himself, who was the first to discover and explain antiferromagnetism for which he won a share of the 1970 Nobel Prize in Physics, remarked that antiferromagnets are "interesting but useless"[19]. The net zero moment makes these materials difficult to characterize experimentally, but antiferromagnets are an irreplaceable component of hard-disk storage. Through an effect known as exchange bias, an antiferromagnetic layer can "pin" a ferromagnetic layer to always be polarized in a particular direction (except in the presence of very large fields, greater than $H_{\text{exchange bias}}$). This creates a reference magnetic layer that can then be used in the read head of hard disk drives, the highly dense information storage technology underpinning millions of computers worldwide. Progress has been made recently in integrating these materials into next-generation magnetic storage, including the first switching of an antiferromagnetic thin film via electric current[20]. There are further advantages these materials possess, such as magnetization dynamics in the terahertz regime, but significant work is still necessary to make these materials competitive with existing technologies[21].

Ferrimagnets are the final class of materials that can exhibit magnetic behavior in the absence of an external field. Ferrimagnetic materials contain two or more non-equivalent magnetic sublattices that are antiferromagnetically coupled. Some of the most common ferrimagnets include rare-earth transition metal alloys such as GdCo, and oxides such as magnetite (Fe_3O_4) and yttrium iron garnet ($Y_3Fe_5O_{12}$)[18,22–24]. It is usually not possible to determine if a material is ferro- or ferrimagnetic from just examining the hysteretic behavior, as they are similar. It is thus required to know the precise stoichiometry and atomic positions of the elements in the unit cell to make educated guesses with how the magnetic species couple. In the case of magnetite, the discovery of ferrimagnets answered a long-standing question as to why the magnetic moment was far below the

predicted value, as the two Fe^{3+} atoms cancel out leading to a net moment of one Fe^{2+} ion. Garnets are another very common ferrimagnet, which will be discussed in the following sections. Like, antiferromagnets, ferrimagnets exhibit some advantages over ferromagnets. The antiferromagnetic coupling is in general stronger ("stiffer") than the exchange coupling in ferromagnets, leading to faster spin dynamics[25].

Two other types of magnetism that are important to mention are diamagnetism and paramagnetism. Diamagnetism is a phenomenon in which the material becomes oppositely polarized to an applied magnetic field. This is present in all materials and results due to the orbits of the individual electrons aligning antiparallel to the applied field to reduce the current associated with the motion of the electron[18]. Diamagnetism is a very weak effect and is roughly independent of temperature.

Paramagnetism occurs when a material is polarized by a magnetic field, resulting in a small magnetic moment in the material that is along the direction of the field and proportional to its magnitude. The simple reason for why this occurs is that if unpaired electrons are present in a material, the spins of these electrons align with the field to reduce the total energy of the system. The quantum theory of paramagnetism modifies this slightly by recognizing that energy levels are quantized. Paramagnetism is strongly temperature dependent, becoming negligible at very high temperatures.

The theory of paramagnetism gives rise naturally to the g factor, which relates the amount of spin and orbital angular momentum in a given atom. The g factor (or Landé equation) is:

$$g = 1 + \frac{J(J+1) + S(S+1) - L(L+1)}{2J(J+1)} \tag{2.2}$$

Where J is the total angular momentum, S is the spin angular momentum, and L is the orbital angular momentum[18].

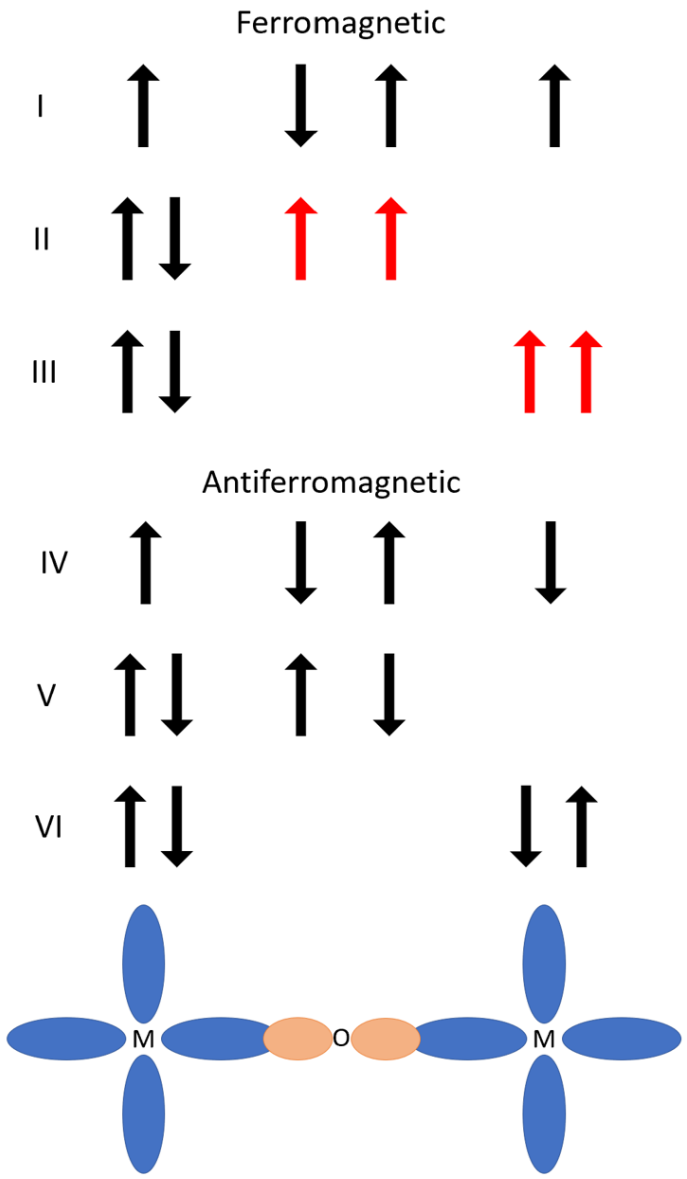

Figure 2.2: Lines I-III show the electronic configurations if the metal ions couple ferromagnetically. Note that lines II and III are forbidden by the Pauli exclusion principle. Lines IV-VI show the electronic configurations possible if the metal ions couple antiferromagnetically. All configurations are possible leading to delocalization and a reduction in the electron's kinetic energy.

Electrons in an atom have two contributions to magnetism (angular momentum in this context): spin and orbital[9]. The spin component is intrinsic to the electron and always has a value of ±1/2, and the orbital component is dependent on the electronic orbitals of the particular atom. For the 3rd period transition metals, there are 5 *3d* orbitals with angular momentum values of -2, -1, 0, 1,

and 2. The 7 *4f* orbitals in the rare-earths are analogous, with angular momentum values of -3, -2, -1, 0, 1, 2, and 3. S, the spin angular momentum, is the sum of the spin components for each electron. L, the orbital angular momentum, is the sum of the orbital components for each electron. Electrons are filled into these orbitals according to the Pauli exclusion principle and Hund's rules, summarized here[9]:

1. Orbitals are filled to maximize S, as this requires placing electrons in different orbitals, minimizing Coulombic repulsion energy.
2. Orbitals are then filled to maximize L, as this requires electrons to be in orbitals that orbits in the same sense around the nucleus, again minimizing Coulombic repulsion.
3. The total angular momentum, J, is the difference of L and S for energy levels that are less than half full, and J is the sum of L and S for energy levels that are more than half full.

$$J = |L - S| \qquad (energy\ level\ less\ than\ half\ full) \tag{2.3}$$
$$J = |L + S| \qquad (energy\ level\ more\ than\ half\ full) \tag{2.4}$$

Note that the case of the energy level being half full, there is no orbital angular momentum. These rules hold for isolated atoms, but do not necessarily hold for atoms in a solid. Especially in the case of transition metals, the *3d* orbitals are close to the Fermi level of the material, and as a result the orbital angular momentum is quenched (essentially zero) by the crystal field in solids. In the rare-earth *4f* orbitals, the effect of the crystal field is much smaller, and Hund's rules are usually a good approximation[12].

The last fundamental topic in classical and quantum magnetism that will be covered here is magnetic damping in solids. Damping is the dissipation of energy through internal mechanisms that transfers energy to the crystal lattice, and can be thought as a viscous, friction-like effect[18]. The magnitude of the damping greatly affects the dynamic behavior of a system, such as the

propagation distance of spin waves and the switching speed[26,27]. Insulating materials have, in general, lower magnetic damping than metallic magnets because the conduction electrons can assist in the energy transfer process. Certain garnets, yttrium iron garnet (YIG) in particular, have some of the lowest magnetic damping values of all known materials[26]. The dynamic magnetic behavior of magnetic systems is governed by the Landau-Lifshitz-Gilbert (LLG) equation:

$$\frac{d\vec{M}}{dt} = \gamma\left(\vec{M} \times \vec{H}\right) - \frac{\alpha}{M}\left(\vec{M} \times \frac{d\vec{M}}{dt}\right) + \gamma\alpha^2\left(\vec{M} \times \vec{H}\right) \quad (2.5)$$

$$\gamma = \frac{ge}{2mc} \quad (2.6)$$

Where $\vec{M}$ is the magnetization vector, γ is a constant, g is the g factor, e is the charge of the electron, m is the mass of the electron, c is the speed of light, M is the value of the magnetization, and $\vec{H}$ is the magnetic field vector[18].

2.1.2 Spin-Orbit Coupling

As described in the previous section total angular momentum, J, is the combination of spin and orbital components, with its value dependent on the electronic configuration of the atom in question. J is used in many calculations because it is a conserved quantity, and thus a well-behaved quantum number. But the reason this is the case is that there is a significant interaction between the spin and orbital components; they are coupled together. This spin-orbit coupling (SOC) is a relatively weak effect, but it underpins a huge number of magnetic phenomena, including anisotropy, magnetostriction, magnetooptics, magnetoresistance, damping, and is also of critical importance in the nascent field of spintronics[9].

Spin-orbit coupling is used to describe the interaction between the orbital motion of the electron and the electron's spin orientation. Considering the surface of the electron as the reference frame, the electron observes the nucleus orbiting around it, creating a magnetic field as the result of the

positive charge moving in a closed loop. This magnetic field influences the direction of the electrons spin, leading to SOC[9,18]. SOC is proportional to the fourth power of the atomic number, so it becomes quite significant for heavy metals such as Pt and Ta[28].

2.1.3 Anisotropy

Anisotropy is a directional dependence on the properties of a material. Anisotropy can have many sources, both intrinsic such as a crystal structure or SOC, and extrinsic such as applied stress on a material. Magnetic materials all exhibit some degree of anisotropy, which can be classified into several major types.

The first of these that will be discussed in magnetocrystalline anisotropy, which couples the magnetic moment to the crystal lattice of the material. A given crystal structure has a certain symmetry of electric field associated with it (crystal field). For asymmetric electronic orbitals ($L \neq 0$), there is an anisotropic interaction of the orbital with the crystal field, leading to certain orientations and certain orbitals to have lower energies[9,29]. In the case of a cubic structure, there are two principle directions: [100] and [111]. The magnetocrystalline anisotropy of a cubic material can be characterized by a series of constants K_i in the following equation:

$$E_{mc} = K_0 + K_1(\alpha_1^2\alpha_2^2 + \alpha_2^2\alpha_3^2 + \alpha_3^2\alpha_1^2) + K_2(\alpha_1^2\alpha_2^2\alpha_3^2) + \cdots \quad (2.7)$$

Where α_i are the cosines of the angles that the magnetization vector makes with the three crystal axes. K_1 and K_2 are known as the first and second order magnetocrystalline anisotropy constants, respectively, and are usually sufficient to describe the anisotropy of a material. In the case of a truly random polycrystalline sample, the net magnetocrystalline anisotropy will be zero, as a result of the random grain orientations.

Magnetoelastic anisotropy relates the mechanical stress in a material to the effect on anisotropy. The magnetostriction constants that couple these two quantities are covered in the next section. It is obvious that a distortion of the crystal lattice would have an effect on the anisotropy, as the lattice already has a large impact on the anisotropy. This can be quantized in a relatively simple form for an isotropic material:

$$E_{me,iso} = \frac{3}{2}\lambda\sigma(\sin\theta)^2 \tag{2.8}$$

Where λ is the magnetostriction coefficient, σ is the applied stress, and θ is the angle between the applied stress and magnetization vector[18]. For a cubic material, magnetoelastic anisotropy energy is a function of both the crystallographic direction and the direction of the applied stress[18]:

$$\begin{aligned} E_{me,cubic} = & -\frac{3}{2}\lambda_{100}\sigma(\alpha_1^2\gamma_1^2 + \alpha_2^2\gamma_2^2 + \alpha_3^2\gamma_3^2) \\ & - 3\lambda_{111}\sigma(\alpha_1\alpha_2\gamma_1\gamma_2 + \alpha_2\alpha_3\gamma_2\gamma_3 + \alpha_1\alpha_3\gamma_1\gamma_3) \end{aligned} \tag{2.9}$$

Where γ_i are the direction cosines of the applied stress.

Shape anisotropy is the effect on the magnetic properties of a sample due to its 3-dimensional shape. Examining the magnetostatic fields within a sample, it is easy to demonstrate that the demagnetizing field is lowest along the longest axis of an arbitrary sample shape[18]. Orienting the demagnetizing field within the sample along the longest axis places the magnetic poles furthest apart. For this reason, the only sample shape with no shape anisotropy is a perfect sphere. There are other limiting cases worth considering, including ellipses (the only other shape for which exact solutions to the demagnetizing field exist), cylinders, and thin films. The general equation for the shape anisotropy constant between two directions a sample is:

$$K_{sh} = \frac{1}{2}\Delta N M^2 \tag{2.10}$$

Where ΔN is the unitless difference in demagnetizing factors along two different directions in the sample and M is the saturation magnetization of the material. The demagnetizing factors are defined to sum to one[9]:

$$N_x + N_y + N_z = 1 \tag{2.11}$$

Where N_i are the demagnetizing factors along three orthogonal axes in the sample. From this equation it can be observed that $N_d = 1/3$ for a sphere. For thin films with z defined as the out of plane direction, $N_x = N_y = 0$ and $N_z = 1$. In the case of thin films where the lateral dimensions are much larger than the thickness (l >>> t), there is essentially no demagnetizing field within the plane of the film as the magnetic charges are effectively infinitely far apart.

It is also possible to define a uniaxial anisotropy constant for a given sample. Some crystal systems, such as hexagonal close packed, are naturally described well by a uniaxial anisotropy constant owing to the much lower symmetry of the hexagonal system, relative to cubic. In this case, there is one anisotropy axis and an anisotropy plane which typically has low anisotropy within the plane. Uniaxial anisotropy is also a useful formalism for describing the net anisotropy in magnetic thin films. Multiple contributions from magnetocrystalline, magnetoelastic, and shape can be combined into one constant, K_u. This is examined in greater detail in the following chapters in the case of epitaxial and polycrystalline garnet thin films. Using the uniaxial anisotropy constant, it is then possible to estimate the anisotropy field (H_k) for the sample:

$$H_k = \frac{2K_u}{\mu_0 M_s} \tag{2.12}$$

Comparison with experimental values of the anisotropy field along the hard axis of the material can be useful in determining if the uniaxial anisotropy calculation is accurate. Alternatively, this equation can be used to calculate the uniaxial anisotropy (or a component thereof) if the anisotropy field is reliably known.

2.1.4 Magnetostriction

The magnetostriction of a material is the change in dimensions when the material is magnetized, expressed as a strain (change in length divided by length)[9,18]. The physical origin of magnetostriction is due to SOC, as the application of a strain (or the presence of a strain due to magnetization) causes a change in the orientation of the electronic orbitals as the spin rotates to follow the magnetization of the system. For a cubic system, the magnetostriction can be fully described by two magnetostriction coefficients: λ_{100} and λ_{111}. These coefficients are intrinsic properties of the magnetic material and are typically small, on the order of 10^{-5}. The magnitude of these coefficients is also known to decrease monotonically as a function of temperature. There are many practical consequences of magnetostriction in bulk samples, but this discussion will be limited to magnetic thin films on substrates. The anisotropy of a system under mechanical strain is quantified by the magnetostriction, in the form of magnetoelastic anisotropy.

For an epitaxial single crystal on a substrate with a (100) or (111) orientation, the magnetostriction can be described using the appropriate coefficient. However, for a random polycrystal it is necessary to define an average value. Akulov first proposed a solution based on the assumption that the magnetostrictively induced volumetric stress is uniform throughout the system[30]:

$$\lambda = \frac{2}{5}\lambda_{100} + \frac{3}{5}\lambda_{111} \tag{2.13}$$

Where λ is the polycrystalline average of the magnetostriction. Vladimirsky, expanded on by Callen and Goldberg, incorporated the elastic constants[31,32]:

$$\lambda = \lambda_{111} + \left(\frac{2}{5} - \frac{\ln c}{8}\right)(\lambda_{100} - \lambda_{111}) \tag{2.14}$$

where c is:

$$c = \frac{2c_{44}}{c_{11} - c_{12}} \tag{2.15}$$

where c_{ij} are the elastic constants. The correction is on the order of a few percent for garnets[33]. Note that while inclusion of the elastic properties of the material provides an improved estimate, an exact solution can only be obtained when the shape of the grains is known[34].

2.2 Garnet Structure and Magnetic Properties

2.2.1 Crystal Structure

Garnet has been used as a gemstone since the Bronze age. Naturally occurring garnets are most commonly composed of iron, calcium, and aluminum silicates[35]. However, the garnet structure is able to accommodate a tremendous variety of elements, which allows for applications as diverse as abrasives, fast lithium conducting battery solid-state electrolytes, high-level radioactive waste sequestration, magnetic storage, and more recently, spintronics[35–39].

The rare-earth iron garnets (REIG) were first synthesized and characterized in the mid-twentieth century by Pauthenet and others[23,24]. The general formula is $R_3Fe_5O_{12}$, where R is a rare-earth ion or yttrium. The unit cell consists of 8 formula units resulting in a large lattice parameter, and is in the *Ia3d* space group[40]. The prototypical REIG, yttrium iron garnet (YIG), has a lattice parameter of 1.2376 nm, and the lattice parameter for the REIG decreases with increasing atomic number due to the lanthanide contraction[41]. As there are 160 atoms in the unit cell, it is difficult to study the system from first principles, but some limited density functional theory studies have been done[42]. Cations occupy three distinct crystallographic sites, listed in order of increasing size and oxygen coordination number: tetrahedral (3 Fe^{3+} per formula unit), octahedral (2 Fe^{3+} per formula unit), and dodecahedral (3 R^{3+} per formula unit)[23]. A diagram of the unit cell and crystallographic sites is shown in figure 2.3.

2.2.2 Magnetic Properties

The REIG structure has three distinct magnetic sublattices, corresponding to the three crystallographic sites. Garnets are ferrimagnets, with the magnetism in the system being mediated via superexchange through the oxygen anions. The tetrahedral sites are antiparallel to the octahedral and dodecahedral sites, so the net magnetization can be described as:

$$M_{net} = M_{dodecahedral} + M_{octahedral} - M_{tetrahedral} \tag{2.16}$$

Where M_i is the magnetization on that sublattice. There are antiferromagnetic superexchange interactions between all three sublattices, but the Fe_{oct} – Fe_{tet} and R_{dodec} – Fe_{tet} interactions are significantly stronger than the competing interactions, leading to the moments of the dodecahedral and octahedral sublattices being ferromagnetically coupled/parallel[43]. The implications of this are that there is a net contribution of one Fe^{3+} ion that is antiparallel to the moment on the rare-earth dodecahedral site.

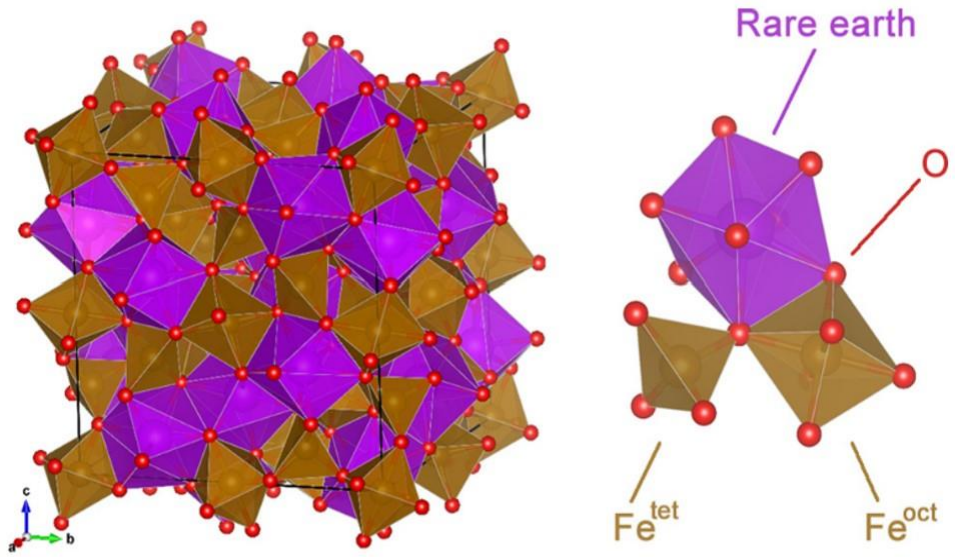

Figure 2.3: Unit cell of the rare-earth iron garnet structure (left) and the three crystallographic sites (right) in the crystal structure: tetrahedral, octahedral, and dodecahedral. From ref. 42. Used with permission.

The rare-earth ion has the largest impact on the static and dynamic magnetic properties of the system. As the number of 4f electrons varies across the lanthanide series, there is a significant

variation in the magnetic moment. In the garnets, the 3+ oxidation state is the ideal stoichiometric case, but off-valence states are known to exist, such as Ce^{4+}, Eu^{2+}, and Tb^{4+} [44–46]. This in turn leads to the presence of off-valence iron due to the requirement of charge neutrality. However, this has proven difficult to quantify with easily accessible laboratory techniques such as x-ray photoelectron spectroscopy (XPS) or wavelength dispersive spectroscopy (WDS), necessitating the use of more exotic techniques and subsequent modeling of the spectra, such as x-ray absorption spectroscopy (XAS) or x-ray magnetic circular dichroism (XMCD), which are only available at large synchrotron facilities[47].

The moments of the rare-earth ions have a much stronger temperature dependence than that of iron owing to the much larger values of the total angular momentum, J. As a result, the moments of the rare-earths become significantly smaller than iron at room temperature. For the heavier rare-earth ions, where the spin and orbital angular momentum add as the *4f* shell is more than half full (Gd, Tb, Dy, Ho, and Er), these materials exhibit a magnetic compensation temperature (T_{Comp}), where the net moment of the material becomes zero(see figure 2.4)[48]. Tm, Yb, and Lu do not exhibit a T_{Comp}, as the moment of these ions is relatively small. There has been several reports of TmIG thin films exhibiting a T_{Comp}, but these values vary in the range 2-80 K depending on the growth method and research group[49,50]. The REIG with rare-earth ions lighter than Gd do not exhibit a magnetic compensation temperature, as the total angular momentum for these ions is smaller, due to the *4f* shell being less than half full and the resulting opposite signs of the spin and orbital angular momentum components[51]. Above T_{Comp}, the moment increases until some temperature, before approaching zero as the Curie temperature is approached. The moments of

the rare-earth ions decrease much more quickly as a function of temperature as a result of the size of their moments, described by the Brillouin function[18]:

$$\frac{M}{M_0} = \frac{2J+1}{2J}\coth\left(\frac{2J+1}{2J} * \frac{gJ\mu_B H}{k_B T}\right) - \frac{1}{2J}\coth\left(\frac{1}{2J} * \frac{gJ\mu_B H}{k_B T}\right) \quad (2.17)$$

Where M is the magnetization at temperature T, M_0 is the zero-temperature magnetization, J is the total angular momentum, g is the g factor, μ_B is the Bohr magneton, H is the applied magnetic field or molecular field, and k_B is the Boltzmann constant.

At the magnetic compensation temperature, the material is effectively an antiferromagnet, as the moment is very nearly zero and the coercivity diverges. The garnets, and other ferrimagnets, also exhibit an angular momentum compensation temperature (T_{Ang}), where the net angular momentum of the system goes to zero. As opposed to the magnetic compensation temperature, which can be measured easily with magnetometry, it is difficult to measure T_{Ang} because it does not readily correspond to observable properties. T_{Ang} is not the same as T_{Comp} because the g factors and gyromagnetic ratios of the sublattices differ. For the transition metals including Fe, the orbital angular momentum is quenched by the molecular field, so the value of $g_{Fe} \approx 2$. The rare-earth elements do not have the orbital component quenched, so $g_{RE} \neq 2$ (except for Gd^{3+}) T_{Ang} occurs when[52,53]:

$$A = A_{Fe} + A_{RE} = \frac{M_{Fe}}{g_{Fe}} + \frac{M_{RE}}{g_{RE}} \quad (2.18)$$

Where A_i is the (net) angular momentum for that species, M_i is the (net) magnetic moment. The g factors (or gyromagnetic ratios) and precise magnetization values are difficult to determine and must be done across the temperature range to determine T_{Ang} in this manner. However, an estimate can be made if the sublattice magnetizations are calculated via model. Using a molecular field coefficients model (see chapter 8), the individual sublattice magnetizations were calculated, and

using the free-ion g factors of the rare-earths and iron several estimated angular momentum compensation temperature values are shown in Table 2.1. Recently however, it has been predicted that the maximum domain wall velocities occur at T_{Ang}, and this has become an experimentally feasible way to determine or estimate this temperature[52–54]. T_{Ang} has not been well studied in REIGs, with Randoshkin performing some experiments on complex compositions intended for bubble domain devices[55,56]. This work will focus on the magnetic compensation temperature.

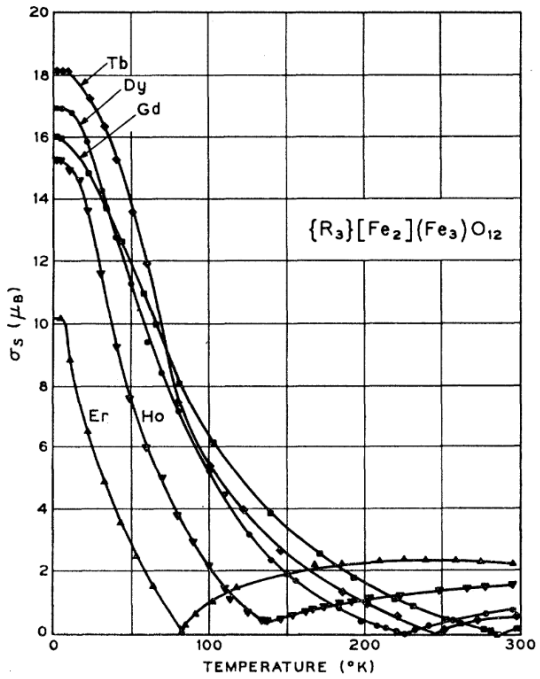

Figure 2.4: Magnetic moment vs. temperature for the REIG that exhibit a compensation temperature (Gd, Tb, Dy, Ho, and Er). From ref. 48. Used with permission.

Table 4.1: Table of magnetic compensation temperatures and estimated angular momentum compensation temperatures calculated via a molecular field coefficients model and free ion g factors[48]. The free ion g factor is a decent approximation for Tm and the other ions (free ion g = 7/6, experimental g = 1.15)[47].

Rare-earth iron garnet	Magnetic Compensation Temperature (K)	Estimated Angular Momentum Compensation Temperature (K)
GdIG	288	300
TbIG	246	350
DyIG	223	355
TmIG	---	75

2.3 Magnetic Proximity Effect

As discussed previously, only a small number of elements order ferromagnetically. For metals, another way to understand this to consider the energy that would be saved by having an unequal proportion of spin up and spin down electrons. There are two components to the possible energy savings: the number of electrons (or states) involved, and the energy saved from ordering ferromagnetically (the exchange integral). This is quantified in the Stoner criterion[57]:

$$Ug(E_F) > 1 \tag{2.19}$$

Where U is the exchange integral, and $g(E_F)$ is the density of states at the Fermi level. Thus, ferromagnetism occurs when there is a large energy savings and a large density of states at the Fermi level, which can be understood as there being many electrons that would change their polarization to save energy. Plotting the density of states and exchange integral as a function of atomic number (figure 2.5), the traditional ferromagnetic elements are immediately apparent[57,58]. In figure 2.5c, there are several elements that are close to the Stoner criterion (the dashed line), but not quite at the threshold. These elements, and others not pictured in this plot, are close enough to being ferromagnetic that a moment can be induced in the material when placed next to a ferromagnetic material. This is known as the magnetic proximity effect (MPE), first demonstrated in Pd[59]. The MPE has since been observed in metals including Pt, Ta, W, Ir, topological insulators such as Bi_2Se_3, and graphene[60–63].

Although the MPE was first reported in 1969 by Hauser, there was already mounting evidence that some additional exchange coupling was present in magnetic/non-magnetic/magnetic thin film structures. Dreyfus *et al.* first reported the theory that an RKKY-type interaction, which is mediated by conduction electrons, was able to couple magnetic layers through an intermediate

nonmagnetic thin film[64]. This was confirmed experimentally in NiFe-M-Co films, where M was Au, Ag, Cr, or Pd, where an additional indirect exchange coupling is necessary to explain the results involving Pd[65]. In 1985 White and Friedman presented a more complete theory on the MPE, which again attributed the MPE in Pd to RKKY interactions through conduction electrons interacting at the interface with the magnetic layer[66].

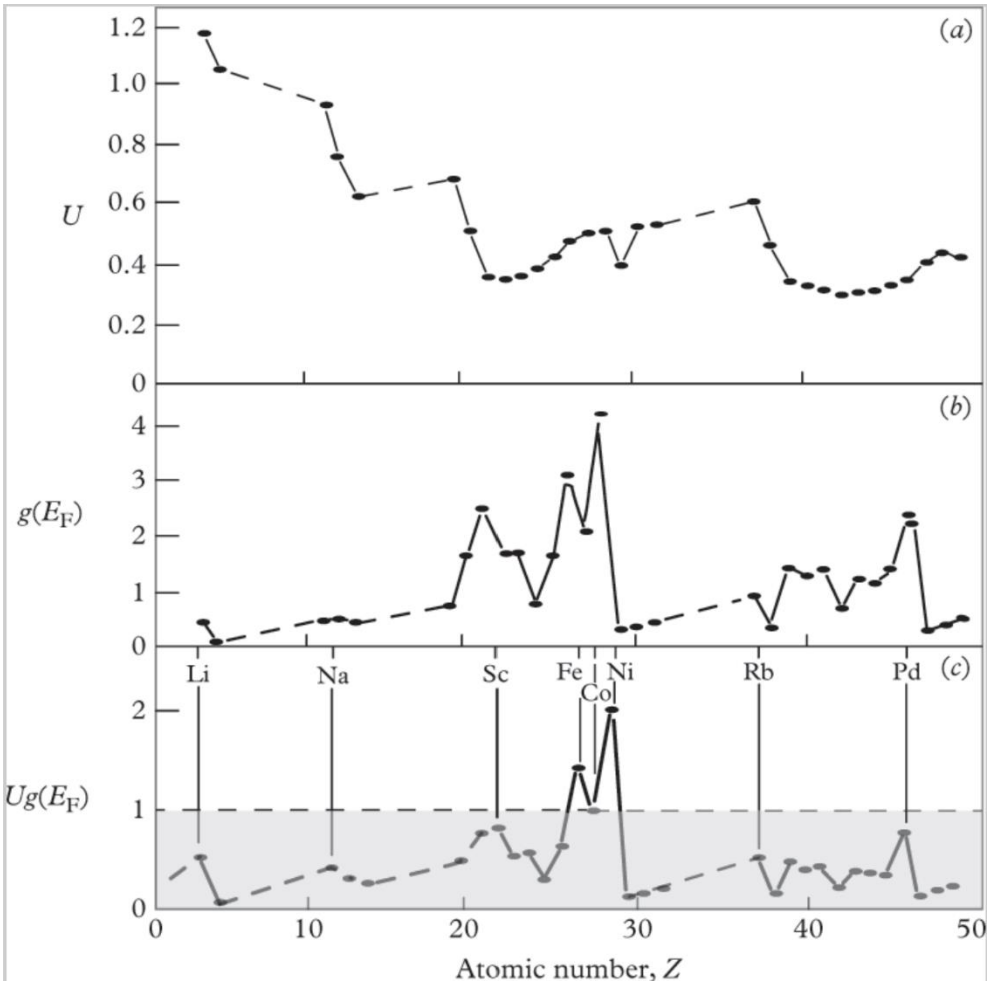

Figure 2.5: Plot of (a) exchange integral in eV, (b) density of states at the Fermi level, and (c) the product of the exchange integral and the density of states at the Fermi level as a function of atomic number. Ferromagnetism occurs when the Stoner criterion is satisfied (dashed line in (c)). Note that some elements are very close to this criterion. From refs. 58-59. Used with permission.

For structures involving magnetic metals, the RKKY interaction serves as a reasonable explanation for the occurrence of the MPE. However, the MPE has also been well documented in heterostructures with magnetic insulators, including spinels and garnets[67–70]. An unanswered

question is what mechanism leads to the occurrence of the MPE when there are no conduction electrons to induce an RKKY type interaction. To elucidate the source of the induced moment in heterostructures with an insulator, several groups have conducted density functional theory (DFT) simulations of these materials. For the case of platinum, the simulations indicate that orbital hybridization and changes to the band structure of the *5d* orbitals in the heavy metal with the *3d* orbitals in the magnetic cation (typically Fe) induces the moment in the *5d* orbitals[70,71]. Calculations indicate similar modification of the band structure in graphene and topological insulators by the presence of the magnetic cation[69,72].

While DFT simulations provide some understanding of the strength of the MPE and when it is likely to occur, an understanding of the phenomenon is still lacking. An indirect way to investigate the mechanism is by studying the proximity effect in materials that have a compensation temperature. Systems that exhibit a magnetic compensation temperature typically have a rare-earth populated sublattice that dominates the net moment at low temperatures and a transition metal sublattice that is dominant at higher temperatures. Several studies on rare-earth-transition metal alloys and the REIG have indicated that the transition metals dominate the magnetotransport of the system, as the electrons in the *3d* orbitals responsible for the magnetism is close to the Fermi level, whereas the *4f* orbitals in the rare-earths are buried far below the Fermi level[45,73,74]. Thus, the conduction electrons in metallic magnets are likely the source of the MPE through the RKKY interaction, and the MPE tracks the magnetization of the transition metal and changes sign at the magnetic compensation temperature[75]. Insulating magnets require a different solution, which has not previously been studied in depth. This is examined in further detail in chapter 6 of this thesis.

The magnetic proximity effect can have relatively large strengths (~0.3 μ_B/Pt atom), but this is confined to the first 1-2 nm of the induced material adjacent to the magnetic layer, decaying exponentially[70,76–78]. As the magnitude is relatively small and the amount of material is miniscule, it is almost impossible to detect with bulk magnetometry. For this reason, x-ray magnetic circular dichroism (XMCD) has commonly been used as a technique to study the MPE, as the elemental specificity allows detection of small magnetic moments in very thin layers[76,79,80]. Polarized neutron reflectometry (PNR) has also been demonstrated as an effective way to study the MPE, by fitting a model to the experimental reflectivity curves it is possible to study proximity induced magnetism, including the depth of penetration into proximitized layers[49,81,82]. It is also possible to examine the contribution of the MPE to spin transport in magnetic/non-magnetic heavy metal film heterostructures. A heavy metal film can generate an anomalous Hall effect-like signal through the spin Hall effect, while a proximitized magnetic layer can generate an additional anomalous Hall effect-like signal, which either adds to or competes with the signal from the spin Hall effect. However, there is some controversy over whether the magnetotransport signals attributed to the MPE are due to proximity or due to other spurious effects such as spin reorientation temperatures, inhomogeneity, other interfacial phenomena (such as the Rashba effect, the Dzyaloshinskii-Moriya interaction, or a two-dimensional electron gas) or other temperature-dependent phenomena within the heavy metal layer[49,67,83–85]. In this work, study of the magnetic proximity effect was conducted with PNR and XMCD to provide elemental and layer resolved specificity.

2.4 Spintronics

2.4.1 Motivation

The incredible technological development of the last half century has been predicated on the ability to squeeze ever greater performance out of integrated circuits. For much of this time period, this

was embodied in the economic and technological prediction that came to be known as Moore's law, predicting a doubling of transistor density every two years[86]. While the end of Moore's law has long been predicted, the state-of-the-art transistor nodes are now on the length scale of a few nanometers, at which point the quantum mechanical behavior of electrons introduces technical challenges that may be impossible to overcome.

To continue to reap the incredible economic benefits and technological advances of the rapid scaling in microelectronics, it has become imperative to explore alternative technologies that can provide greater performance. One of the most promising areas is spintronics, in which the spin of the electron (which can be referred to as "up" or "down") is manipulated[5,87,88]. Since the 1960's it has been known that the behavior of electrons in conductive magnetic materials is different depending on the spin state of the electron[89,90]. The electrons can be treated in a two current conduction model, where the majority spin electrons have a much higher conductivity as there are many states for the electrons to non-spin-flip scatter into and comparatively few for the minority spin electrons, as a result of the spin-split *3d* bands[91]. This property of magnetic metals became technologically relevant with the discovery of giant magnetoresistance in Fe/Cr/Fe multilayers in 1988, a discovery which would go on to win the Nobel prize in Physics less than twenty years later[92]. This was the first major application of spintronics, where the different spins of the electron were relevant to the operation of an electronic device. Magnetoresistive read heads are the critical part of the read head in all modern hard disk drives, which makes up the majority of all data storage.

Magnetic materials are an ideal choice for both short and long term memory, as the hysteretic state is nonvolatile, not requiring energy input to maintain the state[93,94]. Magnetic storage media is

already commonplace in long term storage, and the next frontier is short term memory, or random-access memory (RAM). Conventional DRAM (dynamic RAM) consists of a one transistor, one capacitor structure that requires constant energy input to maintain this state[95,96]. However, magnetic RAM (MRAM) is a very promising alternative. MRAM uses a series of magnetic tunnel junctions (MTJs) to replace the capacitors in conventional DRAM[93,97,98]. MTJs are composed of a layer of very thin oxide between two magnetic metal layers. MTJs based on CoFeB and MgO with perpendicular magnetic anisotropy have shown tunnel magnetoresistance values as high as 600%, allowing for robust sensing of the magnetic state[99,100]. It is desirable to have magnetic memory based on PMA materials as this allows for greater packing density and the use of higher anisotropy materials which results in better data retention rates[97].

There are also opportunities beyond memory for magnetic materials to improve the performance of integrated circuits. Novel designs such as spin based transistors and domain wall logic devices have been realized at small scales, with the capability to perform logic operations in the same manner as conventional complementary metal oxide semiconductor (CMOS) devices[7,101,102]. For a variety of reasons that will be discussed in more detail later, these spin based devices also have the potential to be drastically more energy efficient, far below the thermal limit of conventional devices[103]. Many of these devices are compatible with CMOS back-end-of-line processes, facilitating rapid integration with existing technology[104,105].

There is currently a large interest in developing the next generation of spintronic materials, and the emerging physics behind the manipulation of these materials. Antiferromagnetic materials are very interesting as they offer the potential of dynamics in the terahertz regime, compared to

gigahertz for ferromagnets[21,106]. While these ultrafast dynamics are promising to push performance in next-generation devices, antiferromagnets are more complex to work with, as there is no stray magnetic field or state to detect or manipulate. Nonetheless, antiferromagnetic materials have been switched with electrical methods, and it is possible to detect different antiferromagnetic domains and orientations with specialized device geometries and electrical measurements[20,107–109]. A compromise between the difficult of working with antiferromagnetic materials and the fast dynamics afforded by the strong exchange coupling is ferrimagnetic materials. The strong exchange coupling between the antiparallel sublattices provides similarly rapid dynamics, but the chemically and magnetically different sublattices allow for easy sensing of the state of the material via optical or electrical methods, which are often sensitive to only one sublattice and not the total moment[25,54,110].

Combined with the push for improved materials, novel physics on the horizon promise extremely efficient switching through the use of topological insulating materials and spin-orbit torques (discussed more in a following section). Topological insulators are insulating in the bulk phase, but have topologically protected conducting surface states that are spin momentum locked, allowing transfer of pure spin angular momentum into an adjacent magnetic layer[111–114].

2.4.2 Spin Transfer Torque

The reliable and efficient manipulation of magnetic materials is crucial for the development of magnetic memory and logic. The first response to this issue involved used magnetic fields to alter the state of a device. However, this method has issues of a large stray field that can affect adjacent bits unintentionally, and the power consumption does not scale to lower values in the way that device sizes do. The alternative is through the use of electric fields and electric current, which

offers the additional benefits of scaling well with device sizes and the decades of research and integration into small electronic devices.

The question becomes how to manipulate a magnetic material with electric current. In a metallic ferromagnet, the spin-split bands result in an unequal population of spin up and spin down electrons. This net spin-polarization can be quantified as[12]:

$$P = \left|\frac{n_\uparrow - n_\downarrow}{n_\uparrow + n_\downarrow}\right| \tag{2.20}$$

Where $n_\uparrow$ is the number of spin up electrons and $n_\downarrow$ is the number of spin down electrons. For the transition metals, the value of the polarization ranges from 0.11-0.44[12]. These values of polarization are enough to exert effects on magnetic layers, but it can be improved through materials selection. Certain oxides, such as CrO_2 and Fe_3O_4 and Heusler alloys can have P = 1, which are known as half-metallic magnets[5,12,115]. This very high polarization and long spin diffusion lengths make these materials very promising for applications in next generation MRAM devices.

With the discovery of giant magnetoresistance in Fe/Cr/Fe superlattices, it is well understood why the resistance varies depending on the relative alignment of the magnetic layers. This structure is known as a spin valve, which is functionally the same as an MTJ. The low resistance state occurs when the two magnetic layers are parallel, and the high resistance state is when the layers are antiparallel. What is needed is how to manipulate the direction of one of these magnetic layers to change the resistance of the bit. By passing a spin polarized current, usually generated by a magnetic layer such as Fe, through a magnetic layer, a torque is exerted on this layer if the polarization of the current is opposite to the polarization of the magnetic layer. This effect was

first discovered and characterized by John Slonczewski in 1989 and has since become known as spin-transfer torque (STT)[116].

The mechanism behind STT is quite simple. Flowing a spin-polarized current through a magnetic metal results in a transfer of angular momentum between the polarized electrons and the magnetic moment of the conductive metal, leading to a rotation of the magnetic moment[117]. This can be described through a modification to the Landua Lifshitz Gilbert equation, derived through the conservation of the angular momentum[118,119]:

$$\frac{d\vec{M}}{dt} + \nabla \cdot \overrightarrow{J_m} = -\vec{M} \times \overrightarrow{H_{eff}} - \frac{\alpha}{M_s}\left[\vec{M} \times \left(\frac{d\vec{M}}{dt} + \nabla \cdot \overrightarrow{J_m}\right)\right] \tag{2.21}$$

Where J_m is the magnetization current (spin current x γ, the gyromagnetic ratio).

Spin-transfer torque has been used to implement a huge variety of magnetic devices, including MRAM, which is now available in commercial modules with capacities up to a gigabit. However, there are limitations. The first is that as the mechanism is based on conduction electrons affecting the moment of a magnet as the current flows through it, the mechanism is limited to conductive magnets. Additionally, the efficiency is relatively low. The amount of torque exerted is directly related to the number of spin polarized electrons that reach the magnetic layer to be switched. As spin polarization is relatively low for the transition metal ferromagnets this increases the current density needed to reach the threshold switching current. Also, to achieve higher MRAM densities for higher capacity storage, the bit size must be decreased. Doing this requires a commensurate rise in the magnetic anisotropy according to[97]:

$$\Delta = \frac{E_b}{k_B T} = \frac{\mu_0 H_K M_S V}{2 k_B T} \tag{2.22}$$

Where Δ is the thermal stability parameter, E_b is the energy barrier to magnetization reversal, and V is the volume of the magnetic bit. Δ is typically on the order of 60 for a retention rate of 10 years. This higher anisotropy requires yet higher currents to switch the state of the bit, drawing more energy and leading to greater resistive Joule heating, which is associated with failures in the MgO tunnel barrier, reducing endurance of the memory[120,121]. To bring spintronics to parity with conventional microelectronics, a more efficient switching mechanism and a broader variety of materials must be developed.

2.4.3 Spin Hall Effect

The Hall effect, named after Edwin Hall who discovered it in 1879, is the development of an electric field across a conductive material in a magnetic field, with the electric field perpendicular to both the current direction and the applied magnetic field[122]. The Hall effect (or ordinary Hall effect, OHE) occurs in any conductive material, and is a useful method for characterizing the electrical transport properties of semiconductors and metals[123]. In materials with high spin-orbit coupling (SOC), such as heavy metals (including Pt, Ta, W) and topological insulators (TI, including Bi_2Te_3), a similar effect has been shown to occur, even in the absence of an external magnetic field. First predicted in 1971, this spin Hall effect (SHE) is the production of a pure spin current that is transverse to an electric current flowing through the material[124,125]. In essence, spin up electrons and spin down electrons accumulate on opposite sides of a conduction channel, which can then be measured as a voltage or imaged with the Kerr effect or similar microcopy technique (see figure 2.6)[126,127].

The efficiency of the SHE is characterized with the spin Hall angle (SHA), which is the dimensionless ratio of the generated spin current density and the applied charge current density[128]:

$$\Theta_{sh} = \frac{J_s}{J_c} \quad (2.23)$$

Where θ_{sh} is the SHA, J_s is the spin current density, and J_c is the charge current density. Note that the SHA is negative for some materials, indicating an opposite spin polarization to other materials. The first materials in which the SHE was observed were semiconductors, including GaAs and ZnTe, which produced very small spin accumulation[129,130]. The SHA depends strongly on the SOC in the material, which scales approximately with Z^4 [131]. The first material with a demonstrated significant SHA was platinum with a value of $\theta_{sh} \approx 0.10$, which indicates that the charge current is interconverted to a pure spin current with an efficiency of roughly 10%[132]. The *5d* heavy metals have proven to be excellent spin Hall materials, with Ta and β-phase W demonstrating SHA values on the order of -0.07 and -0.33, respectively[128,133]. Gold is the exception to this rule and the lighter transition metals such as Cu exemplify this Z^4 scaling well, with SHA several orders of magnitude lower than that of the *5d* metals[131].

There has also been reports of ferromagnetic materials having SHA close to 1, but this leads to very small spin diffusion lengths which prevent significant spin accumulation[134]. Topological insulators such as $Bi_{1-x}Sb_x$ and Sb_2Te_3 offer the promise of high conductivity and very large SHA values, even in excess of 50 due to spin momentum locking in the topological surface states[135,136]. However, these exotic materials contain toxic elements and require exotic growth methods such as molecular beam epitaxy, so further material optimization is needed before these materials could realistically be integrated with existing CMOS processes.

The spin Hall effect is the conversion of a charge current to a pure spin current, but the inverse process, the inverse SHE (ISHE) is also of technical interest. The ISHE describes the conversion

of a pure spin current to a charge current, which can be measured experimentally as a voltage in the transverse direction. The ISHE was observed well before the SHE in 1984, as the experiment is somewhat simpler in that it is only necessary to measure a transverse voltage[137]. The ISHE has been known to be significant in systems involving nonmagnetic heavy metals since 2001, where it was found that the ferromagnetic resonance linewidths in metal trilayers increased significantly if the nonmagnetic metal had large spin orbit coupling[138–140]. This increase is due to spin pumping from the heavy metal into the magnetic layer via the ISHE. Similar to the SHE, a weak ISHE has been observed in light ferromagnetic transition metals and other more exotic materials[141].

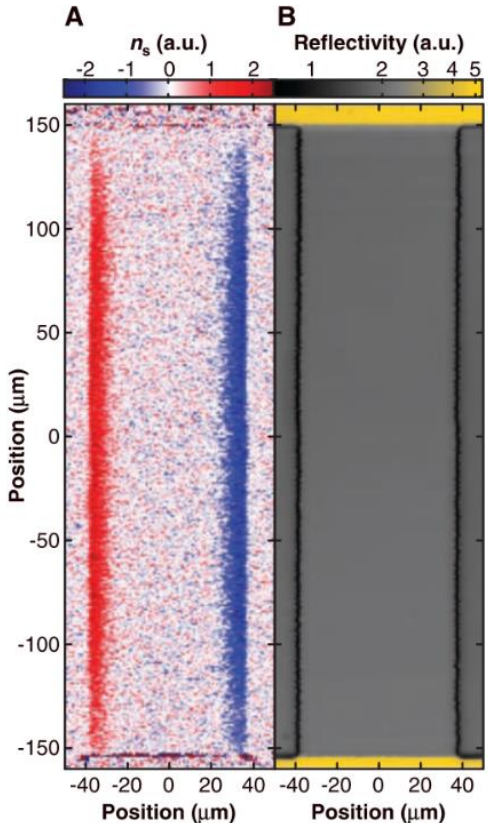

Figure 2.6: Magneto-optical Kerr effect images of the (A) spin density and (B) reflectivity in an unstrained GaAs sample measured at 30 K. The lines indicate the accumulation of spin on opposite sides of the sample, transverse to the charge current. From ref. 126. Used with permission.

The most exciting aspect of spin Hall effects are the ability to produce a pure spin current, without any accompanying electronic motion. This spin current can be pictured as a magnon, the collective

rotation of atomic spins as a continuous wave while the electrons and atoms are stationary (see figure 2.7)[39]. Without the requirement of electronic flow to transmit a spin current, this opens the tantalizing possibility of using insulating magnetic materials to transmit and receive signals. This was first demonstrated by Kajiwara et al. in 2011 in a Pt/YIG structure where an electrical signal in Pt was converted to a pure spin current via the SHE, transmitted into the YIG layer and carried over a distance of ~mm, and interconverted back to an electrical signal by the ISHE in another Pt electrode[39].

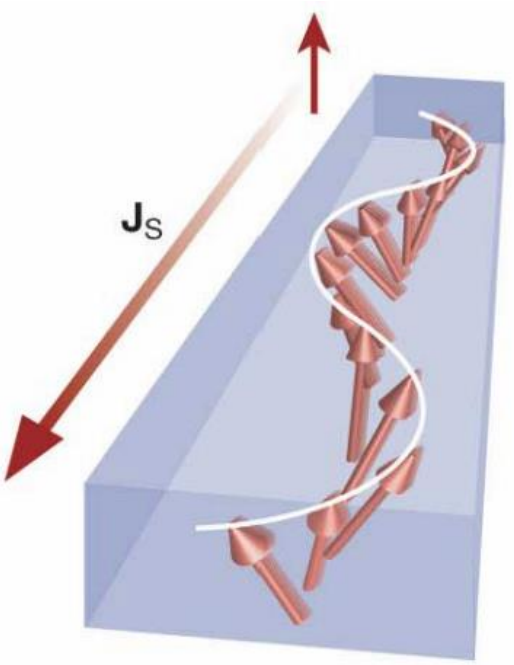

Figure 2.7: Illustration of a spin wave propagating in a magnetic material. The pure spin current J_s propagates through collective motion of the stationary magnetic moments in the material. From ref. 39. Used with permission.

This breakthrough has had a tremendous impact on the scope of magnetic materials that can be integrated into spintronic devices. Without the prerequisite of electrical conductivity, it became possible to integrate magnetite, spinels, garnets, and many other oxides and insulating magnetic materials into novel structures, where the SHE/ISHE in (typically) heavy metals is used to interface with electrical signals. Another important consequence is that this opens the possibility of ultra-low dissipation spintronic devices. No electronic motion occurs to create resistive heating and

ohmic losses with a pure spin current, so the only losses are due to magnetic damping, which is comparatively very efficient[103].

2.4.4 Spin-Orbit Torque

Having now realized an effective way to produce a pure spin current in materials with high spin-orbit coupling, the question becomes if this spin current can be put to use. In 2008 Ando et al. demonstrated that an in-plane current conducted through $Ni_{81}Fe_{19}$/Pt heterostructures modulates the ferromagnetic resonance behavior of the heterostrutures[142]. The spin Hall effect was correctly identified as the source of the torque in this system, but the torque was weak enough to only alter the resonance that was driven externally during the measurement. Liu et al. later demonstrated that in similar heterostructures that sufficient current densities were capable of generating precession via spin injection from the spin Hall effect alone; inducing effects similar to FMR without external intervention[143]. The next major development was the discovery that when a large enough current density is applied along with an external in-plane field, the magnetization can be reversed completely via torque generated from the SHE in adjacent heavy metal layer[133,144].

The origin for this torque, known as spin-orbit torque (SOT), is rooted in the transfer of angular momentum from the crystal lattice to the spin structure in a material, mediated by materials with large spin-orbit coupling[145,146]. Spin-orbit torques act in a fundamentally different manner from spin-transfer torques as the physical origins are distinct. As discussed previously, STT are generated by passing a current through a spin polarizer (usually another magnetic material), and the resulting net spin density does work on a magnetic layer it is conducted through in most commonly a perpendicular current path geometry. SOTs are generated via in-plane current in a heterostructure of a material with high spin-orbit coupling and a magnetic material, through which

a pure spin current is injected into the magnetic layer. The symmetry of these torques is also different, with the SOT being described via[145,147]:

$$\frac{d\vec{m}}{dt} = -\gamma\vec{m} \times \overrightarrow{H_{ext}} + \alpha\vec{m} \times \frac{d\vec{m}}{dt} + \frac{\gamma}{M_s}\vec{T} \quad (2.24)$$

$$\vec{T} = \tau_{FL}\vec{m} \times \vec{\sigma} + \tau_{DL}\vec{m} \times (\vec{m} \times \vec{\sigma}) \quad (2.25)$$

Where $\vec{m} = \vec{M}/M_s$ is the magnetization unit vector, $\vec{T}$ is the torque applied to the system (formally, a torque that does not originate from an energy density), $\vec{\sigma}$ is the injected spin polarization from the SHE, τ_{FL} is the magnitude of the field-like torque, and τ_{DL} is the magnitude of the damping-like torque. The field-like and damping-like (or Slonczewski) torques are so named for their similarities to the effect of an external magnetic field and magnetic damping, respectively, on the dynamics of the system (figure 2.8). Note this discussion and equations are derived for perpendicularly magnetized materials.

For spin-orbit torques to switch the magnetization of a material, an in-plane magnetic field or some other mechanism of symmetry breaking is necessary. The reason for this is rooted in the structure of the domain walls present in the magnetic film. In ultra-thin magnetic films, Néel domain walls (where the magnetization vector rotates perpendicular to the plane of the domain wall) are typically preferred[9]. Homochiral Néel domain walls are commonly stabilized via a significant Dzyaloshinskii-Moriya interaction (DMI), which results in a signal domain wall chirality in the system. However, the result of this is that SOTs are not able to switch the magnetization via domain expansion as all domain walls are shifted in a given direction by the applied torque (see figure 2.9). To prevent this an in-plane field with strength greater than the DMI effective field (H_{DMI}) is applied to break the symmetry of the domain walls[148]. This field then allows magnetization reversal to occur via expansion of the preferred domain orientation and contraction of the other domains in a perpendicular magnetized film.

The requirement of an external in-plane field is somewhat of an obstacle to integration with future devices, but there is much active research to overcome this requirement. Several studies have shown that there are multiple ways of breaking the in-plane symmetry through designed structural asymmetry, microstructural variations, and interaction between STT and SOT in more complex devices[149–152]. SOT also separates the read and write paths for memory. Large writing currents are often necessary to reverse the state of high anisotropy magnetic materials in MRAM, but these high write currents have also been associated with low endurance in the tunnel barrier of MTJs.

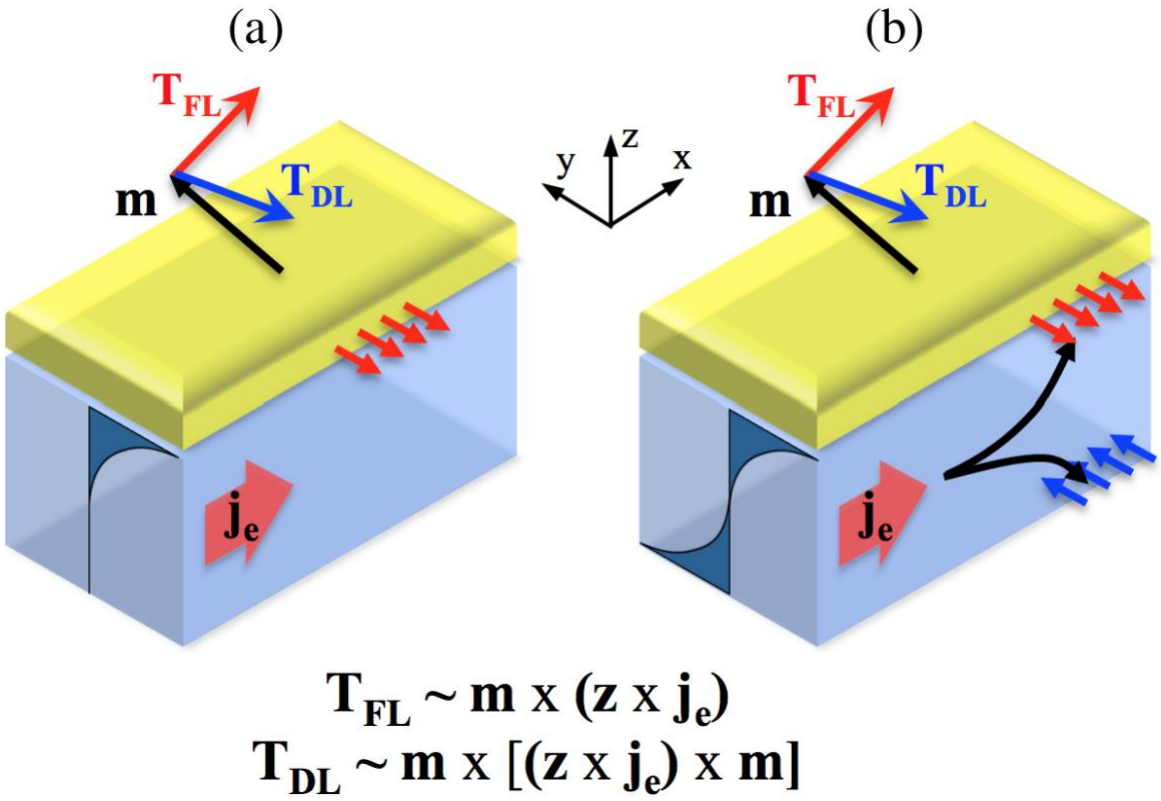

Figure 2.8: Geometry and symmetry of the field-like (FL) and damping-like (DL) spin-orbit torques acting on the magnetization vector (m) in a system. (a) Generation of SOT via the inverse spin galvanic effect. (b) Generation of SOT via the spin Hall effect. Note the result is independent of the mechanism. From ref. 145. Used with permission.

Separating the read and write paths removes this obstacle (the write path is in-plane, not requiring a tunnel current to be used), at the expense of now requiring a three terminal device as opposed to a two terminal one[4]. This will decrease the density of these materials, but even so there may still be application for these materials in processor caches and lower density random access memory[145].

Spin-orbit torque has several benefits over spin-transfer torque. As the mechanism of STT is dependent on conducting electrons through the magnetic material that is to be switched, the most work that each electron to do is transfer one unit of angular momentum, before the electron is then conducted out of the magnetic layer. SOT on the other hand uses a current in-plane geometry, where the charge current is conducted parallel to the magnetic layer. This geometry allows electrons to be repeatedly collide and scatter with atoms in the magnetic layer at the interface, transferring multiple units of angular momentum per electron[145]. The in-plane area is typically several orders of magnitude larger than the cross-sectional area, leading to much larger switching efficiencies relative to STT through the different generation mechanism of the torque and geometry[153]. For this reason, SOT is also more efficient at switching larger sample areas. Finally, STT switching is stochastic in nature, requiring thermal fluctuations to overcome the energy barrier. SOT on the other hand is fully deterministic, not relying on thermal effects and thus allowing for faster operation and a lower error rate[154,155].

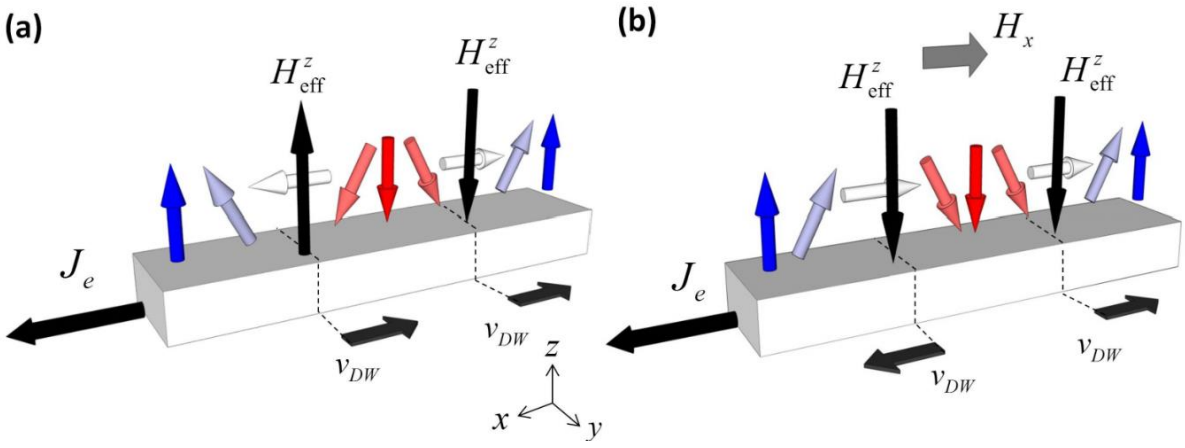

Figure 2.9: (a) Current-induced domain wall motion in a perpendicularly magnetized heterostructure driven via spin-orbit torque. H_{eff}^z is the SOT effective field acting on the chiral Néel domain wall and v_{DW} is the domain wall direction. (b) Current-induced domain wall motion and domain expansion in the presence of an in-plane field H_x, which realigns the moments in the domain walls by overcoming the DMI effective field. From ref. 148. Used with permission.

2.4.5 Garnet Spintronics

The preceding sections have culminated in the following point: it is technologically possible and desirable to create spintronic materials and devices using insulating magnetic materials, in particular the magnetic garnets. The primary obstacle to engineering devices with insulating magnets was the inability to manipulate them outside of an external field. The discovery that the spin Hall and inverse spin Hall effects could be used to transmit electrical signals through yttrium iron garnet and the subsequent development of spin-orbit torques to switch materials through a charge current in an adjacent layer brought these materials to the forefront of spintronics research[39,144].

The next step was to examine the effects of heavy metal generated SOT on an insulating system. Li et al. demonstrated current-assisted switching in the high anisotropy Pt/$BaFe_{12}O_{19}$ system, where the coercivity of the film could be altered via an injected spin current from the Pt layer[156]. Complete switching was not achieved due to the very high coercivity and anisotropy of the barium hexaferrite layer, but the coercivity could be modulated to higher or lower values depending on the current polarity, clearly exhibiting the effect of SOT in the magnetic layer. Current-induced switching was achieved shortly after in a Pt/$Tm_3Fe_5O_{12}$ (TmIG) bilayer structure by Avci et al[8]. The perpendicular anisotropy and low coercivity of the TmIG layer allowed for reversible SOT switching with current densities as low 5×10^{10} A m^{-2}, dependent on the strength of the in-plane symmetry breaking magnetic field (see figure 2.10). These results convincingly demonstrated that magnetic insulators are viable options for next-generation spintronic devices, opening a new materials landscape.

Rare-earth iron garnets offer many benefits as spintronic devices, which will be discussed in detail here. The first is due to its insulating properties. Yttrium iron garnet (YIG) is a good insulator, with an electronic band gap of ~2 eV, larger than that of silicon's 1.1 eV indirect band gap, and the rest of the rare-earth iron garnets are likely similar[157]. Thus, in a bilayer with a heavy metal, virtually no electronic current passes through the garnet layer. This results in a higher current density in the heavy metal compared to a bilayer with a magnetic metal for the same applied current as the conductive cross section is smaller, resulting in higher efficiency. Additionally, there is no resistive Joule heating in the magnetic layer, which can cause endurance problems in devices and lead to loss of the magnetic state[4].

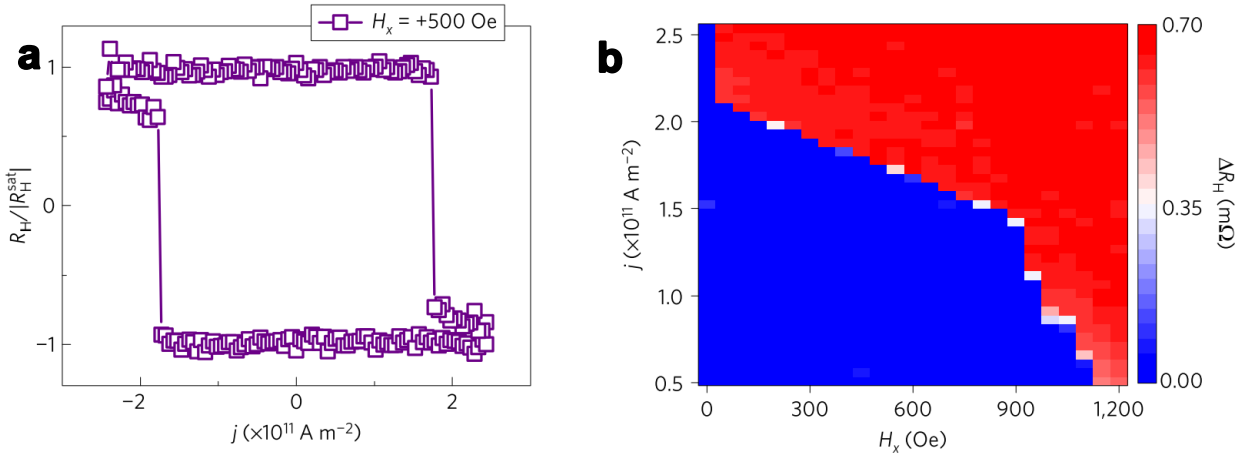

Figure 2.10: (a) Current-induced switching of an insulating magnetic layer in a Pt/TmIG heterostructure under a 500 Oe in-plane field. (b) Switching phase diagram of the Pt/TmIG system, indicating that larger in-plane fields decrease the critical switching current. From ref. 8. Used with permission.

The anisotropy of REIG are also easily controlled. For epitaxial, single crystal films, careful selection of rare-earth ion and substrate allows growth of films with robust perpendicular magnetic anisotropy (PMA), which is desirable for use with highly efficient spin-orbit torques and increased packing density in magnetic storage media[4,45,158,159]. The magnetoelastic anisotropy, determined by the magnetostriction of the rare-earth ion, dominates the total anisotropy of garnet thin films, which allows for tuning of the material system to match the specific application. Outside of single

crystal films, garnets have been extensively studied as polycrystalline materials, where the anisotropy of the material is typically in-plane[160,161]. However, in the following chapter the growth of characterization of polycrystalline garnets with PMA will be discussed in detail.

Garnets are ferrimagnets, comprising three antiferromagnetically coupled sublattices (two in the case of YIG). The superexchange interactions between the sublattices are significantly stronger than the interactions within the sublattices, so the dynamics of the system are more similar to that of antiferromagnets than ferromagnets[162]. The reason for this is rooted in the different reversal mechanism of antiferromagnets and ferromagnets. Ferromagnets reverse via a collective motion of atomic moments (in some cases), where the energy barrier that must be overcome is the anisotropy in the material. On the other hand, antiferromagnets reverse via canting of the individual sublattices, and the energy barrier is the exchange energy between the sublattices[163]. As the exchange energy is several orders of magnitude higher than the anisotropy energy, the result is that the dynamics of antiferromagnets are several orders of magnitude faster than that of ferromagnets, in some cases being in the terahertz regime[21,164].

However, these ultrafast antiferromagnet-like dynamics do not occur throughout the temperature range of the system. As discussed in section 2.2.2, ferrimagnetic materials such as the garnets can have both a magnetic and angular momentum compensation temperature. Antiferromagnetic materials possess identical opposing sublattices, so there is no net angular momentum, which contributes to these ultrafast dynamics[165]. For ferrimagnets, the dynamics are generally faster than that of ferromagnets, but the maximum speeds are achieved at the angular momentum compensation point (temperature for a specific composition, or a given composition at a specified

temperature), as predicted through phenomenological domain wall models and domain wall velocity measurements[25,53,54].

Although the angular momentum compensation point has not been well characterized in garnets, dynamics considerably faster than that of ferromagnets persist even away from this special condition. Much work has been done on domain wall velocity measurements in Pt/REIG garnet devices, from which useful information such as the DMI energy can be extracted. In rare-earth transition metal alloys such as CoTb, the maximum achievable domain wall velocity is typically on the order of 50 m/s, limited by the large magnetic damping of these materials (primarily due to the rare-earth species)[54]. However, the large ecosystem of garnet materials allows for selection of a material that is able to circumvent these restrictions. In particular, a material that has both PMA and ultralow magnetic damping, which was recently achieved with Bi-substituted YIG on a substituted GGG substrate that provided sufficient tensile strain to induce PMA, even with the low magnetostriction of the Bi-YIG system[159]. The domain wall velocity in Pt/Bi-YIG systems was recently measured in excess of 4000 m/s, more than two orders of magnitude faster than ferrimagnetic metals, and demonstrated to have reached the relativistic speed limit imposed by the magnon group velocity in the system[166,167].

In summary, rare-earth iron garnets constitute an exciting system for the development of the next generation of spintronic devices. The robust oxide structure is simple to grow via a variety of methods and exhibits long term stability under ambient atmospheric conditions and a large temperature range, providing an additional benefit relative to metals that commonly must be protected from oxidation and other forms of degradation. The rich chemistry of the garnet system

can be easily tuned to the specific application, through substitution of one or more sublattices with any rare-earth ion or a large variety of nonmagnetic species, and the magnetic anisotropy is predictably modulated through the selection of substrate, for both epitaxial and polycrystalline films. Rare-earth iron garnets provide an enticing opportunity to study both the development of the next generation of information storage materials and a variety of emergent physical phenomena exploring new frontiers in physics and materials science.

3. Methods

3.1 Pulsed Laser Deposition

Pulsed laser deposition (PLD) is a versatile and powerful technique for depositing nanometer-scale thin films[168]. The PLD process works by using an ultrafast laser pulse (~20 ns) to ablate a plume of material from a stoichiometric bulk target of the desired material. PLD offers the benefits of high growth rates, precise transfer of complex stoichiometries, high pressure deposition, and deposition of very low defect films[169]. Epitaxial single crystal films that do not require an *ex situ* anneal step can be grown via PLD. Polycrystalline films can also be grown; however, many materials (including the garnets) are amorphous as grown and require an *ex situ* anneal to crystallize. Very rapid heating of the target material results in congruent melting and subsequent ablation of a plume that deposits on a substrate a few centimeters above the target[170]. PLD is primarily used for deposition of insulating materials such as oxides and nitrides. As such, laser energies must be greater than the bandgap to ensure absorption. Excimer lasers are well-suited to this application as they are capable of ultrafast pulses, can output high energies, and have wavelengths in the appropriate range. A Kr-F excimer laser was used in this work, with a wavelength of 248 nm, corresponding to 5.0 eV. A diagram of one of the PLD systems used in this work is shown in figure 3.1. Note that this system has an integrated DC magnetron sputtering gun for deposition of metal films *in situ*.

The most important parameters in the PLD process are the laser fluence, temperature, and oxygen pressure during deposition. The laser fluence (pulse energy/area of focused laser spot) is the most important variable in growing films of the desired material. In our PLD systems, garnets grow at an optimal fluence of 2.0 J/cm^2 [45]. The pulse energy of the laser varies from 300-400 mJ between

the different chambers, as the optics differ. Fluence is controlled by varying the laser energy and by moving the focusing lens to alter the spot size and shape on the surface of the target. Substrate temperature is the next crucial parameter. Considering single crystal films, a high substrate temperature ensures that the incident ions have sufficient thermal energy to diffuse on the surface before settling into a lattice site. In the case of polycrystalline films, this should be less of a concern, as polycrystalline garnet films are amorphous as grown. When garnets are deposited on a non-garnet substrate such as Si at room temperature, the films do not crystallize under normal annealing conditions. This implies there is an added layer of complexity in the form of "pre-crystallization" or nucleation sites that only form at elevated substrate temperatures during growth. Stadler et al. demonstrated that a novel two-step annealing process can improve crystallinity of garnet films deposited via sputtering, but the crystallization kinetics of polycrystalline films grown by PLD deserves further study[161].

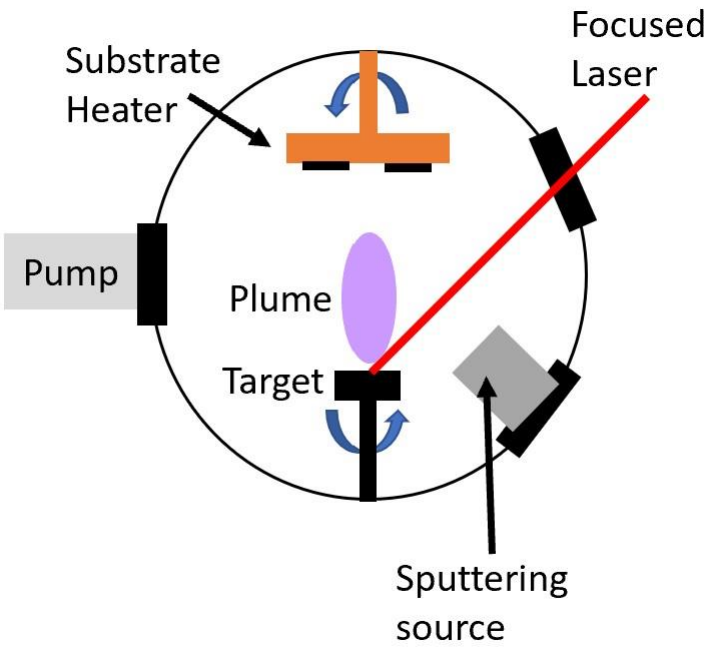

Figure 3.1: Diagram of one of the pulsed laser deposition chambers used in this work.

Oxygen pressure during deposition is the last primary variable for depositing garnet films. In this work, a pressure of 150 mTorr O_2 was used for almost all samples. Deposition at very low oxygen

pressures (less than 10 mTorr) leads to oxygen deficient films, poor crystallinity as evidenced by x-ray diffraction, and lower saturation magnetization. Oxygen pressure during deposition also has a relatively weak impact on the final film composition in the pressure range 10-50 mTorr, but this effect has proven difficult to quantify owing the complexity in precisely measuring the composition of thin films. As garnet films are usually grown under oxygen to prevent oxygen deficiency and improve crystallinity, the base pressure of the system is relatively high (on the order of 10^{-6} Torr) and this has a relatively small impact on film quality.

The targets used in this work were produced by a conventional solid oxide sintering process[160]. The binary oxides (R_2O_3 and Fe_2O_3) were weighed in the correct amounts for a stoichiometric $R_3Fe_5O_{12}$ target. The powders were thin ball milled in methanol for 24 hours, then dried on a hot plate. The powder was then pressed into a cylinder of approximately 30 mm diameter and 5 mm in height. The green body was then calcined at 1150 °C for 5 hours and sintered at 1400 °C for 10 hours. After cooling, the target was examined via x-ray diffraction to determine the phases present. After the first sintering, the targets had a small amount of orthoferrite ($RFeO_3$) present. The green body was then crushed into powder, ball-milled, pressed, calcined, and sintered again, after which the targets were pure phase garnet. The target surfaces were then polished with decreasing grit sizes of grinding paper until a very smooth surface was attained.

By using multiple targets, it is possible to create complex heterostructures of different films, or to create intermediate compositions of the two or more targets. This allows for a massive amount of flexibility when engineering the properties of garnet films, as it is then possible to produce compositions with significantly improved properties relative to films containing a single rare-earth

species. These codepositions and heterostructures will be discussed in further detail later in this work.

Although PLD is useful for complex stoichiometries and rapid prototyping, it has several limitations that should be discussed. The first is that the plume is highly inhomogeneous, necessitating small substrate sizes (1-2 cm) to prevent large variations in film composition and thickness across the surface. The homogeneity can be improved by rastering the substrate assembly, but this introduces considerable complexity. Another downside of the PLD system is that the throughput is relatively low. The chambers used here are not load-locked, as it is necessary to clean the laser window with a diamond polishing paste after each deposition. This prevents buildup of the deposited material on the inside of the window, which leads to laser burns on the window and significant heating which can eventually cause failure. For these reasons, sputtering is often a preferred deposition technique in industry, as the process is more amenable to large areas and high throughputs. However, PLD has greater flexibility in materials discovery and development.

3.2 Sputtering

Sputtering is one of the most common thin-film deposition techniques as it can used to deposit a huge variety of thin film materials with precise control over thickness and composition[171]. The physical process occurs by accelerating a plasma of inert ions, most typically Ar^+, onto the surface of the material to be deposited (the target or source), and material from the source is then "sputtered" from the surface, travels through the vacuum and deposits on the substrates. The plasma is "sparked" by a sufficiently large bias applied across the target to the other electrode. For DC (direct current) sputtering, the target is negatively biased (cathode) to attract the positively

charged Ar^+ ions. The substrate is occasionally positive biased (anode), but it is also common for the chamber to serve as the anode. The impinging Ar^+ ions arrive at a range of angles, resulting in a range of angles of sputtered ions. Sputtering typical occurs at Ar pressures of a few mTorr, which is at a pressure above the ballistic transport regime, leading to multiple collisions before arriving at the substrate surface. The result of these collisions is that step coverage conformality is better than electron beam evaporation, but still not as good as techniques such as chemical vapor deposition and atomic layer deposition[96]. To increase sputtering yield and focus the plasma, strong permanent magnets (magnetrons) can be installed in the sputtering gun behind the target material. The magnetic fields focus the plasma onto the target in a more uniform manner, resulting in higher deposition rates and, importantly, the ability to sputter magnetic thin films[172].

Thickness of sputtered films is simply controlled by turning the bias on or off, extinguishing the plasma, or through the use of a shutter to physically block atoms from reaching the substrate. It is also easy to control the composition of sputtered films. Considering the case of depositing two metals, such as Gd and Co, the relative amount of the two materials in the film can be controlled by adjusting the power applied to each gun and calibrated before the codeposition. Note this requires two sputtering sources and two power supplies. It is also possible to deposit oxide materials without significant oxygen deficiency through reactive sputtering. The most common method of doing this involves having relatively small partial pressure of oxygen (~mTorr) in the chamber during deposition alongside the Ar^+ plasma.

It is relatively simple to sputter conductive materials, as electrons are conducted through the material to replenish electrons that are sputtered from the surface of the material. However, for

insulating materials, the insulating nature quickly leads to the extinguishing of the Ar^+ plasma. To compensate for this, radio frequency (RF) sputtering was developed that uses a RF frequency bias to allow deposition of these materials, by alternatively negatively biasing the target to allow sputtering by the plasma, and positively biasing the target to attract electrons to the surface and prevent charge build up. This is considerably more complicated than DC sputtering, as it requires matching of the frequency and power through additional equipment and will not be discussed here.

The grain structure in sputtered films depends on several factors, including the growth rate and melting temperature of the deposited material. High growth rates tend to lead to small grain size as material is arriving at the substrate surface faster than the atoms can be incorporated into the existing grains. The relative melting temperature and substrate temperature during deposition also dictates the grain structure of the film. For low ratios of the deposition temperature to the melting temperature ($T_{dep}/T_M < 0.2$), columnar grain growth occurs[173,174]. There is initially nucleation of a large number of grains, but there insufficient thermal energy for grain growth to occur, leading to a columnar structure, with the longest side of the grains being perpendicular to the film surface. This is a particular problem for Pt films, as Pt has a melting temperature of over 1900 K. For higher values of T_{dep}/T_M, equiaxed grain growth occurs, where the out of plane dimension is approximately the same as the in plane dimension of the grains[173,174].

3.3 Rapid Thermal Annealing

Rapid thermal anneal (RTA) is the process of quickly heating a sample to a setpoint temperature, holding for some length of time, then rapidly cooling. Annealing was used in this work for two primary reasons: to crystallize amorphous as grown films and to induce thermal mismatch strain between the film and substrate. Figure 3.2 shows the x-ray diffraction of a europium iron garnet

thin film before and after annealing. During the annealing process oxygen was flowed through the system to ensure there was not loss of oxygen at elevated temperatures, or to assist with reaching full oxygen stoichiometry. The substrate holder and tube furnace are made of low thermal expansion silica glasses. The samples were placed on a silicon susceptor, which improved thermal transfer for transparent substrates and films, and allowed for improved system cleanliness by frequent replacement of the susceptor as no other system components contacted the samples. In practice, very rapid heating rates above 50 °C/s can be obtained. Cooling rates are considerably slower and vary throughout the temperature range from tens of degrees per second at high temperatures to one degree or less per second as room temperature is approached.

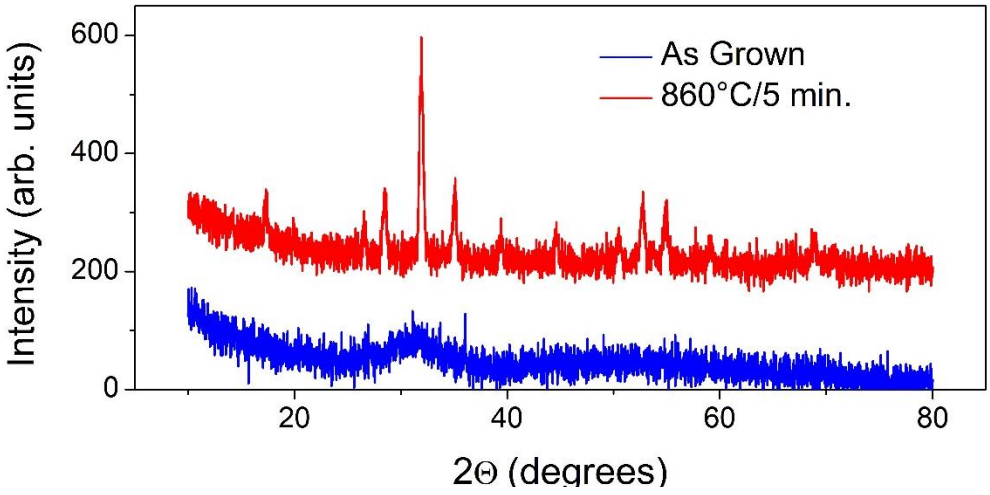

Figure 3.2: X-ray diffraction of an as grown and annealed 21.2 nm EuIG film on (0001) quartz. The as grown film shows no garnet peaks and the annealed film is pure phase garnet. Vertically offset for clarity.

3.4 X-ray Diffraction and X-ray Reflectivity

X-rays were first discovered by Wilhelm Conrad Röntgen in the late 19th century, and less than two decades later X-ray diffraction (XRD) had become an indispensable tool for materials analysis[175,176]. Bragg's law, so named for father and son William Henry and Lawrence Bragg, enabled characterization of crystal structures and resulted in a Nobel prize for the pair[176]. X-rays are an electromagnetic wave, and these waves can interfere with themselves under certain conditions when diffracting off a structure. Bragg's law describes the angle at which the

constructive interference is largest by relating the angle of diffraction and a characteristic length of the crystal structure being examined:

$$2d\sin(\theta) = n\lambda \tag{3.1}$$

Where d is the interplanar spacing of the crystal structure, θ is the angle of incidence, n is an integer, and λ is the wavelength of the x-rays. Copper is the most commonly used x-ray source in diffractometers, with the Kα radiation wavelength of 1.5406 Å. This value is convenient for most crystal structures, which commonly have lattice parameters in the sub-nanometer range[41,177]. Group theory and symmetry arguments describe which reflections are allowed based on the atomic positions within the lattice.

High resolution x-ray diffraction (HRXRD) makes use of very precise motor positioning and high-precision multi-bounce monochromators to allow angular resolution as low as 0.001°. HRXRD is

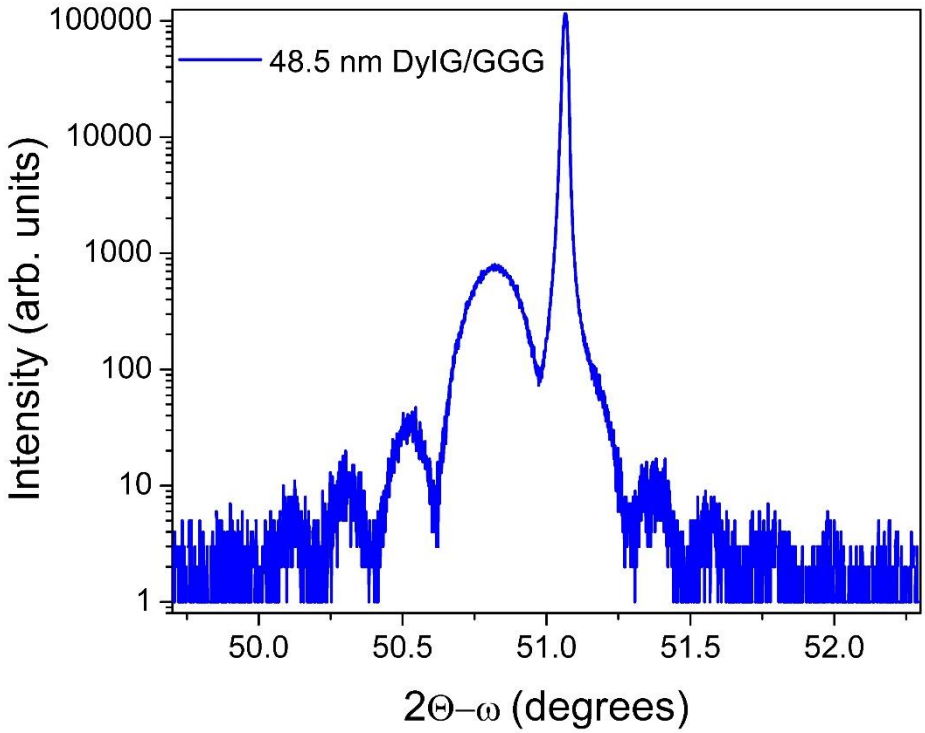

Figure 3.3: High resolution x-ray diffraction plot of a 48.5 nm DyIG film on a GGG substrate.

done in a symmetric geometry, where the detector and x-ray source are both at an angle of θ to the sample. A full discussion of x-ray diffractometers can be found elsewhere[175,178]. This is useful for characterizing single crystals and epitaxial thin films on substrates. An example HRXRD plot is shown in figure 3.3 for a dysprosium iron garnet (DyIG) film on a gadolinium gallium garnet substrate (GGG). The lattice parameter of DyIG is less than GGG, so the film is under in-plane compressive strain, resulting in an out-of-plane expansion of the lattice parameter (d). This increase in d results in a decrease in the diffraction angle, θ. The substrate and film are (111) oriented, and the plot depicts the (444) reflection. The sharp, narrow peak is from the substrate, and the larger broad peak is from the film. The smaller Laue fringes surrounding the film peak are indicative of high film quality, and consistent film thickness. These fringes can be fit to determine the film thickness.

This thesis primarily reports films grown in the (111) orientation, corresponding to the magnetic easy axis of REIG. The garnet structure is cubic, but epitaxial thin films grown on (111) substrates experience a rhombohedral distortion as the in-plane lattice parameter is compressed or extended to match that of the substrate, in the case of fully strained films[45]. The body diagonal of the rhombohedral unit cell perpendicular to the film is readily determined by finding the peak position of the film. However, it is also of interest to calculate the corner angle of the rhombohedral unit cell, which is accomplished by a transformation from rhombohedral (hkl) to hexagonal (HKL) Miller indices, as described by Cullity and Rosenberg[45,178]:

$$\begin{pmatrix} h \\ k \\ l \end{pmatrix} = \begin{pmatrix} 1 & -1 & 0 \\ 0 & 1 & -1 \\ 1 & 1 & 1 \end{pmatrix} \begin{pmatrix} H \\ K \\ L \end{pmatrix} \tag{3.2}$$

The in-plane lattice parameter along the $(11\overline{2})$ direction is given by:

$$d_{112} = \sqrt{\frac{a^2}{h^2 + k^2 + l^2}} \tag{3.3}$$

Where a is the lattice parameter of GGG, 1.2376 nm. This is converted to the in-plane lattice parameter of the hexagonal unit cell[178]:

$$a_H = \sqrt{12 d_{112}^2} \tag{3.4}$$

The corner angle of the rhombohedral unit cell can then be calculated as:

$$\sin\left(\frac{\alpha}{2}\right) = \frac{3}{2\sqrt{3 + \left(\frac{c}{a_H}\right)^2}} \tag{3.5}$$

Where α is the corner angle of the rhombohedral unit cell, and c is body diagonal of the rhombohedral unit cell perpendicular to the film surface. The corner angle can then be used to determine the epitaxial mismatch strain in the (111) oriented film.

HRXRD diffractometers can also be used to measure x-ray reflectivity (XRR). XRR is used primarily in this work to fit a model of the thin film or heterostructure to and determine thickness(es). XRR is collected at much shallower angles than XRD, between the angle of total internal reflection and the angle at which the background level of the detector is reached. The critical angle, measured from normal incidence, is the angle above which the wave is completed reflected back into the denser medium[179]:

$$\sin(\theta_c) = \frac{n_{film}}{n_{air}} \tag{3.6}$$

Where n_{air} is the refractive index of air, n_{film} is the refractive index of the film, and θ_c is the critical angle. For denser films, the critical angle is a larger value. An example XRR plot is shown in figure 3.4, for Pt films on Si of different thickness. The fringe spacing is inversely proportional to the film thickness. In the plot, the critical angle is different for each film due to a difference in density (and thus refractive index) between the films.

The conventional geometry of XRD is useful for bulk samples, powders, and epitaxial thin films. However, for polycrystalline thin films, this results in overwhelming contributions from the substrate and sample holder. To better collect XRD of random, thin film polycrystalline samples, these measurements are conducted in grazing incidence geometry (GIXRD), where the x-ray source is held at a constant angle of 1-2° above the film surface. The detector moves around the sample as in conventional XRD. In most cases, this technique can eliminate peaks from the substrate and sample holder, leading to easier phase identification.

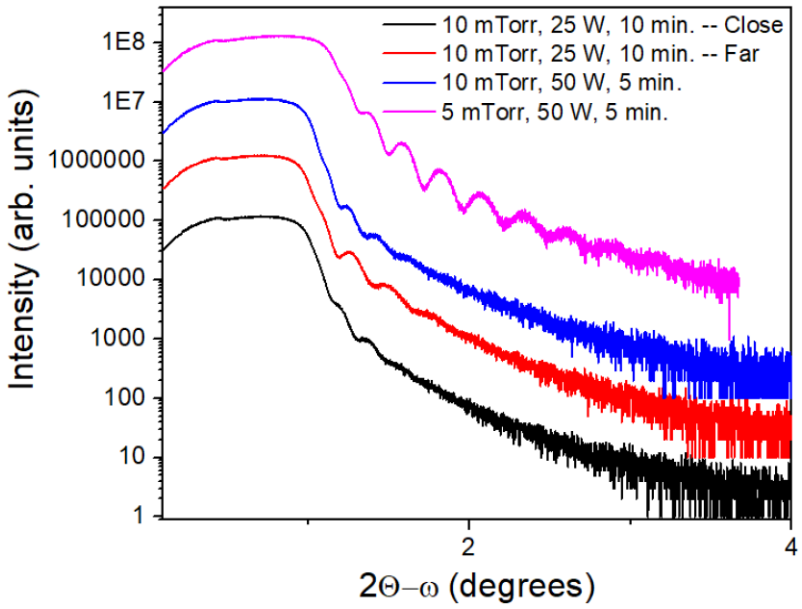

Figure 3.4: Example x-ray reflectivity plot of Pt/Si films, deposited by DC magnetron sputtering under different conditions. Vertically offset for clarity.

3.5 Atomic Force Microscopy and Magnetic Force Microscopy

Scanning probe microscopy (SPM) is a broad class of experimental techniques that are very useful for investigating surface properties of materials. SPM was first demonstrated in 1981 by Binnig et al., for which their later work on the scanning tunneling microscope would win the Noble Prize in Physics in 1986[180–182]. Atomic force microscopy (AFM) is a subset of this field in which a small cantilever is used to scan the topography of a sample[183]. A very fine tip is mounted on the end of the cantilever which vibrates at a known frequency according to its physical characteristics. The

cantilever is scanned over the surface of the sample (the sample is typically scanned while the cantilever is stationary). A laser is reflected off of the cantilever and small changes in its position are detected by a four-quadrant photodetector. From the deflection signal, it is then possible to map out the topography of the film surface[183]. This method is very sensitive, and can readily measure surface roughness that is as low as hundreds of picometer root-mean-square roughness[182,183]. Scan size is typically on the order of microns, which is useful for observing grain boundaries and grain size in thin film materials.

A related technique is magnetic force microscopy (MFM). By coating the tip of the cantilever in a magnetic material (typically Co), the cantilever then interacts with the stray field at the surface of the magnetic sample[182]. The probe is then able to detect the magnetic domain patterns in the material, with lateral resolution on the order of microns or less. It is also possible to implement a small electromagnet into the MFM to study the domain patterns after field sweeps or demagnetized samples. A practical consideration is that the amplitude of deflection force detected by the cantilever is directly related to the stray field and thus the saturation magnetization of the sample. Thus, low magnetization materials, such as dysprosium iron garnet, can be difficult to image via MFM and are better suited to magneto-optical Kerr effect microscopy.

3.6 Vibrating Sample Magnetometry

The vibrating sample magnetometer (VSM) is an indispensable tool in characterizing magnetic materials. The operating principle is based on Faraday's law, that a change in the magnetic flux (Φ_B) through an electric coil induces an electromotive force (ε) that can then be amplified with a sense circuit[18,184]:

$$\mathcal{E} = -N\frac{d\Phi_B}{dt} \tag{3.7}$$

where N is the number of turns in a coil of wire. A common configuration for these sensing coils, known as pickup coils, is two placed on each pole piece in an electromagnet. The sample is mounted on a nonmagnetic sample holder in the air gap between the pole pieces (see figure 3.5). The sample holder is attached to a loudspeaker cone or similar vibrating mechanism, with vibration frequencies of typically 60 Hz and amplitude of a few millimeters. The pickup coils are wired to a lock-in amplifier, which is tuned to the vibration frequency of the VSM, allowing other mechanical or systemic vibrations to be filtered out. The electromagnets used are not usually superconducting, and the resulting maximum field is around one Tesla, although stronger magnetic fields can be generated by adjusting the air gap or pole pieces.

The very high sensitivity of the pickup coils allows precise measurements of the saturation magnetization of most all materials, even in minute quantities. It is possible to measure samples as large as tens of mg of a bulk oxide piece to samples as small as sub 5nm films. The practical limits on the operation are due to noise during the measurement. The sample holders are made of quartz or Pyrex glass, both of which are weakly diamagnetic. Samples were mounted with double sided tape. A temperature controller is commonly integrated into the VSM, which takes the form of a cylinder surrounding the sample holder during operation. Nitrogen or compressed air is flowed through the cylinder, which is heated with resistive elements for above room temperature measurements or cooled with liquid nitrogen for below room temperature measurements. Practical temperature limits are 170 – 500 K.

Silicon and GGG substrates, used extensively throughout this work, are weakly diamagnetic and strongly paramagnetic, respectively. The Gd^{3+} ion has a $4f^7$ ground state, leading to a very strong paramagnetic background due to the 7 unpaired electrons. Additionally, this background becomes nonlinear at fields above a few thousand Oersted, which makes it difficult to determine which saturation has been attained, particularly for the hard axis. For Si, it is generally easier to remove the substrate contribution, but for thin film or weakly magnetic materials, the vastly larger substrate volume (0.5 mm vs < 50 nm thickness) can overwhelm the magnetic signal. The general procedure for analyzing raw VSM data is as follows: remove linear background, height correction to center loop on horizontal axis, and dividing the signal by the volume of magnetic material to obtain the volumetric magnetization in emu/cm^3 or kA/m. The VSM used in this work was a Digital Measurements Systems Vibrating Sample Magnetometer Model 1660.

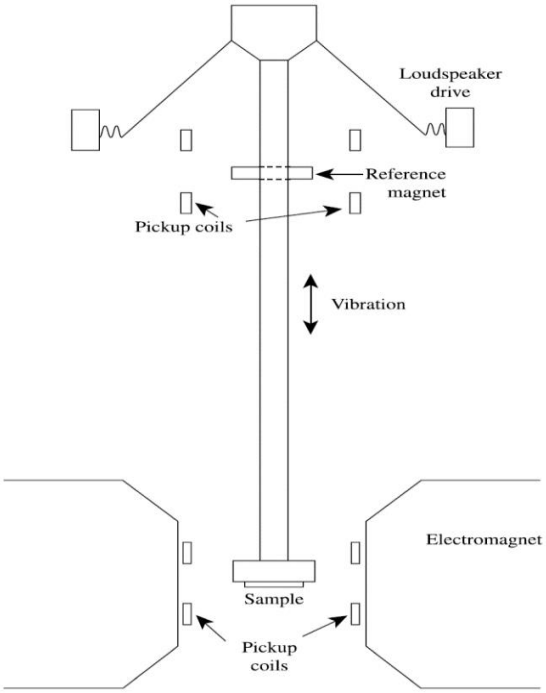

Figure 3.5: Schematic of a vibrating sample magnetometer. From ref. 18. Used with permission.

3.7 Spin Hall Magnetoresistance

The spin Hall magnetoresistance (SMR) that occurs in magnetic insulator/nonmagnetic metal bilayers is an insulating analog of the anisotropic magnetoresistance that occurs in magnetic metals[185]. This phenomenon occurs in materials that are excellent insulators, as the direction of the magnetization in the magnetic layer affects the resistance of the nonmagnetic metal. There are two origins of the SMR: the transmission of a spin current across the interface between the materials and the magnetic proximity effect in the nonmagnetic layer[186,187]. These two mechanisms have different temperature dependencies (the proximity effect is typically only significant well below room temperature) and have been observed across a wide variety of systems. Experimentally, these measurements are done on Hall crosses patterned by optical lithography (see figure 3.6). It is necessary to use a lock-in amplifier to mitigate noise and detect the Hall voltage, which is typically on the order of μV. Current is injected along one axis of the Hall cross, and a magnetic field is swept in a hysteresis loop while the voltage is measured in the transverse direction. The symmetry of the measured signal varies according to[50]:

$$R_H = R_{SMR}\sin(\theta)^2\sin(2\varphi) + R_{AHE}\cos(\theta) + R_{OHE}H_Z \quad (3.8)$$

Where R_H is the Hall resistance, R_{SMR} is the amplitude of the hard axis hysteresis loop, θ is the polar angle of the magnetization, φ is the azimuthal angle of the magnetization, R_{AHE} is the amplitude of the easy axis hysteresis loop, R_{OHE} is the resistivity due to the ordinary Hall effect in the nonmagnetic layer, and H_Z is the magnetic field along the z axis (see figure 3.7).

From equation (3.8), it can be seen that the maximum in-plane SMR amplitude occurs at an angle of φ = 45°. In addition to a field sweep of the data at a constant angle, it is also common to do angle dependent measurements (see figure 3.8). SMR measurements are another reliable method

of determining the coercivity and anisotropy fields of samples, which is useful when VSM is difficult due to low sample moment or a large substrate contribution.

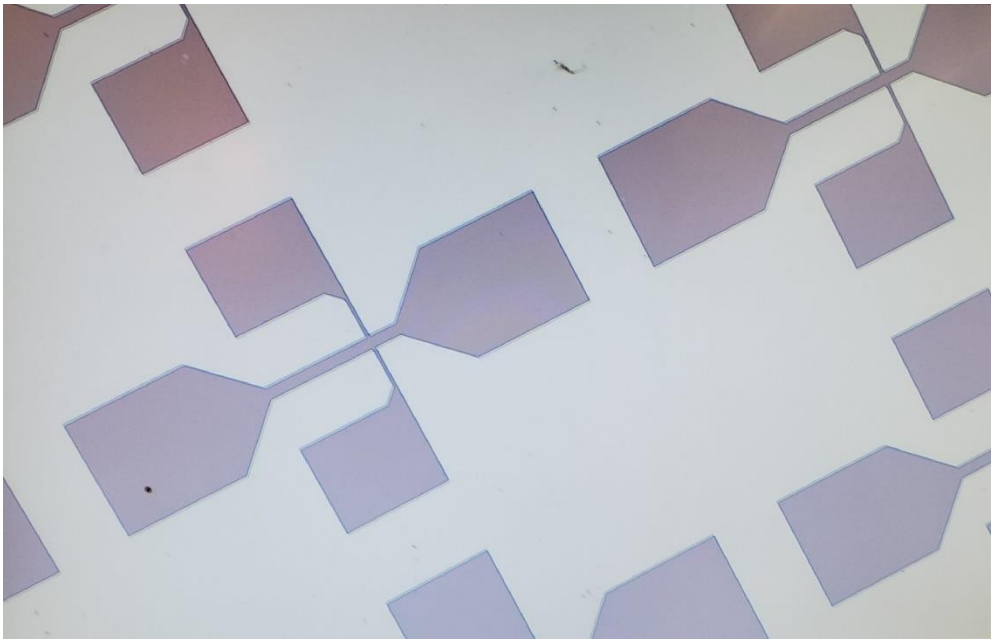

Figure 3.6: Patterned Hall crosses in a Pt/TmIG/GGG heterostructure. The main channel of the Hall cross has dimensions of 200 μm x 20 μm.

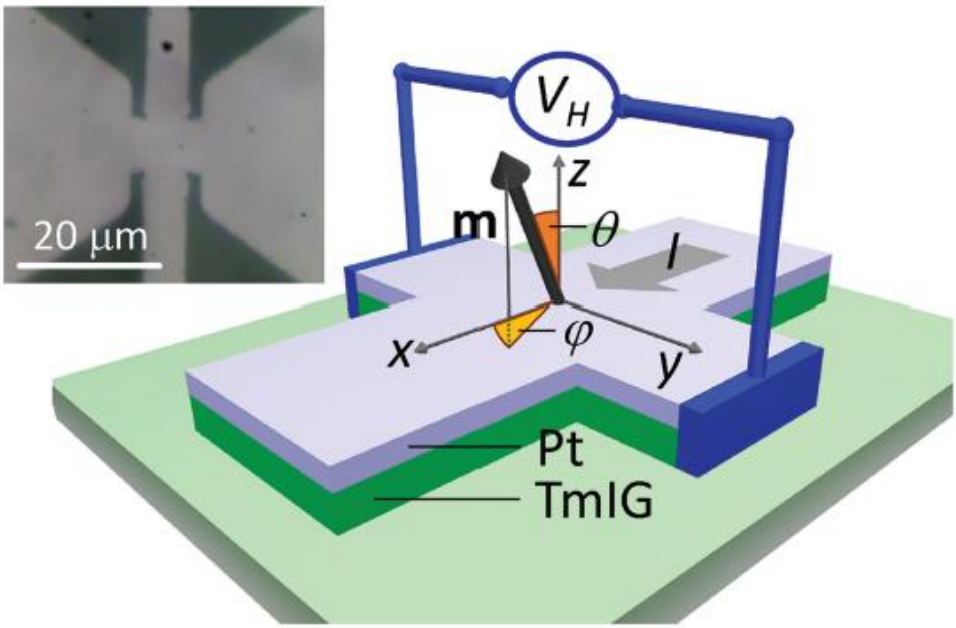

Figure 3.7: Diagram of the coordinate system in spin Hall magnetoresistance measurements. From ref. 50. Used with permission.

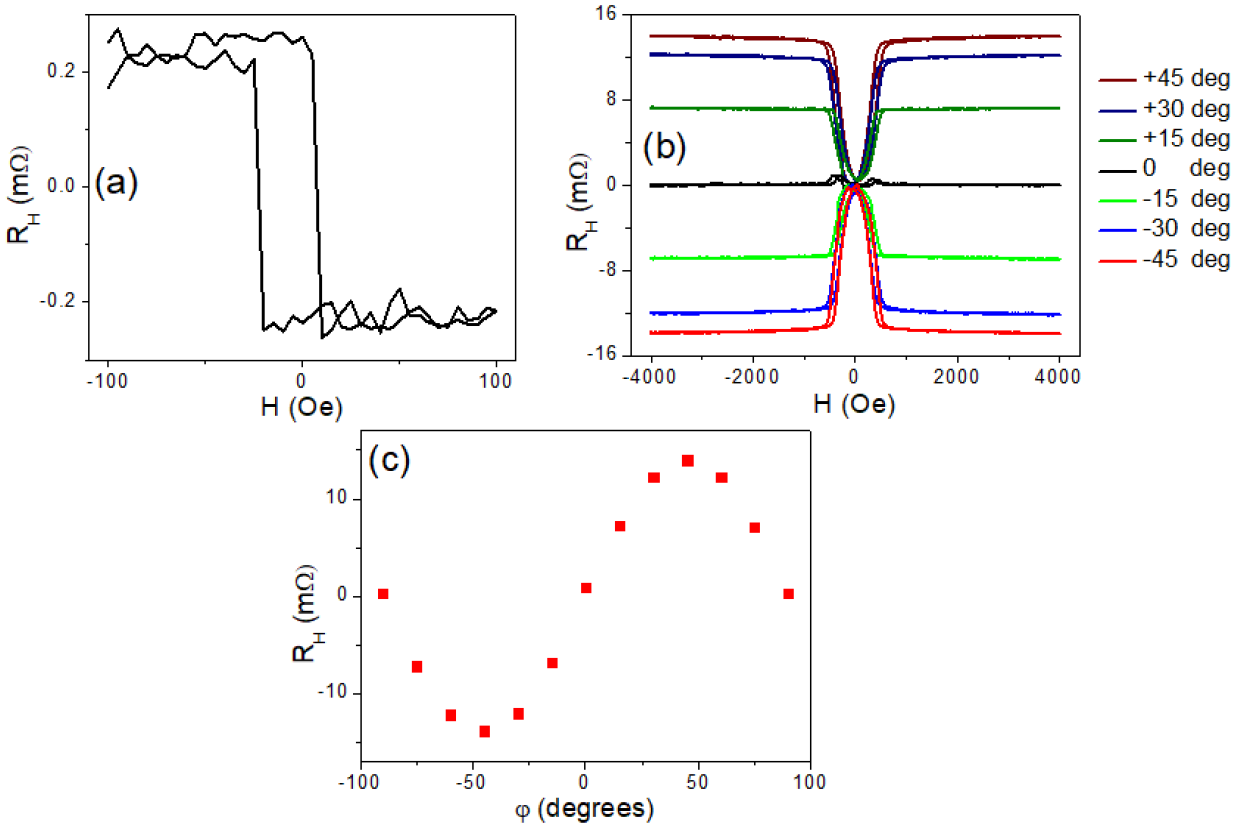

Figure 3.8: Spin Hall magnetoresistance (SMR) measured on a Pt/TmIG/GGG Hall cross. (a) Out of plane AHE-like SMR hysteresis loop. (b) In-plane SMR hysteresis loop at different in-plane angles. (c) Angular variation of the in-plane SMR measured at saturation.

3.8 Polarized Neutron Reflectometry

With the continued improvement of vacuum-based deposition techniques and the constant development of computer technology, there was a large interest in magnetic thin films and multilayers in the 1980's. This culminated in the discovery of giant magnetoresistance in 1988 in Fe/Cr superlattices, research that would go on to win Albert Fert and Peter Grünberg the Nobel Prize in Physics in 2007, less than twenty years after the discovery[92]. The large interest in precisely measuring the coupling of magnetic layers in complex heterostructures coincided nicely with the first reports of polarized neutron reflectometry (PNR) in 1986 by Majkrzak and others[188,189]. PNR utilizes the magnetic moment of the neutron, which interacts with the magnetic moment in a magnetic material. In a specular reflectivity geometry, PNR is able to non-destructively probe the

sample as a function of depth for layers on the order of 0 – 100 nm in thickness[190]. This allows study of complex thin film structures, like those found in magnetic storage media, magnetoresistive read heads, next-generation spintronic devices, and the magnetic proximity effect in materials that are close to the Stoner criterion.

As in x-ray reflectivity, PNR is able to accurately measure layer thicknesses, interface widths, and to determine the densities of the layers, from which conclusions about the composition of each layer can be determined. However, as the neutron has a magnetic moment, it is also responsive to the magnetic moment present in each layer, and the magnetic roughness in the system[191]. This allows determination of the magnetic roughness present in the system, in addition to more fine-grained modeling of the system by incorporating magnetic dead layers and proximity effects. As the measurements are done in specular reflection, PNR is sensitive to the in-plane component of the magnetization only, requiring that films have in-plane anisotropy or have sufficiently low anisotropy fields that an in-plane field can saturate the sample.

There are four neutron cross sections that can be collected during a PNR measurement: non-spin-flip (R^{++} and R^{--}) and spin-flip (R^{-+} and R^{+-}). Non-spin-flip scattering is due to the projection of the magnetization component in the plane of the film onto the polarization axis of the neutrons, and spin-flip scattering is due to magnetization components that are perpendicular to the polarization axis, such as those due to spin spirals or other exotic phenomena[192]. As the spin-flip cross sections do not detect the bulk of the magnetization in the material they tend to be weaker and will not be discussed further in this work.

Reflectivity data is collected similar to x-ray reflectivity as a function of the symmetric angle θ. Neutron instruments often use different wavelengths, so to allow comparison between instruments and wavelengths we define the wavelength-independent parameter Q_Z:

$$Q_Z = \frac{4\pi}{\lambda}\sin(\theta) \tag{3.9}$$

Where λ is the neutron wavelength. Collected reflectivity is plotted as a function of Q_Z, out to the background level (see figure 3.9). The period of the fringes is inversely proportional to the thickness of the layers.

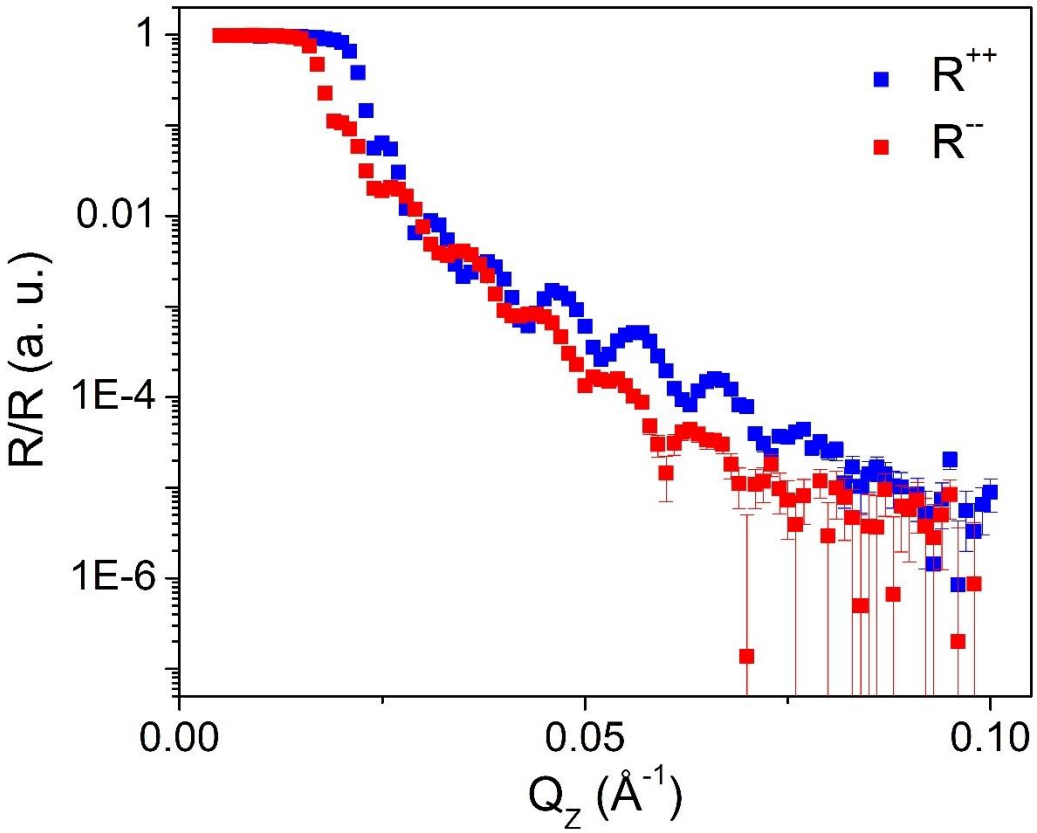

Figure 3.9: Normalized reflectivity data for a Pt(9 nm)/DyIG(54 nm)/GGG heterostructure collected at 10 K. An *ab initio* footprint correction has been done to correct for the GGG paramagnetism. The large error bars at high Q_Z are due to reaching background level.

The splitting of the two reflectivity curves is due to the magnetic moment in the sample, and larger magnetic moments lead to larger splitting. Figure 3.10 shows the spin asymmetry, the normalized difference of the reflectivity data, which is a useful method of highlighting the magnetism in the sample:

$$SA = \frac{R^{++} - R^{--}}{R^{++} + R^{--}} \tag{3.10}$$

Neutron absorption is strongly dependent on the elements present. Gadolinium and Scandium are two of the most neutron absorptive elements, which can introduce experimental artifacts during data collection. The strongly paramagnetic gadolinium garnet substrates used throughout this work also introduce non-linearities in the data. To account for this, an *ab initio* footprint correction is done on the pre-critical edge data. This method uses a theoretical sample model to remove the artifacts due to the GGG substrate, improving the quality of the fits obtained[193,194].

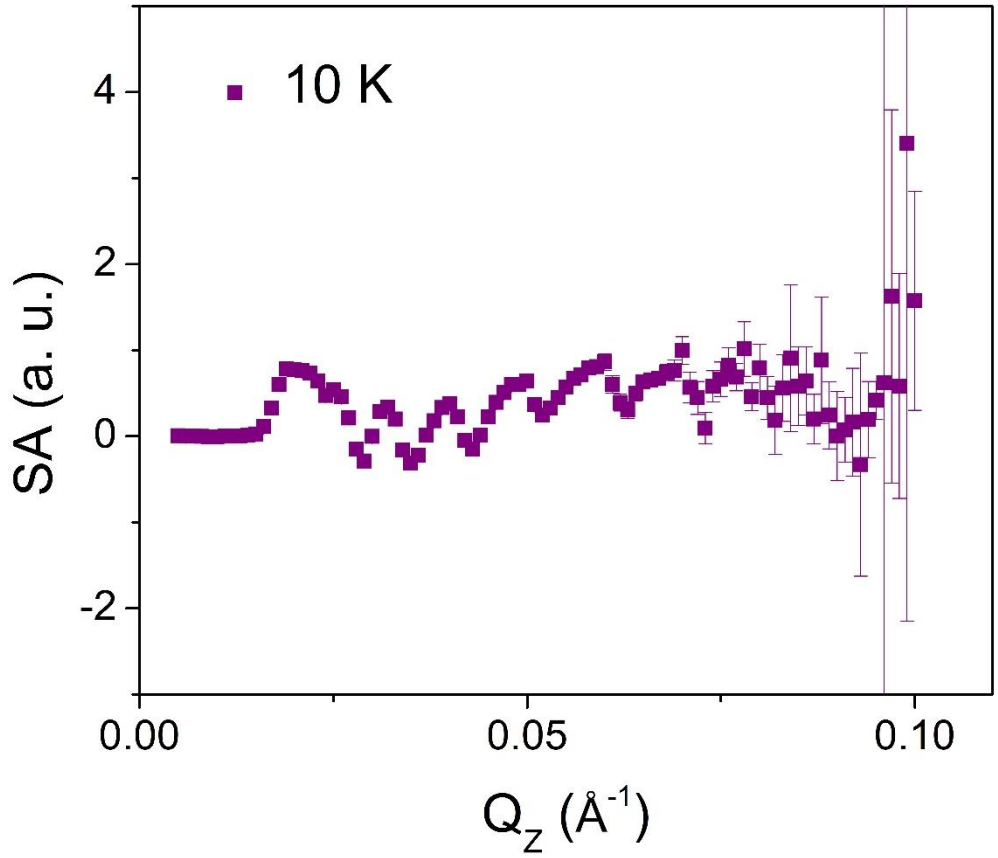

Figure 3.10: Spin asymmetry data for a Pt(9 nm)/DyIG(54 nm)/GGG heterostructure collected at 10 K. The nonzero SA is due to the sample magnetization.

Once the PNR data has been collected, it is reduced (background subtraction, footprint correction, and normalization) and a model is generated to fit the data to. Data reduction is done via Reductus

and fitting is completed with Refl1d (implemented in Python using the Bumps fitting program)[195,196]. Using knowledge of the sample obtained from other characterization (XRR, TEM, VSM, etc.), a model that contains the materials present, layer thicknesses, interface widths, magnetic moments, and magnetic dead layers is postulated. The growth method of the sample will have a large impact on the interfacial roughness; films grown layer-by-layer by molecular beam epitaxy will have very sharp interfaces, whereas in high-temperature grown PLD films, there is some interdiffusion present with the substrate that must be accounted for[197,198]. Garnets films on garnet substrates can easily interdiffuse at high temperatures, and this must be accounted for with an intermediate composition region between the substrate and film[198,199].

As the neutron beam is on the order of several cm across, the entire lateral area of the sample is scanned at once. Depending on the method of sample mounting (an inset sample holder vs. silver paste for example) a bare spot on the sample must be accounted for in the modeling as well[194].

The fitted reflectometry data is used to produce a scattering length density (SLD) profile, which is a cross-section of the sample through the thickness of the film. The real part of the SLD, rho, corresponds to the density of the sample, from which the composition of the layer can be inferred. The imaginary part of the SLD, irho, depends on the neutron absorption of the material, and is strongly element-dependent (in this study, Gd is the only element with non-negligible neutron absorption). Magnetism is captured in rhoM, which can show both parallel and antiparallel coupling in different layers, in addition to proximity effects in other layers[49,200]. The magnetic angle is relevant for spin-flip scattering only. An example Pt(10 nm)/DyIG(25 nm)/GGG (100) film is shown in figure 3.11, which required a complex model to fit[194]. The model used consists

of two layers to account for the Pt and two layers to account for the interdiffused region between the GGG substrate and DyIG film. The added complexity of these extra layers greatly increases the time required for the model to run and begins to stray into the realm of overfitting the data. For the data shown here, a different sample was used after many degenerate solutions to the model were obtained.

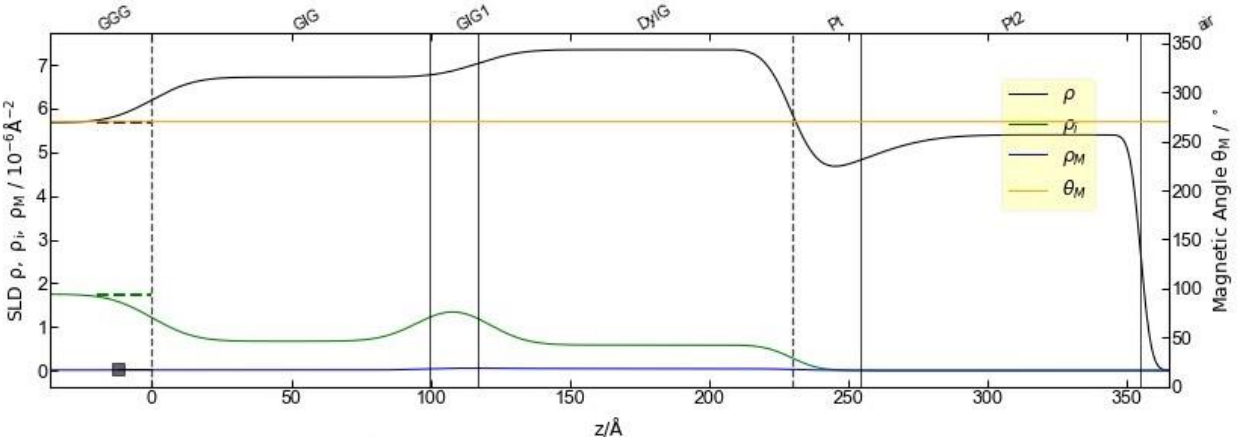

Figure 3.11: Scattering length density profile of a Pt/DyIG/GGG film, fit to a model with a structure of Pt2/Pt/DyIG/GIG1/GIG/GGG.

For temperature dependent PNR studies, it is common practice to fit the temperature-independent components of the model (layer thicknesses, interface widths) simultaneously, while allowing the temperature-dependent components of the model (typically the magnetization) to vary independent of each other. At low temperatures, it proved necessary to introduce an "ice" layer to account for gases that had adsorbed on the surface during data collection.

Neutrons are produced via a nuclear reactor or spallation neutron source[201]. All PNR experiments done here were conducted at the National Institute of Standards and Technology (NIST) Center for Neutron Research (NCNR), on the Polarized Beam Reflectometer (PBR) instrument.

3.9 X-ray Magnetic Circular Dichroism

The relationship between magnetism and light has long been known, which were fully integrated through James Clerk Maxwell's seminal work that related the electric and magnetic parts of electromagnetic wave radiation[202]. The interaction of light with magnetic materials occurs through the rotation of the plane of polarization of the light, which was discovered in transmission by Michael Faraday in 1846 and in reflection John Kerr in 1877[203,204]. These two magnetoptical effects, the Faraday and Kerr effects, are used in modern characterization of magnetic materials, through Faraday rotation and magneto-optic Kerr effect (MOKE) microscopes. Faraday and MOKE instruments typically use light in the visible spectrum, which is able to probe the total magnetization of many materials[205].

For complex magnetic alloys and ferrimagnets, it is often difficult to determine the magnetic structure through magnetometry and symmetry arguments alone. However, each element has a distinct electronic structure that can be probed via high energy x-rays. X-ray absorption spectroscopy (XAS) is useful for probing the electronic states of solid materials, as the x-ray absorption of elements occurs at very specific and distinct wavelengths, according to the allowed electronic transitions for core electrons to excited valence states[206,207]. These wavelengths are tabulated for most elements at the different absorption edges, which probe different core electrons. The shape of the absorption spectra can also be interpreted or fit to a theoretical model to determine the coordination, valence state, and site occupancy of a specific element in a crystal structure[207].
To study the magnetism of materials via these core level electrons, it is necessary to use polarized light. Circularly polarized light can be described as the sum of two plane-polarized waves that are out of phase by $\pi/2$, one quarter of a wavelength. Left circularly polarized and right circularly

polarized waves interact in different waves with electrons that contribute to a net magnetic moment in a material, as there are different absorption probabilities[208]. The sum of the two polarizations produces the XAS for the material, but the difference of the two polarizations produces an effect called x-ray magnetic circular dichroism (XMCD). XMCD can then be used to qualitatively draw conclusions about the magnetic ordering in a material, and can also be used to quantitatively determine the strength of the spin and orbital magnetic moments in the material[208].

XMCD was first predicted in 1985 and experimentally observed in 1986, so it is a relatively new technique[209,210]. These first studies were followed by many others that quickly verified the theoretically determined XMCD sum rules. These sum rules relate the integrated peak areas across two closely related absorption edges to determine the spin and orbital components of the magnetization of that element in the material[211]. For transition metals, the $L_{2,3}$ absorption edges, corresponding to the transition of *2p* core electrons to *3d* valence states are most commonly studied. The sum rules for transition metal $L_{2,3}$ edges are[211]:

$$\langle L_z \rangle = -\frac{4q}{3r} n_h \tag{3.11}$$

$$2\langle S_z \rangle = -\frac{6p - 4q}{r} n_h - 7\langle T_z \rangle \tag{3.12}$$

Where $\langle L_z \rangle$ is the orbital magnetic moment in μ_B/atom, $2\langle S_z \rangle$is the spin magnetic moment in μ_B/atom, q is the integrated $L_{2,3}$ XMCD, r is the integrated $L_{2,3}$ XAS , p is the integrated L_3 XMCD, n_h is the number of *3d* holes (a material and element specific parameter), $\langle T_z \rangle$ is the expectation value of the magnetic dipole operator. The total magnetic moment of the ion is the sum of $\langle L_z \rangle$

and $2\langle S_z \rangle$. See figure 3.12 for a diagram of Fe $L_{2,3}$ XAS and XMCD with labels indicating the values of p, q, and r.

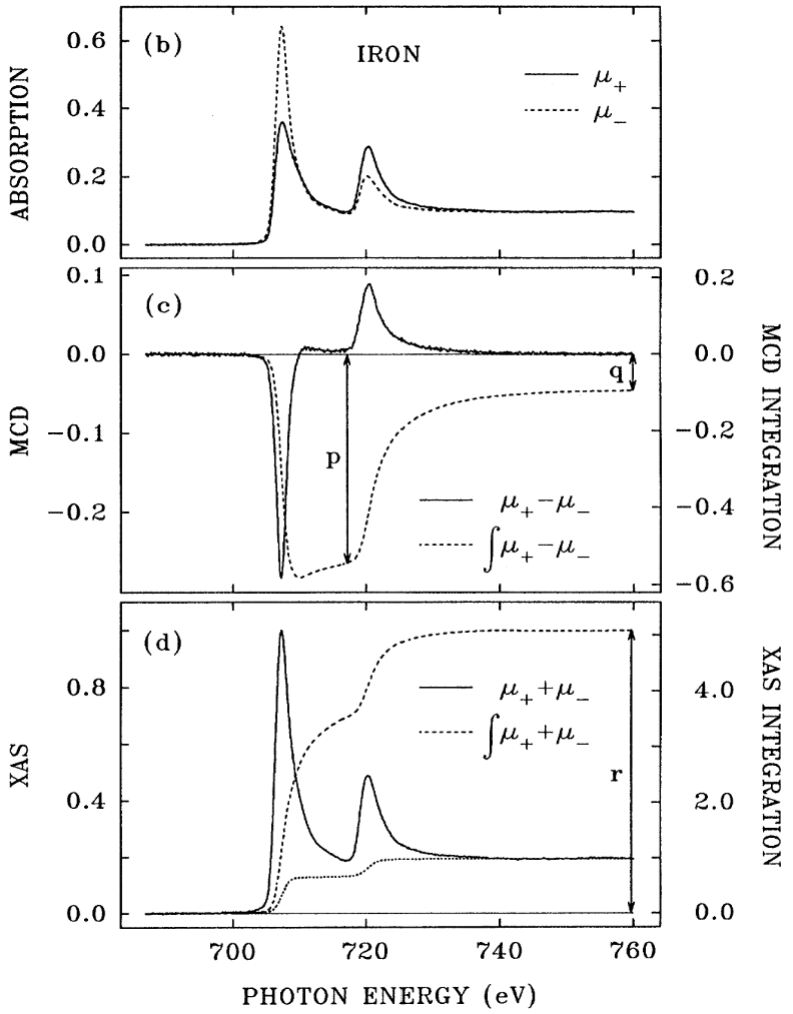

Figure 3.12: XAS and XMCD at the $L_{2,3}$ edges for Fe. The points where p, q, and r were determined are shown. From ref. 211. Used with permission.

For transition metals, the value of T_z is usually negligible under the assumption that the *3d* orbitals are cubically symmetric. For Fe in REIG, $n_h \approx 4.7$. As mentioned in previous sections, the orbital moment for transition metals in solids is usually quenched by the crystal field, and this has been observed experimentally via XMCD in the garnets[44]. The obtained values from the sum rules also need to be corrected for the percent polarization of the beam, the sample angle during measurement, and a factor of 1/0.69 must be applied to account for errors in the sum rule for $3d^5$ ions[212,213].

For rare-earth elements, the *3d* core electron to *4f* valence state transition is probed at the $M_{4,5}$ edges. The sum rules at the $M_{4,5}$ edges are[44,47]:

$$\langle L_z \rangle = \frac{2q}{r} n_h \tag{3.13}$$

$$S_{eff} = \frac{5p - 3q}{r} n_h \tag{3.14}$$

Where q is the integrated $M_{4,5}$ XMCD, r is the integrated $M_{4,5}$ XAS, p is the integrated M_5 XMCD, n_h is the number of holes in the *4f* shell (dependent on the rare-earth present), and S_{eff} is the effective spin moment. For the rare-earth ions the $\langle T_z \rangle$ is non-negligible, as the *4f* orbitals are highly localized and not spherically symmetric[44]. To account for this an effective S_{eff} is defined[47]:

$$S_{eff} = 2\langle S_z \rangle + 6\langle T_z \rangle \tag{3.15}$$

Assuming that the ratio of $\langle S_z \rangle / \langle T_z \rangle$ is constant, values of $\langle S_z \rangle$ and $\langle T_z \rangle$ calculated numerically from multiplet theory for free atoms can be used to determine $2\langle S_z \rangle$ to complete the sum rules[47,214,215]:

$$2\langle S_z \rangle = \frac{2S_{eff}}{2 + \frac{\langle T_z^{free} \rangle}{\langle S_z^{free} \rangle}} \tag{3.16}$$

XAS and XMCD data requires some pre-processing before sum rules can be accurately applied. This typically consists of a subtraction of a linear background and vertical offset. The next step is to remove the white line steps at the absorption edges from the data. There are many possible ways to do this, with three common methods being to remove a step at each absorption peak with a Voigt, Gaussian cumulative distribution function, or inverse tangent profile. The step at the lower energy absorption edge (i.e. L_3 in transition metal $L_{2,3}$ XAS) is usually twice the height of

the higher energy absorption edge[211]. The data is then integrated to find p, q, and r. A flat spot in the integrated profile is selected to avoid any errors from a non-zero background slope.

The sign of the XMCD signal can be used to determine the coupling of the different magnetic elements present in a sample. Considering the garnet structure, the net Fe is antiparallel to the rare-earth moment. The sign of the XMCD signal can be correlated to whether the element is aligned parallel or antiparallel to the applied magnetic field, and thus the rest of the sample[75]. For example, a positive Dy M_4 peak indicates that it is parallel to the magnetic field, and a negative Fe L_2 indicates that the net Fe is antiparallel to the magnetic field (see figure 3.13). This condition occurs below the compensation temperature of DyIG, and the signs of the two signals are reversed above the compensation temperature[194].

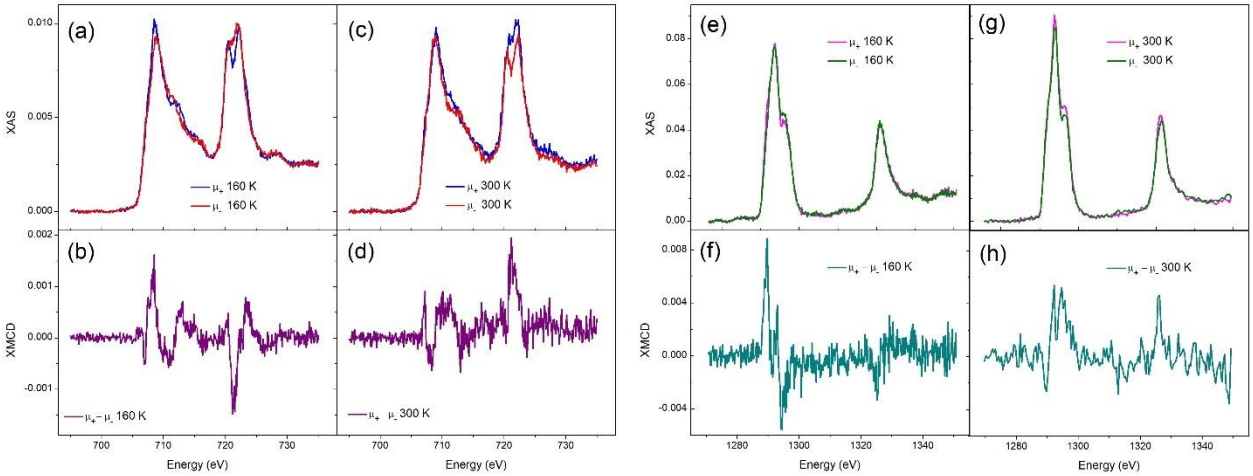

Figure 3.13: XAS and XMCD spectra of a Pt(9 nm)/DyIG(54 nm)/GGG film with a compensation temperature of 220 K. (a) Fe $L_{2,3}$ XAS at 160 K. (b) Fe $L_{2,3}$ XMCD at 160 K. (c) Fe $L_{2,3}$ XAS at 300 K. (d) Fe $L_{2,3}$ XMCD at 300 K. (e) Dy $M_{4,5}$ XAS at 160 K. (f) Dy $M_{4,5}$ XMCD at 160 K. (g) Dy $M_{4,5}$ XAS at 300 K. (h) Dy $M_{4,5}$ XMCD at 300 K.

XAS and XMCD data is typically collected in total electron yield (TEY) and/or total fluorescence yield (TFY). TEY measures the electric current produced by a sample when the incident x-rays excite electrons to the valence states at the resonant frequency. TEY is most sensitive to the top few nanometers of the sample surface and may lead to anomalous results due to surface termination

differences or a composition gradient in a film. Additionally, TEY can be difficult in insulating materials such as garnets, as they are not electrically conductive. Mounting the sample with a small amount of silver paste on one corner or a very thin layer of a metal deposited on the surface can alleviate this problem. TFY measures the number of photons released when an electron excited into the valence state relaxes down into a core orbital. TFY is thus sensitive to a much larger thickness of the sample than TFY, as a photon can easily escape from deeper within a sample than an electron, which is prone to recombination with a core hole. However, TFY is significantly weaker than TEY and may require much longer counting times to achieve the same signal-to-noise ratio.

XMCD thus gives the ability to have element and site-resolved magnetic moments in many samples. The very high sensitivity of XMCD makes it useful for studying magnetism in weakly magnetic systems, and magnetic proximity effects in heavy metals and topological insulators[79,81,216]. The cost of this very high specificity is that it is only available at large synchrotron facilities, such as the Advanced Photon Source (APS) at Argonne National Lab, where all of the XMCD in this work was collected.

4. Polycrystalline Europium Iron Garnet with Perpendicular Magnetic Anisotropy

4.1 Motivation

Research on rare-earth iron garnets for spintronics has previously focused on the use of epitaxial thin films grown on garnet substrates[39,217,218]. Single crystal REIG grown by PLD exhibit exquisite structural perfection, low surface roughness, and bulk-like saturation magnetization[50,158]. The correct selection of rare-earth ion (and associated magnetostriction coefficient) and strain state (compressive or tensile) can lead to perpendicular magnetic anisotropy (PMA) in thin film garnets. As the magnetocrystalline anisotropy and shape anisotropy ($\propto M_s^2$) are low for the garnets, the magnetoelastic contribution dominates. Relatively low amounts of compressive (tensile) strain and a positive (negative) magnetostriction coefficient is sufficient to generate PMA in epitaxial garnet films[158,219]. As discussed in previous sections, it is desirable to have thin films with PMA as opposed to in-plane magnetic anisotropy (IMA) as this allows study of novel spin textures such as skyrmions and manipulation of the magnetization with the damping-like spin-orbit torque (SOT)[8,220].

However, there are limitations to epitaxial garnet films. The primary obstacle is that they require the use of expensive garnet substrates, of which there are limited commercial options. In addition to the cost and limited selection, these garnet substrates are not easily compatible with existing CMOS (complementary metal oxide semiconductor) processing in modern chip foundries, requiring slow etching by acid[221]. One promising alternative is through the use of 2-dimensional layer transfer processes, facilitated by graphene. Work by Kim et al. has shown that it is possible to grow a large variety of materials, including REIG, on a monolayer or bilayer of graphene that

has been deposited on a different substrate, such as GGG[222]. In a remote epitaxy process (see figure 4.1), the REIG grows as a single crystal on top of the graphene layer(s), as the graphene layer is thin enough to not obstruct the electric polarization of the atoms in the underlying substrate[223]. This allows the growth of thin films, that can then be exfoliated through a mechanical stressor. The exfoliated films can then be placed on another substrate and fabricated into devices[224]. This also offers a potential for expensive substrates to be reused many times by simply replacing the graphene layer and depositing another film.

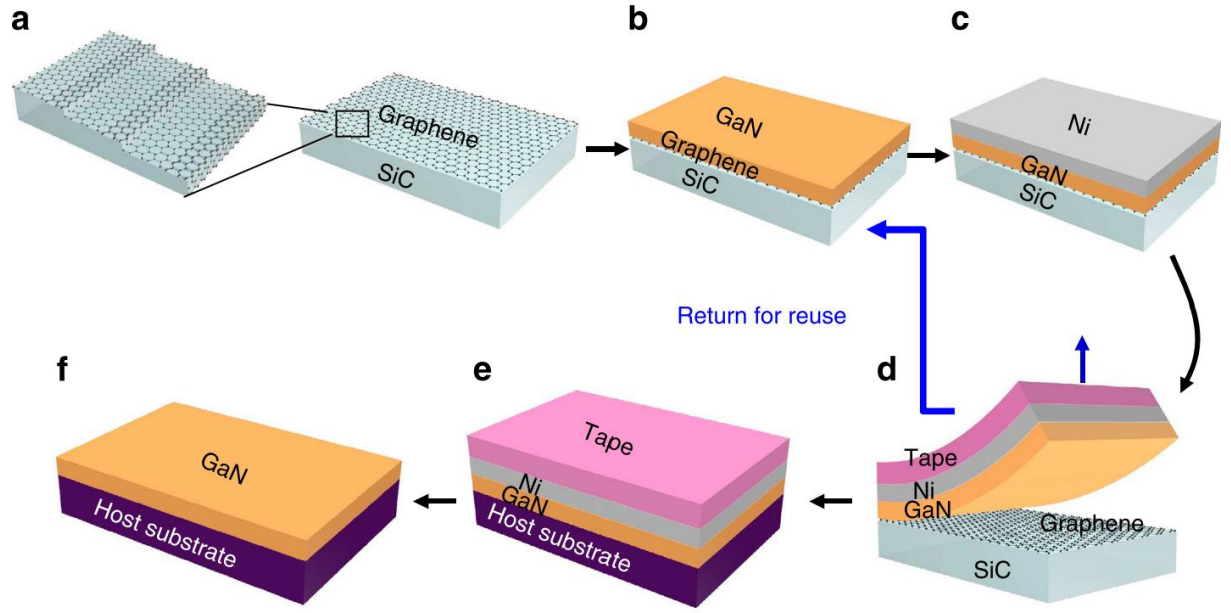

Figure 4.1: Schematic of a remote epitaxy and 2-dimensional layer transfer process. (a) Deposition of graphene on a SiC substrate. (b) Growth of an epitaxial GaN film on the graphene layer. (c) Deposition a Ni mechanical stressor layer. (d) Removal of the GaN film via adhesive tape. (e) Transfer of the tape/Ni/GaN stack to the desired substrate. (f) Removal of the Ni and tape, completing the transfer process. From ref. 222. Used with permission.

Although technologies such as 2-dimensional layer transfer are promising, they suffer from a high degree of complexity and resulting low yields. A better alternative would be to grow REIG on non-garnet substrates that are of interest to industry, in particular silicon. However, this would preclude growing epitaxial, single crystal REIG films as there is no epitaxial relationship. The

goal is then to determine if it is possible to grow REIG thin films with comparable properties on non-garnet substrates.

Epitaxial single crystal REIG films on garnet substrates are characterized as grown, without the need for any further annealing or post processing. In the PLD chambers used in this work, the substrate temperature during growth is 650 °C, which is sufficient for crystallization to occur and the resulting observed high quality of films. However from previous work it is known that polycrystalline garnet films on non-garnet substrates require an *ex situ* anneal at a temperature higher than the deposition temperature to induce crystallization, typically in the range of 750-900 °C [160,225]. As an aside, this crystallization process is actually quite complex. One could assert that it is not necessary for high deposition temperatures for polycrystalline films as they would be annealed *ex situ* at a higher temperature anyways. However, this is not the case. Our group has repeatedly found that films grown at room temperature do not crystallize well (if at all) when annealed following the sample procedure. This indicates that there is some sort of complex "pre-crystallization" process that occurs during growth. Stadler et al. have explored novel two-step annealing procedures to improve crystallinity of room-temperature sputtered films with some success, but more work is needed[161]. A TEM study of films grown at different temperatures before and after annealing would be enlightening.

However, this high temperature annealing serves as a solution to our problem: how do we generate PMA in films without an epitaxial relationship with the substrate? The hypothesis is that this could still be done via magnetoelastic anisotropy, but the source of strain would be thermal expansion

mismatch with the substrate. The requirement of a high temperature anneal creates a large ΔT which can result in considerable strains for a relatively small thermal expansion mismatch.

The next step is to select a garnet that will be appropriate for this situation. As the polycrystalline films are random and the source of the anisotropy is magnetoelastic, it is necessary for both magnetostriction coefficients to be of the same sign. This ensures that for any grain orientation, the response to the same applied stress will be the same, although the magnitude of the response may vary. The magnetostriction coefficients of several REIG are shown in Table 4.1. Europium iron garnet (EuIG) was selected for this project as it had been recently shown that both (111) and (100) orientations of single crystal EuIG grown under compressive strain on GGG substrates exhibit PMA, and both of EuIG's magnetostriction coefficients are positive[45,226–228].

Table 4.1: Table of magnetostriction coefficients for selected rare-earth iron garnets[228].

Rare-earth element	λ_{100} (10^{-6})	λ_{111} (10^{-6})
Y	-1.4	-2.4
Sm	21	-8.5
Eu	21	1.8
Gd	0	-3.1
Tb	-3.3	12
Dy	-12.5	-5.9
Ho	-3.4	-4.0
Er	2.0	-4.9
Tm	1.4	-5.2
Yb	1.4	-4.5

4.2 Growth and Structural Characterization

As EuIG has both magnetostriction coefficients greater than zero, the film must be placed in compressive strain to produce the correct effect on the anisotropy. EuIG has a relatively high thermal expansion coefficient of 10.4 x 10^{-6} K^{-1}, which when combined with the need for temperature stability to at least 900 °C, severely limits the options of substrates with higher thermal expansion[229]. The best option was determined to be the (0001) cut of quartz (Z-quartz), which has a thermal expansion coefficient (TCE) of 13.71 x 10^{-6} K^{-1} [230]. Several other oxide substrates and silicon were selected to study the film growth and properties as a function of TCE. Table 4.2 shows the thermal expansion coefficients and other parameters of the films.

The films were deposited by PLD under the same conditions in which single-crystal films have been grown in our group[8,45,50]. The films were then rapid thermal annealed at 860 °C for 5 minutes in an oxygen environment. This procedure is similar to what others who have grown polycrystalline garnets have described[231,232]. For the substrates studied (fused SiO_2, Si, (1120) quartz (X-quartz), yttria-stabilized zirconia (YSZ), and Z-quartz), the films crystallize readily for thicknesses in the range of 40 nm, which is a typical thickness. A 40 nm EuIG has sufficient moment to allow easy characterization of the magnetic properties while still having a relatively low deposition time. No preferred crystallographic texture was observed in these films, and a plot of the GIXD for these films is shown in figure 4.2 along with the reference intensities. It was not possible to measure the shift in peak position across the different substrates as the peaks are too broad. Residual stress measurements on high-angle reflection were also unable to determine reliably the stress in the films, due to the weak signal and lateral heterogeneity of the films due to the PLD process. Average grain size was determined to be approximately 50 nm.

It is well known in the garnet literature that it is not possible to grow polycrystalline garnet films on non-garnet substrates with garnet thicknesses of less than approximately 20 nm[205,225,233,234]. The exact cause for this is unknown but is suspected to be related to the large size and complexity of the unit cell, leading to slow crystallization dynamics in ultra-thin films. In contrast, it is possible with PLD to grow epitaxial garnet films of nearly any thickness, down to as thin as 1-2 nm and as thick as 1 μm[47,235]. The XRD (post-annealing) of a typical polycrystalline film of 14 nm in thickness is shown in figure 4.3, where no major garnet peaks can be clearly observed.

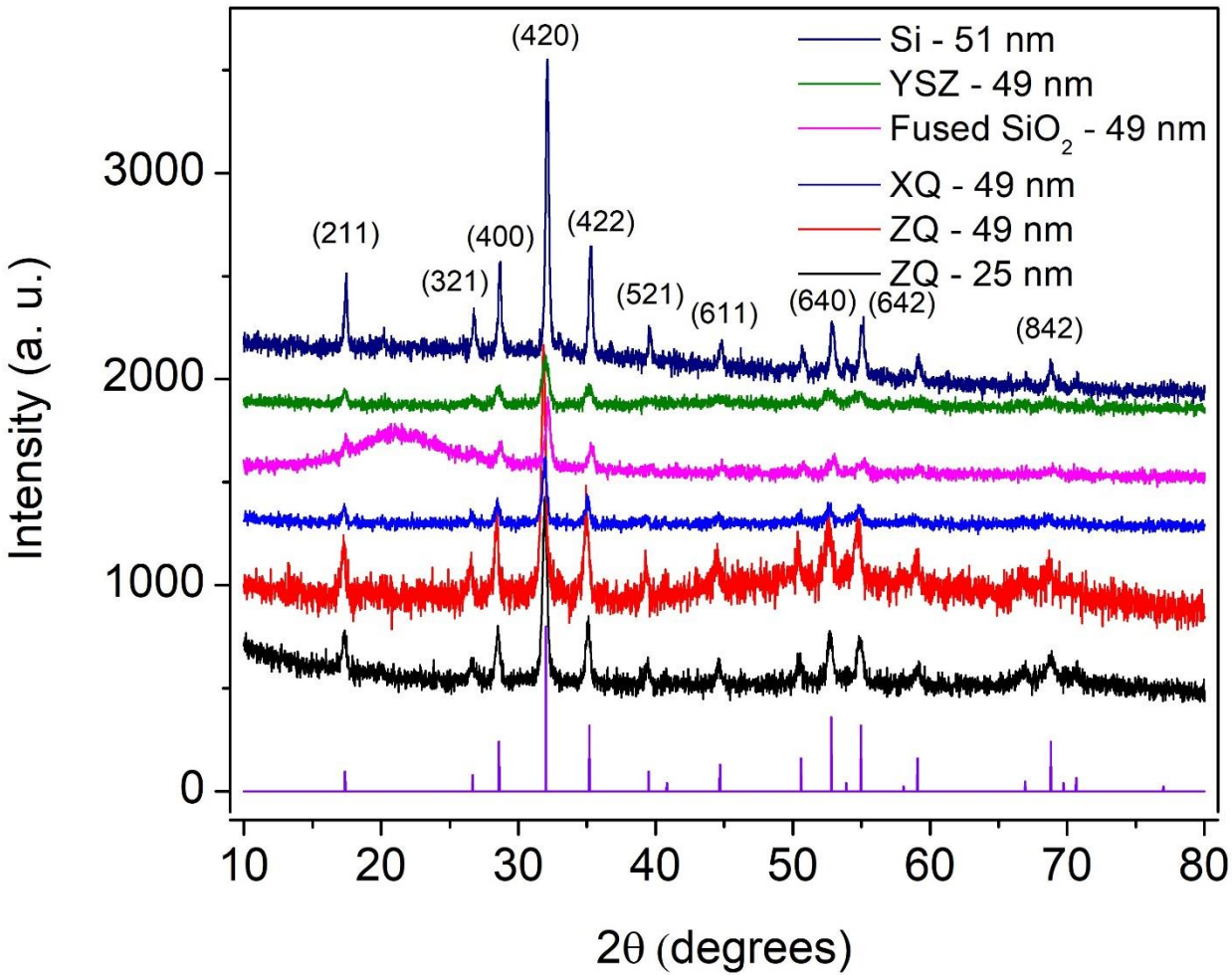

Figure 4.2: Grazing incidence XRD of EuIG films grown on different substrates. The reference intensities are shown at the bottom of the plot. All major garnet peaks are present in the expected ratios. No secondary phases are present. Vertically offset for clarity.

The next obstacle regarding EuIG is the appearance of secondary phases at thickness above 60 nm. The garnet system has a complex stoichiometry and crystal structure, and there are many other

binary and ternary oxides that can form with the elements in this system. Although other garnets have been grown across a wide range of thicknesses (including YIG and DyIG), EuIG was limited to the range of 20-60 nm in thickness[33,193,235]. At higher thicknesses, the garnet peaks began to disappear, and a number of anomalous peaks appeared at relatively low angles (see figure 4.4).

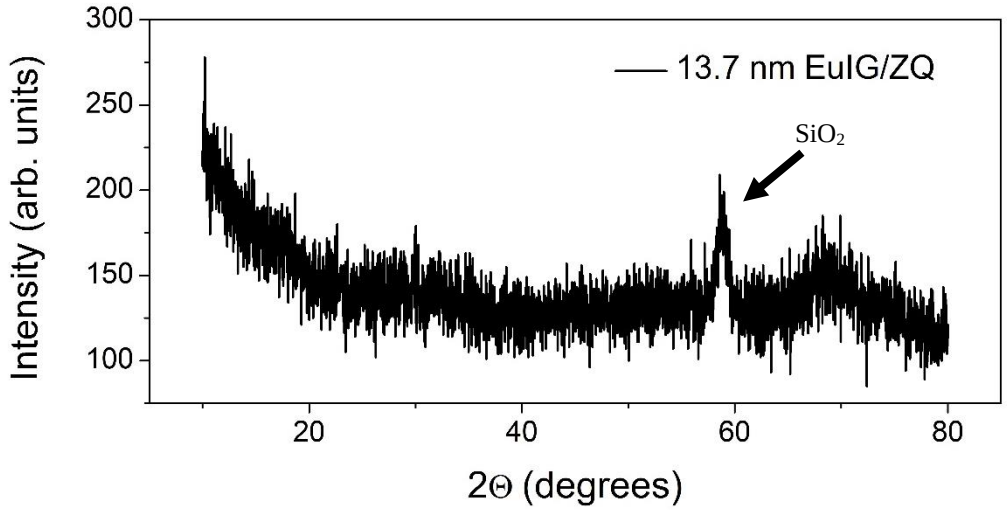

Figure 4.3: XRD of a 13.7 nm EuIG/ZQ film showing no garnet peaks due to the low thickness. The large peak is due to the substrate and other minor peaks may be due to secondary phases.

These are believed to be primarily due to the orthoferrite ($EuFeO_3$), although binary oxides of iron and europium are also possible. There was negligible magnetic moment for these samples as well. Surface roughness was measured by atomic force microscopy (AFM) and was found to be less than 1 nm for all of the films measured. There was no indication that film roughness was related to the substrate, and no significant relationship between film thickness and roughness. This sub-nanometer roughness is in comparable to epitaxial single crystal films[45,50].

4.3 Magnetism and Uniaxial Anisotropy

Substrates with different thermal expansion coefficients, both greater than and less than of EuIG were used to grow films. After analyzing the XRD and determining that garnet was the only phase present, the magnetic hysteresis loops were measured via VSM. In figure 4.5, there is an observed large effect on the anisotropy of the films with the change in substrate. Figure 4.5 a-b, with Z-quartz as the substrate, are the only films to exhibit a higher out of plane (OP) remanence,

indicating an out of plane easy axis and PMA. Although there is a significant IP remanence, the OP direction is clearly preferred when in a compressive strain state. The other substrates, which place the film in either a tensile strain state or have very little strain have higher in-plane (IP) remanence. This is attributed to the magnetoelastic anisotropy. The uniaxial anisotropy for this system can be described with[33]:

$$K_u = -\frac{3}{2}\lambda\sigma - \frac{\mu_0}{2}M_s^2 \tag{4.1}$$

Where λ is the average magnetostriction (see section 2.1.4) and σ is the uniaxial stress in the film. The in plane uniaxial stress is the product of the thermal expansion coefficient mismatch ($\Delta\alpha = \alpha_{substrate} - \alpha_{film}$) and the temperature differential from the RTA temperature to room temperature, where all measurements were conducted. The effective anisotropy field can be calculated from the uniaxial anisotropy according to equation (2.11).

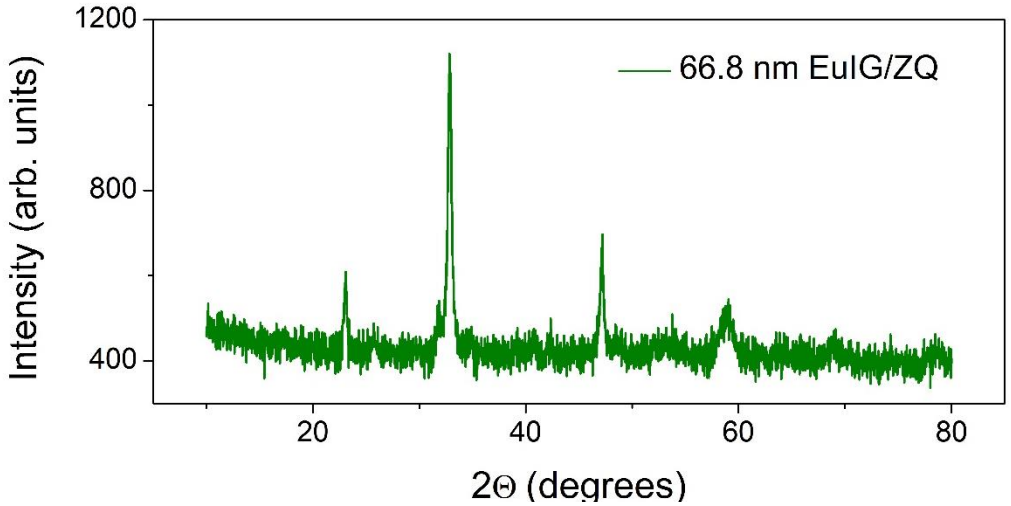

Figure 4.4: XRD of a 66.8 nm EuIG/ZQ film showing no garnet peaks due to the high thickness. Peaks present are due to the $EuFeO_3$ orthoferrite and binary Eu_2O_3 and Fe_2O_3 oxides.

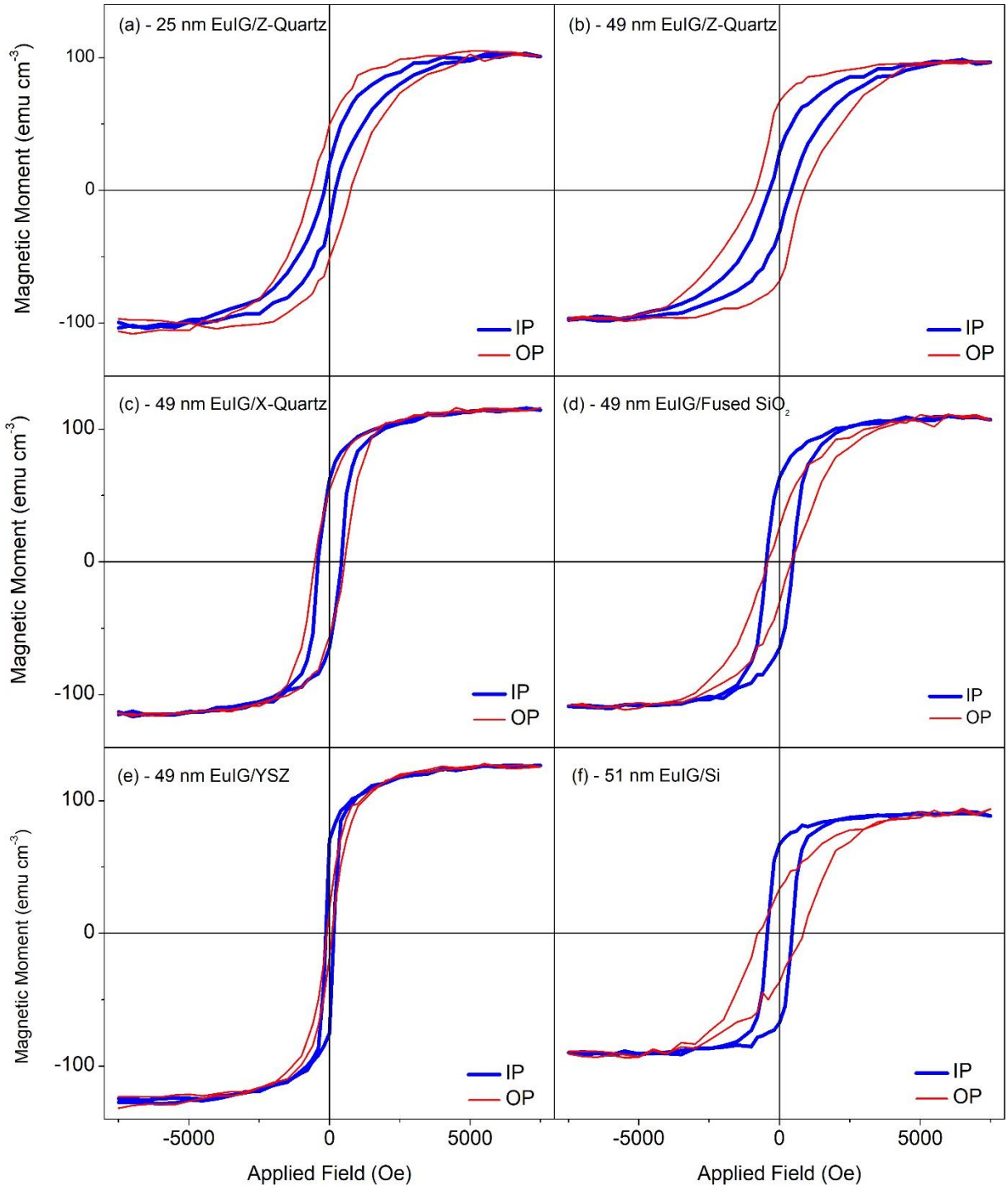

Figure 4.5: VSM hysteresis loops (out of plane, OP, and in plane IP) of EuIG films on different substrates. (a) 25 nm EuIG on Z-quartz. (b) 49 nm EuIG on Z-quartz. (c) 49 nm EuIG on X-quartz. (d) 49 nm EuIG on fused SiO_2. (e) 49 nm EuIG on YSZ. (f) 51 nm EuIG on Si. From ref. 33. Used with permission.

To compare the predicted uniaxial anisotropy from equation 4.1 and the experimental data, the uniaxial anisotropy was estimated from the hysteresis loops via the anhysteretic loop method[18,33].

The uniaxial anisotropy of the films can be estimated from hysteresis loops that have been generated by averaging the magnetization values at the same field on both passes of the loop in the first quadrant. The integral area between the anhysteretic IP and OP loops is the experimental uniaxial anisotropy. This is shown schematically in figure 4.6. The experimental and theoretical values of the uniaxial anisotropy are shown in Table 4.2. There is a decent agreement between the values, but importantly the trend is consistent with the trend in thermal expansion mismatch.

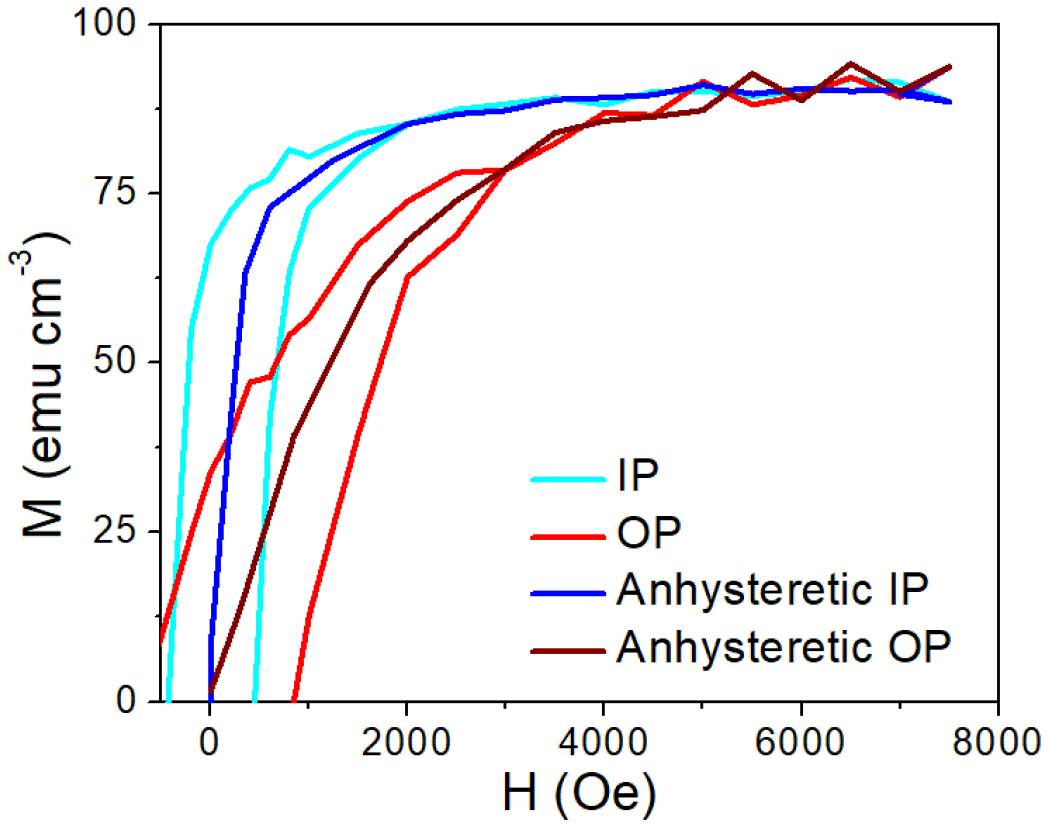

Figure 4.6: The first quadrant of VSM IP (cyan) and OP (red) hysteresis loops and anhysteretic IP (navy) and OP (burgundy) loops of a EuIG/Si film. The uniaxial anisotropy is the area between the navy and burgundy curves.

Magnetic force microscopy (MFM) was collected on an AC demagnetized 49 nm EuIG/Z-quartz sample. The demagnetization cycle began at 10 kOe, with alternating field directions decreasing by 10% each step until < 1 Oe was reached. The contrast is low as the saturation magnetization is low for the garnets, but it is possible to see regions of light and dark contrast, corresponding to up and down domains (see figure 4.7).

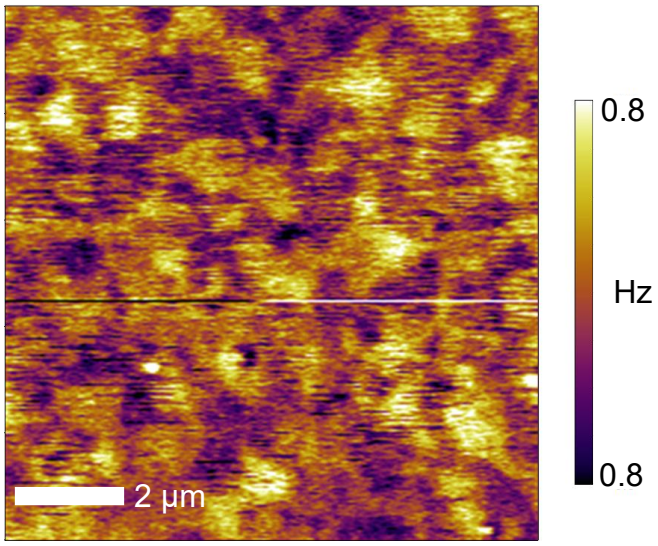

Figure 4.7: Magnetic force microscopy image of a 49 nm EuIG/Z-quartz film after AC demagnetization. Regions of light and dark contrast correspond to up and down magnetized domains. The white spots and horizontal lines are due to surface particles and an experimental artifact, respectively.

Table 4.2: Table of linear thermal expansion coefficients, thermal mismatch stain, calculated anisotropy, and anisotropy determined from anhysteretic hysteresis loops of EuIG films on different substrates.

Material	**α (10^{-6} K^{-1})**	**Calculated thermal mismatch strain**	**Calculated K_{me} (10^3 J m^{-3})**	**Calculated K_u (10^3 J m^{-3})**	**Measured K_u (10^3 J m^{-3})**	**TCE ref.**
EuIG	10.4	---	---	---	---	[229]
Fused SiO_2	0.52	-0.00828	-30.9	-37.0	-5.00	[236]
Si	2.6	-0.00654	-24.4	-30.5	-6.80	[237]
X-quartz	7.48	-0.00245	-9.15	-15.2	-2.30	[230]
YSZ	10.3	-8.38 x 10^{-5}	-0.313	-0.635	-0.694	[238]
Z-quartz	13.71	0.00277	1.04	0.433	1.08	[230]

4.4 Spin Transport in Pt/EuIG Heterostructures

To assess the feasibility of polycrystalline REIG for spintronics, 4 nm of Pt was deposited on a 49 nm EuIG/Z-quartz film, which was then patterned into Hall crosses using a top-down optical lithography and ion milling[45]. The dimensions of the Hall cross were 620 μm x 50 μm. The

anomalous Hall-effect like spin Hall magnetoresistance measurements were measured with a standard technique with a lock-in amplifier to detect the small signals, which were on the order of μV[8]. A linear background has been subtracted from the data and a vertical height correction was also performed. The OP and IP hysteresis loops are shown in figure 4.8. The OP loop tracks the net magnetization vector, so the voltage polarity reverses at the coercivity of the patterned film. The amplitude of the AHE in the OP loop is nearly identical to values reported in single crystal EuIG by Rosenberg et al., and is also very similar to values reported in other garnets (TbIG, TmIG, and YIG)[8,45,50]. It was not possible to saturate the IP loop under the experimental apparatus's maximum applied field of 10 kOe, which is significantly higher than the anisotropy field of ~ 5 kOe of the unpatterned film. The reason for this is speculated to be a change in the strain state of the EuIG film and domain wall pinning due to the patterning.

To evaluate the quality of the interface between the EuIG and Pt, the spin mixing conductance can be calculated from the amplitude of the IP and OP SMR hysteresis loops[239,240]. The spin mixing conductance ($G_{\uparrow\downarrow} = G_r + iG_i$) quantifies the transparency of the interface between a magnetic material (metal or oxide) and a non-magnetic metal with high spin-orbit coupling[241]. The two components of $G_{\uparrow\downarrow}$ can be calculated for a heavy metal/magnetic insulator[239]:

$$\frac{\Delta\rho_1}{\rho} = \theta_{sh}^2 \frac{\lambda}{d_n} \frac{2\lambda G_r \tanh\left(\frac{d_n}{2\lambda}\right)^2}{\sigma + 2\lambda G_r \coth\left(\frac{d_n}{2\lambda}\right)^2} \tag{4.2}$$

$$\frac{\Delta\rho_2}{\rho} \approx \frac{2\lambda^2\theta_{sh}^2}{d_n} \frac{\sigma G_i \tanh\left(\frac{d_n}{2\lambda}\right)^2}{\left(\sigma + 2\lambda G_r \coth\left(\frac{d_n}{\lambda}\right)\right)^2} \tag{4.3}$$

Where $\Delta\rho_1$ is the amplitude of the hard axis SMR resistivity, $\Delta\rho_2$ is the amplitude of the easy axis SMR resistivity, ρ is the resistivity of the non-magnetic material, θ_{sh} is the spin Hall angle ($\theta_{sh} \approx 0.08$ in Pt), λ is the spin diffusion length ($\lambda \approx 1.4$ nm in Pt), d_n is the non-magnetic metal thickness, and $\sigma = \rho^{-1}$ is the conductivity of the non-magnetic metal layer[143,239]. The spin mixing conductance has units of $\Omega^{-1}m^{-2}$. These equations can be rearranged into a more convenient format to solve for the unknown quantities G_r and G_i:

$$G_r = \frac{\frac{\Delta\rho_1}{\rho}\frac{d_n}{\lambda\theta_{sh}^2}\sigma}{2\lambda\tanh\left(\frac{d_n}{2\lambda}\right)^2 - 2\frac{\Delta\rho_1}{\rho}\frac{d_n}{\theta_{sh}^2}\coth\left(\frac{d_n}{2\lambda}\right)} \tag{4.4}$$

$$G_i \approx \frac{\Delta\rho_2}{\rho}\frac{d_n}{2\lambda^2\theta_{sh}^2}\frac{\left(\sigma + 2\lambda G_r\coth\left(\frac{d_n}{\lambda}\right)\right)^2}{\sigma\tanh\left(\frac{d_n}{2\lambda}\right)^2} \tag{4.5}$$

The values of $\Delta\rho_1$ and $\Delta\rho_2$ can be determined from the hysteresis loops and the thickness of the nonmagnetic metal by considering Ohm's law for the transverse resistivity and making the appropriate substitutions for the voltage to electric field and current to current density[242]:

$$R_H = \frac{V_H}{I} = \frac{E_H * w}{j * d_n * w} = \frac{\rho_H}{d_n} \tag{4.6}$$

$$\rho_H = R_H * d_n \tag{4.7}$$

Where R_H is the measured Hall resistance, V_H is the transverse Hall voltage across the Hall bar, I is the current, E_H is the electric field due to the Hall voltage, w is the width of the Hall bar, j is the current density, d_n is the thickness of the nonmagnetic metal, and ρ_H is the Hall Resistivity.

As it was not possible to saturate the IP SMR hysteresis loop, it is not possible to calculate the spin mixing conductance. However, if we assume that $\lambda G_r << \sigma$, we can calculate a lower bound for the imaginary part of the spin-mixing conductance[8,45,50]:

$$G_i \approx \frac{\Delta\rho_2}{\rho}\frac{d_n}{2\lambda^2\theta_{sh}^2}\frac{\sigma^2}{\sigma\tanh\left(\frac{d_n}{2\lambda}\right)^2} \tag{4.8}$$

Using this equation, we are able to calculate that the imaginary part of the spin-mixing conductance of the Pt/EuIG/Z-quartz interface to be 5.1 x 10^{12} $\Omega^{-1}m^{-2}$, which is close to other values reported from our group on single crystal REIG/Pt heterostructures[45]. This indicates that spintronics based on polycrystalline REIG are a feasible alternative to single crystal films.

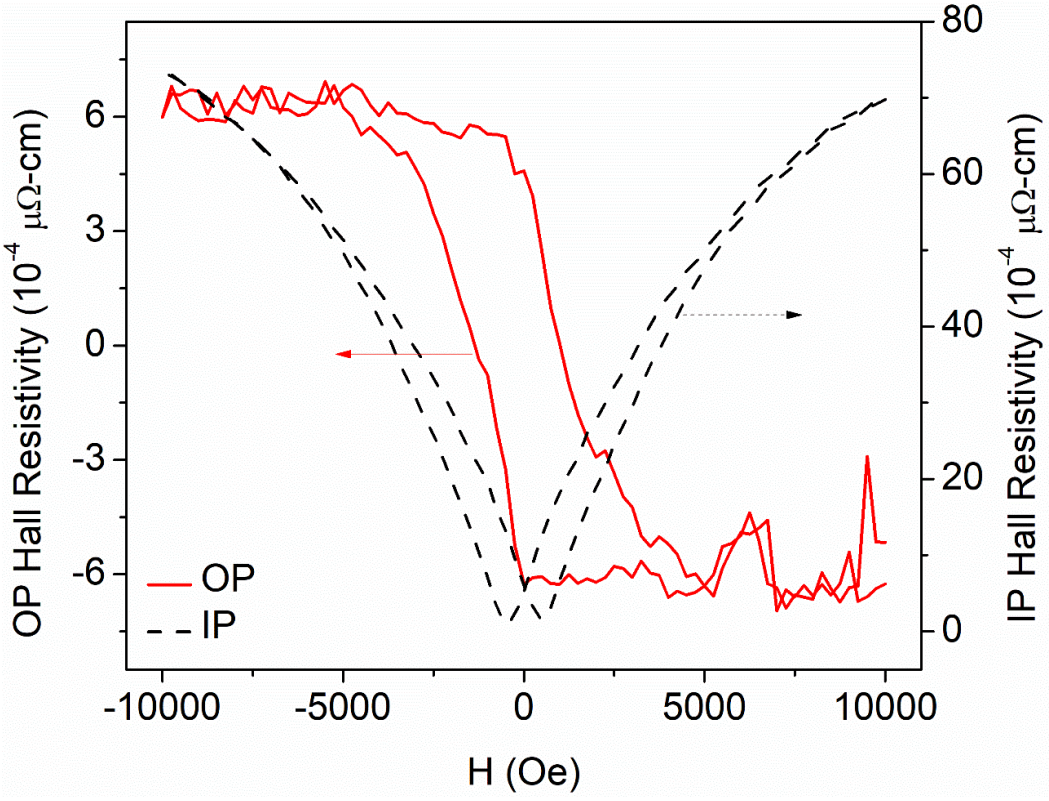

Figure 4.8: Anomalous Hall effect-like spin Hall magnetoresistance hysteresis loop (black) measured using an out-of-plane magnetic field and spin Hall magnetoresistance hysteresis loop measured with an in-plane magnetic field. The Hall cross was patterned from a Pt(4 nm)/EuIG(49 nm)/Z-quartz film. From ref. 33. Used with permission.

5. Polycrystalline Dysprosium Iron Garnet with Perpendicular Magnetic Anisotropy on Silicon

5.1 Single Crystal Dysprosium Iron Garnet

Building on the conclusions from the previous section, the next goal was to integrate PMA garnet films directly on Si substrates. However, the magnetostriction coefficients of EuIG are of the opposite sign to produce an OP easy axis when under in-plane tension after a high temperature anneal on a low thermal expansion Si substrate. For this reason, this next section focuses on dysprosium iron garnet (DyIG). DyIG, YIG and holmium iron garnet (HoIG) all have negative values for both of the magnetostriction coefficients, but DyIG was selected because YIG does not have PMA on Si because of its comparatively high shape anisotropy due to a larger magnetization and weak magnetostriction coefficients, and HoIG has smaller magnetostriction coefficients than DyIG[228]. It is desirable to have higher magnetostriction and thus higher anisotropy, as it is possible to decrease these values via codeposition or alloying with other garnets, such as YIG, if needed for the application. There were no previous studies on DyIG epitaxial thin films, so the first section will focus on the characterization of a selection of single crystal films.

A bulk DyIG target was synthesized by ball milling, cold pressing, calcining, and sintering the binary oxide powders in the appropriate stoichiometry[160]. X-ray diffraction was done after the first sintering step, which showed a minority $DyFeO_3$ orthoferrite phase. The green body was then ground into powder and all steps repeated, after which the XRD showed pure phase garnet.

The lattice parameter of bulk DyIG is 1.2405 nm, which informs the choice of single crystal garnet substrates selected[41]. There are a number of commercially available garnet substrates with

different compositions and lattice parameters, including $Gd_3Ga_5O_{12}$ (GGG, 1.2376 nm), $G_{2.6}Ca_{0.4}Ga_{4.1}Mg_{0.25}Zr_{0.65}O_{12}$ (SGGG, 1.2480 nm), and $Gd_3Sc_2Ga_3O_{12}$ (GSGG, 1.2554 nm). The uniaxial anisotropy of DyIG films can be described using the equation derived by Quindeau et al.[50]:

$$K_{u,sc} = -\frac{K_1}{12} + \frac{9}{4}\lambda_{111}c_{44}\left(\frac{\pi}{2} - \beta\right) + \frac{\mu_0}{2}M_s^2 \quad (5.1)$$

Where K_1 is the first order magnetocrystalline anisotropy (< - 500 J m^{-3}), λ_{111} is the magnetostriction coefficient along (111), c_{44} is the shear modulus (76.4 GPa for YIG), β is the corner angle of the rhombohedrally distorted unit cell, and M_s is the saturation magnetization[243,244]. From this equation, it can be observed that the negative magnetostriction coefficient and a tensile strain state should result in PMA. Table 5.1 lists the lattice parameters, corner angles, calculated anisotropy, and other parameters for single crystal films on different substrates.

Table 5.1: Table of lattice parameter, lattice mismatch, unit cell volume, rhombohedral corner angle (β), and calculated anisotropy field for 40 nm nominal thickness DyIG films on different substrates.

Substrate	**Lattice parameter (nm)**	**Lattice mismatch**	**Unit cell volume (nm^3)**	**β (°)**	**Calculated $\mu_0 H_K$ (mT)**
DyIG (bulk)	1.2405	---	1.9089	---	---
GGG	1.2376	0.23 %	1.9164	89.7	190 (IP)
SGGG	1.2480	-0.60 %	1.8966	90.4	80 (OP)
GSGG	1.2554	-1.19 %	1.8856	90.8	240 (OP)

Figure 5.1 shows HRXRD scans for nominally 40 nm thick DyIG/GGG, DyIG/SGGG, and DyIG/GSGG films. As expected from the lattice parameters, the film on GGG is in compressive strain while the other two are in tensile strain. The lattice parameters were extracted from the peak positions according to Bragg's law and the corner angle of the unit cell was calculated according

to the method from section 3.4. Lattice parameters increase monotonically with increasing in-plane tensile stress, while the unit cell volume decreases monotonically for the epitaxial thin films.

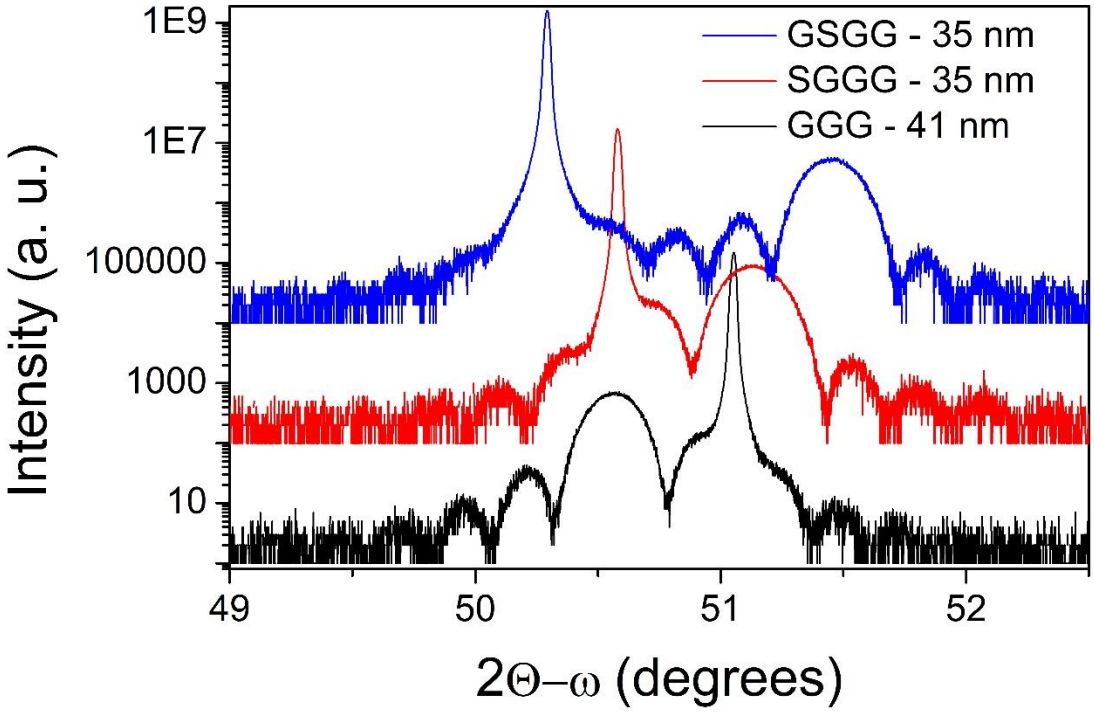

Figure 5.1: High resolution x-ray diffraction of nominal 40 nm DyIG films on different substrates. The sharp peaks are from the substrates and the largest round peaks are film peaks. Vertically offset for clarity.

The epitaxial DyIG films were then measured on the VSM (see figure 5.2). As predicted, the film on GGG has in-plane (IP) anisotropy and the films on SGGG and GSGG have out-of-plane anisotropy (OP, PMA). All three films have very low coercivities, less than 10 mT, similar to EuIG but significantly lower than terbium iron garnet (TbIG) single crystal films[45,226]. However, it was not possible to saturate these films in the VSM along the hard axis direction in a maximum field of 1 T. This contrasts sharply with the predicted anisotropy fields on the order of 100 mT from equation (5.1). As it is unlikely that the value of the shear modulus differs significantly from the YIG value used here, the magnetostriction coefficients in the thin films are likely different from the bulk values. Non-bulk values of the magnetostriction coefficients in thin films have been observed in other rare earth iron garnet systems[45,245]. The observed differences in saturation

magnetization are attributed to noise in the measurement, and slightly varying conditions between depositions in the PLD chamber.

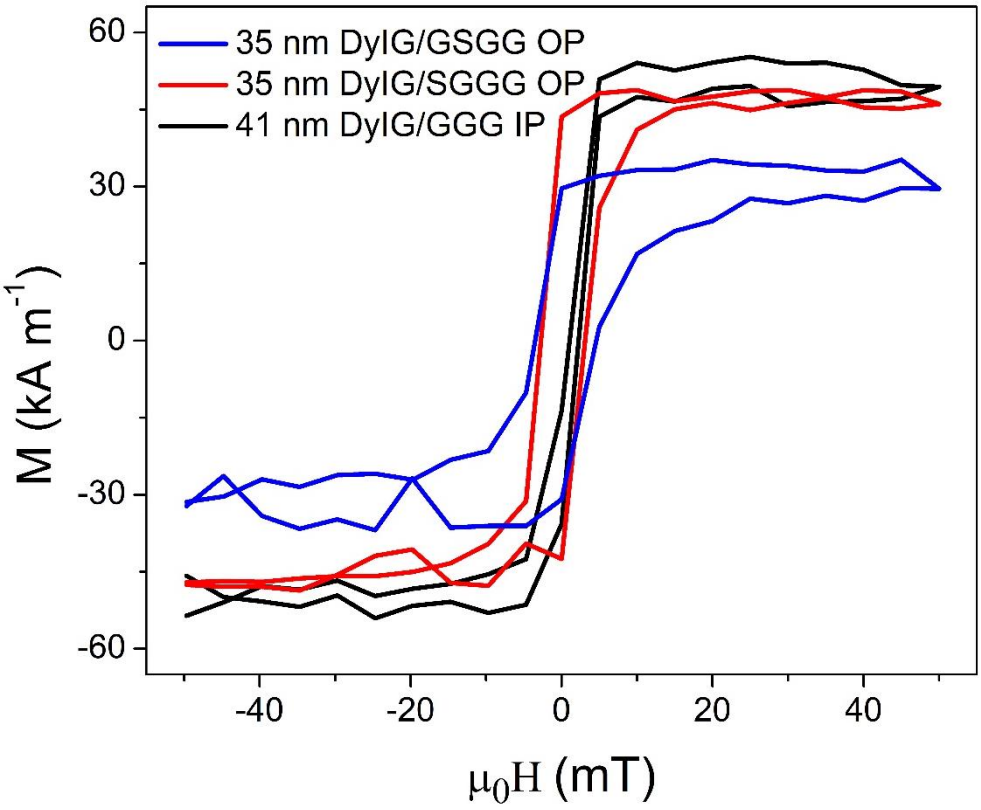

Figure 5.2: VSM hysteresis loops along the easy axis for DyIG films grown on different substrates. Films grown on GGG have IP anisotropy, and films on SGGG or GSGG have OP anisotropy.

Ferromagnetic resonance is a common method to measure the Gilbert damping and anisotropy of materials. There were no previous reports of damping in DyIG films, so a measurement was attempted on a 116 nm DyIG/GGG sample. A thick, single crystal sample with IP anisotropy was selected to minimize the damping, which increases due to confinement in thin films, scattering from grain boundaries, and different magnon modes in PMA films[159,246]. Magnetic materials commonly have resonance in the microwave region and placing a sample in contact with a coplanar wave guide in an electromagnet allows measurement of the absorbed power during a frequency sweep at constant field or, more commonly, a field sweep at constant frequency. The absorbed power is ideally the derivative of a Lorentzian function, but is commonly composed of both

symmetric and antisymmetric components[45,247]. For this experiment, only a symmetric Lorentzian was used in fitting:

$$P = \frac{-2a(H - H_{res})}{((H - H_{res})^2 + \Delta H^2)^2} \tag{5.2}$$

Where P is the absorbed power, a is the amplitude (a fitting parameter), H is the applied magnetic field, H_{res} is the resonant magnetic field at a given frequency, and ΔH is the FMR linewidth. For this sample, only five frequencies were collected in the range 3-5 GHz (see figure 5.3) as the electromagnet could not apply enough field to shift the resonant peak to higher fields. The data was fit to the symmetric Lorentzian derivative in equation (5.2), and the resonant fields and linewidths were determined. The resonant field is then plotted versus the applied frequency and the value of the gyromagnetic ratio is extracted from the slope according to[26]:

$$\omega = 2\pi|\gamma|(H_{res} - 4\pi M_s) \tag{5.3}$$

Where $\omega/2\pi$ is the frequency and γ is the gyromagnetic ratio. The FMR linewidth is then plotted as function of the applied frequency, and a linear fit is obtained according to[26]:

$$\Delta H = \frac{2\alpha}{\sqrt{3}|\gamma|}\frac{\omega}{2\pi} + \Delta H_0 \tag{5.4}$$

Where α is the Gilbert damping, and ΔH_0 is the inhomogeneous line broadening. A value of 0.23 is obtained for the DyIG/GGG film, which is quite large compared to the values for YIG (~10^{-5}) and permalloy (~0.005)[26,193,248]. This is not surprising, as the stronger spin orbit coupling of rare-earth ions is known to increase the Gilbert damping. Damping has been reported for other rare-earths including lutetium iron garnet (~10^{-4}), thulium iron garnet (10^{-3} - 10^{-2}) , and EuIG (10^{-3})[45,50,249,250]. In previous work by Rosenberg et al., it was not possible for them to measure the damping of TbIG as it was too large[45]. Work by Vella-Coleiro et al. on domain wall motion in bulk samples showed that the domain wall mobility and damping for DyIG were roughly one order

of magnitude larger than EuIG, and TbIG was roughly two orders of magnitude larger than EuIG, providing some context for these very large damping values[251].

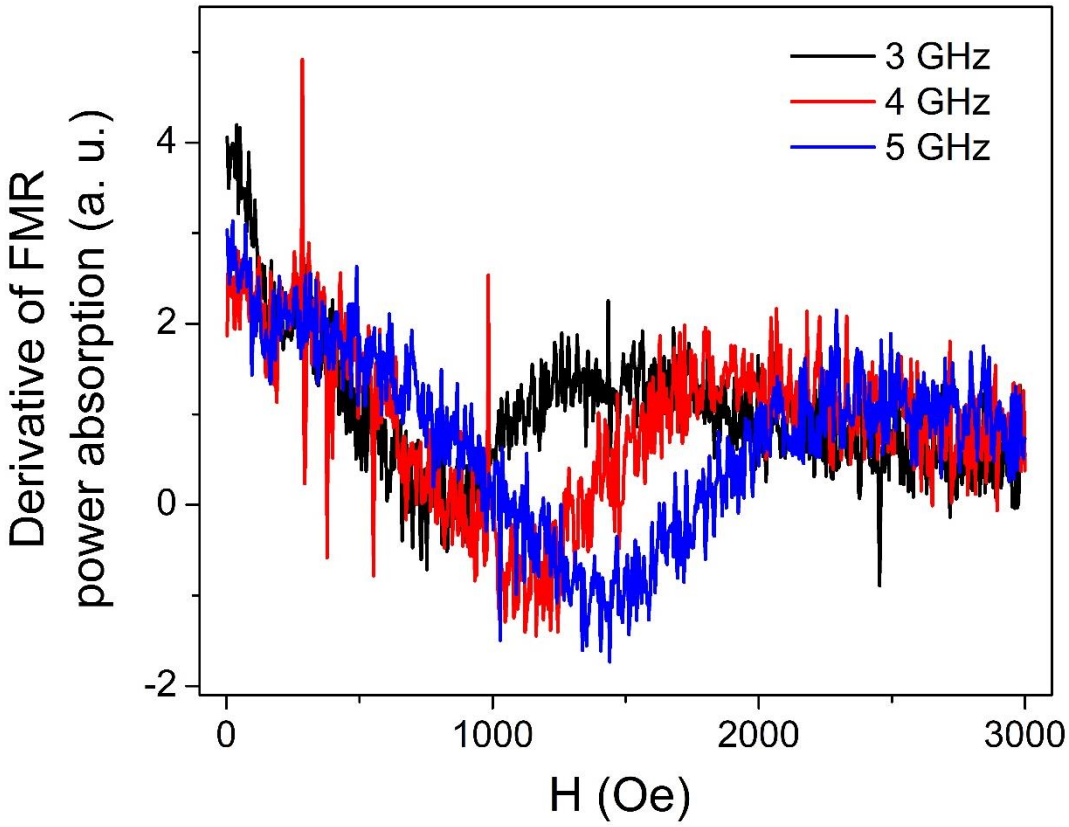

Figure 5.3: Ferromagnetic resonance of a 116 nm DyIG/GGG film collected from 3-5 GHz. A damping value of $\alpha = 0.23 \pm 0.02$ was extracted.

Polarized neutron reflectometry (PNR) was collected on a 116 nm DyIG/GGG sample at room temperature to investigate the depth dependence of the magnetization. Previous PNR studies on garnets have established the need for an interfacial gadolinium iron garnet (GIG layer) in the region between the film and substrate[199,252]. The scattering length density (SLD) profile can be seen in figure 5.4, which shows a composition gradient at the interface with the substrate, as expected, in the nuclear, imaginary, and magnetic SLD. As the gadolinium iron garnet substrate has the same crystal structure, very similar lattice parameters, and similar ionic radii to the DyIG film, the Gd^{3+} easily exchanges for the Dy^{3+} and the Ga^{3+} for the Fe^{3+}. The extent of the interdiffusion is over a 5-10 nm region and depends greatly on the growth conditions. In these PLD grown films, the

substrates are at an elevated temperature (650 °C) for an extended period of time (dependent on the deposition time) leading to interdiffusion. The magnetization obtained from PNR is very close to the value obtained from VSM. The fitting indicated the presence of a small magnetic dead layer at the top and bottom surface of the film, of approximately 1.6 nm in thickness each. This is also consistent with known magnetic dead layers in TmIG and other garnet films[47]. The PNR was collected under an in plane 700 mT field to saturate the film and retain the neutron polarization.

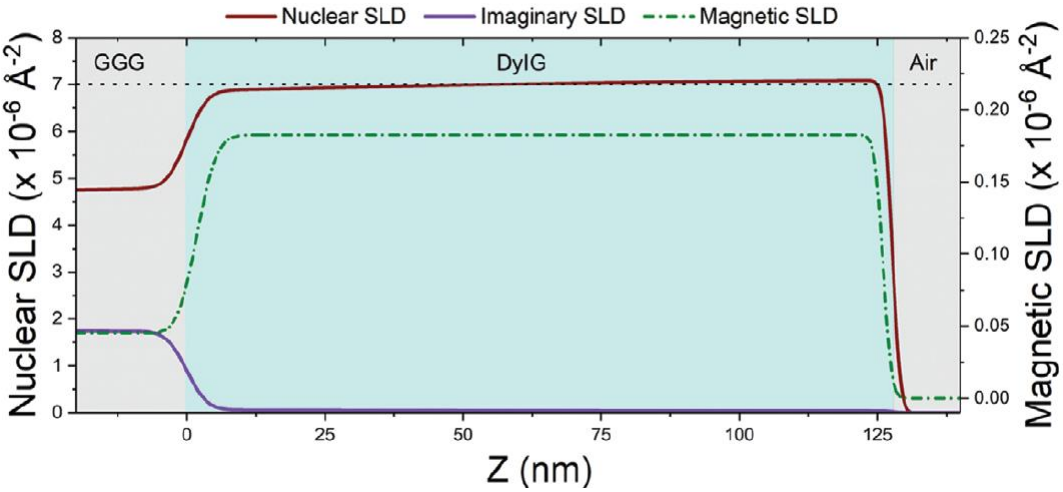

Figure 5.4: Scattering length density profile of a 116 nm DyIG/GGG film. There is an interdiffused region at the substrate interface and small magnetic dead layers at the top and bottom surfaces of the film.

The fitted reflectometry curves and spin asymmetry are shown in figure 5.5. There is excellent agreement throughout the Q_Z range between the model and experimental data. The close agreement in the spin asymmetry also demonstrates that the model accurately captures the magnetic behavior of the film.

5.2 Polycrystalline Dysprosium Iron Garnet

Polycrystalline rare-earth iron garnet films with perpendicular magnetic anisotropy (PMA) require a source of strain to induce enough magnetoelastic anisotropy to overcome the shape anisotropy of the film. This has been demonstrated in EuIG/Z-quartz (see chapter 4) and also in $Dy_{3-x}Bi_xFe_{5-y}Ga_yO_{12}$/glass and $Dy_{3-x}Ce_xFe_{5-y}Al_yO_{12}$/Si through a thermal expansion mismatch with the substrate[33,253,254]. The substituted DyIG films were engineered with Bi or Ce substitution to give

larger magnetooptical effects and with Ga or Al to reduce the shape anisotropy of the films. There has also been a report of a mixed anisotropy in gadolinium iron garnet films on Si, which is occurs due to the very low room temperature magnetization as the compensation temperature is nearly 300 K[255]. However, the inclusion of substitutions into the structure increases the complexity of processing and reduces the control of the stoichiometry, owing to the volatility of Bi and Ga, and the tendency to form secondary phases without the use of a seed layer[233,254]. Thus, it is desirable to have a PMA polycrystalline garnet film on Si without the need for substituted ions. Integration onto Si substrates also opens up the exciting possibility of future integration with complementary metal oxide semiconductor processing (CMOS) which underpins nearly all modern computers.

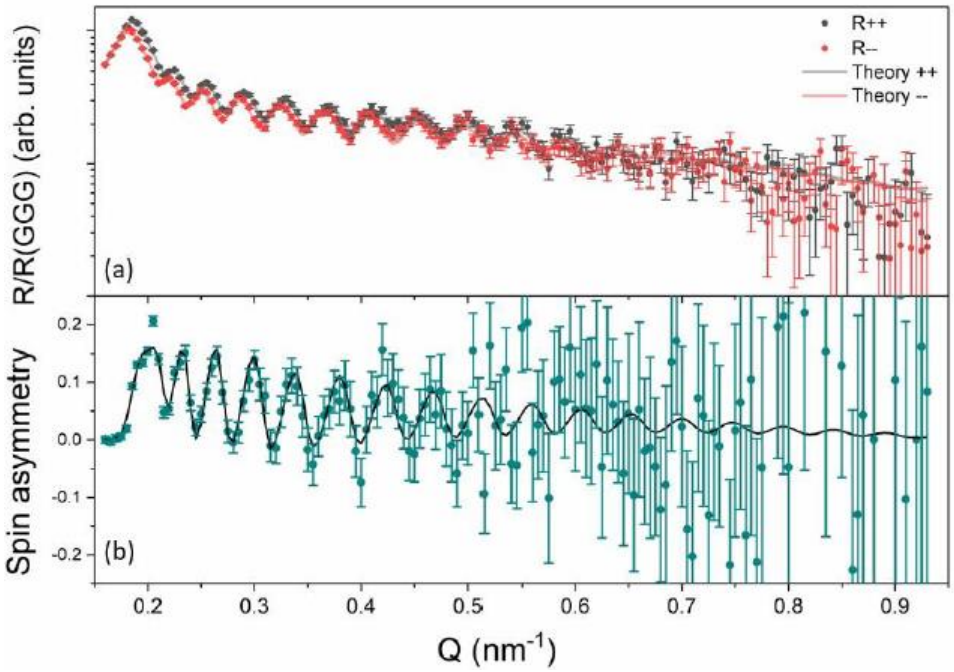

Figure 5.5: (a) Experimental reflectometry data and fitted model for a 116 nm DyIG/GGG film. (b) Spin asymmetry calculated from reflectometry data and model.

PNR was collected on a 40 nm DyIG/Si film to study the depth dependence of the magnetization of a polycrystalline garnet film. The reflectometry was collected under an in-plane field of 700 mT, which was sufficient to saturate the film in-plane. In figure 5.6, some intermixing at the substrate interface can be observed. PNR provides a lateral average of the film, so it is difficult to

say whether this is entirely due to interdiffusion of Dy, Fe, and/or O ions into the Si substrate (which seems unlikely owing to the very low solubility of Fe in Si), or due to local and long-range surface roughness across the sample surface. This reasoning can be extended to the magnetic SLD, which shows a tail region into the Si substrate, which is likely the result of the PNR averaging the roughness over the surface of the sample. Despite this, the film shows a relatively constant density profile through the thickness of the film, similar to the single crystal case. The magnetic SLD matches the value obtained from magnetometry. The reflectometry curves and spin asymmetry in figure 5.7 again shows excellent agreement between the model and experimental data, reflected in the very low value of the $\chi^2 = 1.55$ fitting parameter.

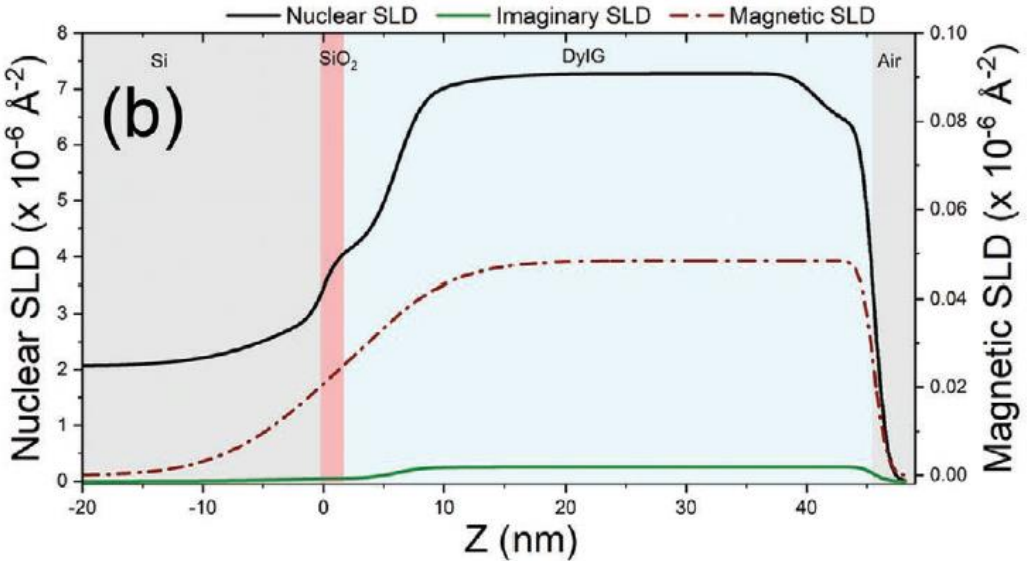

Figure 5.6: Scattering length density profile of a polycrystalline 40 nm DyIG/Si film. The tail of the nuclear and magnetic SLD into the Si substrate is likely due to short and long range interfacial roughness, and not intermixing with the Si substrate.

Further structural characterization was done on the DyIG/Si films via XRD and atomic force microscopy (AFM). Figure 5.8 shows the XRD of two different thicknesses of DyIG/Si, with all major garnet peaks present. Note that for the 39 nm film the peak intensities are quite large, far larger than the thinner film. This is usually indicative of large grains sizes, as they diffract more strongly with less scattering. To investigate film roughness, AFM was done on several different films. Surprisingly, for films that are greater than ~40 nm in thickness and annealed at

temperatures 850 °C or higher, huge grain sizes were observed, or the order of 10 μm across in a 38 nm film (see figure 5.9)[193]. The grain boundaries are straight with an average of 6 sides per grain, as expected from a site saturated nucleation and growth model of grain growth[174]. The grains also show a radiating pattern out from the center of the grains. This is believed to be due to a growth-induced surface instability caused by the very rapid growth. It is also possible that these are very low angle grain boundaries.

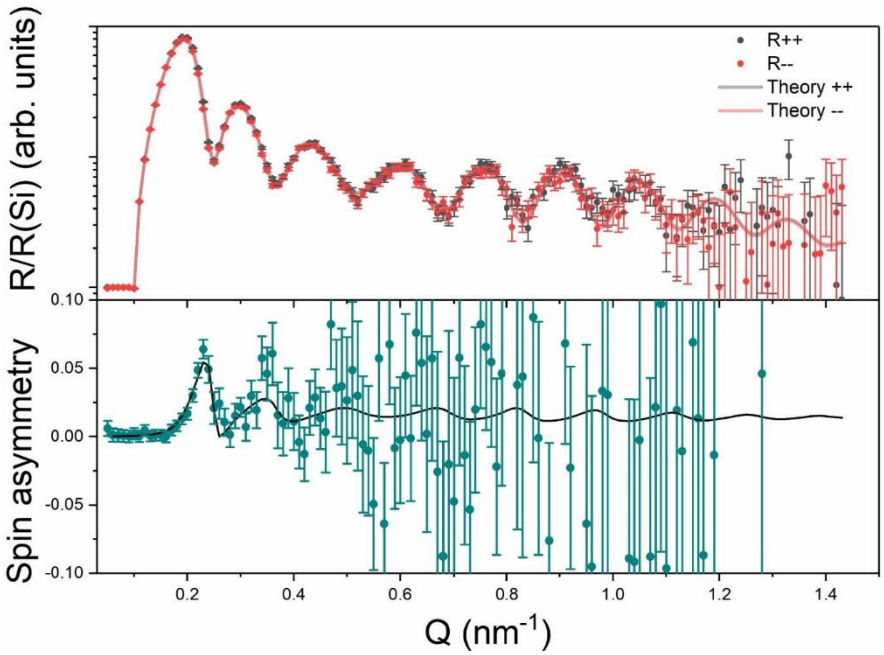

Figure 5.7: Experimental reflectometry data and fitted model of a 40 nm DyIG/Si film normalized by the reflectivity of the substrate. The bottom panel shows the spin asymmetry of the film.

To study this further, films that were annealed at different temperatures in the range 750-950 °C and with different thicknesses were also characterized with AFM. It was found that there was a very weak dependence on grain size of the films above temperatures of 850 °C and thicknesses of 40 nm. Below these values, grain size decreased precipitously, to values on the order of 100 nm, similar to what was seen in EuIG/Z-quartz films[33]. Even with the visible grain boundaries and topographical features, the RMS roughness of the films is less than 1 nm.

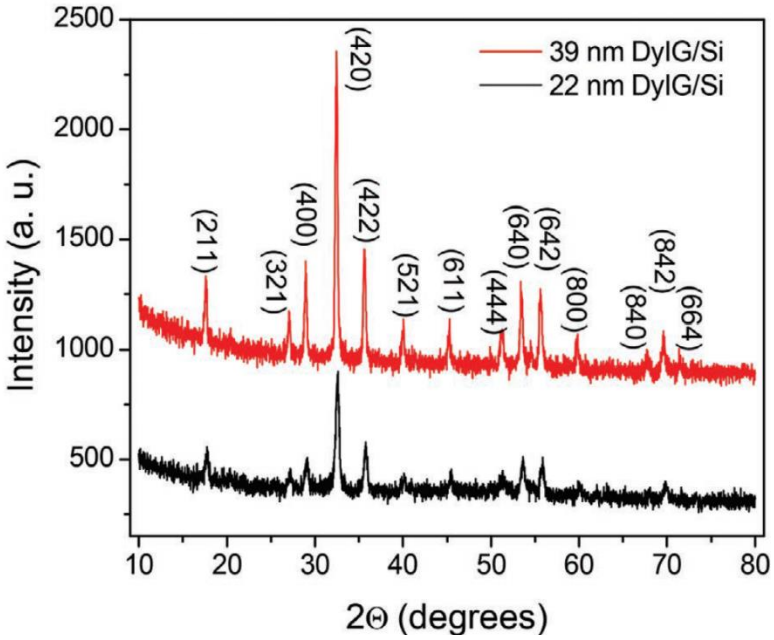

Figure 5.8: Grazing incidence x-ray diffraction of DyIG/Si films. No secondary phases are present. Vertically offset for clarity.

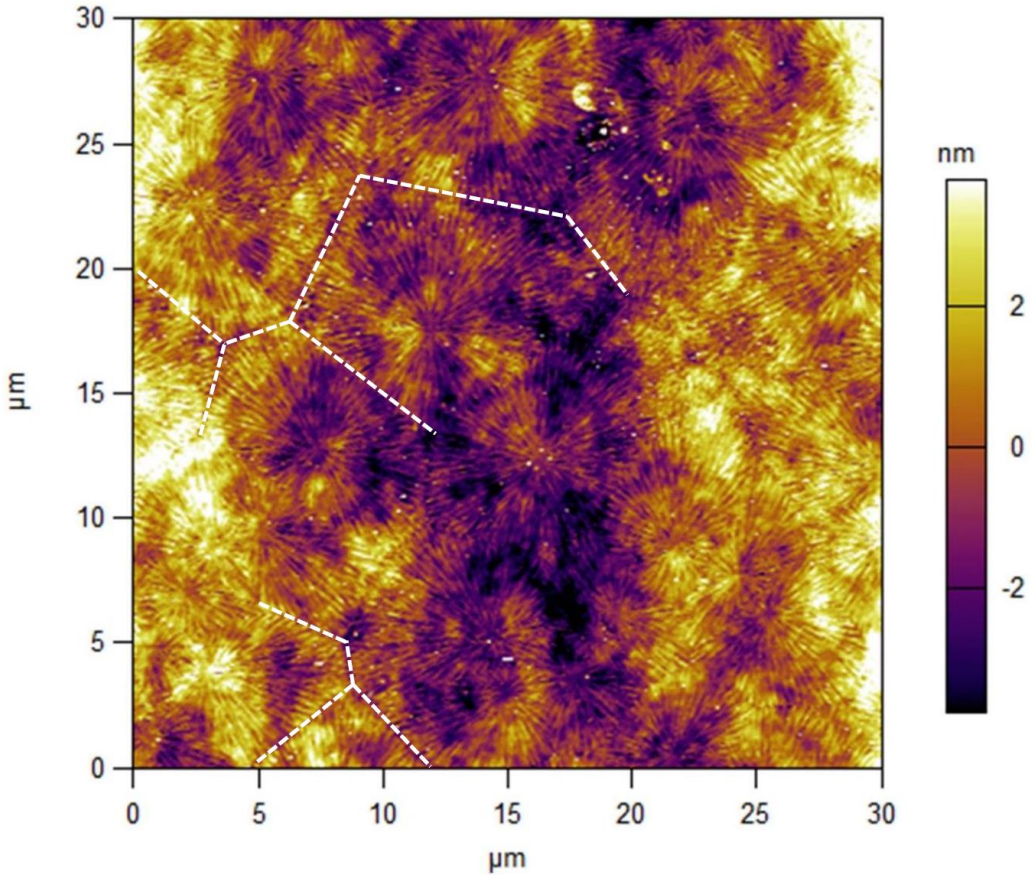

Figure 5.9: AFM image of a 38 nm DyIG/Si film annealed at 950 °C. Grain sizes on the order of 10 μm are visible, with some grain boundaries indicated by dashed lines. Each grain shows a nucleation site from which shallow, radiating topographical features emanate.

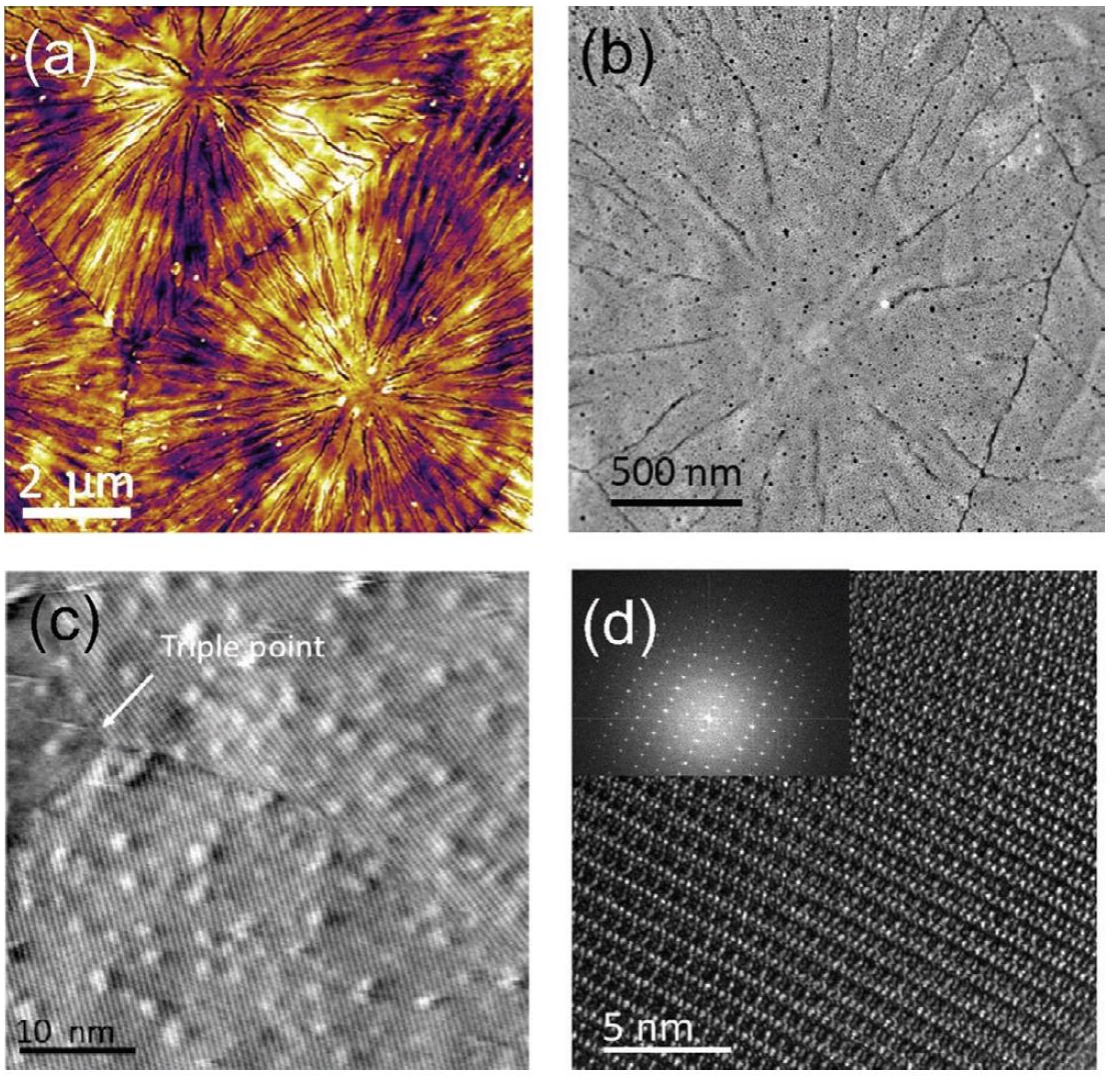

Figure 5.10: (a) AFM scan of a 38 nm DyIG/Si sample annealed at 950 °C with a radiating groove pattern emanating from the center of the grains. (b) ADF-STEM image of a 22 nm DyIG sample grown on a 200 nm Si_3N_4 membrane showing similar topographical features to the AFM scan. (c) ADF-STEM image near a triple point of a DyIG/Si_3N_4 film showing lattice fringes in two of the grains. (d) HR-TEM image of a DyIG film obtained in cross-section showing the fringes corresponding to the films lattice spacing. The inset shows the FFT of the image. No large defects are present. From ref. 193. Used with permission.

To learn more about the grains in these films, they were then characterized with scanning transmission electron microscopy (STEM) and high-resolution transmission electron microscopy (HRTEM). Figure 5.10b shows an annular dark field-STEM (ADF-STEM) image of a 22 nm DyIG film grown on a 200 nm Si_3N_4 membrane. The grain boundaries and radiating grain pattern emanating from the center of the grains is easily seen, confirming the results obtained from AFM. The image in figure 5.10c shows a triple point between three grains and lattice fringes in two of

the grains. These fringes do not cross the grain boundary as they are for different crystallographic directions, and the groove patterns do not interfere with the fringes, indicating that they are either surface features or extremely low angle grain boundaries within the grains due to the very rapid growth during the anneal. Figure 5.10d shows a HRTEM image of a DyIG film capture in cross-section, with fringes corresponding to the lattice spacing in the material. No line or other major defects are visible. The inset in the figure is the fast Fourier transform (FFT) of the image.

To assess the feasibility of DyIG/Si films as a platform for spintronics, the magnetic behavior of the films was measured via VSM. For all films grown on Si, with thicknesses ranging from 22 – 116 nm, robust PMA was demonstrated, with coercivities ranging from a few hundred Oe to nearly 5 kOe (see figure 5.11). The films have saturation magnetization close to the bulk value of 31 emu cm^{-3} [256]. In figure 5.11 for DyIG films roughly 39 nm thick, the coercivity and anisotropy field of the films increases with increasing annealing temperature, which corresponds to greater thermal mismatch strain in the film. This can be quantified in the total uniaxial anisotropy:

$$K_{u,pc} = -\frac{3}{2}\lambda\frac{E}{1-\nu}\Delta\alpha_T\Delta T - \frac{\mu_0}{2}M_s^2 \tag{5.5}$$

Where λ is the polycrystalline average of the magnetostriction coefficients, E is Young's modulus, ν is Poisson's ratio, $\Delta\alpha_T$ is the difference in thermal expansion coefficients between the film and substrate, ΔT is the temperature differential from the annealing temperature to room temperature, μ_0 is the permittivity of free space, and M_s is the saturation magnetization. The thermal expansion coefficient of Si is well tabulated, and was integrated over the temperature range of interest to produce an average value[177]. The thermal expansion of YIG was used in lieu of DyIG, as this value was not available. The thermal expansion of YIG varies insignificantly in the range of 296-1399 K[257]. The Young's modulus of YIG was also substituted for DyIG[258]. Equation (5.5) predicts

anisotropy fields of 5.3 kOe, 9.6 kOe, and 10.1 kOe for the films annealed at 750, 850, and 900 °C, respectively. These values qualitatively agree with experiment. The strain in the polycrystalline films is expected to be higher than that of single crystal films, and the presence of grain boundaries act as domain wall pinning sites, explaining the higher coercivity relative to the single crystal films, which are remarkably soft, similar to YIG and softer than EuIG, TbIG, and TmIG[45,50,193,259].

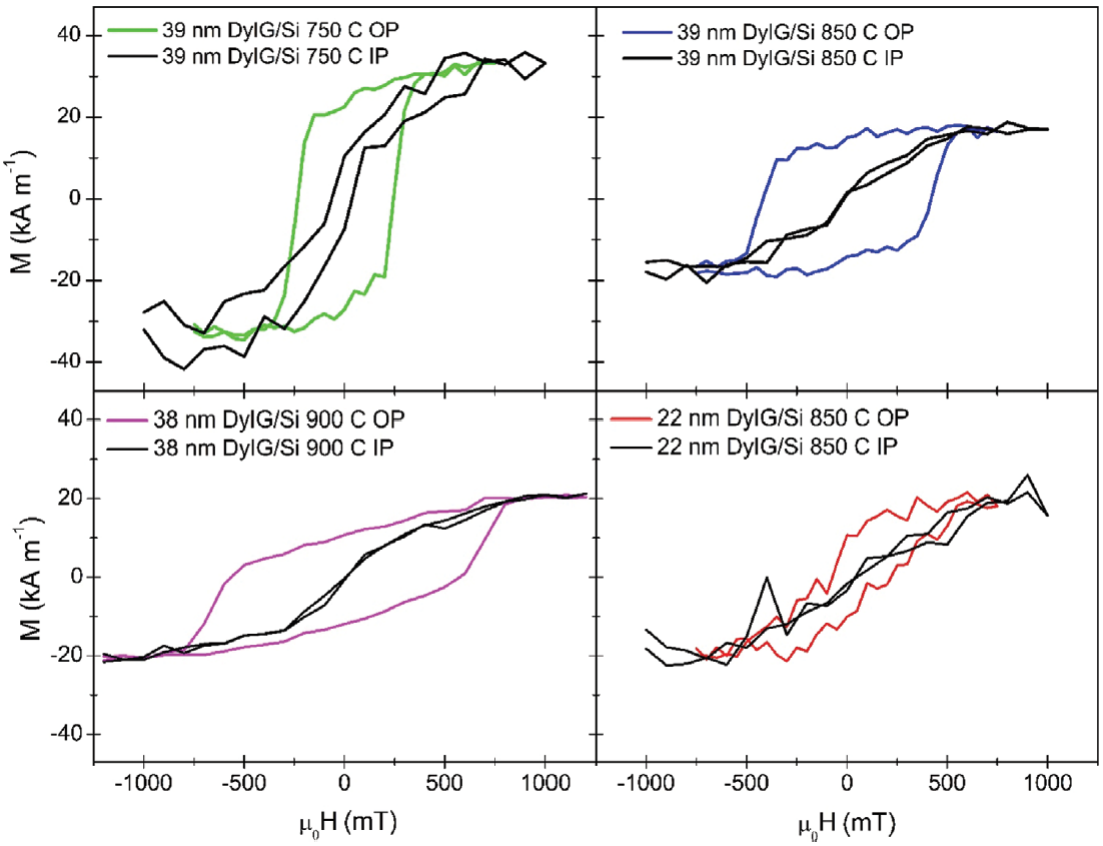

Figure 5.11: VSM hysteresis loops of DyIG/Si samples of different annealing temperatures and thickness. All samples demonstrate PMA and have low in-plane remanence. Anisotropy field and coercivity increase with increasing annealing temperature. From ref. 193. Used with permission.

As the DyIG/Si films demonstrate robust PMA across a variety of sample thicknesses and processing conditions, the potential for integration into heterostructures and spintronic devices was then evaluated. A 4 nm layer of Pt was deposited via DC magnetron sputtering on a 22 nm DyIG/Si film and Hall crosses were patterned using optical lithography and ion milling. Spin Hall magnetoresistance and anomalous Hall effect resistance was measured on 620 μm by 50 μm Hall

crosses. A vertical offset and a linear background due to the ordinary Hall effect of Pt were removed from the data (figure 5.12). The out of plane AHE-like SMR loop shows sharp switching at 2.5 kOe, which is higher than that of the unpatterned film. Additionally, the in plane SMR loop is not saturated even at 10 kOe, the limit of the electromagnet, much higher than the 5 kOe anisotropy field of the unpatterned film. These changes in anisotropy are attributed due to alterations in the strain state due to patterning of the film, and geometrical effects (the shape anisotropy) of the Hall crosses which could have a pronounced effect due to the large aspect ratio relative to the unpatterned (square) film. A macrospin model (proportional to $\sin^2$) was fit to the in plane data to estimate the anisotropy field of 12 kOe and an IP SMR amplitude of 42.4 x 10^{-4} μΩ cm[8]. The amplitude of the out of plane loop is 11.0 x 10^{-4} μΩ cm, which is nearly identical to other garnet/Pt heterostructures measured (EuIG, TbIG, TmIG, and YIG)[45,50]. Following the method outlined by Rosenberg et al. to estimate a lower bound for the imaginary part of the spin mixing conductance, a value of G_i = 1.05 x 10^{13} Ω^{-1} m^{-2} is obtained, which is again similar to other single crystal and polycrystalline garnet/Pt heterostructures.

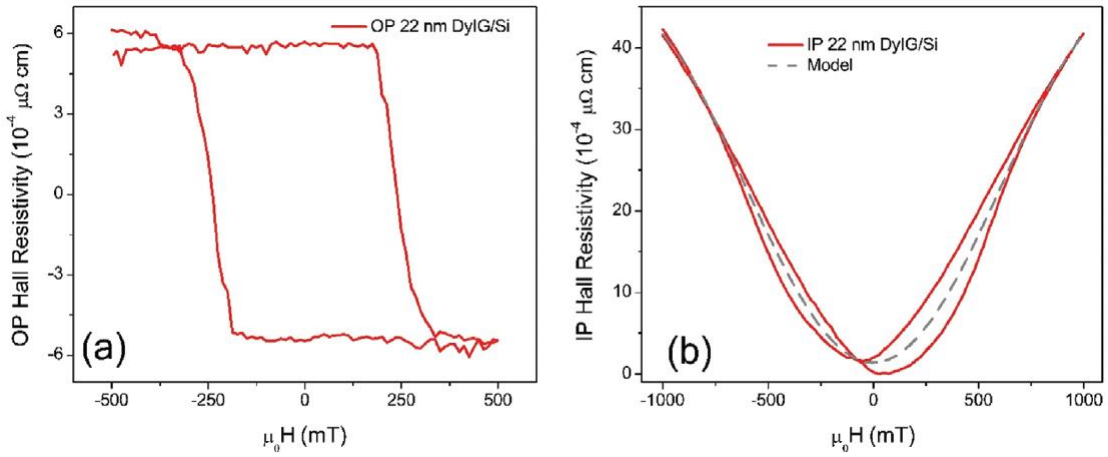

Figure 5.12: (a) Out of plane AHE-like SMR hysteresis loop on a Pt(4 nm)/DyIG(22 nm)/Si heterostructure patterned into Hall crosses. (b) In plane SMR loop on the same device. The dashed line indicates a fit to a macrospin model to estimate the anisotropy field and amplitude of the hysteresis loop. From ref. 193. Used with permission.

5.3 Magnetic Compensation Temperature

Studies on bulk DyIG have previously demonstrated a compensation temperature of 220 K[23,48]. Temperature dependent VSM hysteresis loops were collected on three samples to compare with literature values (figure 5.13). First, a small piece of the DyIG target used to grow films via PLD that was synthesized in the stoichiometric ratio of the binary oxide powders was measured. The T_{Comp} was found to be the same as previously determined within experimental error. Next, a polycrystalline 60 nm DyIG/Si film was measured, finding nearly the same value of the compensation temperature as the bulk piece. Finally, a 60 nm epitaxial single crystal DyIG/GGG film was examined, and surprisingly the compensation temperature was approximately 190 K, 30 K lower than the bulk sample and polycrystalline film.

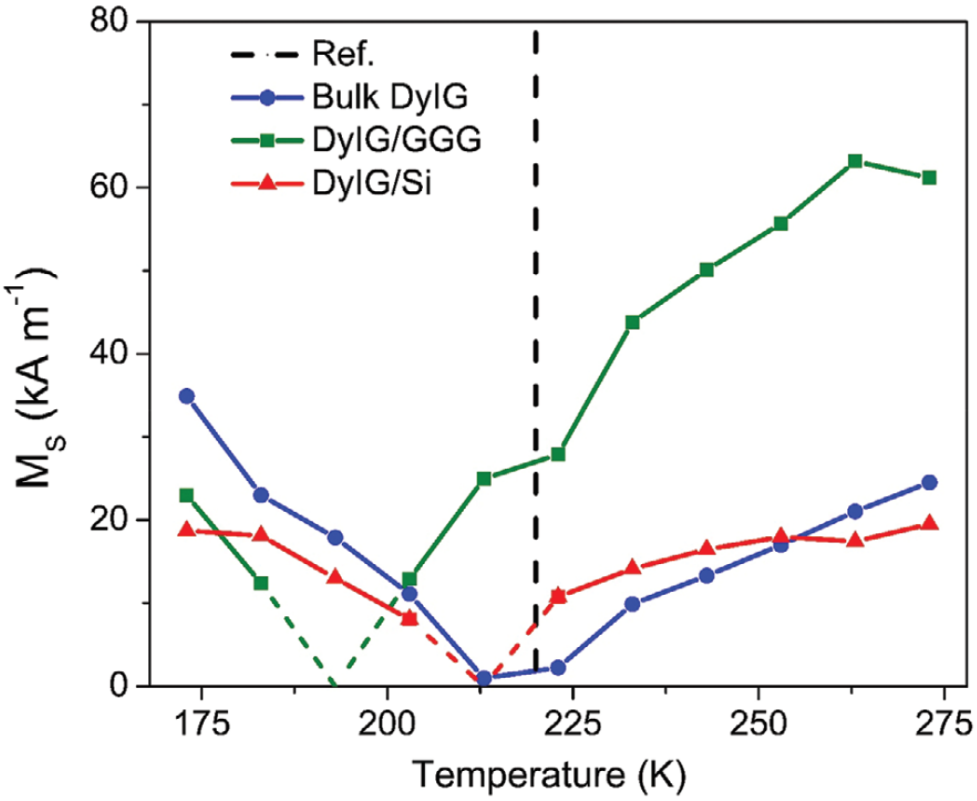

Figure 5.13: Magnetic moment versus temperature curves for a bulk DyIG sample, DyIG/GGG epitaxial single crystal film, and DyIG/Si polycrystalline film. Dashed lines indicate interpolation from experimental data to account for low moment and a divergent coercive field. Note that the DyIG/GGG sample has a compensation temperature 30 K lower than the other samples. From ref. 193. Used with permission.

Interestingly, the measurement of the moment near compensation is limited by the small moment of the samples, not by the coercive field of the material, as is the case with TbIG, which exhibits a rapidly diverging coercivity near T_{Comp}[45]. All three DyIG samples measured demonstrate small coercive fields until very close to the compensation temperature (see figure 5.14).

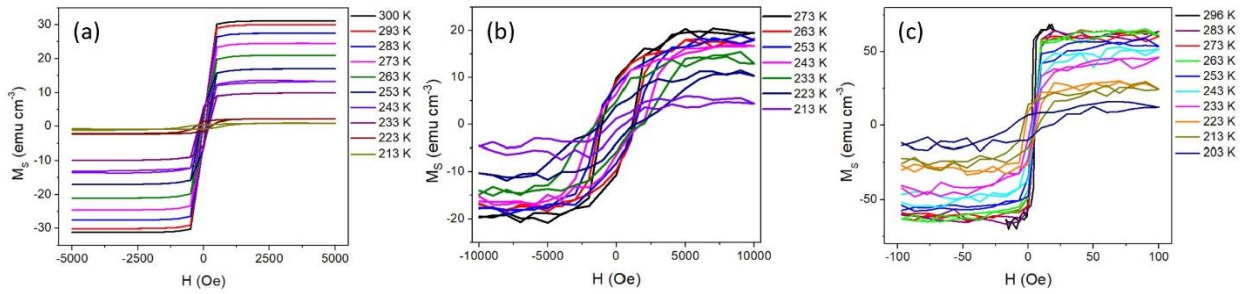

Figure 5.14: VSM hysteresis loops at different temperatures for (a) bulk DyIG, (b) 60 nm DyIG/Si polycrystalline film, and (c) 60 nm DyIG/Si epitaxial single crystal film.

This discrepancy is similar to TbIG/GGG reported by Rosenberg et al., also from our group, where TbIG films had T_{Comp} 80 K higher than bulk[45]. The exact reason for this difference is still under investigation, but the most likely answer seems to lie in the off stoichiometry of the films. These films are known to be slightly off-stoichiometric and contain some fraction of Tb^{4+} ions (in Rosenberg et al.'s work). We postulate the excess rare-earth ions are anti-site defects, where they occupy the octahedral site in the garnet structure. The excess rare-earth (iron) have the potential to increase (decrease) the compensation temperature owing to the larger (smaller) moment of the rare-earth (iron) ion. Another important consideration is that the temperature dependence and canting of the rare-earth ion moments is significant[260]. It is possible that the antisite rare-earths experience a stronger crystalline field in the octahedral sites, resulting in reduced canting of the moments. This would result in the antisite rare-earth ions having a larger moment than the dodecahedral rare-earth ions (per ion), requiring a relatively small amount of off stoichiometry to produce a significant change in compensation temperature. The polycrystalline film does not demonstrate this deviation from the literature value of T_{Comp}, despite being grown under the same

conditions and at the same time as the single crystal film. The reason for this is understood to be that the high temperature anneal used to induce crystallization in the polycrystalline films allows the ions to diffuse to and occupy the ideal site in the lattice, a step that does not occur in the growth of single crystal films. This is explored further in chapter 8 in the discussion of the molecular field coefficients model and is still an area of active research.

6. Magnetic Proximity Effect in Magnetic Insulator/Heavy Metal Heterostructures across the Compensation Temperature

6.1 Motivation and Existing Work

The magnetic proximity effect (MPE) has been observed in nonmagnetic heavy metals (HM), graphene, and topological insulators when integrated in heterostructures with magnetic materials[69,261–263]. While graphene and topological insulators demonstrate more exotic physics associated with the presence of an MPE, the MPE in HMs is related to a modification in the spin-dependent band structure of the material. In particular, metals such as Pd, W, Ir, and Pt are close to the Stoner criterion for the presence of ferromagnetism (see chapter 2 for more details)[58]. The HMs have had much recent interest because of their large spin Hall angles and applications in spin-orbit torque generation. There is current debate over whether the MPE is partially responsible for the anomalous Hall effect (AHE) and other spintronic phenomena in bilayers with magnetic materials[49,67]. A more complete understanding of the proximity effect will be necessary to optimize these materials and structures for next-generation spintronic devices.

A large variety of magnetic materials including transition metal ferromagnets, chalcogenides, rare-earth transition metal alloys, and insulating ferrimagnets have been integrated with HMs to examine the MPE[70,75,77,264]. Of the heavy metals, Pt has been the most well studied and has also resulted in the most consistent data. Reports on the MPE in Pt have consistently reported that the MPE is positive, and any controversy results from the strength of the MPE or whether it is present in a particular materials system, such as in Pt/YIG or Pt/$CoFe_2O_4$[70,264–266]. In the case of Pd, XMCD results have shown that the MPE appears to be positive, but the sign of the AHE is negative, which conflicts with both effects being positive in Pt[80,267]. W has received the least

attention of the three metals, likely related to the difficulty in polarizing the material even at low temperatures, but existing results have indicated that the MPE is negative, along with the sign of the AHE in heterostructures.

There are several possible reasons for these discrepancies. The first is that the interface between the magnetic layer and the HM, which is strongly dependent on growth and processing, has a very large effect on spin transport and the strength of the MPE. The second is that there is a fundamentally different origin of the MPE in structures with metallic and insulating magnets. This has been confirmed by studying similar systems with metallic and insulating magnets, such as Pt/Fe vs. Pt/YIG and $YBa_2Cu_3O_7/La_{2/3}Ca_{1/3}MnO_3$ (metallic) vs. $YBa_2Cu_3O_7/LaMnO_{3+\delta}$ (insulating)[261,264,268]. Most of the literature has focused on integration with transition metal ferromagnets, which attributes the MPE to an RKKY-like interaction between the *d* electrons[269]. Predictions on the sign of the MPE based on this mechanism and Hund's rules assert that the less than half-filled shells of W and Ta should lead to a negative MPE and the greater than half-filled shells of Pd, Pt, and Ir lead to a positive MPE[261,270]. This has proven reliable for metallic structures to this point, but insulators pose a more complex problem.

The lack of mobile electrons precludes an RKKY type interaction as being the source of the MPE in insulating magnets. First principles band structure calculations of magnetic insulators integrated with Pt and graphene have demonstrated that the presence of a magnetic ion (at the surface only) results in a shift in the spin-dependent density of states, resulting in a net moment[70,72]. However, this does not elucidate the mechanism. It is proposed that the MPE in heterostructures with

insulating magnets is mediated via a superexchange interaction between the proximitized material and the magnetic ions closest to the surface.

Ferrimagnets are interesting materials for ultrafast spintronic devices owing to their low moments and ultrafast dynamics. This class of magnetic materials (both metallic and insulating) can also have a magnetic compensation temperature (T_{Comp}). The MPE in rare-earth transition metal/Pt heterostructures has been studied across T_{Comp}, and it was determined that the MPE in Pt is always parallel to the transition metal moment[75]. The reasoning for this finding is that the rare-earth *4f* electrons are highly localized relative to the transition metal *3d* electrons, which polarize the *5d* electrons of Pt.

However, the MPE across T_{Comp} has not been well studied in magnetic insulators. Work on the MPE with magnetic insulators has to this point involved primarily magnetic materials with a T_{Comp}, or the MPE was not measured in both temperature ranges. One study on $(Bi_{0.25}Sb_{0.75})_2Te_3$/TmIG found that the MPE did reverse sign between 20 and 90 K, but the film did not demonstrate a compensation temperature in this range, implying a difference in the exchange coupling between the topological insulator and the rare-earth and iron sublattices of the garnet.

In this study we attempted to answer how the magnetic proximity effect couples to dysprosium iron garnet (DyIG) across T_{Comp} (220 K)[194]. We anticipated that the MPE would couple to the net Fe moment and thus change sign across T_{Comp}. DyIG was selected for this study as it has strong in-plane anisotropy, making it amenable to polarized neutron reflectometry (PNR) measurements, and its ideal location of the compensation temperature, which is low enough to result in measurable

values of the MPE yet high enough to easily study the bulk film with magnetometry. An additional component of the experiments was to evaluate the effect of *in situ* vs. *ex situ* deposited HM. The cleanliness of the interface has a major effect of the ability to fit the PNR data, and likely has larger implications for optimizing spintronic devices based on these materials.

6.2 Structural Characterization

DyIG films were grown via pulsed laser deposition at a laser fluence of 2.0 J/cm^2, substrate temperature of 650 °C, 150 mTorr O_2 pressure, base pressure of 5.0 x 10^{-6} Torr, and a cooling rate of 10 °C/minute, as described previously[33,45,50,193]. Multiple samples were studied, with the HM sputtered under the following conditions:

- *ex situ* Pt in a chamber with a base pressure of 2 x 10^{-8} Torr at 5 mTorr Ar, and 50 W power
- *in situ* Pt in the PLD chamber at a base pressure of 1 x 10^{-6} Torr, 5 mTorr Ar, and 30 W power
- *in situ* W in the PLD chamber at a base pressure of 1 x 10^{-6} Torr, 5 mTorr Ar, and 100 W power

The *ex situ* Pt and the *in situ* W samples were grown using the standard substrate holder, which results in a film area of ~9x9 mm^2 on a 10x10 mm^2 substrate. The *in situ* Pt sample was grown by affixing the substrate to a blank via silver paste. A comparative study of the two mounting methods did not result in significant differences in structural quality or magnetic properties (see figure 6.1). Silver paste was used to mount the sample for PNR study, as the shadowed area around the edge of the sample requires modeling when fitting the reflectometry data, which nearly doubles the total parameters and more than doubles the computation time.

The structural and magnetic characterization of the *in situ* Pt(9 nm)/DyIG(54 nm)/GGG sample is shown in figure 6.2. A visible film peak and several Laue fringes indicate high structural quality (low intermixing and low surface roughness). The hysteresis loop indicates bulk magnetization, high remanence, and a low coercivity of 0.25 mT.

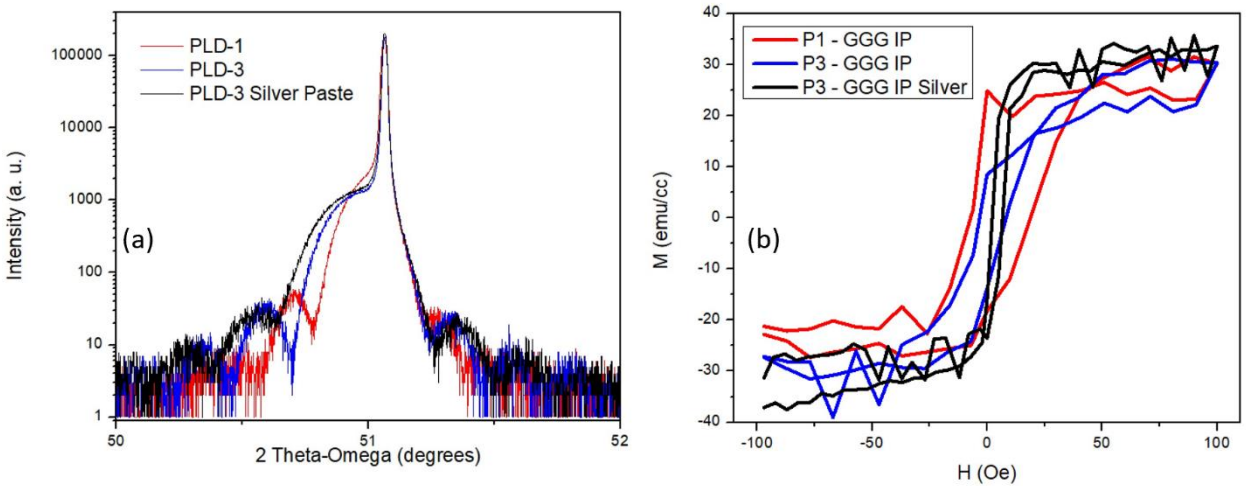

Figure 6.1: (a) High resolution x-ray diffraction of DyIG/GGG films grown in two different PLD chambers (PLD-1 and PLD-3) and mounting methods (substrate holder and silver paste). (b) VSM hysteresis loops of the samples. No significant differences are observed in any structural or magnetic properties.

To examine the exquisitely important interface between the garnet and heavy metal layers, high-resolution transmission electron microscopy (HRTEM) was collected. When the interface of *in situ* deposited Pt is compared with that of *ex situ* deposited metal (figure 6.3), there is a glaring difference. As has been observed several times in heterostructures grown by this group, *ex situ* deposited metal films have a carbon-like surface contamination between the two layers[47]. This limits the direct contact between the HM and garnet, which may inhibit any MPE and interfacial spin transport. The Pt layer is fairly rough. This is suspected to be due to the 45° incident angle of the sputtering source in the PLD chamber, which leads to rougher films, the relatively high base pressure of the system, and possible delamination during the focused ion beam (FIB) milling sample preparation for TEM. Energy dispersive spectroscopy (EDS) measurements were also collected on the *in situ* deposited Pt/DyIG sample (figure 6.4). The EDS clearly shows a sharp

interface on the bottom surface of the Pt and a rough upper surface. The message is less clear for the Fe and Dy scans, but this is due to overlapping peaks in the EDS spectra, which makes deconvolution of these elements difficult.

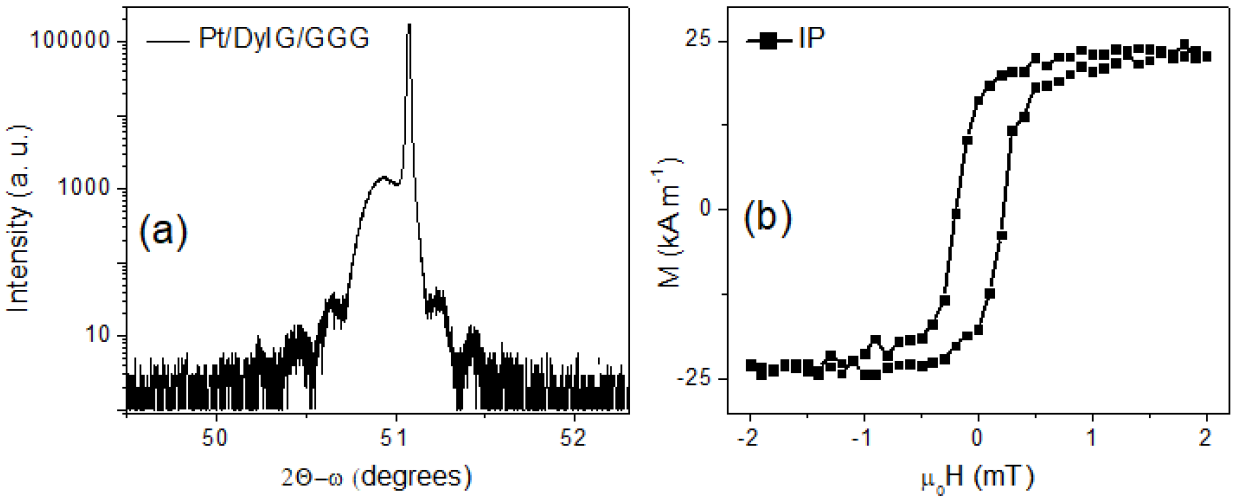

Figure 6.2: Characterization of *in situ* grown Pt(9 nm)/DyIG(54 nm)/GGG heterostructure. (a) High resolution x-ray diffraction of the (444) reflection. (b) In-plane VSM hysteresis loop.

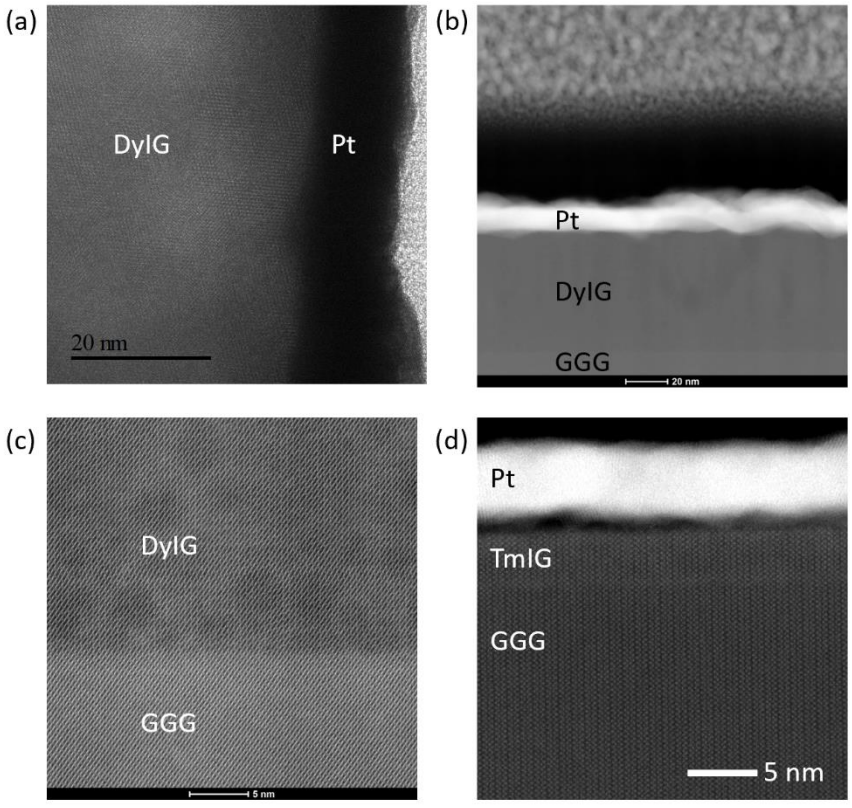

Figure 6.3: (a) HR-TEM image of the Pt/DyIG interface. (b) ADF-STEM image of the Pt/DyIG interface. Note no contamination between Pt/DyIG and the rough upper Pt layer. (c) ADF-STEM image of the DyIG/GGG showing a narrow interfacial region. (d) ADF-STEM image of Pt/TmIG/GGG structure with *ex situ* deposited Pt. Note the dark (low atomic number, suspected carbon-based) interfacial contamination layer.

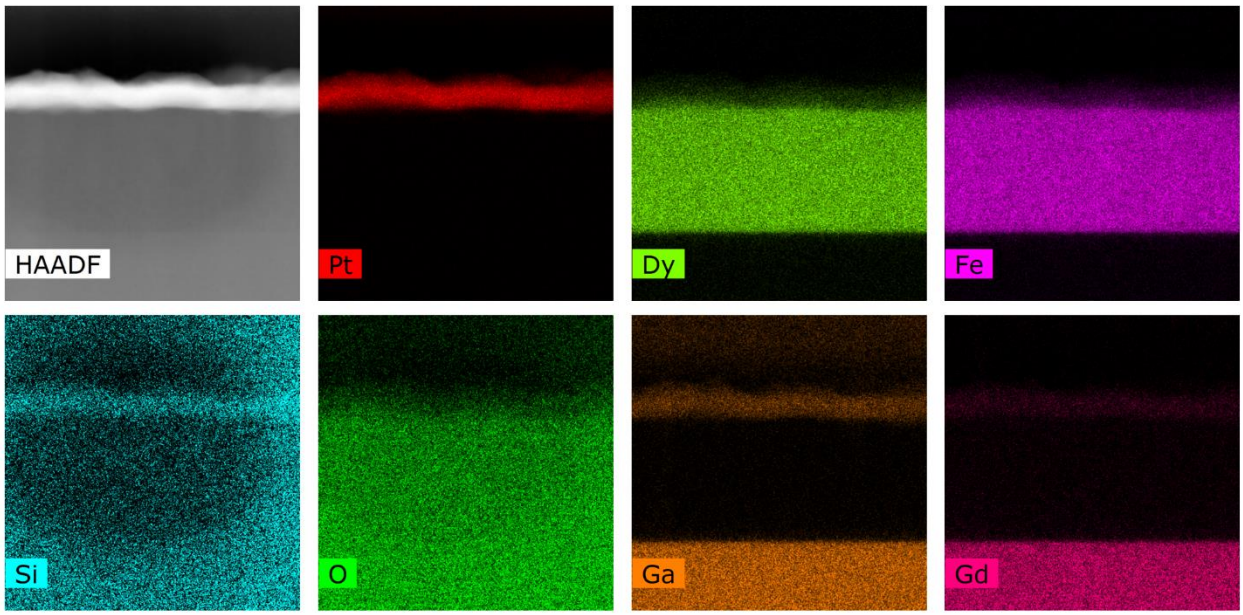

Figure 6.4: ADF-STEM image along with elemental EDX maps of the Pt/DyIG/GGG sample. Little intermixing is present at the Pt and substrate interfaces.

6.3 X-ray Magnetic Circular Dichroism

X-ray magnetic circular dichroism (XMCD) is the most common direct technique for studying proximity effects due to its elemental specificity and exquisite sensitivity. XMCD measurements were conducted on the *in situ* Pt/DyIG/GGG film and a W/DyIG/GGG film. XMCD and PNR complement each other very well, with XMCD offering elemental specificity and PNR allowing understanding of the magnetization profile. Pt and W have been reported to have the opposite sign of the MPE in heterostructures with transition metals[261]. Only one study has reported W MPE in structures with magnetic insulators, demonstrating an antiparallel coupling above the compensation temperature in W/TmIG[49]. The most commonly measured x-ray absorption (XAS) edges for Fe are $L_{2,3}$, $M_{4,5}$ for Dy, and $L_{2,3}$ for Pt and W. The O K edge can also be measured, but O is not magnetic in the garnet system so no XMCD is observed (see figure 6.5). XMCD was collected both below and above the compensation temperature. Recall that below T_{Comp}, the rare-earth dodecahedral and iron octahedral sublattices dominate the net moment, and above T_{Comp} the

tetrahedral iron is the dominant sublattice. Thus, XMCD collected across this temperature will be of opposite sign.

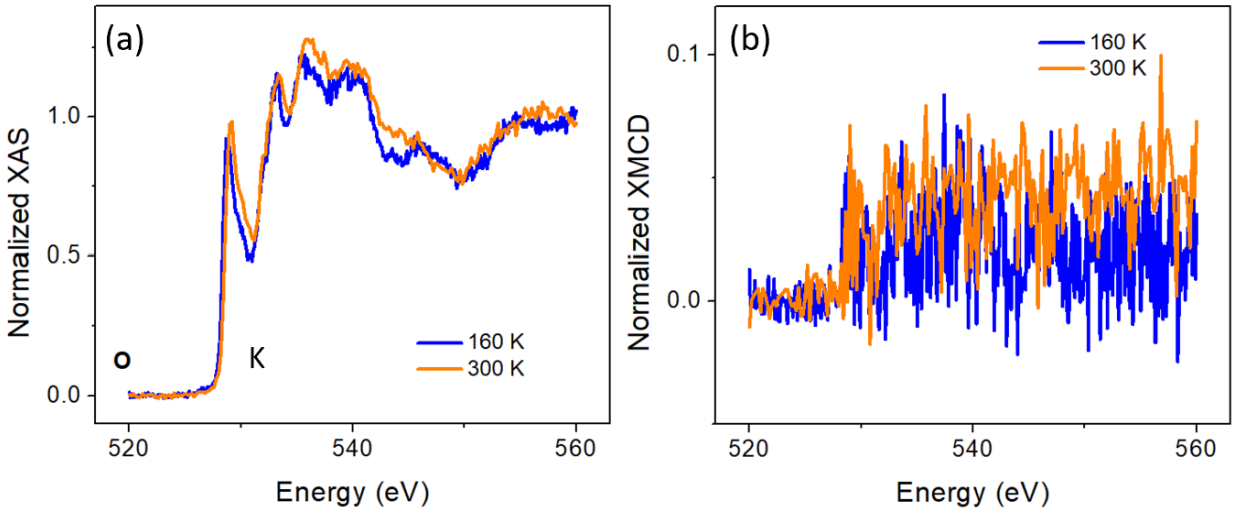

Figure 6.5: (a) XAS and (b) XMCD of a Pt/DyIG/GGG sample collected at the O K edge.

XMCD measured in a Pt/DyIG/GGG sample at the Fe $L_{2,3}$ edges demonstrate a clear signal that changes sign from 160 to 300 K (figure 6.6). At the L_3 edge, there is one main peak flanked by two smaller peaks of opposite sign. The central peak is due to the tetrahedral Fe and the outer two peaks are from the octahedral Fe. From elemental Fe, we know that a negative L_3 edge signal and positive L_2 edge signal indicate that the material is parallel to the applied field[211]. Thus, in figure 6.6b we can see that at 160 K the tetrahedral Fe is antiparallel to the applied field and the garnet moment, and then becomes parallel to both the net moment and field at 300 K, as expected. A similar scenario occurs with the Dy signal, which is more complex than Fe but switches sign when moving from low to high temperature. Note that other reports of Fe L_3 edge XMCD demonstrates significantly smaller outer octahedral peaks[49,263]. This is due to several factors, the primary of which is different surface termination and bulk site occupancies due to differing film stoichiometries as a result of the growth conditions or post processing. The second is that the use of total electron yield (TEY) vs. total fluorescence yield (TFY), which are more sensitive to the surface and bulk of the film, respectively, can result in differently shaped spectra, even for the

same film. In general, TFY is the preferred technique for garnets as the signal depends on excited photons, rather than excited electrons which can result in charge transfer events and have poor generation efficiency due to the insulating nature of these materials.

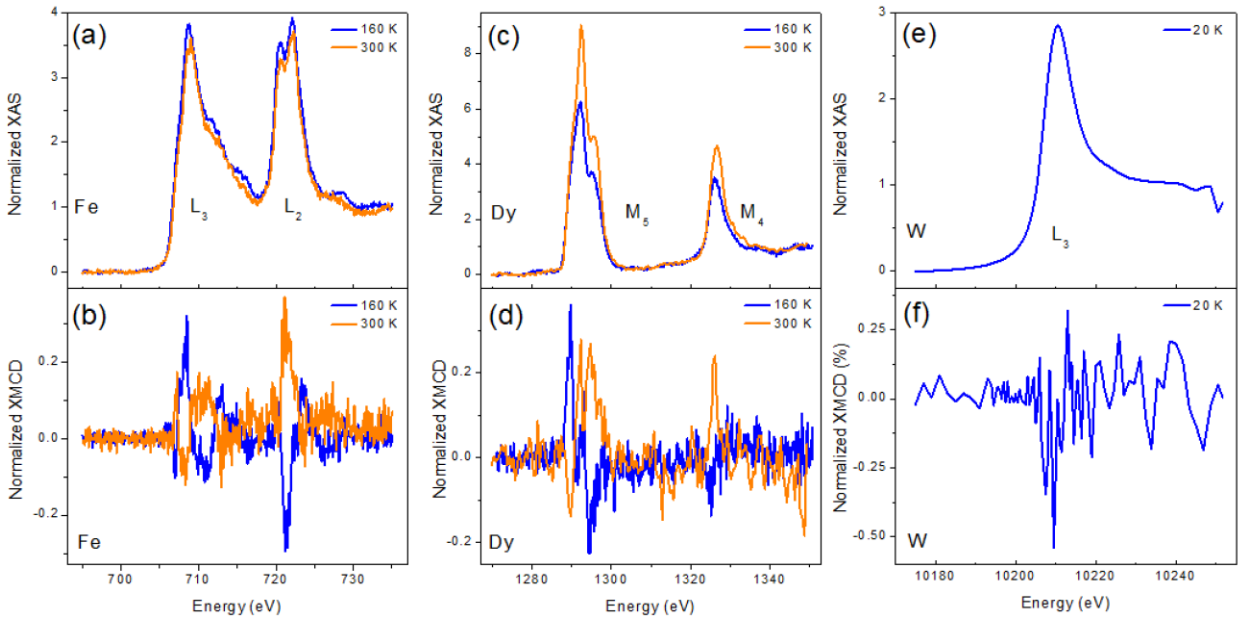

Figure 6.6: XAS (a,c) and XMCD (b,d) at 160 and 300 K of a Pt/DyIG/GGG film. XAS (e) and XMCD (f) of a W/DyIG/GGG at 20 K.

XMCD was first attempted at the L_2 edge of Pt in the *in situ* grown sample (figure 6.7). We were unable to detect any XMCD due to Ga Kα interference at the L_3 edge requiring measurement at the weaker L_2 edge and the large thickness of Pt in the sample (9 nm). The MPE is confined to the first 1-3 nm near the surface so the rest of the Pt layer contributes to the XAS but not XMCD, diluting the magnetic signal.

The W(5 nm)/DyIG(42 nm)/GGG sample was then measured at the W L_3 edge as the L_3 signal is typically stronger than L_2. A small, negative XMCD signal was detected at 20 K, but not at 200 K or higher temperatures (figure 6.6f). The sign of the MPE is inferred to be positive if the L_3 edge is negative, based on measurements in transition metal/heavy metal heterostructures[77,261].

This indicates that the W MPE is positive, contrasting with measurements in all metallic heterostructures and the previous report of MPE in W/TmIG by Shao et al. at the N_3 edge of W[49,270].

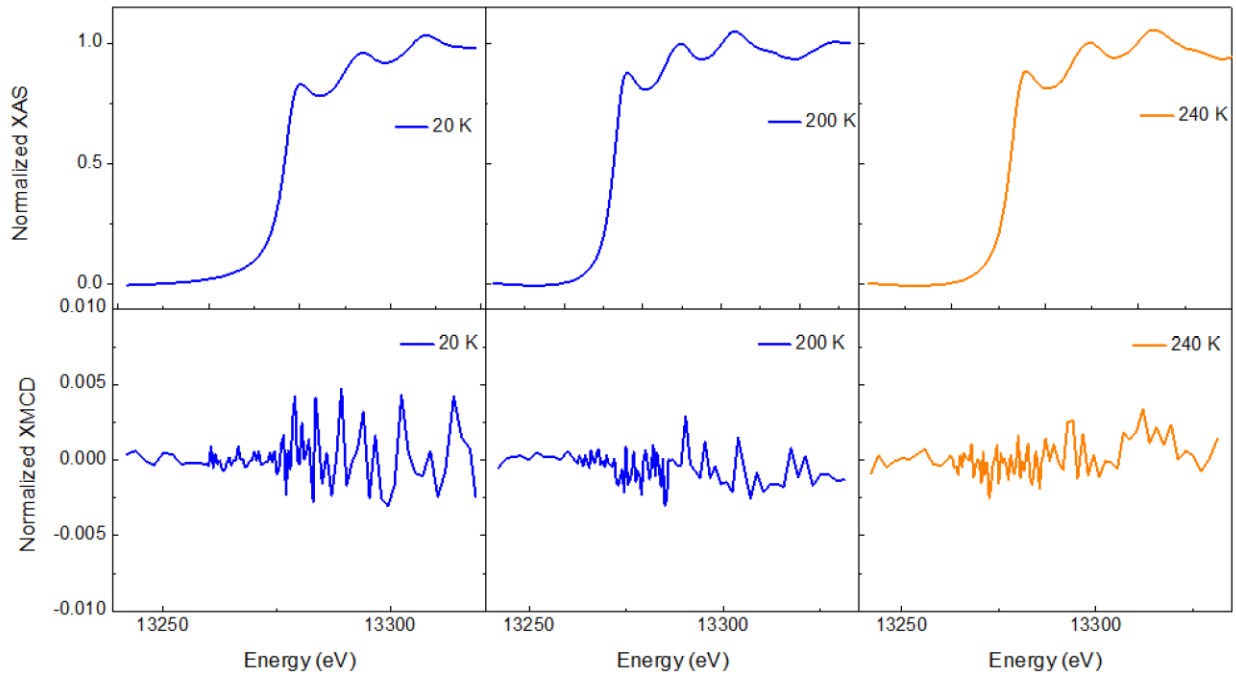

Figure 6.7: XAS and XMCD of an *in situ* grown Pt/DyIG/GGG sample at the Pt L_2 edge at 20, 200, and 240 K.

6.4 Polarized Neutron Reflectometry

Polarized neutron reflectometry is an excellent technique for direct measurement of proximity effects as it is highly sensitive to even subtle magnetic effects[262,271]. PNR is sensitive to the in-plane component of the magnetization only, requiring that samples have in-plane anisotropy or sufficiently low anisotropy fields to rotate the magnetization in-plane. The cross-sectional density and interface structure of the films can be resolved with great precision and fitted to a sample model using a curve fitting program such as Refl1D[196]. The experimental procedure was to measure PNR at 10, 200, 240, and 300 K. This allows for the study at conditions where the MPE is predicted to be the strongest, just above and below compensation temperature, and room temperature, where any MPE is expected to be negligible[194]. Measurement at room temperature

also allows for a simpler fit of the structure of the sample, as the paramagnetic contributions from the GGG substrate are lower at high temperatures.

First, PNR was measured on the *ex situ* deposited Pt(10 nm)/DyIG(25 nm)/GGG film. The scattering length density (SLD) profile is shown in figure 6.8. The model used in the fitting consisted of the following structure: GGG/GIG1/GIG2/DyIG/Pt/Pt2/Ice. All four temperature conditions were fit simultaneously, allowing only the magnetic components of the model to vary with temperature. The GIG layers are due to interdiffusion with the substrate and the ice layer is only present at 10 K and is due to adsorbed gases on the sample surface. It is immediately apparent that there is an interfacial layer between the garnet and Pt. The SLD for Pt is far below the bulk value of 6.3 10^{-6} $Å^{-2}$. This indicates that there is some interfacial layer on top of a smooth DyIG surface, and the Pt density is below bulk. Fitting the reflectometry curves resulted in many degenerate solutions, of which the most physically realistic is shown. It was not possible to obtain a realistic magnetic SLD for this film, as the interfacial layer, complexity of the model, and extra parameters due to the shadow effect near the sample edge proved exceedingly difficult to fit.

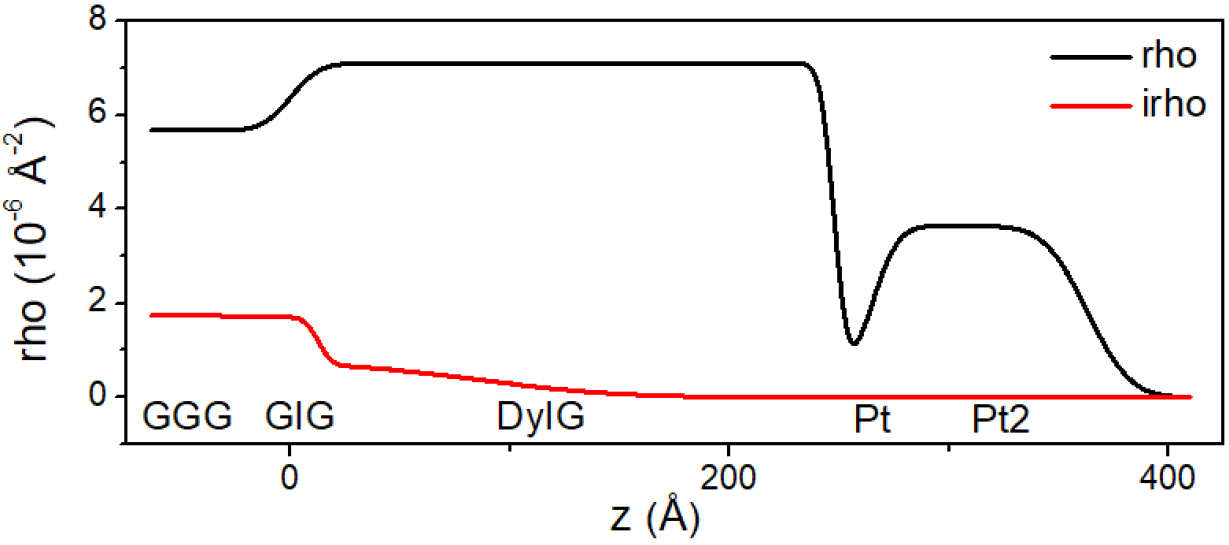

Figure 6.8: SLD profile for *ex situ* deposited Pt/DyIG/GGG heterostructure. Note the dip in SLD corresponding to interfacial contamination at the DyIG/Pt interface.

As it was not possible to obtain a satisfactory magnetic SLD for this sample, the measurements were repeated with an *in situ* grown Pt(9 nm)/DyIG(54 nm)/GGG sample. The fitted reflectometry curves are shown in figure 6.9a, where an excellent agreement is obtained over the Q_Z range at each temperature condition. The spin asymmetry, $SA = (R^{++} - R^{--})/(R^{++} + R^{--})$ highlights the magnetization in the sample. The SA is proportional to the magnetic moment and the splitting of the two reflectivity curves. The model also provides good agreement with the experimental data, indicating that the model captures the magnetic behavior of the sample in addition to the structural information.

The model used for fitting consisted of a minimum number of parameters, with the structure GGG/DyIG/Pt/Pt2/Ice resulting in the optimal fit. The ice layer is only needed at 10 K. The four temperature conditions were again fit simultaneously, keeping the structural components of the sample constant. The one exception is that the Pt and Pt2 interfaces at 10 K were allowed to vary, which resulted in a small difference from the higher temperature data sets. The reason for this discrepancy is attributed to adsorption of gases in the rough, columnar, upper Pt2 layer that slightly changes the SLD and interface profile. An ab initio footprint correction was also applied to each temperature condition. The GGG substrate has a strongly non-linear paramagnetic behavior, which resulted in experimental artifacts at low Q_Z, which were removed via the footprint correction and resulted in significant improvements in the fitting.

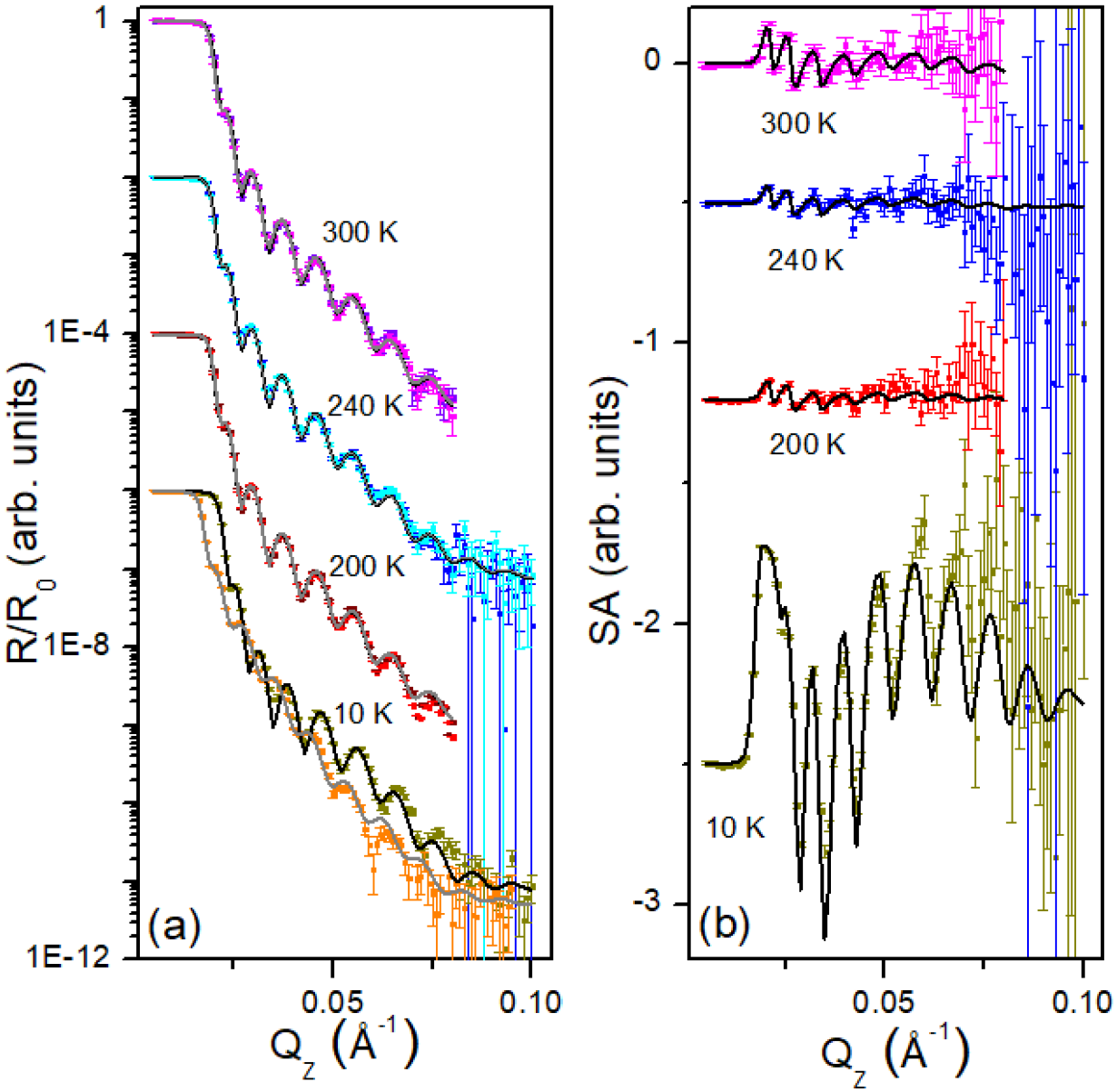

Figure 6.9: (a) Fitted polarized neutron reflectometry curves and (b) spin asymmetry of *in situ* grown Pt/DyIG/GGG at 10, 200, 240, and 300 K. Vertically offset for clarity. Error bars are representative of 1 σ.

The scattering length density profiles obtained from the reflectometry model is shown in figure 6.10. In contrast to the *ex situ* deposited sample, there is no drop in SLD at the Pt/DyIG interface, with a smooth transition between the two layers. The SLD of each is close to bulk for the respective materials, indicating that close to bulk density is achieved in each layer. The rough upper Pt2 layer that was observed in TEM is also visible here, indicated by the low SLD. This

does not have an impact on the MPE in this film, as magnetic polarization in the HM layer is typically confined to the first few nanometers nearest the interface.

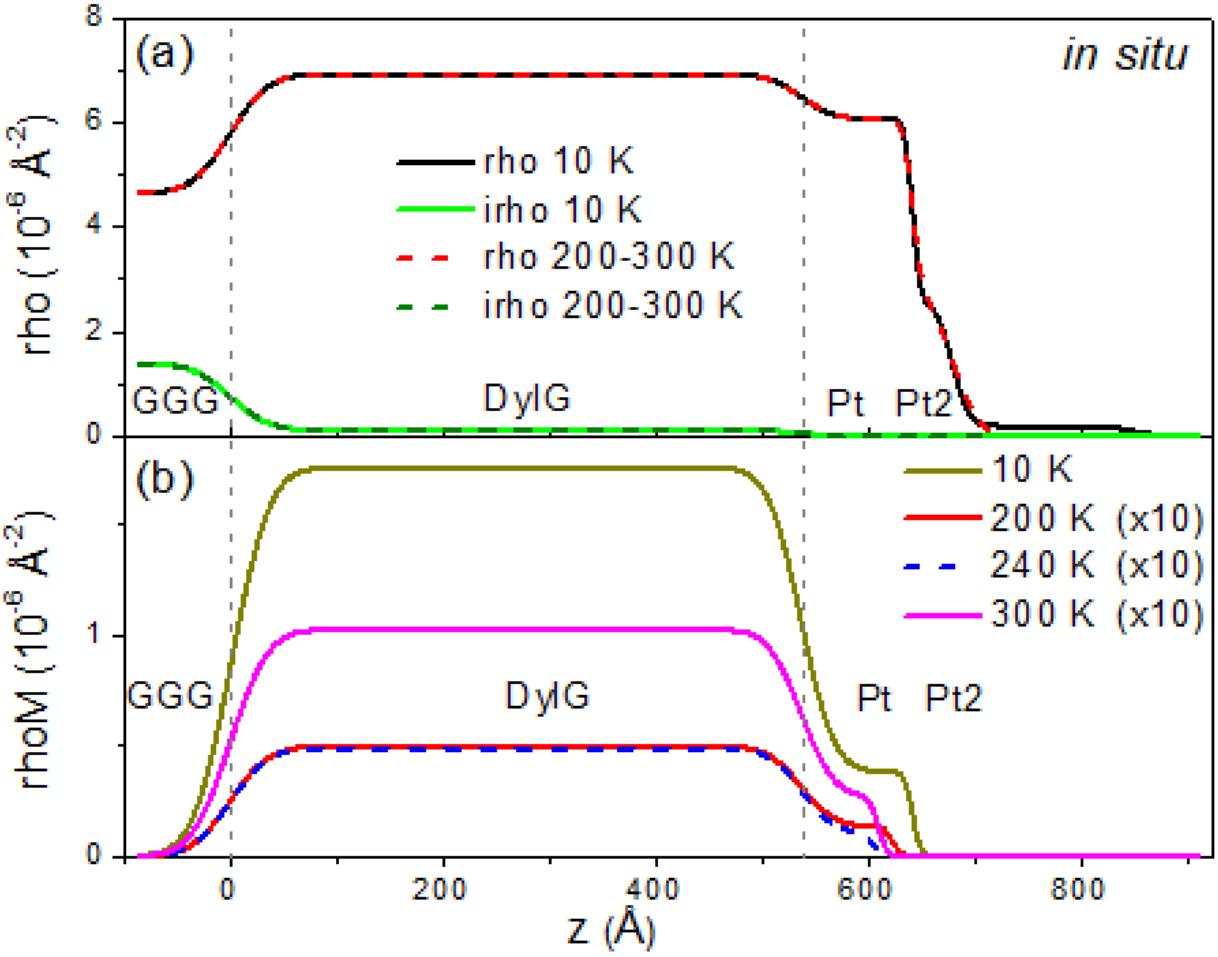

Figure 6.10: (a) Real and imaginary parts of the SLD indicating density and neutron absorption, respectively. There is a sharp transition with no interfacial contamination and no drop in SLD at the DyIG/Pt interface. (b) Magnetic SLD at each temperature. The MPE is clearly visible and positive in the Pt layer at 10 and 300 K.

The magnetic SLD of the DyIG layer matches saturation magnetization values measured via magnetometry (200, 240, and 300 K) and literature (10 K)[48]. There are negligible magnetic dead layers at the top and bottom surfaces of the DyIG layer. Interestingly, there is a positive MPE observed at 10 and 300 K, with values of 0.22 ± 0.01 and 0.014 ± 0.005 μ_B/Pt atom at 10 and 300 K, respectively. Note that the values of the 200 and 240 K MPE are too close to the detection limit to say whether a positive MPE is in fact present. Likewise, the value measured at 300 K is near the detection limit, but demonstrates reasonable error bars at the 95% confidence level. The

magnitude of the MPE at 10 K is comparable to previous measurements on Pt with ferromagnetic metals and magnetic insulators. The higher temperature condition exhibits weak, but definitively positive and nonzero MPE (99% confidence interval as determined from fitting). Also note that for 200 and 240 K it is not possible to say whether a positive MPE is present, but the model is not consistent with a negative MPE at these (or any) temperature measured.

At 10 K, it appears that nearly all of the Pt layer is magnetized. It should be emphasized that complete polarization is not a physically realistic scenario and is a result of our model being insensitive to the penetration depth of the MPE in the Pt layer. Rather, the model is more sensitive to the total magnetic moment in the Pt layer and is unable to capture its distribution using our framework. We expect that the MPE is confined to the first 1-3 nm, as previously demonstrated and as inferred from our inability to observe an XMCD signal at the Pt L_2 edge.

To explore this further, we examined several alternative PNR models with different constraints. First, we consider the scenario where we limit the depth of the MPE to a maximum of 3 nm in the Pt layer. The fitted PNR curves and spin asymmetry are shown in figure 6.11. The primary differences between the fits are observed at 10 K in the high Q_z region of the reflectometry and the $Q_z \sim 0.04$ region of the spin asymmetry. In the SA, the model does not capture the amplitude of the SA oscillations in this range, indicating that the model is missing some part of the magnetic behavior of the sample. The SLD profiles are displayed in figure 6.12, where the structural components are unchanged except for the Pt and Pt2 SLD and interfaces. The MPE decays to zero before the constrained maximum 3 nm depth.

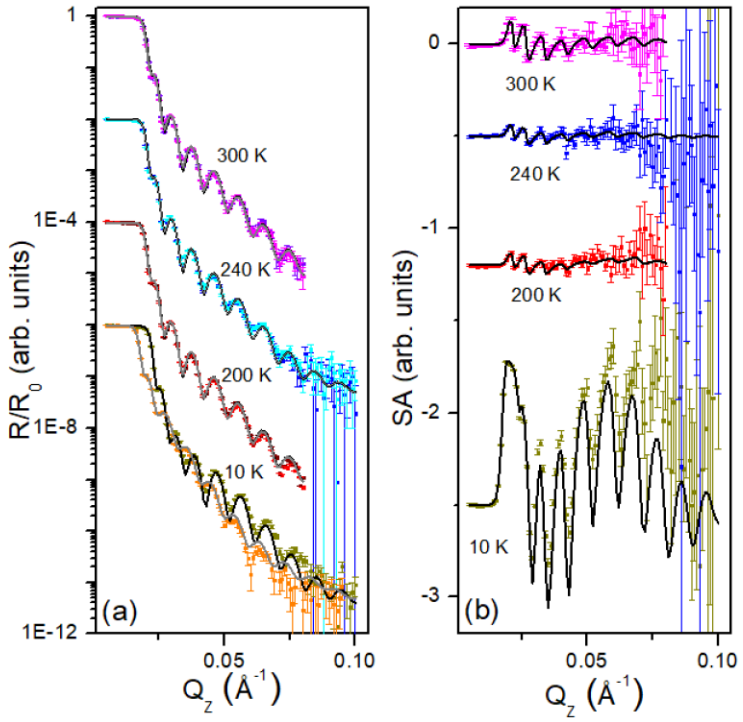

Figure 6.11: PNR model with the depth of the MPE constrained to a maximum of 3 nm. (a) Fitted PNR curves and (b) SA of *in situ* grown Pt/DyIG/GGG at 10, 200, 240, and 300 K.

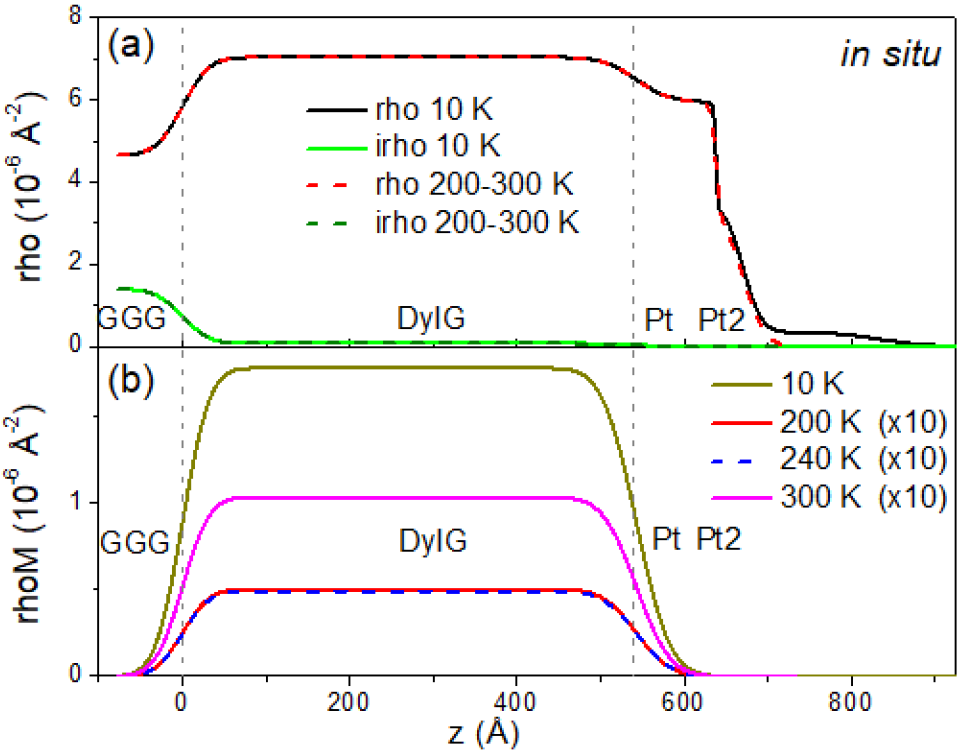

Figure 6.12: PNR model with the depth of the MPE constrained to a maximum of 3 nm. (a) Real and imaginary parts of the SLD indicating density and neutron absorption, respectively. (b) Magnetic SLD at each temperature.

Next, to improve the quality of the model with a restricted depth of the MPE, the DyIG/GGG interface was allowed to vary at 10 K and the depth of the MPE was fixed at 3 nm. The difference in interface roughness at low temperature is an experimental artifact due to misalignment at high Q_z values and due to warping of the substrate as the system is cooled and does not represent a physically distinct interface at this temperature compared to the others. The fitted reflectometry curves and spin asymmetry are shown in figure 6.13. Similar to the original model shown in figure 6.9, agreement is excellent throughout the Q_z range. This is reflected in the small difference in χ^2 between the two models (summarized in table 6.1).

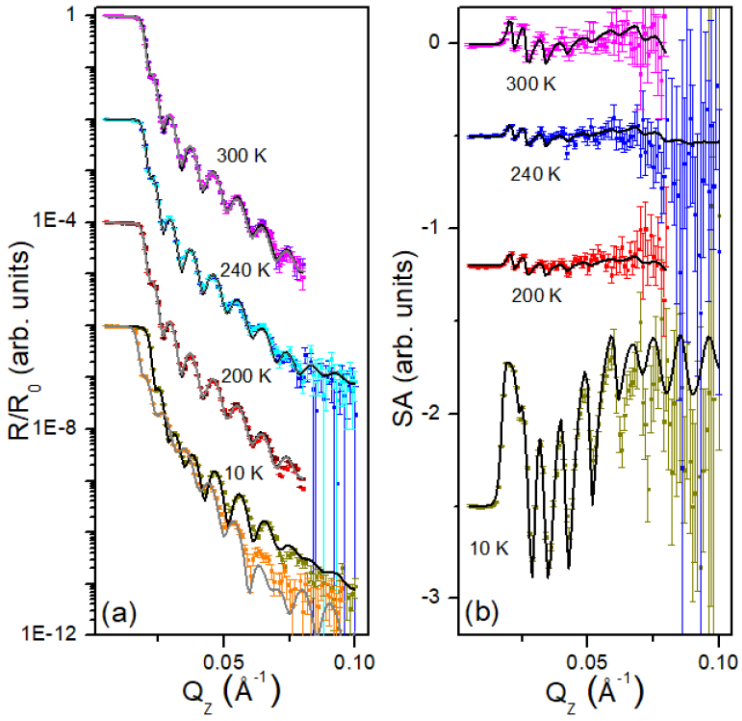

Figure 6.13: PNR model with the depth of the MPE constrained to exactly 3 nm and the DyIG/GGG interface allowed to vary at 10 K. (a) Fitted PNR curves and (b) SA of *in situ* grown Pt/DyIG/GGG at 10, 200, 240, and 300 K.

The SLD profile (figure 6.14) for this model exhibits a slightly different DyIG/GGG interface at 10 K, and 10 K is the only temperature at which the MPE is clearly visible. Under this model, the MPE at 10 K has a strength of 1.08 ± 0.02 μ_B/Pt atom, larger than values reported for ferromagnet/heavy metals bilayers. This value is unphysically large and reflects that the PNR

fitting is most sensitive to the total magnetic moment in the Pt layer and not the distribution. Indeed, calculating the product of the MPE depth and the magnetization per Pt atom results in a very similar value for the first model described and this alternative. A middle ground between these two models is likely the best representation of the actual situation. The magnetic interfaces at both the top and bottom are both significantly steeper than in the other models, which is indicative of an improved magnetic fit that is obtained by slight relaxation of the structural parameters.

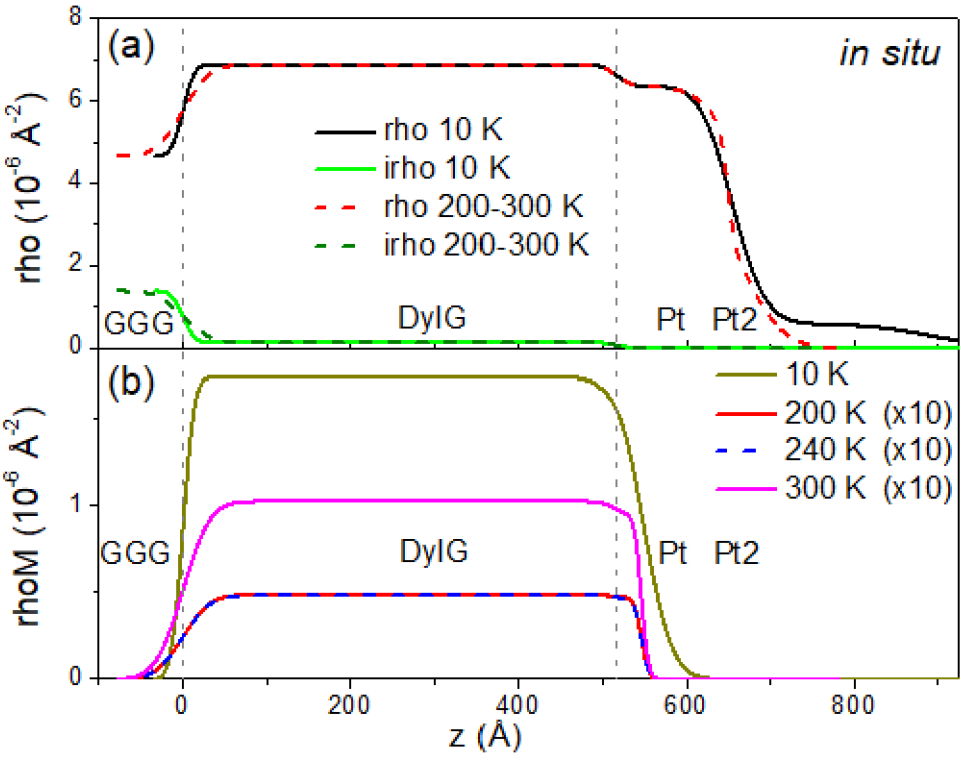

Figure 6.14: PNR model with the depth of the MPE constrained to exactly 3 nm and the DyIG/GGG interface allowed to vary at 10 K. (a) Real and imaginary parts of the SLD indicating density and neutron absorption, respectively. (b) Magnetic SLD at each temperature.

Importantly, these three models arrive at the same general structural fit. Also, the MPE is consistently positive at 10 and 300 K in all models, and the models are inconsistent with a negative proximity effect at any temperature. This indicates that the assumptions and proposed structure are robust in the face of alternative models.

A final question that must be addressed is how important is the presence of the proximity effect to the fitted model. To answer this, the magnetic components were removed from the original model shown in figure 6.9 and 6.10. The result is a fairly large increase in χ^2 without proximity and a decrease in the accuracy of the fit (most visible in the 10 K SA in figure 6.15b).

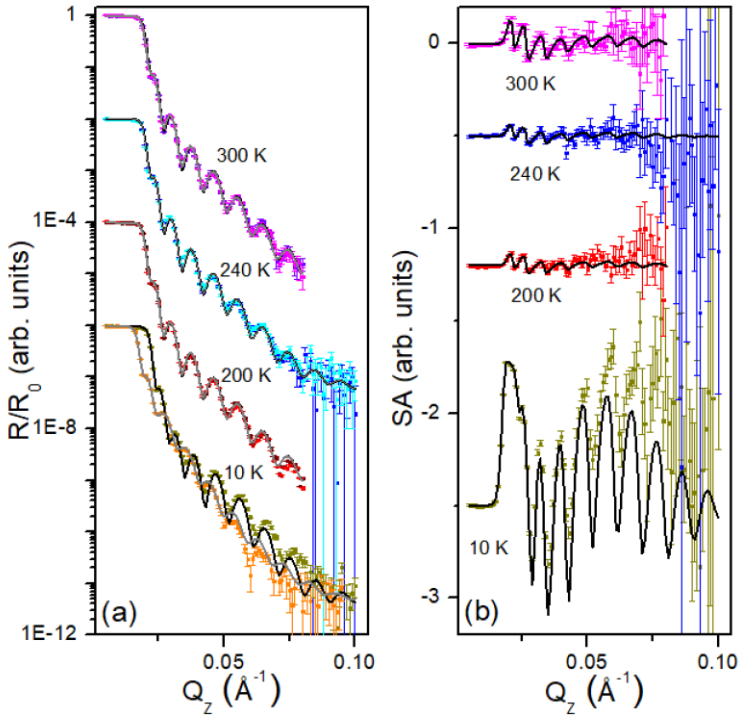

Figure 6.15: PNR model without a MPE in the Pt layer. (a) Fitted PNR curves and (b) SA of *in situ* grown Pt/DyIG/GGG at 10, 200, 240, and 300 K.

The SLD profile (figure 6.16) of the fit without a proximity effect is very similar to the original model, again demonstrating that the structural fit is robust to alternative models of the data. The magnetic profiles have a similar interface roughness, and the magnetism penetrating into the Pt is only a result of this magnetic roughness.

The magnitude and depth of the MPE in each of the models discussed is displayed in Table 6.1, along with the value of χ^2 for each fit. The χ^2 values and the fitted PNR curves of the models indicate that the first model presented without constraints and the model in which the structure was allowed to vary slightly present the best fits of the data. Across all three models containing a

proximity effect, the MPE is convincingly demonstrated at 10 K and 300 K. At 200 and 240 K however, the values of the MPE are less definitive. One possible reason for this is that the magnetization of the DyIG layer is too low to induce a proximity effect in the Pt at these temperatures (saturation magnetization is ~10 emu cm^{-3} at these temperatures). In Pt/CoFeTaB/Pt heterostructures studied as a function of temperature, it was observed that a threshold magnetization in the magnetic layer is necessary to induce a MPE. It is possible than DyIG is below the required threshold at these temperatures, but the MPE is measurable at room temperature when the magnetization of DyIG is larger.

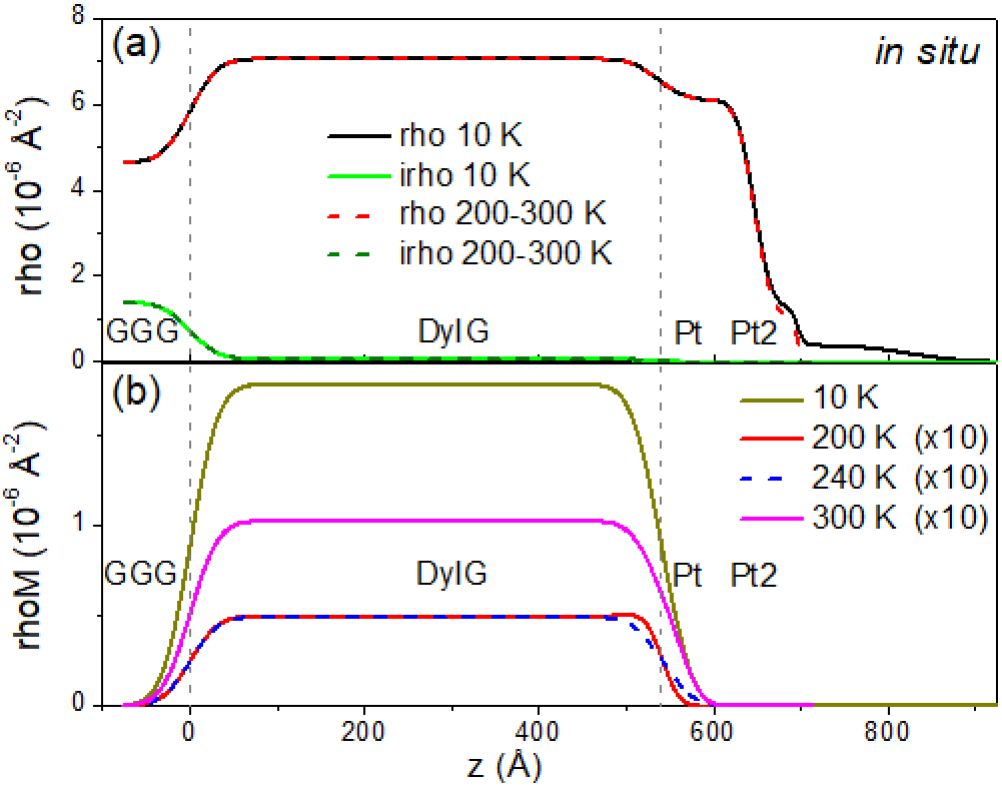

Figure 6.16: PNR model without a MPE in the Pt layer. (a) Real and imaginary parts of the SLD indicating density and neutron absorption, respectively. (b) Magnetic SLD at each temperature.

This surprising result differs with our hypothesis that the MPE tracks the net Fe magnetization, demonstrating that instead the MPE tracks the net magnetization of the system. This is in contrast to the MPE in rare-earth transition metal/HM heterostructures where the MPE tracks the moment of the transition metal sublattice and lends further credence to the assertion of a fundamentally different mechanism in magnetic insulators.

Table 6.1: Table of χ^2 values, MPE strength, and MPE depth for the four models of the *in situ* Pt/DyIG/GGG film, listed in the order presented.

Description of Model	Temperature (K)	χ^2	μ_B/Pt atom	MPE depth (nm)
Constrained structure	10	10.24	0.22 ± 0.01	9.6 ± 0.2
	200		0.007 ± 0.003	4.4 ± 2.0
	240		0.005 ± 0.004	1.8 ± 2.0
	300		0.014 ± 0.005	2.2 ± 2.0
MPE constrained to maximum of 3 nm	10	13.80	0.129 ± 0.034	2.8 ± 0.2
	200		0.037 ± 0.037	1.3 ± 1.2
	240		0.008 ± 0.042	1.4 ± 1.4
	300		0.030 ± 0.021	2.0 ± 1.1
MPE constrained to 3nm, structure relaxed	10	9.71	1.080 ± 0.024	3.0
	200		0.027 ± 0.007	3.0
	240		0.026 ± 0.008	3.0
	300		0.057 ± 0.009	3.0
Constrained structure, no MPE	---	13.30	---	---

6.5 Spin Hall Magnetoresistance

The spin Hall magnetoresistance (SMR) and spin mixing conductance, $G_{\uparrow\downarrow}$, are useful parameters for evaluating the spin transport at magnetic insulator/heavy metal interfaces. The amplitude of

the AHE and SMR in perpendicularly magnetized HM/garnet heterostructures are used to calculate the $G_{\uparrow\downarrow}$ using the method of Chen et al[239]. To evaluate the effect of *in situ* Pt deposition vs. previously reported values from *ex situ* deposition, a Pt(3 nm)/TmIG(9 nm)/GGG film was patterned into Hall crosses via optical lithography and ion milling. TmIG was selected because it has PMA, and a low enough anisotropy field to measure the in-plane SMR and calculate $G_{\uparrow\downarrow}$. A W(5 nm)/DyIG(54 nm)/GGG was also patterned to measure the sign of the AHE for comparison to Pt.

The electrical measurements on the Pt/TmIG/GGG are summarized in figure 6.17. The out-of-plane AHE measurement shows a square loop with robust PMA and a coercivity of ~20 Oe. The amplitude of the OP AHE Hall resistance (H_R) is similar to previously reported values on garnets grown in this research group[8,50]. Interestingly, the maximum of the IP SMR measurements is more than double the previously reported values. This implies that the real part of the spin mixing conductance, which is associated with the damping-like spin-orbit torque, is greater in these films. The in-plane angular dependence of the SMR measurement also demonstrates the expected $\sin(2\varphi)$ behavior. Calculating the spin mixing conductance yields values of $G_r = 4.74 \times 10^{13}\ \Omega^{-1}\ m^{-2}$ and $G_i = 1.93 \times 10^{12}\ \Omega^{-1}\ m^{-2}$. This is smaller than the values reported by Quindeau et al. and Avci et al., but this is likely due to the lower thickness and higher resistivity of the Pt layer[8,50]. The quality of the Pt is unfortunately limited by the base pressure and geometry of the PLD system, precluding a direct comparison of the metallic layers. However, the impact of having a cleaner interface between the heavy metal and garnet layers is clear.

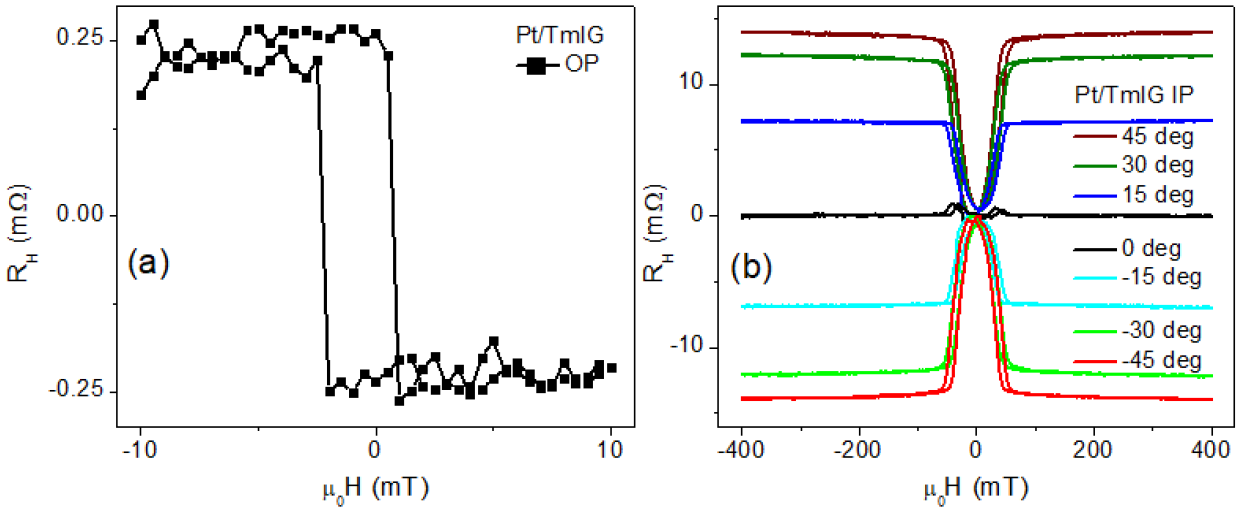

Figure 6.17: (a) Out-of-plane anomalous Hall effect and (b) in-plane spin Hall magnetoresistance of an *in situ* grown Pt/TmIG/GGG Hall cross.

The SMR was also measured in a W/DyIG/GGG bilayer to determine the sign of the anomalous Hall effect due to conflicting reports in W/TmIG[49,272]. We measured a positive AHE along the in-plane easy axis of the DyIG film (figure 6.18b), matching the sign of Pt/REIG and consistent with Bose et al. The probe station in which this measurement was collected was unable to supply a large enough field during a field sweep to fully saturate the W/DyIG sample due to large amounts of noise in the measurement. Future measurements on W films will require a capping layer to prevent surface oxidation.

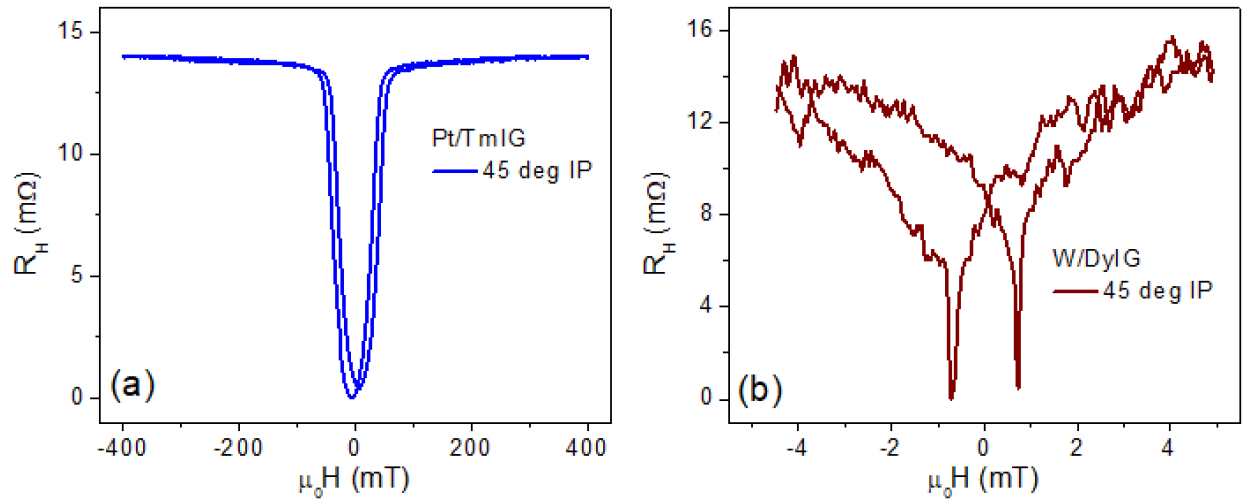

Figure 6.18: In-plane SMR on *in situ* grown (a) Pt/TmIG and (b) W/DyIG Hall crosses.

The angular dependence of both the Pt/TmIG and W/DyIG samples are plotted in figure 6.14, displaying the expected sin(2φ) dependence. For the W/DyIG sample, a permanent magnet with a larger field was used to fully saturate the sample, leading to a higher value of the Hall resistance than in figure 6.18. The Hall resistance is four times larger with W than Pt, consistent with the much larger spin Hall angle of β-phase W, ~0.33[128,273]. The W films here were determined to be pure β-phase by x-ray diffraction.

Using the amplitude of the SMR in both samples and other materials parameters a comparison of the spin mixing conductance can be made. The material parameters obtained from literature and devise specific parameters are summarized in table 6.2. The real part of the spin mixing conductance in the W/DyIG sample is roughly three orders of magnitude lower than that of Pt. This is almost entirely due to the much larger resistivity of the W layer, which is consistent with both β-phase and partial oxidation of the layer. Like with the Pt sample, improvements in the sputtering process could likely improve the value of $G_{\uparrow\downarrow}$.

Table 6.2: Table of device specific and materials parameters used to calculate the real part of the spin mixing conductance for *in situ* deposited Pt/TmIG/GGG and W/DyIG/GGG Hall crosses.

Film	Heavy metal thickness (nm)	Resistivity (μΩ cm)	Spin diffusion length (nm)	Spin Hall angle	G_r (Ω^{-1} m^{-2})
Pt/TmIG	3.6	53.9	1.4	0.08	4.75×10^{13}
W/DyIG	5.2	549.6	3.5	0.33	5.06×10^{10}

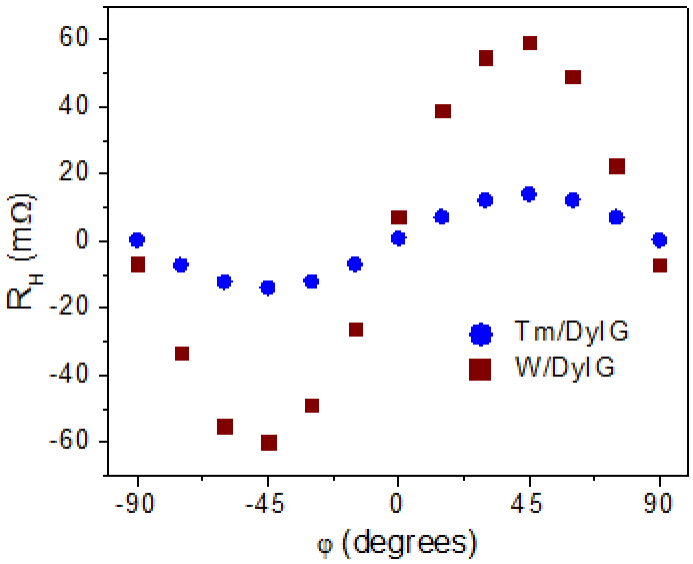

Figure 6.19: Angular dependent SMR Pt/TmIG and W/DyIG Hall crosses measured under a constant in-plane magnetic field.

6.6 Discussion of Results and Mechanism

The interface between heavy metals and magnetic insulators plays a tremendous role in the presence and strength of the magnetic proximity effect. It stands to reason that removing any interfacial contamination caused by *ex situ* processing will improve the interfacial spin transparency, which is demonstrated in the greater amplitude of the spin Hall magnetoresistance measured in the Pt/TmIG sample. Additionally, interfacial differences may explain the conflicting reports on the MPE in Pt/YIG and Pt/$CoFe_2O_4$ systems. A more direct comparison with a thicker, higher quality Pt film to determine what the values of the spin mixing conductance would be of use. Further work on W/REIG films would also be of use, as the much larger spin Hall angle of W could lead to improve device performance, despite the higher resistivity of W thin films.

The surprising result that the sign of the MPE is invariant as a function of temperature and the heavy metal utilized in magnetic insulators/HM bilayers is strong evidence that a fundamentally different mechanism exists for the proximity effect in insulating magnetic systems[194]. In the

absence of a definitive mechanism, the literature consensus for the source of the MPE in metallic systems is through a RKKY-type interaction between the *3d* and *5d* electrons of the transition and heavy metals. This explains the observed change in sign of the MPE in rare-earth transition metal/HM alloys. However, the lack of conduction electrons in insulating magnetic oxides requires that the exchange coupling occur through a different mechanism, which we attribute to a superexchange-type interaction with the cations closest to the interface. The author proposes that the heavy metal interacts with the net of the superexchange interactions at the interface, so that the proximitized moment couples to the net moment of the magnetic layer, not the moment of an individual sublattice(s). Also, while W reported negative MPE in heterostructures with metallic magnets, we report positive MPE in bilayers with insulating garnets. These results indicate that the superexchange-type interaction with the heavy metal results in only positive MPE. The author recommends further study of the proximity effect in W, which has received little attention due to the lower strength relative to Pt.

7. Ultra-Thin Polycrystalline Garnet films in DyIG/Pt/GGG/Si Heterostructures

7.1 Requirement of Ultra-Thin Films for Spintronics

The next generation of spintronic devices will likely focus on the spin-orbit torque effects from in-plane current injection in a material with a high spin Hall angle. SOT offers the potential for highly efficient switching of any type of magnetic material, insulating and metallic. However, practical considerations limit the materials systems and heterostructures that can be manipulated with this type of magnetic torque. SOT effects decay with the inverse of magnetic layer thickness, requiring that magnetic layers with a thickness of less than 10 nm be used[274]. For many metallic films and single crystal rare-earth iron garnets, this is easily achieved, with garnets with thicknesses as low as 2.4 nm reported[47].

However, polycrystalline REIG films on non-garnet substrates do not crystallize below a thickness of ~20 nm. The large unit cell of the garnets (~1.2 nm) and kinetic limitations are possible causes for the inability to crystallize, even for higher annealing temperatures than are used for thicker polycrystalline films. In previous work on magnetoptical garnet materials substituted with optically active Ce and Bi ions, a seed layer has been used to crystalline thin active layers. Using a top-down or bottom-up method, a YIG layer has been used to crystallize BiYIG and CeYIG films that are prone to forming more thermodynamically stable secondary phases, owing to the large size of the Ce^{3+} and Bi^{3+} ions[205,225]. This method is effective for this application, but for SOT spintronics, it is necessary for the total magnetic layer to be thin, and the YIG seed layer is magnetic. Additionally, YIG is in-plane magnetized when grown as a polycrystalline film owing to its large saturation magnetization and weak magnetostriction coefficients.

A potential solution is to utilize a nonmagnetic garnet as a seed layer, such as $Gd_3Ga_5O_{12}$ (GGG). However, crystallization of polycrystalline garnet films on non-garnet substrates requires a high temperature annealing step. This RTA results in significant interdiffusion which severely degrades the magnetic properties of the magnetic layer (figure 7.1).

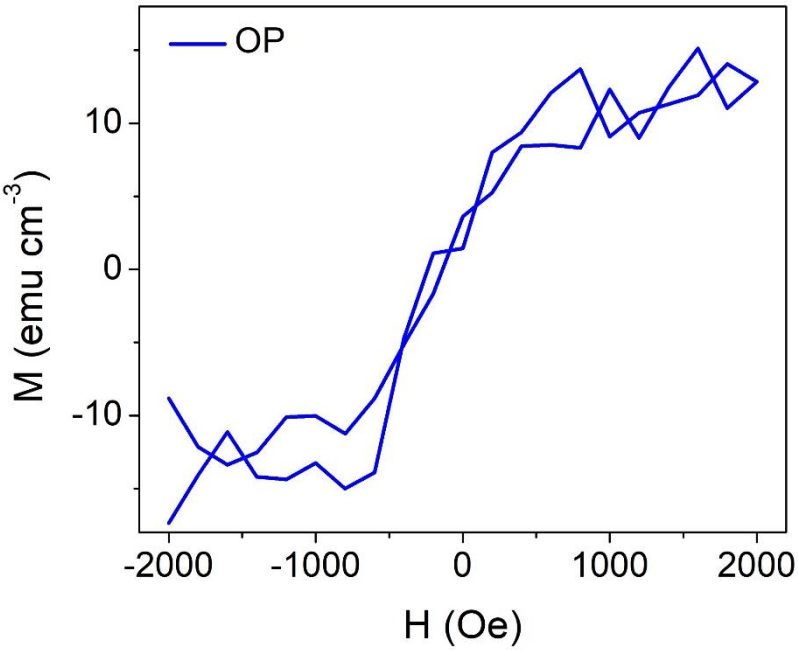

Figure 7.1: OP VSM hysteresis loop of a DyIG(10 nm)/GGG(50 nm)/Si film after RTA at 750 °C for 5 min. Interdiffusion reduces the saturation magnetization and eliminates the perpendicular magnetic anisotropy expected for DyIG/Si.

A potential solution to this interdiffusion problem is through the use of a diffusion barrier. The barrier must be thin enough or have the proper crystal structure to allow templating and crystallization of the upper garnet layer, but still thick enough to prevent significant diffusion. Aldosary et al. reported inverted single crystal YIG/Pt/GGG (110) structures where the YIG is "epitaxially" grown on the Pt layer[275]. The GGG substrate was annealed to form terraces on the surfaces, and the sputtered Pt preserved these terraces. The PLD grown YIG then crystallized into a single crystal on top of this Pt layer after annealing, with the magnetic, structural, and spin transport properties being very similar to conventional Pt/YIG/GGG structures. Similar results were reported recently in (111) oriented films by Geprägs et al[276].

The second obstacle that needs to be overcome for efficient SOT switching of polycrystalline films relates to the very high anisotropy of DyIG/Si, with H_C = 5 kOe and H_K = 10 kOe[193]. DyIG has both magnetostriction coefficients negative which, along with YIG and HoIG, is the only garnet to meet this requirement for PMA on Si substrates via thermal expansion mismatch. However, the large magnetostriction coefficients result in very high anisotropy, several times larger than that of TmIG and YIG in which highly-efficient SOT switching has been reported[8,277]. However, it is possible to codeposit intermediate compositions of YIG and DyIG (Y-DyIG, $Y_xDy_{3-x}Fe_5O_{12}$) to reduce the average magnetostriction coefficients and increase the saturation magnetization, which increases the shape anisotropy and decreases the uniaxial anisotropy. As the garnets have identical crystal structures with slightly different lattice parameters, the system easily crystallizes to pure phase garnet (figure 7.2). No peak shift is visible from the grazing incidence XRD due to the similarity of the lattice parameters.

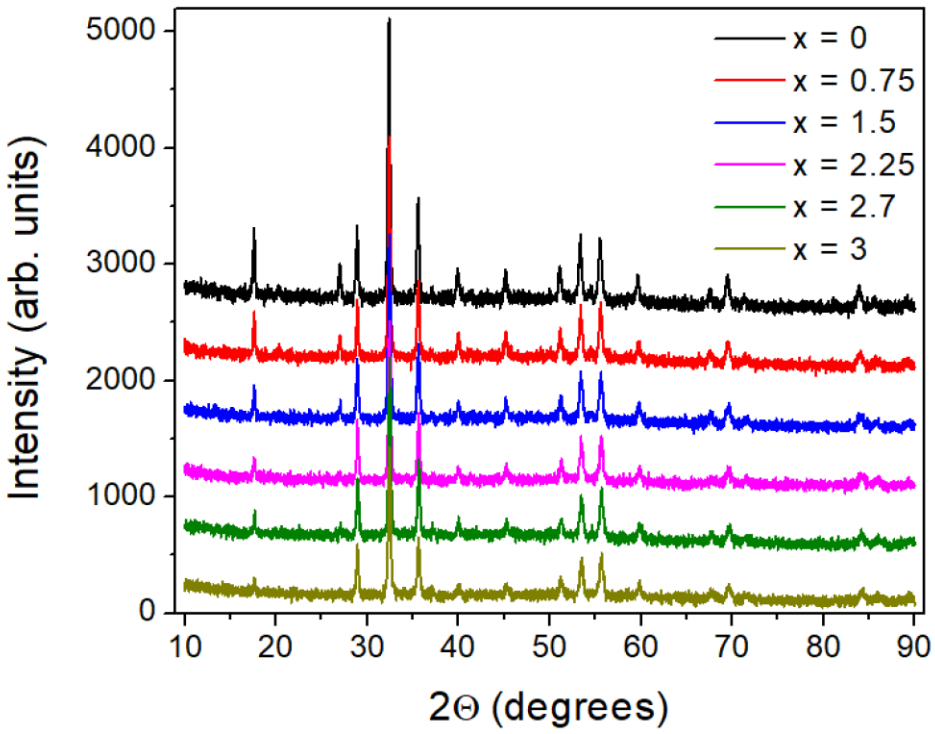

Figure 7.2: Grazing incidence XRD of $Y_xDy_{3-x}Fe_5O_{12}$/Si annealed at 750 °C/5 min. Vertically offset for clarity

The hysteresis loops for Y-DyIG are shown in figure 7.3. The saturation magnetization scales very linearly with composition, and a square hysteresis loop with obvious perpendicular magnetization is retained until x ~ 1.5. The end members have properties nearly identical to previously reported thin films.

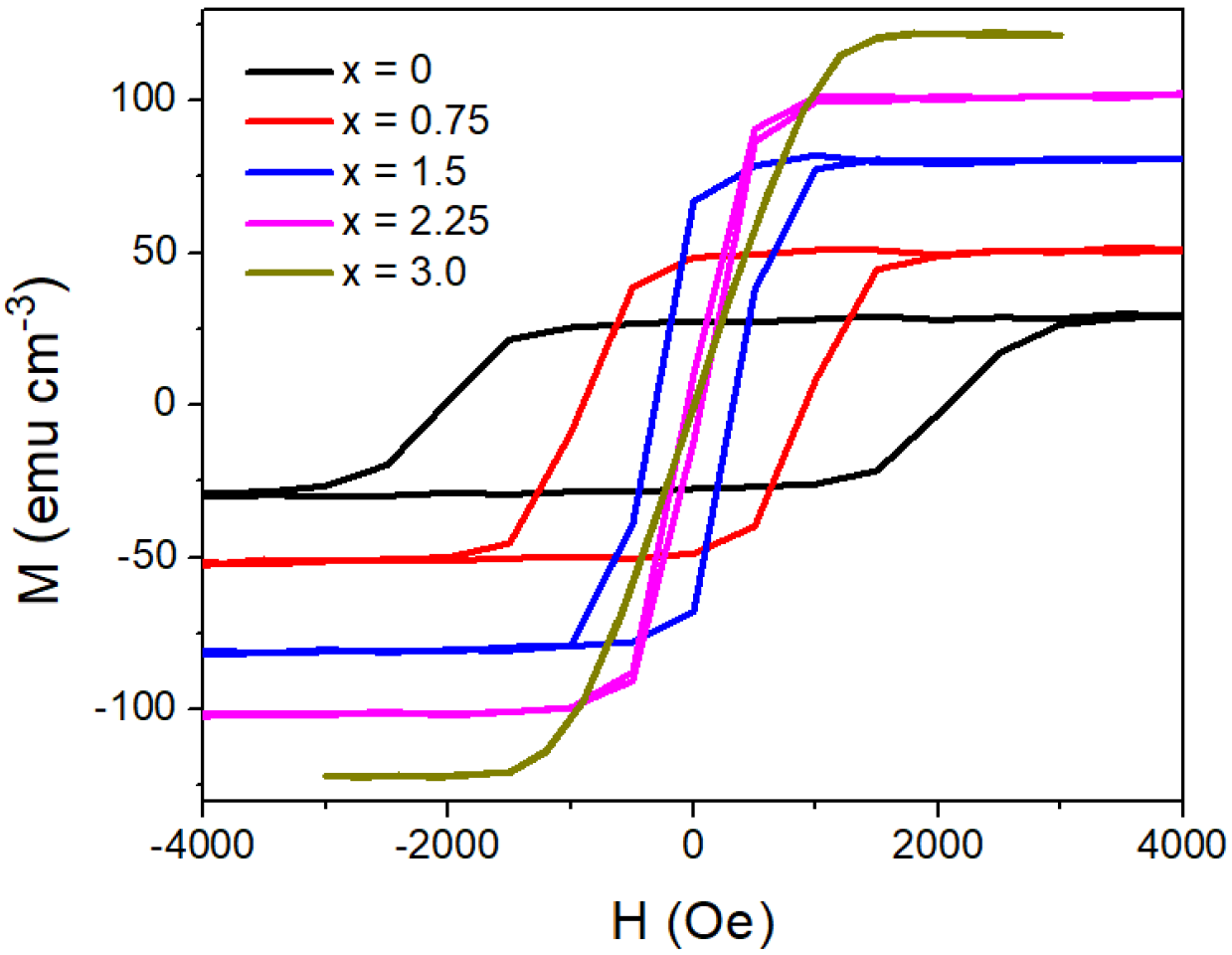

Figure 7.3: VSM hysteresis loops for $Y_xDy_{3-x}Fe_5O_{12}$/Si annealed at 750 °C/5 min. Perpendicular magnetization is retained until x ~ 1.5.

Modifying the composition through codeposition with YIG is therefore a viable way to obtain low anisotropy, perpendicularly magnetized polycrystalline garnet films on Si. Note that the anisotropy varies somewhat with film thickness, so the ideal composition will depend on film thickness, annealing conditions, and application. For certain combinations of rare-earth ions, growth induced anisotropy due to preferential ordering of the rare-earths in the non-equivalent

dodecahedral sites can be significant, but this is not expected for this system due to the relatively small difference in ionic radii of Dy and Y[159,278]. Further complicating the issue is that for polycrystalline films, the exact temperature at which the microstructure stops changing during the anneal is not known, making quantification of the components of the anisotropy difficult. A thorough study on single crystal Y-DyIG films would be of interest to determine if growth-induced anisotropy is present in this system.

7.2 DyIG/Pt/GGG/Si Heterostructures

Using the procedure for growing inverted YIG/Pt/GGG heterostructures, we attempted to extend this to polycrystalline films. GGG seed layers on Si substrates have been demonstrated in the previous section. The remaining piece of the puzzle is a suitable diffusion barrier. Refractory heavy metals such as Ta, W, and Pt have commonly been used as diffusion in barriers in microelectronics and other applications. One of our PLD systems (named PLD-3) features an integrated sputtering gun that allows deposition of metals *in situ*. Pt was selected as the diffusion

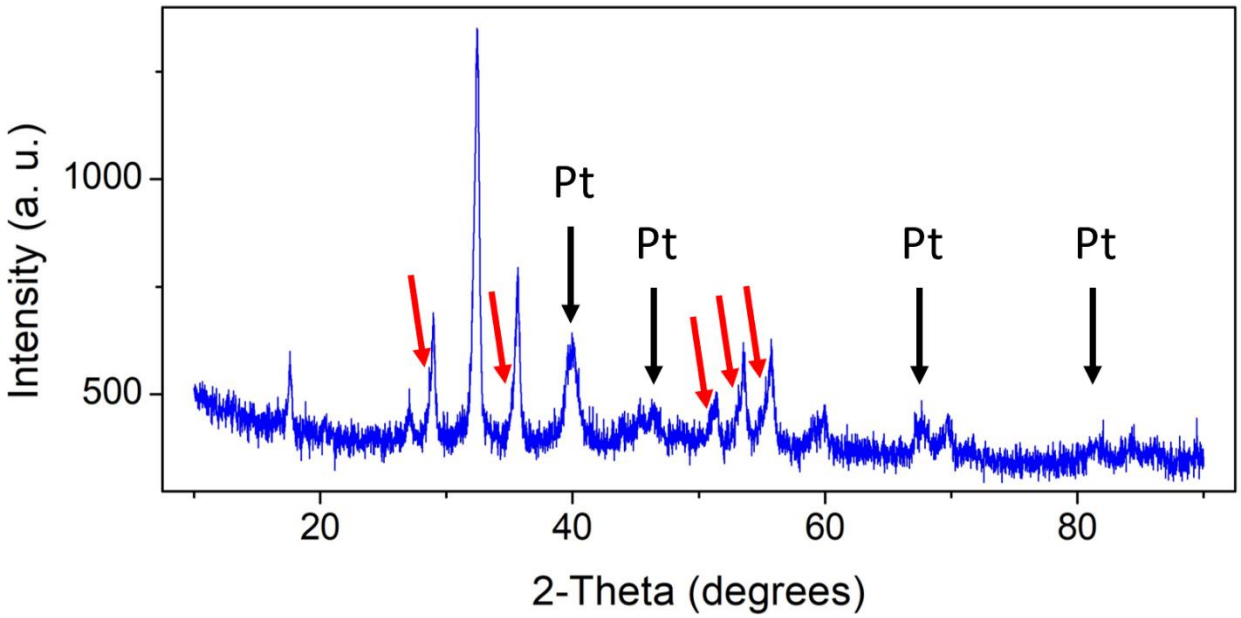

Figure 7.4: X-ray diffraction of a DyIG(10 nm)/Pt(2 nm)/GGG(50 nm)/Si film. Pt peaks are indicated with the black arrows. All other peaks are garnet reflections. The red arrows indicate shoulder peaks that may be from the thinner DyIG layer.

barrier because of its success in previous studies, usefulness as a spin current generator, relatively high resistance to oxidation, and single-phase crystal structure.

The deposition procedure was as follows: deposit 50 nm of GGG under standard garnet PLD conditions, cool to room temperature to sputter Pt *in situ*, deposit 10 nm of DyIG under standard garnet PLD conditions *in situ*, and finally anneal *ex situ* at 750 °C/5 min. in O_2 flow. X-ray diffraction of a representative sample is shown in figure 7.4. Pt peaks are marked, and there are no PtO_2 peaks present, although oxidation at the garnet interfaces cannot be entirely ruled out. There is a weak shoulder on some of the garnet peaks in the range 25-35° that may be due to the DyIG layer, but this is difficult to determine due to the similarity of the DyIG and GGG crystal structures and lattice parameters.

Next, different heterostructures of DyIG(10 nm), Pt(2 nm), and GGG(50 nm) were deposited on Si to determine the effect of different stacks. Layer thicknesses were kept consistent between depositions. From figure 7.5, it clear that DyIG/Si and DyIG/Pt/Si do not crystallize to form garnet. This is unsurprising, as garnets below ~20 nm do not crystallize on Si, and the face-centered cubic crystal structure of Pt likely does not provide a templated surface to crystallize the garnet. However, when the GGG layer is inserted, the films crystallize well into pure phase garnet. Inclusion of the Pt layer results in no significant modification to the XRD of the garnets, with a few Pt peaks visible. This clearly demonstrates that the GGG seedlayer is necessary for crystallization, while the use of the Pt diffusion barrier provides no obvious detriment to the structural quality of the films.

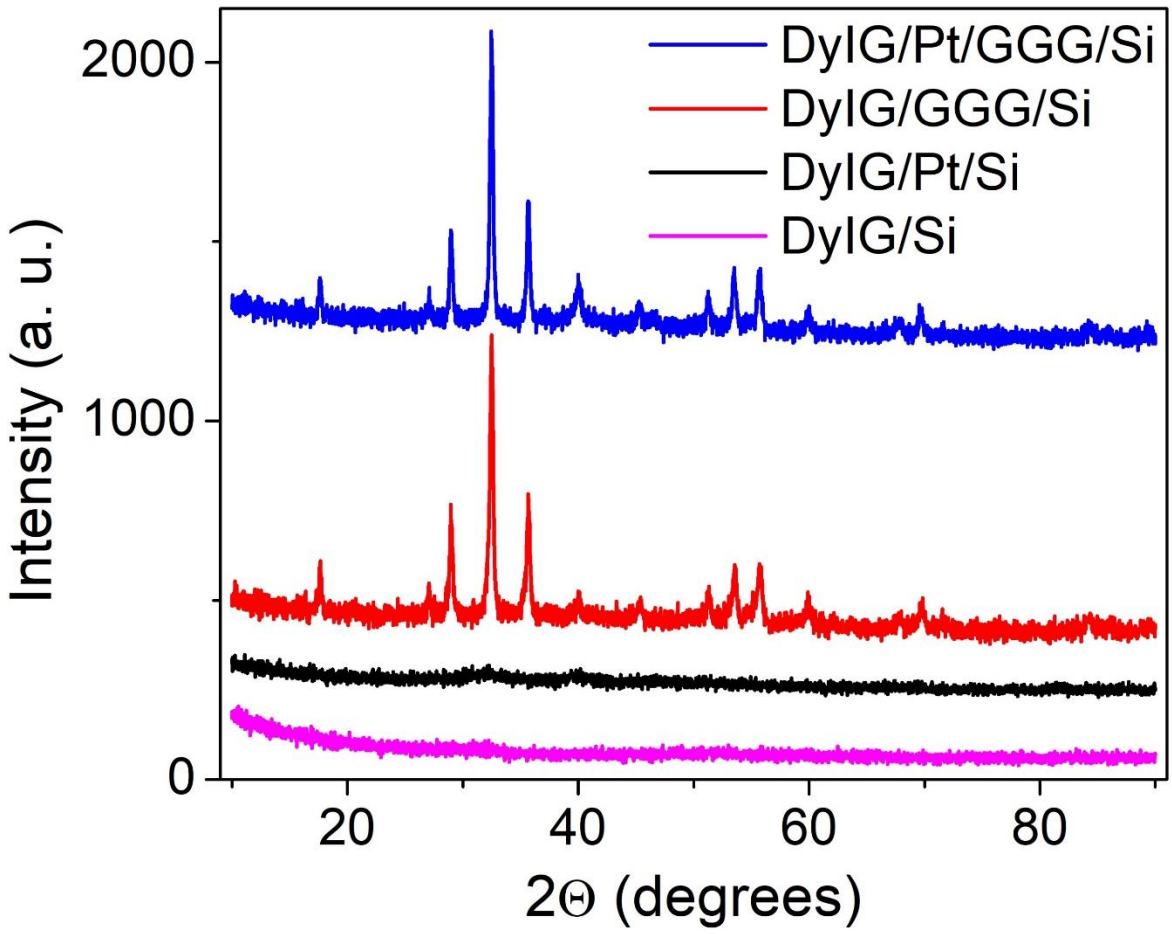

Figure 7.5: X-ray diffraction of different heterostructures of DyIG, Pt, and GGG. The thick GGG layer is necessary to crystallize the thin upper DyIG layer. The Pt layer does not inhibit the crystallization of the garnet. Vertically offset for clarity.

The magnetic properties of the DyIG/Pt/GGG/Si heterostructure were then measured via VSM (figure 7.6). There is clear perpendicular magnetic anisotropy, with the magnetization slightly lower than the bulk value. There is some error in the layer thicknesses determined by x-ray reflectivity due to the complexity of fitting a four layer structure, and this error is propagated into calculation of the saturation magnetization, which may explain the depressed value. The coercivity of the film is ~250 Oe, with an in-plane anisotropy field of ~2 kOe. The anisotropy is much lower than previously reported DyIG/Si films, which is likely due to strain relaxation in the GGG and Pt layers. Polycrystalline garnets thinner than 40 nm also typically see a decrease in coercivity and anisotropy field, so strain relaxation in the magnetic layer is also a possible cause[33,193].

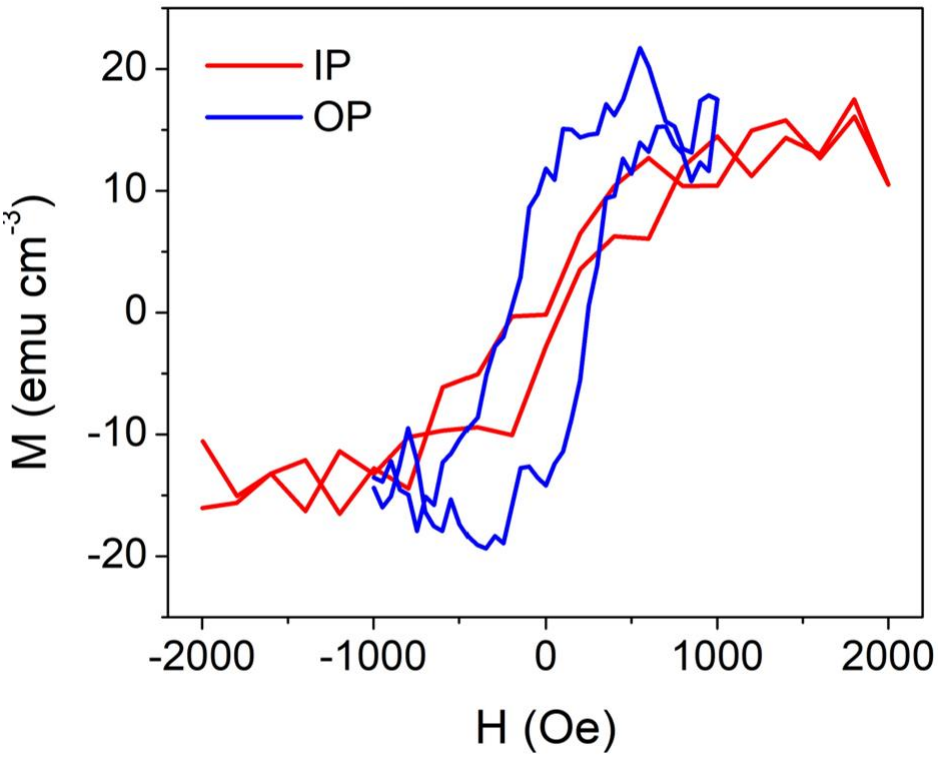

Figure 7.6: VSM hysteresis loop of a DyIG/Pt/GGG/Si heterostructure with perpendicular magnetic anisotropy.

7.3 Future Directions

Further work needs to be done on this interesting heterostructure. The next steps are to deposit additional films and optimize the layer thicknesses, deposition temperatures, and annealing procedures. Following this optimization, examination of the film via cross-sectional TEM is recommended to determine the extent of any interdiffusion in the structure and whether the Pt layer dewetted into islands or is continuous. Patterning of the films into Hall crosses to measure the spin transport measurements for comparison to previous work on polycrystalline garnet films and eventual spin-orbit torque switching measurements on these structures will be needed. If efficient SOT switching is possible, this structure could serve as a useful paradigm for growth of other materials which are difficult to grow in thin films. Additionally, this direct integration on Si

offers the potential for eventual integration into existing CMOS processes as part of the next generation of spintronic memory technologies.

8. Molecular Field Coefficients Model of Rare-Earth Iron Garnet Magnetism

8.1 Molecular Field Coefficient Model

Molecular field theory was developed in the early twentieth century as a means of explaining classical paramagnetism, with Pierre Weiss building on work by Pierre Curie that culminated in the Curie-Weiss Law[18,279]:

$$\chi_m = \frac{C}{(T-\theta)} \tag{8.1}$$

Where χ_m is the magnetic susceptibility, C is a material specific constant (the Curie constant), T is the temperature in K, and θ is a critical temperature above which the Curie-Weiss law holds for any paramagnetic material. This critical temperature would later be shown to be the Curie temperature. Weiss explained this behavior by asserting that an intramolecular interaction, which he termed the "molecular" field, existed between the moments of the individual atoms and resulting in macroscopic paramagnetism. Weiss would go on to extend this theory to explain classical ferromagnetism, that this internal molecular field is strong enough that it can self-magnetize magnetic materials below the Curie temperature, even in the absence of an external field[279]. This model was unable to explain why not all pieces of iron are spontaneously magnetic (namely, the formation of domains), but was a huge leap in understanding and modeling of ferromagnetism.

The explanation and quantitative modeling of antiferromagnetism (and the not yet discovered phenomena of ferrimagnetism) was not adequately explained until Louis Néel's seminal work in 1932[280]. Néel, who was a student of Weiss, applied Weiss' molecular field theory to explain the

susceptibility of antiferromagnets and characterized the temperature at which the antiferromagnetic behavior of the material disappears, now called the Néel temperature. In 1948, Néel was the first to postulate that materials could be ferrimagnetic, explaining a longstanding question regarding the total magnetism of the first known magnetic material, magnetite (Fe_3O_4)[281]. Ferrimagnets have more than one inequivalent magnetic sublattice, with the net moment being the difference of the antiferromagnetically coupled sublattices. Néel would go on to win the 1970 Nobel Prize in Physics for these discoveries.

Although empirical, molecular field theory has persisted as a reasonably accurate model for magnetic susceptibilities of magnetic and antiferromagnetic materials and has also proven quite useful as a model of magnetism in ferrimagnets. The use of a molecular field model to understand the behavior of the garnets was first done by Kittel in his explanation of the ferromagnetic resonance of REIG, then more concretely developed into a model by determining the molecular field coefficients by Anderson[282–285]. This was extended by Gerald Dionne beginning in 1970, who attempted to explain the behavior of YIG substituted with nonmagnetic ions, then to rare-earth iron garnets substituted with non-magnetic ions[162,260,286]. The model presented in this work is primarily based on the latter two of Dionne's papers, and will be discussed in detail in the following paragraphs.

Anderson and Dionne's molecular field coefficients (henceforth referred to as MFC) model considers the pair-wise antiferromagnetic superexchange intra- and inter-sublattice interactions. It is important to note that each sublattice couples antiferromagnetically to all the other sublattices and itself. However, the strengths of these interactions depends greatly on the bond length and

angles between the cations, and the interaction between the octahedral and tetrahedral sites is by far the strongest, leading to the ferrimagnetic state of YIG[287]. Dionne was seeking to explain the non-linear behavior of the substitution of non-magnetic Sc^{3+} onto the octahedral sites of YIG (see figure 8.1). The Néel theory of antiferromagnetism and a statistical model developed by Gilleo was unable to sufficiently explain the data[288,289].

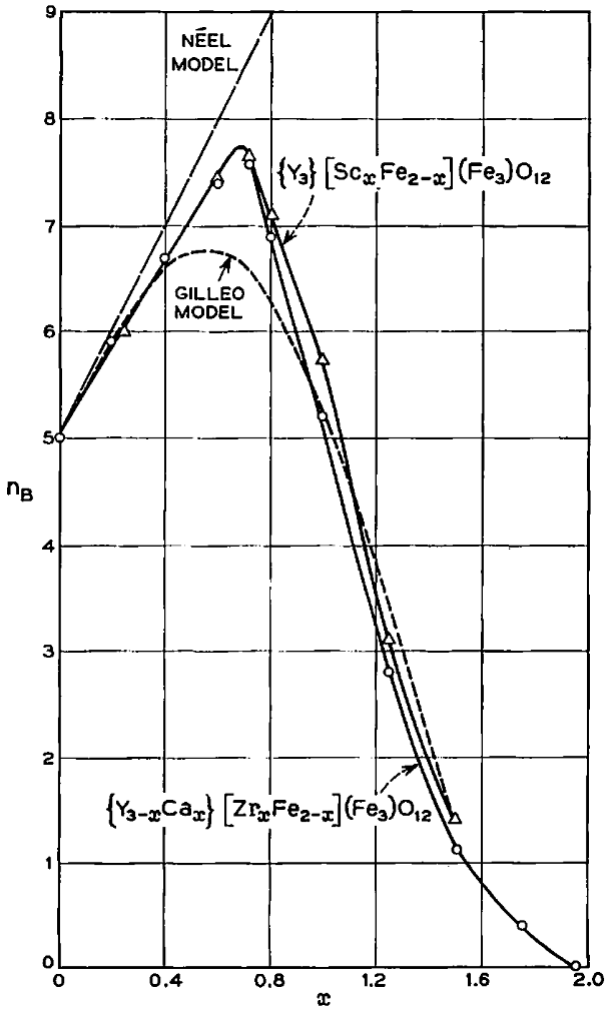

Figure 8.1: Plot of the magnetic moment of $\{Y_3\}[Sc_xFe_{2-x}](Fe_3)O_{12}$ and $\{Y_{3-x}Ca_x\}[Zr_xFe_{2-x}](Fe_3)O_{12}$ compared to the Néel and Gilleo theories. From ref. 287. Used with permission.

Dionne's model of substituted YIG used three MFCs and is based on the observation by Geller that substitution in one sublattice primarily affects the intrasublattice interactions of the *other* sublattice, not the one on which the substitution occurs[162,290]. The total magnetism in the system is:

$$M(T) = M_d(T) - M_a(T) \tag{8.2}$$

Where:

$$M_d(T) = M_d(0)B_{sd}(x_d) \tag{8.3}$$

$$M_a(T) = M_a(0)B_{sa}(x_a) \tag{8.4}$$

$M_i(T)$ is the magnetization the i^{th} sublattice as function of temperature, $M_i(0)$ is the zero-temperature moment of the i^{th} sublattice, and $B_{si}(x_i)$ is the Brillouin function for the i^{th} sublattice (see section 2.2.2 for more details):

$$B_{si} = \frac{2J_i + 1}{2J_i}\coth\left(\frac{2J_i + 1}{2J_i} * x_i\right) - \frac{1}{2J_i}\coth\left(\frac{1}{2J_i} * x_i\right) \tag{8.5}$$

Note J_i is the same as S_i for Fe^{3+} due to the quenching of orbital angular momentum. The MFCs are incorporated into the x_i terms, which also include the physical constants from the hyperbolic cotangent expressions:

$$x_d = \frac{J_d g \mu_B}{k_B T * f}(N_{dd}M_d + N_{ad}M_a) \tag{8.6}$$

$$x_a = \frac{J_a g \mu_B}{k_B T * f}(N_{aa}M_a + N_{ad}M_d) \tag{8.7}$$

Where N_{ii} are the intrasublattice interactions, N_{ij} are the intersublattice interactions, and f is a rare-earth dependent empirically determined scale factor added during this work to improve agreement with experiment and model stability. Note $N_{ij} = N_{ji}$ due to symmetry. To account for the substitution of nonmagnetic ions onto the a (octahedral) and d (tetrahedral) sites, we define $k_d = y/3$ and $k_a = x/2$, where k_d and k_a are the fraction of nonmagnetic ions on the respective site in $\{Y_3\}[R_xFe_{2-x}](Q_yFe_{3-y})O_{12}$, where R and Q are ions that exclusively occupy the octahedral (such as Sc^{3+} or Zr^{4+}) and tetrahedral sites (such as Si^{4+}), respectively. The zero temperature moments are modified in an empirically determined fashion:

$$M_d(0) = 3gJ_d\mu_B N(1 - k_d)(1 - 0.1k_a) \tag{8.8}$$

$$M_a(0) = 2gJ_a\mu_B N(1-k_a)(1-k_d^{5.4}) \quad (8.9)$$

Where N is Avogadro's number, and the integer terms refer to number of ions in that site per formula unit. The MFCs are modified in the following way:

$$N_{dd} = -30.4(1-0.43x) \quad mole/cm^3 \quad (8.10)$$

$$N_{aa} = -65.0(1-0.42y) \quad mole/cm^3 \quad (8.11)$$

$$N_{ad} = 97.0(1-0.125x-0.127y) \quad mole/cm^3 \quad (8.12)$$

The intrasublattice interactions are antiferromagnetic, and the intersublattice a-d interactions are also antiferromagnetic, but stronger than the competing interactions, leading to net ferrimagnetism. The rationale for this formalism is that incorporating nonmagnetic ions dilutes the average strength of the antiferromagnetic exchange interactions, leading to a reduction in the Curie temperature (see next section)[287]. This model provides very precise results for substituted bulk samples and powders, especially in the low substitution regimes where canting is limited. Higher substitution amounts leads to strong non-linearities in the net moment and rapid depression of the T_{Curie}[291].

The extension of this model to allow for magnetic ions on the c site is straightforward. The intrasublattice c-c interactions are negligible, and the intersublattice c-a and c-d interactions are rare-earth dependent and determined through fitting of experimental data[260]. In general, N_{ac} and N_{cd} are much weaker than those interactions involving only the octahedral and/or tetrahedral sublattices, due to much longer bond lengths resulting from the larger ionic radii. Dionne's 1976 paper allowed for up to three distinct c (dodecahedral)

site ions, and this was the model used as the basis for this work. A subset of the modified equations is shown here, for the 1st magnetic c-site ions (x) only:

$$M(T) = \left|M_d(T) - M_a(T) - M_{cx}(T) - M_{cy}(T) - M_{cz}(T)\right| \quad (8.13)$$

$$x_d = \frac{J_d g \mu_B}{k_B T * f}\left(N_{dd}M_d + N_{ad}M_a + N_{cdx}M_{cx} + N_{cdy}M_{cy} + N_{cdz}M_{cz}\right) \quad (8.14)$$

$$x_{cx} = \frac{J'_{cx} g_{cx} \mu_B}{k_B T * f}\left(N_{cdx}M_d + N_{acx}M_a\right) \quad (8.15)$$

$$M_{cx}(0) = 3x g_{cx} J'_d \mu_B N(1 - k_c) \quad (8.16)$$

The total angular momentum for the rare-earth ions on the c-site is an effective value (J` = J x cos(ϕ)) that is required to replicated the 0 K data exactly, and is probably due to canting at low temperature, such as the double umbrella structure observed in terbium iron garnet via neutron diffraction[260,292,293]. Like the model for YIG, this extended model provides very accurate fits to bulk and powder samples in the literature. Substituting a nonmagnetic rare-earth ion into the c-site (such as yttrium, bismuth, or lutetium) is accommodated by setting that value of M_{ci} to zero. At the time this work was conducted, nanometer thin films were not experimentally possible. In extending this work to thin films, the model is not modified to account for known phenomena such as the reduction in Curie temperature in thin films relative to bulk[294,295].

8.2 Modifications and Extensions to Model

The goal of extending this model is two-fold: to allow for the possibilities of off-stoichiometry and for the presence of non-ideal valence states. Our group reported significant off-stoichiometry, measured via x-ray photo-electron spectroscopy (XPS) (see figure 8.2) and wavelength dispersive spectroscopy (WDS) in PLD grown TbIG/GGG and EuIG/GGG films[45]. Additionally, some TbIG films exhibited a compensation temperature of ~330 K, far from the bulk value of 247 K[48]. In

this work, we also reported a significant compensation temperature discrepancy in DyIG (20 K lower than the 220 K literature and bulk value)[193]. XPS reveals that both sets of films have a rare-earth to iron ratio (RE:Fe) greater than 0.6, indicating that there is excess rare-earth present. The XPS also indicates there is a significant amount of Tb^{4+} and Eu^{2+} in the respective garnet films. It is, however, difficult to quantify the relative amount of each valence state. Determining the presence of Fe^{2+} is not possible via XPS. This raises multiple possibilities worth exploring (note that we are limiting our scope to TbIG as this material has been more thoroughly characterized):

- Does off-stoichiometry alone explain the discrepancy in compensation temperature?
- Does the excess rare-earth occupy the octahedral sites, particularly in the case of the Tb^{4+} ion due to its smaller ionic radius?
- Is, and if so how much, Fe^{2+} is present in the films?
- Alternatively, do Fe^{3+} vacancies balance charge in the films if there is insufficient Fe^{2+} present to account for the excess Tb^{4+}?

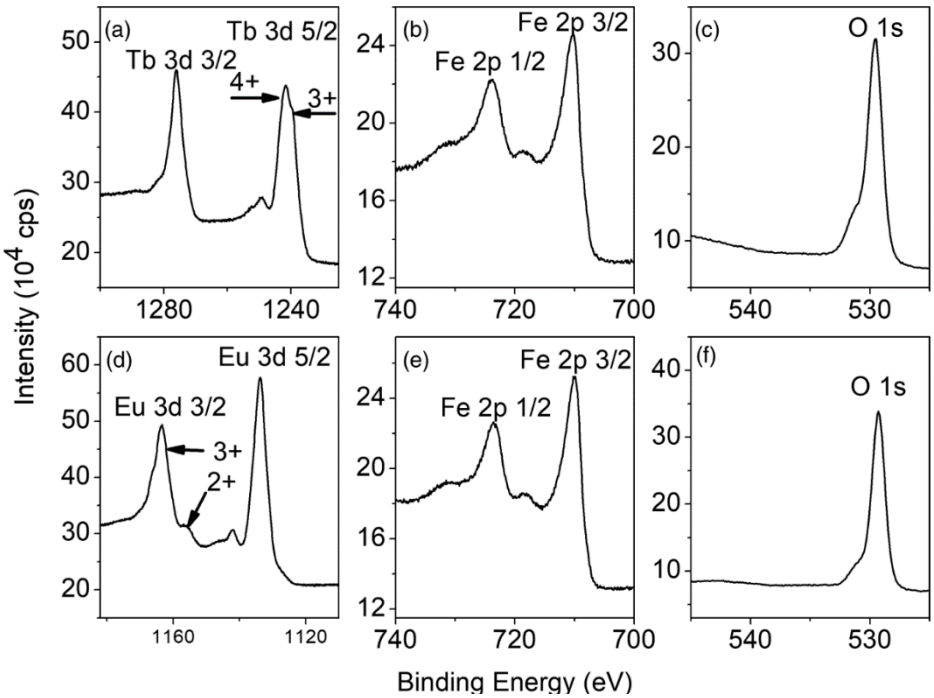

Figure 8.2: (Tb, Eu) *3d*, Fe *2p*, and O *1s* spectra of TbIG and EuIG thin films on GGG substrates. In the rare-earth spectra, valence state peaks are labeled. From ref. 45. Used with permission.

Determining the answers to these questions has proved extremely difficult experimentally. Accurate composition determination of thin films is difficult via XPS due to the variety of sensitivity factor databases and the small amount of material present in nanometer scale films. WDS has proved more reliable in determining compositions, but this necessitates the use of much thicker films (>300 nm), during which the deposition conditions likely are not the same as during the deposition of ultra-thin films as a steady state is not reached at the target surface during such short deposition times. X-ray magnetic circular dichroism (XMCD) allows elemental specificity and relatively simple determination of the magnetism of the ion. It is also possible to fit the x-ray absorption spectroscopy (XAS) and XMCD data to determine the fraction of Fe^{2+}, and the amount of iron on each crystallographic site. The drawbacks to this method are that this is not possible to apply the same procedure for Tb^{4+} because the lifetime broadening is larger than any peak shift or broadening expected to be observed in XAS due to a different valence state in the rare-earth ions. The practical issues are that XMCD requires synchrotron radiation, for which beamtime proposals are extremely competitive. Once this data is obtained, it is rather non-trivial to fit the spectra and determine the occupancy and valence of the iron sublattices, but it can be completed[47,296].

These limitations in mind, it was attempted to incorporate off-stoichiometry, non-ideal site occupancies, and non-ideal valence states into the model. This model was translated from the original Fortran and implemented in Python, using common libraries and packages. First the case of off-stoichiometry (RE:Fe $\neq 0.6$) is considered. The primary assumptions are:

- The excess RE (Fe) is incorporated on to the octahedral (dodecahedral) sublattice as an antisite defect. This assumes there are no vacancies in the structure, and is based on the relatively similar size of the ionic radii of the heavier rare-earth ions and Fe^{3+}

- The site determines the MFCs acting on the ion that is in that site. For instance, a Tb^{3+} ion on an octahedral site is affected by the same coefficients as an Fe^{3+} on the octahedral site. No change is assumed in the MFCs.

This is put into practice by weighting the percentage of the octahedral (dodecahedral) site that is occupied by excess Tb (Fe). The only modifications are to the x_a and x_{ci} equations and to the calculation of the zero temperature moments, which is accomplished in the same manner via weighting the amount of each ion. The other results fall out through the existing mathematical framework.

The ability to account for non-ideal site occupancies are already built into the model, for most of the possible combinations. First, this allows the ability to evaluate if site-specific ion substitutions, such as Sc^{3+}, occupy the octahedral site exclusively, or if some fraction also occupy the dodecahedral and tetrahedral sites. Sc^{3+} is known to occupy only the octahedral site in bulk materials, but it has not yet been studied in single crystal thin films which are under a significant stress due to epitaxial lattice mismatch[287]. By keeping the amount of Sc^{3+} in the film constant, different amounts can be distributed to each of the three sublattices (treating it as a non-magnetic substitution on each sublattice) and then compared to experimental magnetometry to determine if the expected site occupancy accurately describes the data. The case of non-ideal site occupancy of an ideal stoichiometry film is not considered, for the reason that extensive antisite defects are believed unlikely to occur, else the garnet phase would likely not crystallize (or show secondary phases, which has not been observed) and the magnetometry would be far off of bulk values (which has likewise not been observed). This method requires no additional assumptions.

Finally, the ability to introduce non-ideal valence states is incorporated into the model. Several variations are considered, but the common assumptions are as follows:

- The system is charge neutral. This is accomplished via compensation through off-valence states of both cations (Tb^{4+} and Fe^{2+} vs. Tb^{3+} and Fe^{3+}) or via cation vacancies ($[Tb^{4+}] = 1/3[Fe^{3+}$ vacancies]).
- The molecular field coefficients are determined by the site, not the ion or valence state of the ion sitting on that particular site. Thus, the molecular field coefficients are not modified outside of the existing structure to account for nonmagnetic substitutions.

Specific cases regarding site occupancy of off-stoichiometric and off-valence state ions will be discussed in the next section. The assumptions of off-stoichiometry and non-ideal site occupancies discussed in the preceding paragraphs are applied here as well. To account for the different magnetization of the non-ideal valence states, the values of the total angular momentum (J) are updated accordingly according to Hund's rules (see Table 8.1).

Table 8.1: Table of S, L, and J values for possible cations present in the garnet structure. Note that angular momentum is quenched by the crystal field in transition metals, so Fe^{2+} has no orbital angular momentum.

Ion	S	L	J
Fe^{3+}	5/2	0	5/2
Fe^{2+}	2	0	2
Tb^{3+}	3	3	6
Tb^{4+}	7/2	0	7/2

The value of the total angular momentum has a significant effect on the temperature dependence of the magnetization, as described by the Brillouin function (see figure 8.3). Higher values of J lead to a more rapid decay in the magnetization of the ion. Note that the orbital angular momentum

of the transition metal is quenched by the crystal field, but it is not quenched for the rare-earth[44]. The effective value of Tb^{4+} is calculated using the same canting angle as with Tb^{3+}.

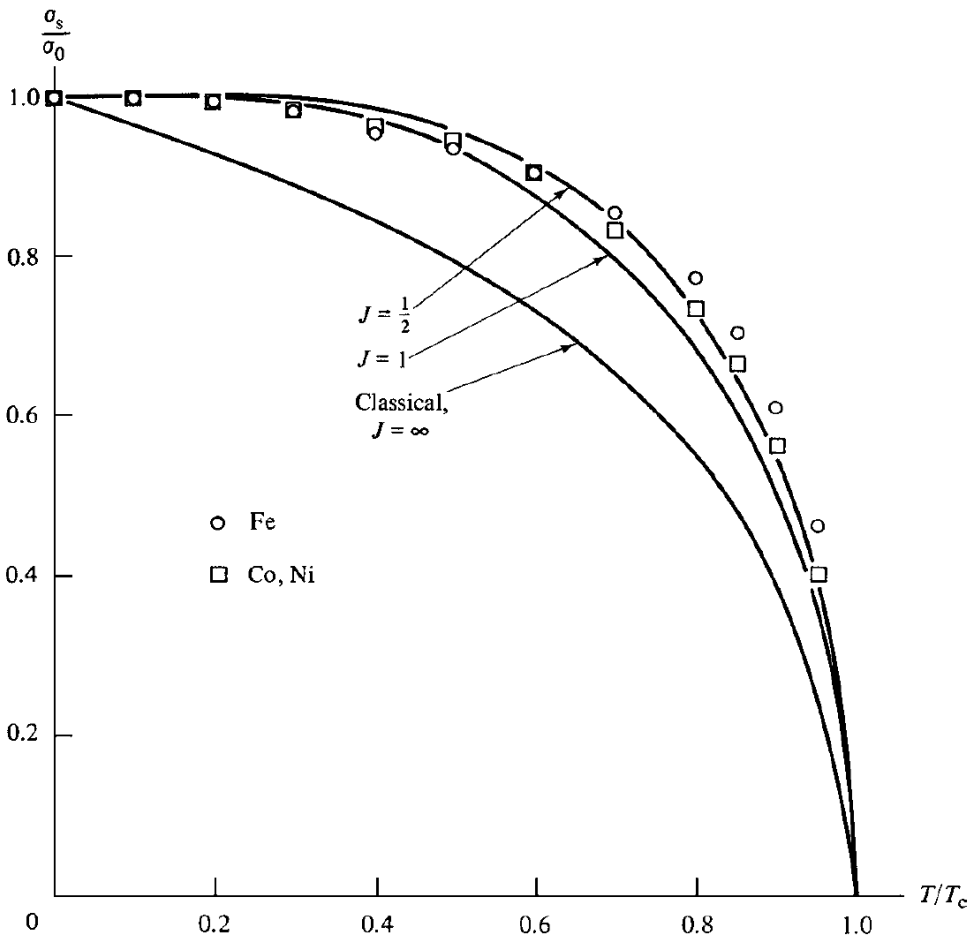

Figure 8.3: Plot of the normalized saturation magnetization as a function of the reduced temperature (T/T_{Curie}) for different values of the total angular momentum, J, according to the Brillouin function. Higher values of J lead to a more rapid decay in the saturation magnetization, until the classic limit (the Langevin function) is reached. From ref. 18. Used with permission.

8.3 Comparison with Substituted and Off-Stoichiometric TbIG

8.3.1 Varying Rare-Earth to Iron Ratio

The first attempt is to account for the compensation temperature discrepancy purely through off-stoichiometry. A plot of the compensation temperature of TbIG vs the rare-earth to iron ratio (RE:Fe) is shown in figure 8.4. As outlined in the previous section, the excess Fe (Tb) occupies the dodecahedral (octahedral) sublattice, with no vacancies in the structure. The compensation temperature varies linearly with RE:Fe, which is expected as the dodecahedral and octahedral

sublattices couple ferromagnetically. The data is over the maximum range possible with the model, before it fails to produce physically realistic results. The limits over the range are due to its basis on fitting experimental data, which experiences similar limitations over the amount of nonmagnetic substitutions that can be accommodated[162].

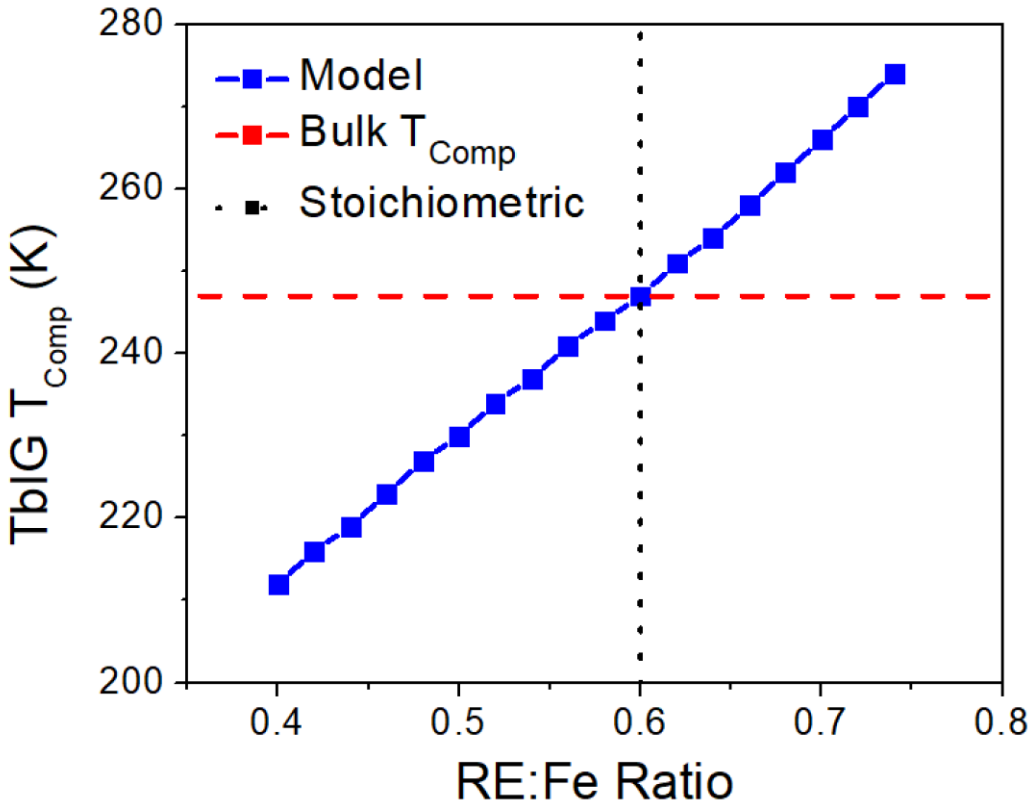

Figure 8.4: Plot of the compensation temperature of TbIG as a function of the RE:Fe ratio. The horizontal dashed line indicates the bulk value of T_{Comp} and the vertical dotted line indicates the ideal RE:Fe ratio of 0.6.

Comparing to experimental data from Rosenberg et al., who reported a RE:Fe ratio of 0.7 in TbIG/GGG films with a compensation temperature of 330 K, this model of the off-stoichiometry is able to partially describe the elevated compensation temperature, but is unable to fully account for the discrepancy[45]. Fakhrul et al. also reported non-ideal stoichiometries in TbIG and Bi-substituted TbIG (BiTbIG)[297]. These films were grown in a different PLD chamber under different conditions, and exhibited much smaller discrepancies from the bulk TbIG T_{Comp} of 247 K. The

results are summarized in Table 8.2. The BiTbIG has a much larger difference relative to the TbIG films, which is possibly related to the large size of the Bi^{3+} ion.

Table 8.2: Table of the experimental and predicted T_{Comp} for several TbIG and BiTbIG films with different RE:Fe ratios. (data from Fakhrul et al.[297])

Film	RE:Fe Ratio	Experimental T_{Comp} (K)	Predicted T_{Comp} (K)
TbIG	0.540	245	237
TbIG	0.570	253	243
TbIG	0.700	259	266
BiTbIG	0.673	230	254

In comparing the two sets of TbIG samples, the modifications made to model are capable of explaining some discrepancy in the compensation temperature from the bulk value. The predicted T_{Comp} is more accurate when the RE:Fe ratio is closer to the bulk value, indicating that more highly off-stoichiometric films have additional structural and magnetic irregularities that are not captured under this limited set of assumptions. Additional studies of the effect of off-stoichiometry would be of interest, as there have been other observations of non-bulk T_{Comp} values, such as in DyIG and TmIG[49,193].

8.3.2 Scandium Substituted TbIG and Non-Ideal Site Occupancies

The substitution of nonmagnetic ions into the rare-earth iron garnet system has been well studied in bulk powders and micron thick films used for bubble domain materials[38,287,291,298,299]. Several ions were identified that occupy exclusively one of the three crystallographic sites in the garnet structure, such as Sc^{3+} and Zr^{4+} on the octahedral sites and Si^{4+} on the tetrahedral sites[287,291]. For these site-specific substitution, the properties such as saturation magnetization and the compensation temperature varied in a predictable fashion for low to moderate substitution levels, allowing simple tuning of the properties to suit a particular application, commonly in

magnetoptics[254]. However, the effect of site-specific nonmagnetic ion substitution has not yet been studied in nanometer scale thin films, and the effects on spin transport have yet to be investigated.

The anomalous Hall effect-like spin Hall magnetoresistance (AHE) has been measured in a large number of garnet/Pt heterostructures, including Y-, Eu-, Tb-, Dy-, and Tm- iron garnet[45,50,187,193,226]. These measurements have found that the amplitude of the easy axis AHE resistivity is approximately the same, regardless of rare-earth ion present. The exact magnitude of the resistance measured is dependent on the shape of the Hall cross used and the interface between the garnet and Pt[300]. This implies that the AHE and other spin transport properties of the films are primarily related to the iron sublattices, not the net moment. Further evidence that it is not related to the net moment is that the AHE does not tend to zero at the magnetic compensation temperature as the net moment goes to zero, but does change sign at this temperature, when the iron sublattice associated with the net moment switches to the tetrahedral sublattice[45,49]. Some studies have posited that the reason for this is that the iron *3d* orbitals associated with the magnetism in the films are close to the Fermi energy, while the rare-earth *4f* orbitals are far below the Fermi energy and do not participate strongly in magnetotransport measurements[74].

To examine this, a target with the composition of $Tb_3Fe_{3.5}Sc_{1.5}O_{12}$ was synthesized from the binary oxides powders according to solid-oxide sintering methods[160]. This composition was selected as it is known to be close to the maximum amount of Sc^{3+} the garnet system can accommodate without the presence of secondary phases[40]. This large amount of Sc^{3+}, which occupies 1.5/2 of the octahedral sites, allows deposition of any intermediate composition in $Tb_3Fe_{5-x}Sc_xO_{12}$ for $0 \leq x \leq 1.5$ via codeposition with a stoichiometric TbIG target. A series of single crystal epitaxial thin

films were then grown with varying amounts of Sc^{3+}, and the structural, magnetic, and spin transport properties of the films were then measured[301]. This section will focus on the contribution of this author, which is related to the magnetometry modeling.

The experimentally determined stoichiometry (via WDS), room temperature magnetization, compensation temperature, and Curie temperature of the films are displayed in table 8.3. Also included in the table are the predicted values of the room temperature magnetization, T_{Comp}, and T_{Curie}. Note RE:Fe is the ratio of RE to the total Fe+Sc.

Table 8.3: Table of the experimental and predicted 300 K magnetization, compensation temperature, and Curie temperature for off-stoichiometric, Sc-substituted TbIG films. From ref.[301]

Stoichiometry	**Sample**	**Sc content (x/2)**	**RE:Fe Ratio**	**300 K Magnetization (kA/m)**	**T_{Comp} (K)**	**T_{Curie} (K)**
$Tb_{2.79}Fe_{5.21}O_{12}$	S1 – experiment	0	0.536	37	263	503
	S1 – model			31	236	537
$Tb_{2.84}Fe_{4.87}Sc_{0.29}O_{12}$	S2 – experiment	0.29	0.550	53	193	423
	S2 – model			51	206	497
$Tb_{2.90}Fe_{4.57}Sc_{0.53}O_{12}$	S3 – experiment	0.53	0.569	54	173	403
	S3 – model			59	195	460
$Tb_{2.83}Fe_{4.41}Sc_{0.76}O_{12}$	S4 – experiment	0.76	0.547	59	< 173	333
	S4 – model			74	171	435

The experimental magnetometry of the films scale as expected from the experiments on bulk material:

- Room temperature magnetization increases with Sc^{3+} content
- Compensation temperature decreases
- Curie temperature decreases

This is expected as the octahedral sublattice is exclusively substituted with nonmagnetic ions. T_{Comp} is lowered as the net magnetization of the dodecahedral and octahedral sublattices is reduced. The room temperature magnetization increases because the films are above T_{Comp}, and the magnetization of the non-dominant sublattices is reduced from the bulk value. Finally, T_{Curie} is depressed with Sc^{3+} substitution as the superexchange interactions are diluted with the presence of the nonmagnetic ion, allowing thermal energy to overcome the exchange energy at a lower temperature.

The model captures as all of these effects, which is unsurprising because it was empirically derived from substituted garnet data. The agreement with the experimental data is quite good for all but S4 for the room temperature magnetization values, which can at least partially be attributed to noise in the experimental data from the colossal paramagnetic background of the $Gd_3Ga_5O_{12}$ substrates. The compensation temperature exhibits slightly larger discrepancies, which may be partially attributed to noise, but this is not enough to account for the differences of more than roughly 10 degrees in some samples. The Curie temperature exhibits poor agreement for all but S1. There are a few reasons for this. The first is that the model was based on bulk data, and not nanometer scale thin films. Curie temperature depression relative to the bulk material has been observed in magnetic thin films[302]. The other factor is that in experimental magnetization vs. temperature curves, the magnetization approaches zero rather sharply, which is commonly approximated as $\sim\sqrt{T_{Curie} - T}$. However, the model approaches zero asymptotically (see figure 8.5), resulting in much higher predictions of T_{Curie}. It is possible to estimate values of the T_{Curie} by extrapolating the model data to approximate the sharp decrease in magnetization near the Curie

temperature, but these values are still far off of experimental values, indicating that a combination of these two factors likely leads to the discrepancy.

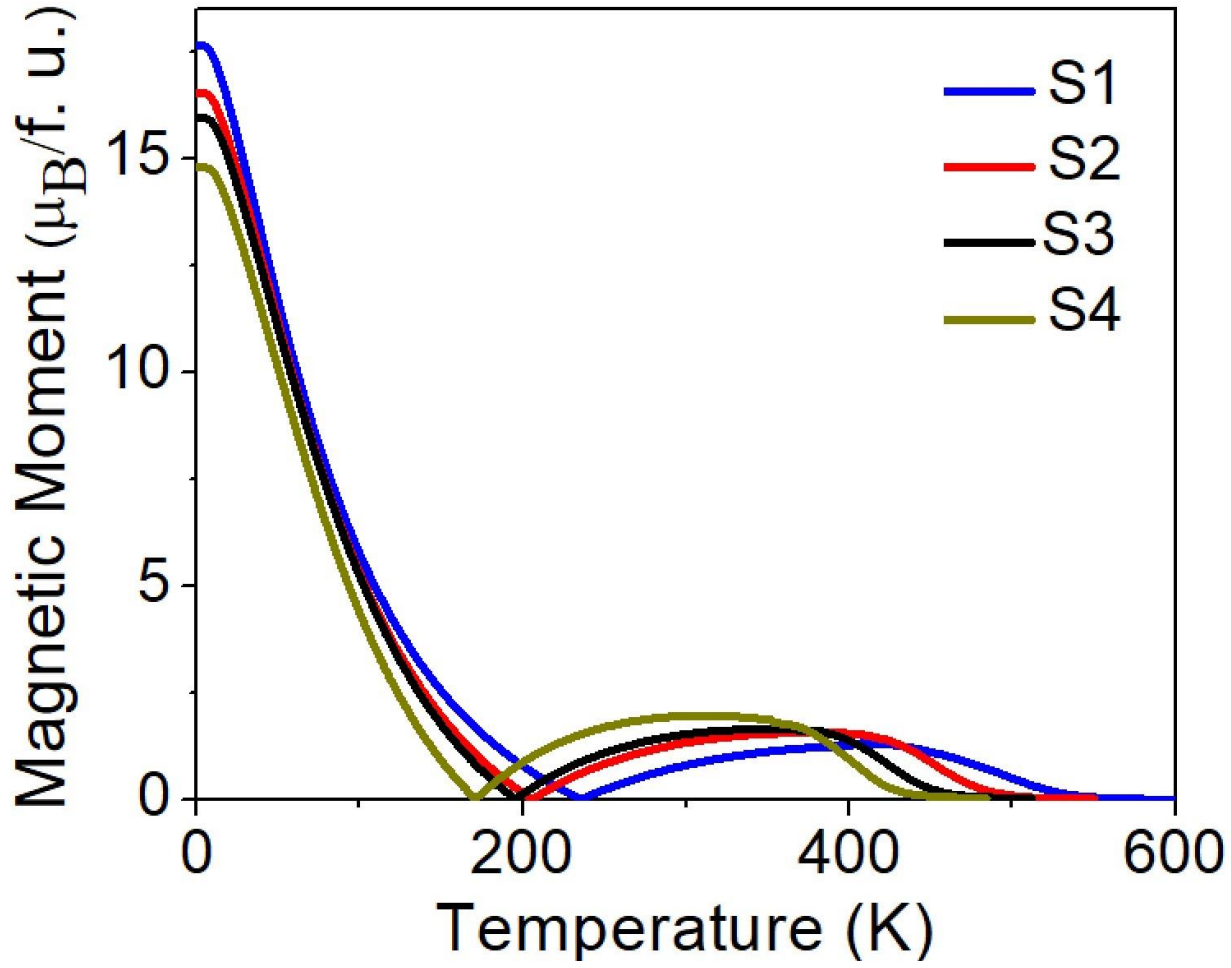

Figure 8.5: Plot of the magnetization versus temperature curves predicted via the molecular field coefficients model, accounting for non-ideal RE:Fe ratio and Sc^{3+} substitution (see table 8.3). Note that the magnetization approaches zero asymptotically, making accurate determination of the Curie difficult.

Despite these shortcomings in the model, there are still useful conclusions that can be drawn from this data. Using the existing framework, it is possible to model the substitution of a portion or all of the Sc^{3+} onto the dodecahedral or tetrahedral sublattices, instead of exclusively occupying the octahedral sublattice, as expected. However, when this was studied, the agreement with the experimental data became much worse. This is expected, as the depression in T_{Comp} requires the reduction in magnetization of the octahedral or dodecahedral sublattice (eliminating the tetrahedral sublattice as an option), and the amount of Tb^{3+} deficiency in the films indicates that only a small

amount of Sc^{3+} could be accommodated on the dodecahedral sublattice, which, if it occurs at all, would have a minimal effect on the magnetic properties under our set of assumptions. Thus, it is possible to concretely say that the Sc^{3+} occupies exclusively the octahedral site.

8.3.3 Non-Ideal Valence States

Garnet films grown by PLD in this group have exhibited non-ideal valence states in both Fe (Fe^{2+}) and the rare-earth ions (Tb^{4+} in particular)[296,297,301]. This is a complex problem to approach for several reasons. The first is that accurate determination of the composition is already difficult, with the most reliable technique in common use (WDS) requiring very thick films, which are not always practical to grow and whose properties differ somewhat from thinner films[297]. Additionally, quantification of the amount of each valence state is yet more complex. The most successful technique has been through the fitting of XAS and XMCD spectra[47]. This technique requires high quality XMCD spectra, only available from synchrotron facilities, and complex fitting methodology beyond the scope of this thesis. In summary, the off-stoichiometric garnets explored in this section are based on qualitative observations from shoulder peaks and features in XAS and XPS data, but from this we can draw some conclusions[296,301].

First, consider the case of non-ideal valence states in TbScIG. To ensure charge neutrality, it is assumed there is an equal amount of Fe^{2+} and Tb^{4+}. The next assumption is that the site distribution for the non-ideal valence ions is the same as that of ideal 3+ valence states. This is justified as under the previously defined framework iron (rare-earth) rich garnets have the excess species occupy the dodecahedral (octahedral) sites. As the Fe^{2+} (Tb^{4+}) ions are larger (smaller) than the 3+ valence of that species, they are no less likely to occupy the larger (smaller) non-ideal sites in

the garnet structure than the 3+ valence. The model is modified to accommodate this as described in the previous section.

Figure 8.6 plots the compensation temperature of the 4 compositions listed in table 8.3. The trend for all compositions is that increasing off-valence ions decrease the compensation temperature. This is unsurprising, because the value of the total angular momentum is lower for Fe^{2+}/Tb^{4+} than Fe^{3+}/Tb^{3+}, resulting in a depressed value of the total magnetization of the two sublattices that dominate the net moment below the compensation temperature. However, this does not improve the fit to the experimental data, as the experimental data is above (S1), below (S3) or in the range of (S2) predicted by the model. The films are grown under identical conditions where only the ratio of laser shots to each target is varied, so if there was a variation in the amount of off-valence ions one could expect this to vary monotonically with composition, or potentially be invariant. This model indicates that this is however not the case, and that the assumption of equal amounts of off-valence ions to provide charge balance does not improve the fit.

The next method to explore non-ideal valence states is to consider the possibility of vacancies in the crystal structure. Based on the work done by Rosenberg et al. in rare-earth rich TbIG, the films are known to have an excess of Tb and there is some amount of Tb^{4+} present in the films[45]. However, it is unclear if there is Fe^{2+} present in the system as the valence states of Fe cannot be resolved via XPS. It is possible there is only off-valence Tb, as Tb^{4+} is a stable half-filled $4f^7$ ion while Fe^{2+} is $3d^6$ vs. the half-full $3d^5$ for Fe^{3+}. Here we consider the situation of iron vacancies in the system that charge balance the Tb^{4+} according to the equation (Kröger-Vink notation):

$$3[\,Tb_{Tb}^{4+}\,] = [\,V_{Fe}^{3-}\,] \tag{8.17}$$

Where $[Tb_{Tb}^{4+}]$ is the concentration of Tb^{4+} ions and $[V_{Fe}^{3+}]$ is the concentration of Fe vacancies. For charge balance there is 1/3 the number of Fe^{3+} vacancies as there are Tb^{4+} ions per formula unit. There are three possible situations for Fe vacancies in the garnet structure: purely octahedral, purely tetrahedral, or some distribution between the two sites. The case of only octahedral and only tetrahedral vacancies are considered separately in figure 8.7.

The results of removing Fe through vacancies and charge balancing through Tb^{4+} is roughly as expected. First, consider octahedral vacancies. As the magnetization of the low temperature dominant sublattices are reduced, the compensation temperature decreases. The trend is not entirely linear, which is attributed to weakening of the intersublattice interactions at a faster rate than the dilution factors can account for because the total angular momentum of Tb^{4+} is lower than that of Tb^{3+}. For the case of purely tetrahedral vacancies, the compensation temperature increases for the same reason (reduction of the moment of the high temperature dominant sublattice). Interestingly, the change is larger than that of the octahedral vacancies and the curvature of the data is more pronounced. The reason for this is not immediately apparent, but could be due to the stronger coupling between the tetrahedral and dodecahedral sublattices[260]. For larger values of x (x = Fe vacancies and 3x = Tb^{4+} per formula unit), the compensation temperature is close to that reported by Rosenberg et al, but the rare-earth to iron ratio does not match reported XPS measurements, indicating that this is not a complete explanation of the difference[45].

8.3.4 Explanation of the Observed Magnetic Compensation Temperature in Rare-Earth Rich TbIG Films

As discussed previously, TbIG films grown by our group reported by Rosenberg et al. have demonstrated magnetic compensation temperatures of ~330 K, 80 K higher than bulk[45,48]. These

films were also highly off-stoichiometric, with a RE:Fe ratio of 0.7, as measured by XPS, and contained a significant amount of Tb^{4+} (see figure 8.2). To this point, we have attempted to account for this difference via off-stoichiometry, non-ideal valence states, and purely octahedral or purely tetrahedral vacancies, none of which provide a sufficient explanation for the discrepancy.

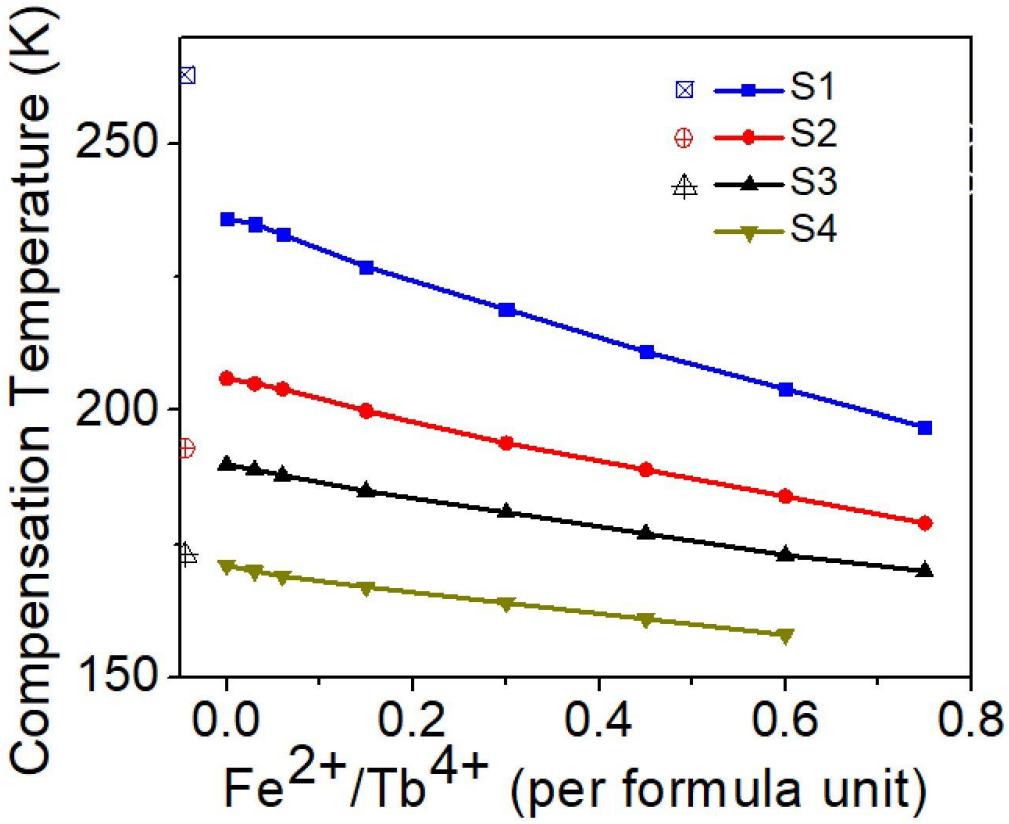

Figure 8.6: Compensation temperature of TbIG films with different amounts of Fe^{2+}/Tb^{4+} per formula unit. Experimental data (detailed in Table 8.3) is indicated by the open symbols.

To resolve this issue, Rosenberg et al. measured XMCD on the Fe L_3 edge which was then fit to determine the fraction of Fe^{3+}_{oct}, Fe^{3+}_{tet}, and Fe^{2+}_{oct} [296]. The results on thin films indicated that there was less than 5% Fe^{2+} present, and the ratio of Fe_{oct}:Fe_{tet} was very nearly 2:3, the ideal value. Repeating the same experiment on a sample of bulk TbIG powder also produced almost the exact same ratio. Rietveld analysis on bulk TbIG XRD also confirmed this ideal 2:3 ratio of octahedral to tetrahedral Fe[296].

This information in hand, we can draw some new conclusions. The first is that as the ratio of octahedral to tetrahedral Fe is the same as bulk and is now known, the two sublattices are modified in the same manner. In other words, because the ratio of octahedral to tetrahedral sites is the same as bulk then the amount of vacancies and/or antisite Tb defects is fixed between the two sublattices, reducing the number of unknowns. Second, as there is known to be excess Tb in the films (RE:Fe = 0.7, bulk is 0.6), the excess Tb must be occupying the octahedral lattice sites, offsetting some of the required octahedral Fe vacancies.

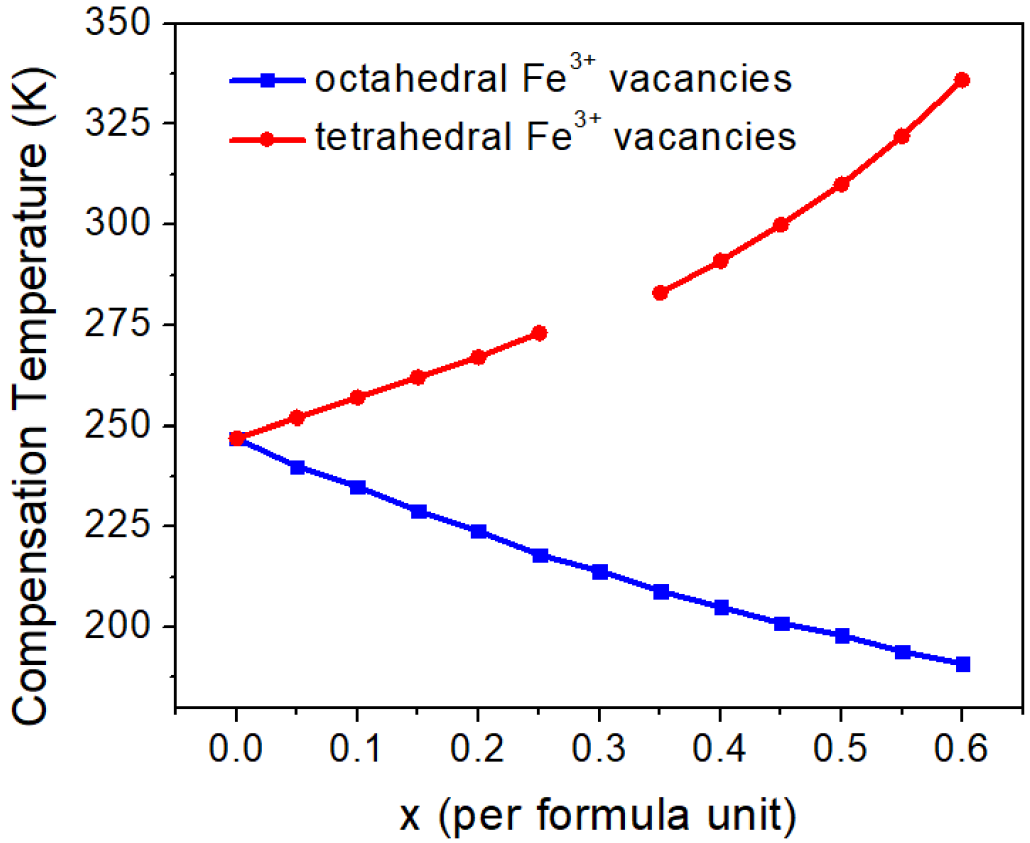

Figure 8.7: Compensation temperature of TbIG as a function of Fe vacancies (x per formula unit) and Tb^{4+} ions (3x per formula unit) for purely octahedral and purely tetrahedral vacancies.

Using these results, the molecular field coefficient model can be used to estimate the M vs. T behavior under these new restrictions. Fe can be systematically removed from the octahedral and

tetrahedral sublattices in the ratio of 2:3, respectively. This is accommodated in the model by treating the vacancies as non-magnetic ions, assuming that the molecular field coefficients are unchanged. Next, a portion of the octahedral iron vacancies can be occupied by excess Tb. By varying the fraction of octahedral iron vacancies that are occupied by Tb, the RE:Fe ratio and compensation temperature can be modified with an additional parameter to try and match the two experimental values. The results of these assumptions are plotted in figure 8.8.

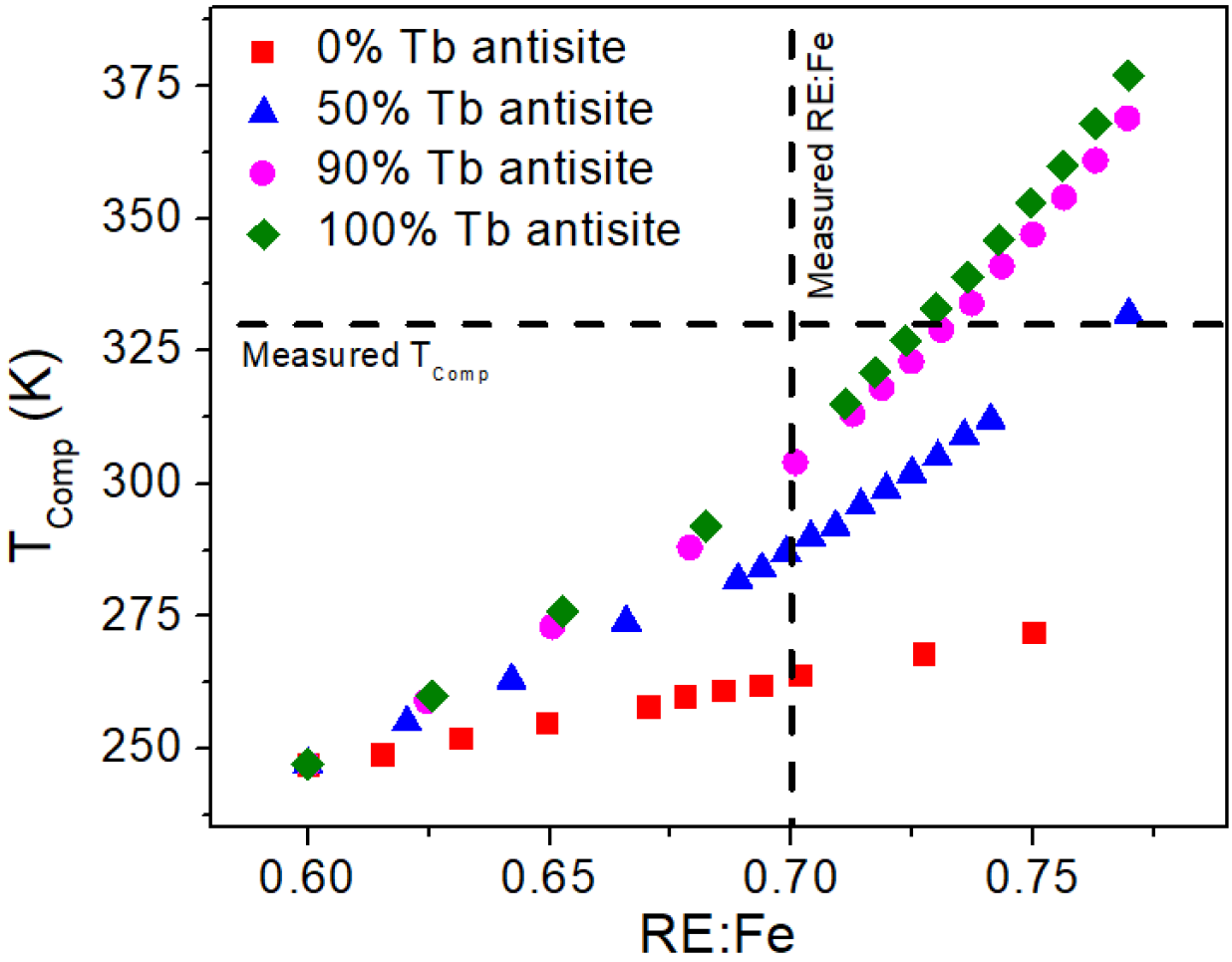

Figure 8.8: Plot of compensation temperature vs. RE:Fe ratio for TbIG. The ratio of octahedral:tetrahedral Fe is constant. For higher RE:Fe, more vacancies are introduced onto the Fe sublattices, in the ratio 2:3 (oct:tet). A fraction of the octahedral vacancies are occupied by excess Tb as antisite defects. The horizontal and vertical dashed lines correspond to the experimental T_{Comp} and RE:Fe, respectively.

Using this model, it is possible to reproduce the experimentally observed composition and magnetic compensation temperature within experimental error of the two parameters. The results indicate that nearly all of the octahedral Fe vacancies are replaced by excess Tb ions[296]. The most interesting aspect is that the ratio of octahedral to tetrahedral Fe remains unchanged, which explains the shortcomings of previous attempts to quantify the discrepancy. Any further improvement in the model will require the addition of Tb^{4+} ions and the determination of their distribution across the dodecahedral and octahedral sites.

One additional point that should be made is that the canting of the rare-earth ion moment in the dodecahedral sites is significant in the garnets[260]. An aspect that is not possible to account for using this model is that the canting is different when an antisite rare-earth ion is on an octahedral site, where the crystalline electric field is presumably stronger due to the smaller size of the site. This would result in a larger moment of the rare-earth ion when located on an octahedral site vs. a dodecahedral site, requiring a smaller amount of excess rare-earth to explain a discrepancy in compensation temperature. The canting angles reported by Dionne are determined empirically; a first principles density functional theory of the behavior of the rare-earth moments could possibly determine how the canting varies with crystallographic site.

In the larger context of the valence states present and the known presence of vacancies, these results also support the conclusions made. Fakhrul et al. recently reported that there is far more Tb^{4+} in TbIG thin films than has been previously described, in some cases more than 50% of the total Tb[297]. The smaller Tb^{4+} ion likely occupies a fraction the octahedral vacancies as anti-site defects. As most or all of the octahedral vacancies are occupied by Tb antisite defects, the

octahedral sublattice is nearly full. The vacancies in the system are then primarily confined to the tetrahedral sublattice, which intuitively makes sense as the vacancies should prefer to occupy the smallest site (or, rather the cations prefer to occupy the larger sites).

Concluding, it is possible to study a wide variety of non-ideal garnets via the modified molecular field coefficients model developed here. Reasonable agreement is achieved for low levels of off-stoichiometry in TbIG and BiTbIG and substitution of diamagnetic ions in TbScIG. A comprehensive understanding of the effects of off-stoichiometry and non-ideal valence states in the garnet system is still lacking. This is complicated by the difficulty in precisely measuring and controlling the stoichiometry of these films, in addition to the expertise and experimental facilities needed to collect and fit XMCD spectra, which is the most precise way to obtain site occupancy information in these systems. However, based on the work shown here it is possible to make some assertions as to the magnitude of the effects of off-stoichiometry, non-ideal valence states, and vacancies in the system. In reality, a combination of these factors is likely present in all garnet films. Further work is needed in this exciting area.

9. Conclusion

9.1 Summary and Conclusions

Rare-earth iron garnets have the potential to advance the development of spintronic devices, which promise to improve energy efficiency and computational power. The ability to modulate the properties of thin films through the choice of rare-earth ion and substrate make these materials very well-suited to the demands of modern devices.

In chapter 4, the first report of perpendicular magnetic anisotropy and spin transport in polycrystalline rare-earth iron garnets is presented. The anisotropy in the system is controlled via thermal expansion mismatch with the substrate, and the choice of EuIG which has the same sign for both magnetostriction coefficients results in anisotropy that is easily understood through a simple uniaxial anisotropy model. This allows use of non-garnet substrates (provided the correct strain state is supplied). The spin transport measurements report nearly identical results to that of single crystal materials, indicating that the presence of grain boundaries and different crystallographic orientations do not affect the spintronic properties significantly.

In chapter 5, the work on polycrystalline garnets with PMA is extended to Si substrates using DyIG. DyIG offers numerous benefits over EuIG, in that the anisotropy is higher (due to both the higher thermal expansion mismatch and larger magnitude of the magnetostriction coefficients) and the presence of a magnetic compensation temperature in DyIG. A discrepancy from the bulk value of the compensation temperature in epitaxial DyIG films is reported. Very large grain sizes are discovered in DyIG/Si films, on the order of 10 μm in diameter in 40 nm thick films. PNR measurements indicate constant density and magnetization profiles through the thickness of

polycrystalline and epitaxial films, with small interfacial regions with the substrates and negligible magnetic dead layers. Similar to polycrystalline EuIG, the spin transport properties of polycrystalline garnet films are comparable to all other epitaxial garnet films measured.

In chapter 6, the magnetic proximity effect in HM/DyIG heterostructures is examined via PNR and XMCD. It was discovered that the MPE couples to the net magnetic moment of the system, in contrast to rare-earth transition metal/Pt bilayers in which the MPE tracks the magnetic moment of the transition metal sublattice. This indicates a fundamentally different mechanism of the MPE in heavy metals in contact with magnetic insulators and metallic ferromagnets. In metallic systems, the MPE is likely related to RKKY interactions with the conduction *d* electrons, whereas insulating systems require the interactions to be through a superexchange-type interaction. Additionally, the importance of a sharp, contamination free interface in garnet/metal heterostructures is examined.

In chapter 7, we report the first ultrathin polycrystalline garnet films. Magnetic layers less than 10 nm thick are necessary for manipulation with highly efficient spin orbit torques. This is achieved on Si substrates via a novel heterostructure that makes use of a paramagnetic GGG seedlayer which templates the growth of the upper ferrimagnetic layer DyIG, with a Pt diffusion barrier inserted between to prevent interdiffusion and subsequent deterioration of the magnetic properties.

In chapter 8, the molecular field coefficient developed by Dionne and others is expanded to include non-idealities observed in our garnet films. The expanded model can account for off-

stoichiometry, non-ideal site occupancy, vacancies, and non-ideal valence states. This is compared to experimental data on off-stoichiometric TbIG and Bi-TbIG, Sc-substituted TbIG, and TbIG featuring a compensation temperature 80 K higher than the bulk value. The success of the model in explaining these discrepancies indicates that a large variety of previously unknown and unexplored non-idealities are existent in the garnet structure. While the garnet system is very robust and easy to grow, this highlights that there may be a large deviation from the structural perfection assumed in previous works.

9.2 Future Work and Outlook

The next steps for this project are to the refine the growth process for ultrathin polycrystalline garnets. Further optimization of the composition, layer thicknesses, and processing temperatures should improve the crystalline quality and magnetic properties. Then, patterning devices to measure the spin Hall magnetoresistance and perform spin-orbit torque switching measurements should be conducted to compare switching efficiency with metallic ferromagnets grown directly on Si. The results of this study will provide an indication of the long-term feasibility for these materials as candidates for future memory technologies and commercialization. Further exploration of methods to grow ultrathin garnet films on non-garnet substrates, such as strongly textured Pt, will also be prudent.

With the increasing computational power at researcher's disposal, additional first principles calculations on the very large unit cell of garnets would be of interest. In particular, calculation of the band structure and density of states for HM/garnet bilayers would be helpful in identifying the coupling of the proximity effect to different magnetic species and the strength of this interaction. Further studies on the integration of garnets with novel materials such as topological insulators

and graphene are also encouraged. As the garnets provide many benefits over metallic magnets, the study of emergent physical phenomena is assisted by the insulating nature, low magnetic damping, and dynamic behavior in the vicinity of the magnetic and angular momentum compensation temperatures.

The end of Moore's law and the scaling of modern microelectronics has long been predicted but is yet to arrive. The unrelenting drive towards higher performance, greater efficiency, and smaller sizes has resulted in tremendous advances in materials development and processing. As this envelope continues to be pushed, the expansion into different materials ecosystems can only be a benefit. Insulating magnetic materials, rare-earth iron garnets in particular, offer a series of benefits that are difficult to achieve in other systems, and further development will improve the compatibility with existing technology. Spintronics are slowly making their way into mainstream microelectronics, and the incorporation of new materials as they mature will allow for improved efficiency and device performance. As the world becomes more reliant on digital devices, improvements to existing technology, which more now than ever comes from improvements to materials, is a requirement for continued progress.

References

1. Agency, I. E. *Data Centres and Data Tranmission Networks*. (2020).
2. Shehabi, A. *et al. United States Data Center Energy Usage Report*. *Lawrence Berkeley National Laboratory* (2016). doi:LBNL-1005775
3. Masanet, E., Shehabi, A., Lei, N., Smith, S. & Koomey, J. Recalibrating global data center energy-use estimates. *Science (80-.).* **367**, 984–986 (2020).
4. Apalkov, D., Dieny, B. & Slaughter, J. M. Magnetoresistive Random Access Memory. *Proc. IEEE* **104**, 1796–1830 (2016).
5. Wolf, S. A. *et al.* Spintronics: A spin-based electronics vision for the future. *Science (80-.).* **294**, 1488–1495 (2001).
6. Vélez, S. *et al.* High-speed domain wall racetracks in a magnetic insulator. *Nat. Commun.* **10**, 4750 (2019).
7. Luo, Z. *et al.* Current-driven magnetic domain-wall logic. *Nature* **579**, 214–218 (2020).
8. Avci, C. O. *et al.* Current-induced switching in a magnetic insulator. *Nat. Mater.* **16**, 309–314 (2017).
9. O'Handley, R. C. *Modern Magnetic Materials: Principles and Applications*. (John Wiley & Sons, Inc., 2000).
10. Quarterman, P. *et al.* Demonstration of Ru as the 4th ferromagnetic element at room temperature. *Nat. Commun.* **9**, 2058 (2018).
11. Heisenberg, W. Mehrkörperproblem und Resonanz in der Quantenmechanik. *Zeitschrift für Phys.* **38**, 411–426 (1926).
12. Blundell, S. *Magnetism in Condensed Matter*. (Oxford University Press, 2001).
13. Dirac, P. A. M. On the theory of quantum mechanics. *Proc. R. Soc. London. Ser. A, Contain. Pap. a Math. Phys. Character* **112**, 661–677 (1926).
14. Pauli, W. Über den Zusammenhang des Abschlusses der Elektronengruppen im Atom mit der Komplexstruktur der Spektren. *Zeitschrift für Phys.* **31**, 765–783 (1925).
15. Ruderman, M. A. & Kittel, C. Indirect exchange coupling of nuclear magnetic moments by conduction electrons. *Phys. Rev.* **96**, 99–102 (1954).
16. Kasuya, T. A Theory of Metallic Ferro- and Antiferromagnetism on Zener's Model. *Prog. Theor. Phys.* **16**, 45–57 (1956).
17. Yosida, K. Magnetic properties of Cu-Mn alloys. *Phys. Rev.* **106**, 893–898 (1957).
18. Cullity, B. D. & Graham, C. D. *Introduction to Magnetic Materials*. (John Wiley & Sons, Inc., 2009).
19. Media, N. The Nobel Prize in Physics 1970. *NobelPrize.org* (2021).
20. Wadley, P. *et al.* Spintronics: Electrical switching of an antiferromagnet. *Science (80-.).* **351**, 587–590 (2016).
21. Olejník, K. *et al.* Terahertz electrical writing speed in an antiferromagnetic memory. *Sci. Adv.* **4**, eaar3566 (2018).
22. Cai, K. *et al.* Ultrafast and energy-efficient spin–orbit torque switching in compensated ferrimagnets. *Nat. Electron.* (2020). doi:10.1038/s41928-019-0345-8
23. Pauthenet, R. Magnetic Properties of the Rare Earth Garnets. *J. Appl. Phys.* **30**, S290–S292 (1959).
24. Geller, S. & Gilleo, M. A. Structure and ferrimagnetism of yttrium and rare-earth–iron garnets. *Acta Crystallogr.* **10**, 239–239 (1957).
25. Stanciu, C. D. *et al.* Ultrafast spin dynamics across compensation points in ferrimagnetic

GdFeCo: The role of angular momentum compensation. *Phys. Rev. B - Condens. Matter Mater. Phys.* **73**, 220402(R) (2006).
26. Chang, H. *et al.* Nanometer-Thick Yttrium Iron Garnet Films with Extremely Low Damping. *IEEE Magn. Lett.* **5**, 6700104 (2014).
27. Je, S. G. *et al.* Spin-orbit torque-induced switching in ferrimagnetic alloys: Experiments and modeling. *Appl. Phys. Lett.* **112**, 062401 (2018).
28. Narayanapillai, K. *et al.* Spin-transfer versus spin-orbit torque MRAM. *Proc. - Int. Nanoelectron. Conf. INEC* **2016-Octob**, 1–2 (2016).
29. Slonczewski, J. C. Origin of magnetic anisotropy in cobalt-substituted magnetite. *Phys. Rev.* **110**, 1341–1348 (1958).
30. Akulov, N. S. On the applications of the law of ferromagnetic anisotropy for calculation of the properties of polycrystalline iron. *Z. Phys.* **66**, 533–542 (1930).
31. Vladimirsky, K. V. No Title. *Compt. Rend. Acad. Sci. URSS* **41**, 10 (1943).
32. Callen, H. B. & Goldberg, N. Magnetostriction of polycrystalline aggregates. *J. Appl. Phys.* **36**, 976–977 (1965).
33. Bauer, J. J., Rosenberg, E. R. & Ross, C. A. Perpendicular magnetic anisotropy and spin mixing conductance in polycrystalline europium iron garnet thin films. *Appl. Phys. Lett.* **114**, 052403 (2019).
34. Lee, E. W. Magnetostriction and magnetomechanical effects. *Reports Prog. Phys.* **18**, 184–229 (1955).
35. Curry, K. C. Industrial Garnet. *Min. Eng.* **72**, 59–61 (2020).
36. Pfenninger, R., Struzik, M., Garbayo, I., Stilp, E. & Rupp, J. L. M. A low ride on processing temperature for fast lithium conduction in garnet solid-state battery films. *Nat. Energy* **4**, 475–483 (2019).
37. Laverov, N. P. *et al.* Synthetic minerals with the pyrochlore and garnet structures for immobilization of actinide-containing Wastes. *Geochemistry Int.* **48**, 1–14 (2010).
38. Van Uitert, L. G. *et al.* Control of bubble domain properties in garnets. *Mater. Res. Bull.* **6**, 1185–1200 (1971).
39. Kajiwara, Y. *et al.* Transmission of electrical signals by spin-wave interconversion in a magnetic insulator. *Nature* **464**, 262–266 (2010).
40. Gilleo, M. A. A. & Geller, S. Substitution for Iron in Ferrimagnetic Yttrium-Iron Garnet. *J. Appl. Phys.* **29**, 380–381 (1958).
41. Espinosa, G. P. Crystal chemical study of the rare-earth iron garnets. *J. Chem. Phys.* **37**, 2344–2347 (1962).
42. Nakamoto, R., Xu, B., Xu, C., Xu, H. & Bellaiche, L. Properties of rare-earth iron garnets from first principles. *Phys. Rev. B* **95**, 024434 (2017).
43. Geller, S. The Statistics of Superexchange Interaction and Ionic Distribution in Substituted Ferrimagnetic Rare Earth Iron Garnets. *J. Phys. Chem. Solids* **16**, 21–29 (1960).
44. Vasili, H. B. *et al.* Direct observation of multivalent states and 4f→3d charge transfer in Ce-doped yttrium iron garnet thin films. *Phys. Rev. B* **96**, 014433 (2017).
45. Rosenberg, E. R. *et al.* Magnetism and spin transport in rare-earth-rich epitaxial terbium and europium iron garnet films. *Phys. Rev. Mater.* **2**, 094405 (2018).
46. Avci, C. O. *et al.* Interface-driven chiral magnetism and current-driven domain walls in insulating magnetic garnets. *Nat. Nanotechnol.* (2019). doi:10.1038/s41565-019-0421-2
47. Caretta, L. *et al.* Interfacial Dzyaloshinskii-Moriya interaction arising from rare-earth orbital magnetism in insulating magnetic oxides. *Nat. Commun.* **11**, 1090 (2020).

48. Geller, S., Remeika, J. P., Sherwood, R. C., Williams, H. J. & Espinosa, G. P. Magnetic study of the heavier rare earth iron garnets. *Phys. Rev.* **137**, 1034–1038 (1965).
49. Shao, Q. *et al.* Exploring interfacial exchange coupling and sublattice effect in heavy metal/ferrimagnetic insulator heterostructures using Hall measurements, x-ray magnetic circular dichroism, and neutron reflectometry. *Phys. Rev. B* **99**, 104401 (2019).
50. Quindeau, A. *et al.* Tm3Fe5O12/Pt Heterostructures with Perpendicular Magnetic Anisotropy for Spintronic Applications. *Adv. Electron. Mater.* **3**, 1600376 (2017).
51. Geller, S., Williams, H. J., Sherwood, R. C., Remeika, J. P. & Espinosa, G. P. Magnetic study of the lighter rare-earth ions in the iron garnets. *Phys. Rev.* **131**, 1080–1082 (1963).
52. Kim, K. *et al.* Fast domain wall motion in the vicinity of the angular momentum compensation temperature of ferrimagnets. *Nat. Mater.* **16**, 1187–1192 (2017).
53. Caretta, L. *et al.* Fast current-driven domain walls and small skyrmions in a compensated ferrimagnet. *Nat. Nanotechnol.* **13**, 1154–1160 (2018).
54. Siddiqui, S. A., Han, J., Finley, J. T., Ross, C. A. & Liu, L. Current-Induced Domain Wall Motion in a Compensated Ferrimagnet. *Phys. Rev. Lett.* **121**, 057701 (2018).
55. Randoshkin, V. V. Magneto-Optical Garnet Films With High G-Factor. *Electro-Optic Magneto-Optic Mater. Appl.* **1126**, 103 (1989).
56. Randoshkin, V. V, Polezhaev, V. A., Sysoev, N. N. & Sazhin, Y. N. Dynamics of domain walls in bismuth-ytterbium-containing garnet ferrite films in the vicinity of the angular momentum compensation point. *Phys. Solid State* **45**, 513–518 (2003).
57. Krishnan, K. M. *Fundamentals and Applications of Magnetic Materials*. (Oxford University Press, 2016).
58. Janak, J. F. Uniform susceptibilities of metallic elements. *Phys. Rev. B* **16**, 255–262 (1977).
59. Hauser, J. J. Magnetic Proximity Effect. *Phys. Rev.* **187**, 580–583 (1969).
60. Wilhelm, F. *et al.* Systematics of the induced magnetic moments in 5d layers and the violation of the third hund's rule. *Phys. Rev. Lett.* **87**, 207202 (2001).
61. Moskaltsova, A., Krieft, J., Graulich, D., Matalla-Wagner, T. & Kuschel, T. Impact of the magnetic proximity effect in Pt on the total magnetic moment of Pt/Co/Ta trilayers studied by X-ray resonant magnetic reflectivity. *AIP Adv.* **10**, 015154 (2020).
62. Lang, M. *et al.* Proximity induced high-temperature magnetic order in topological insulator - Ferrimagnetic insulator heterostructure. *Nano Lett.* **14**, 3459–3465 (2014).
63. Wang, Z., Tang, C., Sachs, R., Barlas, Y. & Shi, J. Proximity-induced ferromagnetism in graphene revealed by the anomalous hall effect. *Phys. Rev. Lett.* **114**, 016603 (2015).
64. Dreyfus, B., Maynard, R. & Quattropani, A. Long-Range Magnetic Coupling in Metals. *Phys. Rev. Lett.* **13**, 342–343 (1964).
65. Bruyère, J. C. *et al.* Coupling effect between the magnetizations of two thin layers separated by a thin nonmagnetic metallic layer. *J. Appl. Phys.* **36**, 944–945 (1965).
66. White, R. M. & Friedman, D. J. Theory of the magnetic proximity effect. *J. Magn. Magn. Mater.* **49**, 117–123 (1985).
67. Huang, S. Y. *et al.* Transport magnetic proximity effects in platinum. *Phys. Rev. Lett.* **109**, 107204 (2012).
68. Kikkawa, T. *et al.* Interfacial ferromagnetism and atomic structures in high-temperature grown Fe3O4/Pt/Fe3O4 epitaxial trilayers. *J. Appl. Phys.* **126**, 143903 (2019).
69. Li, M. *et al.* Magnetic proximity effect and interlayer exchange coupling of ferromagnetic/topological insulator/ferromagnetic trilayer. *Phys. Rev. B* **91**, 014427 (2015).
70. Amamou, W. *et al.* Magnetic proximity effect in Pt/CoFe2 O4 bilayers. *Phys. Rev. Mater.*

2, 011401(R) (2018).
71. Liang, X. *et al.* Influence of Interface Structure on Magnetic Proximity Effect in Pt/Y3Fe5O12 Heterostructures. *ACS Appl. Mater. Interfaces* **8**, 8175–8183 (2016).
72. Hallal, A., Ibrahim, F., Yang, H., Roche, S. & Chshiev, M. Tailoring magnetic insulator proximity effects in graphene: First-principles calculations. *2D Mater.* **4**, 025074 (2017).
73. Goering, E., Gold, S. & Schütz, G. HoFe - Garnet soft XMCD measurements below and above the compensation temperature. *J. Synchrotron Radiat.* **8**, 422–424 (2001).
74. Binder, M. *et al.* Magnetization dynamics of the ferrimagnet CoGd near the compensation of magnetization and angular momentum. *Phys. Rev. B - Condens. Matter Mater. Phys.* **74**, 1–5 (2006).
75. Swindells, C. *et al.* Proximity-induced magnetism in Pt layered with rare-earth–transition-metal ferrimagnetic alloys. *Phys. Rev. Res.* **2**, 033280 (2020).
76. Wilhelm, F. *et al.* Layer-resolved magnetic moments in Ni/Pt multilayers. *Phys. Rev. Lett.* **85**, 413–416 (2000).
77. Poulopoulos, P. *et al.* X-ray magnetic circular dichroic magnetometry on Ni/Pt multilayers. *J. Appl. Phys.* **89**, 3874–3879 (2001).
78. Suzuki, M. *et al.* Depth profile of spin and orbital magnetic moments in a subnanometer Pt film on Co. *Phys. Rev. B - Condens. Matter Mater. Phys.* **72**, 054430 (2005).
79. Ruegg, S. *et al.* Spin-dependent x-ray absorption in Co / Pt multilayers and Co 50 Pt 50 alloy. *J. Appl. Phys.* **69**, 5665–5657 (1991).
80. Vogel, J., Fontaine, A., Cros, V. & Petroff, F. Structure and magnetism of Pd in Pd/Fe multilayers studied by x-ray magnetic circular dichroism at the Pdsedges. *Phys. Rev. B - Condens. Matter Mater. Phys.* **55**, 3663–3669 (1997).
81. Katmis, F. *et al.* A higherature ferromagnetic topological insulating phase by proximity coupling. *Nature* **533**, 513–516 (2016).
82. Mogi, M. *et al.* Large Anomalous Hall Effect in Topological Insulators with Proximitized Ferromagnetic Insulators. *Phys. Rev. Lett.* **123**, 16804 (2019).
83. Yang, H. *et al.* Significant Dzyaloshinskii–Moriya interaction at graphene–ferromagnet interfaces due to the Rashba effect. *Nat. Mater.* 1–5 (2018). doi:10.1038/s41563-018-0079-4
84. Rowan-Robinson, R. M. *et al.* The interfacial nature of proximity-induced magnetism and the Dzyaloshinskii-Moriya interaction at the Pt/Co interface. *Sci. Rep.* **7**, 16835 (2017).
85. Ramaswamy, R. *et al.* Spin orbit torque driven magnetization switching with sputtered Bi2Se3 spin current source. *J. Phys. D. Appl. Phys.* **52**, 224001 (2019).
86. Moore, G. M. Cramming more components onto integrated circuits With unit cost. *Electronics* **38**, 114 (1965).
87. Zutic, I., Fabian, J. & Sarma, S. D. Spintronics: Fundamentals and applications. *2Reviews Mod. Phys.* **76**, 323–410 (2004).
88. Hirohata, A. *et al.* Review on spintronics: Principles and device applications. *J. Magn. Magn. Mater.* **509**, 166711 (2020).
89. Mott, N. F. *Electrons in transition metals*. *Advances in Physics* **13**, (1964).
90. Fert, A. & Campbell, I. A. Two-current conduction in nickel. *Phys. Rev. Lett.* **21**, 1190–1192 (1968).
91. Chappert, C., Fert, A. & Van Dau, F. N. The emergence of spin electronics in data storage. *Nat. Mater.* **6**, 813–823 (2007).
92. Baibich, M. N. *et al.* Giant magnetoresistance of (001)Fe/(001)Cr magnetic superlattices.

Phys. Rev. Lett. **61**, 2472–2475 (1988).
93. Endoh, T., Koike, H., Ikeda, S., Hanyu, T. & Ohno, H. An Overview of Nonvolatile Emerging Memories-Spintronics for Working Memories. *IEEE J. Sel. Top. Circuits Syst.* **6**, 109–119 (2016).
94. Meena, J. S., Sze, S. M., Chand, U. & Tseng, T. Y. Overview of emerging nonvolatile memory technologies. *Nanoscale Res. Lett.* **9**, 526 (2014).
95. Sbiaa, R. & Piramanayagam, S. N. Recent Developments in Spin Transfer Torque MRAM. *Phys. Status Solidi - Rapid Res. Lett.* **11**, 1700163 (2017).
96. Kittl, J. A. *et al.* High-k dielectrics for future generation memory devices (Invited Paper). *Microelectron. Eng.* **86**, 1789–1795 (2009).
97. Apalkov, D., Dieny, B. & Slaughter, J. M. Magnetoresistive random access memories. *Proc. IEEE* **104**, 1796–1830 (2016).
98. Bhatti, S. *et al.* Spintronics based random access memory: a review. *Mater. Today* **20**, 530–548 (2019).
99. Ikeda, S. *et al.* A perpendicular-anisotropy CoFeB-MgO magnetic tunnel junction. *Nat. Mater.* **9**, 721–724 (2010).
100. H. Yamada *et al.* Engineered Interface of Magnetic Oxides. *Science (80-.).* **305**, 646–648 (2004).
101. Behin-Aein, B., Datta, D., Salahuddin, S. & Datta, S. Proposal for an all-spin logic device with built-in memory. *Nat. Nanotechnol.* **5**, 266–270 (2010).
102. Currivan-Incorvia, J. A. *et al.* Logic circuit prototypes for three-terminal magnetic tunnel junctions with mobile domain walls. *Nat. Commun.* **7**, 1–7 (2016).
103. Nikonov, D. E., Bourianoff, G. I. & Gargini, P. A. Power dissipation in spintronic devices out of thermodynamic equilibrium. *J. Supercond. Nov. Magn.* **19**, 497–513 (2006).
104. Jansen, R. Silicon spintronics. *Nat. Mater.* **11**, 400–408 (2012).
105. van der Laan, G. & Figueroa, A. I. X-ray magnetic circular dichroism - A versatile tool to study magnetism. *Coord. Chem. Rev.* **277**, 95–129 (2014).
106. Wienholdt, S., Hinzke, D. & Nowak, U. THz switching of antiferromagnets and ferrimagnets. *Phys. Rev. Lett.* **108**, 1–5 (2012).
107. Gomonay, O., Baltz, V., Brataas, A. & Tserkovnyak, Y. Antiferromagnetic spin textures and dynamics. *Nat. Phys.* **14**, 213–216 (2018).
108. Baltz, V. *et al.* Antiferromagnetic spintronics. *Rev. Mod. Phys.* **90**, 015005 (2018).
109. Jungwirth, T. *et al.* The multiple directions of antiferromagnetic spintronics. *Nat. Phys.* **14**, 200–203 (2018).
110. Finley, J. & Liu, L. Spintronics with compensated ferrimagnets. *Appl. Phys. Lett.* **116**, 110501 (2020).
111. Hsieh, D. *et al.* A topological Dirac insulator in a quantum spin Hall phase. *Nature* **452**, 970–974 (2008).
112. Pesin, D. & MacDonald, A. H. Spintronics and pseudospintronics in graphene and topological insulators. *Nat. Mater.* **11**, 409–416 (2012).
113. Šmejkal, L., Mokrousov, Y., Yan, B. & MacDonald, A. H. Topological antiferromagnetic spintronics. *Nat. Phys.* **14**, 242–251 (2018).
114. Mogi, M. *et al.* Current-induced switching of proximity-induced ferromagnetic surface states in a topological insulator. *Nat. Commun.* **12**, 1404 (2021).
115. Lee, S. C., Lee, T. D., Blaha, P. & Schwarz, K. Magnetic and half-metallic properties of the full-Heusler alloys Co 2TiX (X=Al,Ga;Si,Ge,Sn;Sb). *J. Appl. Phys.* **97**, 10C307 (2005).

116. Slonczewski, J. C. Conductance and exchange coupling of two ferromagnets separated by a tunneling barrier. *Phys. Rev. B* **39**, 6995–7002 (1989).
117. Sun, J. Z. Current-driven magnetic switching in manganite trilayer junctions. *J. Magn. Magn. Mater.* **202**, 157–162 (1999).
118. Slonczewski, J. C. Current-driven excitation of magnetic multilayers. *J. Magn. Magn. Mater.* **159**, L1–L7 (1996).
119. Ralph, D. C. & Stiles, M. D. Spin transfer torques. *J. Magn. Magn. Mater.* **320**, 1190–1216 (2008).
120. Cubukcu, M. *et al.* Ultra-Fast Perpendicular Spin-Orbit Torque MRAM. *IEEE Trans. Magn.* **54**, 9300204 (2018).
121. Kent, A. D. & Worledge, D. C. A new spin on magnetic memories. *Nat. Nanotechnol.* **10**, 187–191 (2015).
122. Hall, E. H. On a New Action of the Magnet on Electric Currents. *Am. J. Math.* **2**, 287–292 (1879).
123. Kittel, C. *Introduction to Solid State Physics*. (John Wiley & Sons, Inc., 2005).
124. Dyakonov, M. I. & Perel, V. I. Current-induced spin orientation of electrons in semiconductors. *Phys. Lett. A* **35**, 459–460 (1971).
125. Sinova, J., Valenzuela, S. O., Wunderlich, J., Back, C. H. & Jungwirth, T. Spin Hall effects. *Rev. Mod. Phys.* **87**, 1213–1260 (2015).
126. Kato, Y. K., Myers, R. C., Gossard, A. C. & Awschalom, D. D. Observation of the spin hall effect in semiconductors. *Science (80-.).* **306**, 1910–1913 (2004).
127. Valenzuela, S. O. & Tinkham, M. Direct electronic measurement of the spin Hall effect. *Nature* **442**, 176–179 (2006).
128. Pai, C. F. *et al.* Spin transfer torque devices utilizing the giant spin Hall effect of tungsten. *Appl. Phys. Lett.* **101**, 122404 (2012).
129. Zhao, H., Loren, E. J., Van Driel, H. M. & Smirl, A. L. Coherence control of hall charge and spin currents. *Phys. Rev. Lett.* **96**, 246601 (2006).
130. Stern, N. P. *et al.* Current-induced polarization and the spin hall effect at room temperature. *Phys. Rev. Lett.* **97**, 126603 (2006).
131. Wang, H. L. *et al.* Scaling of spin hall angle in 3d, 4d, and 5d metals from Y3Fe5 O12 /metal spin pumping. *Phys. Rev. Lett.* **112**, 1–5 (2014).
132. Kimura, T., Otani, Y., Sato, T., Takahashi, S. & Maekawa, S. Room-temperature reversible spin hall effect. *Phys. Rev. Lett.* **98**, 156601 (2007).
133. Liu, L., Pai, C. F., Tseng, H. W., Ralph, D. C. & Buhrman, R. A. Spin-Torque Switching with the Giant Spin Hall Effect of Tantalum. *Science (80-.).* **336**, 555 (2012).
134. Keller, M. W. *et al.* Near-unity spin Hall ratio in NixCu1-x alloys. *Phys. Rev. B* **99**, 214411 (2019).
135. Khang, N. H. D., Ueda, Y. & Hai, P. N. A conductive topological insulator with large spin Hall effect for ultralow power spin–orbit torque switching. *Nat. Mater.* **17**, 808–813 (2018).
136. Farzaneh, S. M. & Rakheja, S. Intrinsic spin Hall effect in topological insulators: A first-principles study. *Phys. Rev. Mater.* **4**, 114202 (2020).
137. Bakun, A., Zakharchenya, B., Rogachev, A., Tkachuk, M. & Fleĭsher, V. Observation of a surface photocurrent caused by optical orientation of electrons in a semiconductor. *Soviet Journal of Experimental and Theoretical Physics Letters* **40**, 1293 (1984).
138. Mizukami, S., Ando, Y. & Miyazaki, T. Ferromagnetic resonance linewidth for NM/80NiFe/NM films (NM = Cu, Ta, Pd and Pt). *J. Magn. Magn. Mater.* **226**–**230**, 1640–

1642 (2001).
139. Tserkovnyak, Y., Brataas, A. & Bauer, G. E. W. Enhanced Gilbert Damping in Thin Ferromagnetic Films. *Phys. Rev. Lett.* **88**, 117601 (2002).
140. Tserkovnyak, Y., Brataas, A. & Bauer, G. E. W. Spin pumping and magnetization dynamics in metallic multilayers. *Phys. Rev. B - Condens. Matter Mater. Phys.* **66**, 224403 (2002).
141. Miao, B. F., Huang, S. Y., Qu, D. & Chien, C. L. Inverse spin hall effect in a ferromagnetic metal. *Phys. Rev. Lett.* **111**, 066602 (2013).
142. Ando, K. *et al.* Electric manipulation of spin relaxation using the spin hall effect. *Phys. Rev. Lett.* **101**, 036601 (2008).
143. Liu, L., Moriyama, T., Ralph, D. C. & Buhrman, R. A. Spin-torque ferromagnetic resonance induced by the spin Hall effect. *Phys. Rev. Lett.* **106**, 036601 (2011).
144. Miron, I. M. *et al.* Perpendicular switching of a single ferromagnetic layer induced by in-plane current injection. *Nature* **476**, 189–193 (2011).
145. Manchon, A. *et al.* Current-induced spin-orbit torques in ferromagnetic and antiferromagnetic systems. *Rev. Mod. Phys.* **91**, 035004 (2019).
146. Gambardella, P. & Miron, I. M. Current-induced spin-orbit torques. *Philos. Trans. R. Soc. A Math. Phys. Eng. Sci.* **369**, 3175–3197 (2011).
147. Kim, J. H. *et al.* Spin-orbit torques associated with ferrimagnetic order in Pt/GdFeCo/MgO layers. *Sci. Rep.* **8**, 1–8 (2018).
148. Pai, C. F., Mann, M., Tan, A. J. & Beach, G. S. D. Determination of spin torque efficiencies in heterostructures with perpendicular magnetic anisotropy. *Phys. Rev. B* **93**, 144409 (2016).
149. Yu, G. *et al.* Switching of perpendicular magnetization by spin-orbit torques in the absence of external magnetic fields. *Nat. Nanotechnol.* **9**, 548–554 (2014).
150. Orio, R. L. De *et al.* Robust Magnetic Field-Free Switching of a Perpendicularly Magnetized Free Layer for SOT-MRAM. *Solid State Electron.* **168**, 107730 (2020).
151. Chuang, T. C., Pai, C. F. & Huang, S. Y. Cr-induced Perpendicular Magnetic Anisotropy and Field-Free Spin-Orbit-Torque Switching. *Phys. Rev. Appl.* **11**, 061005 (2019).
152. Wang, M. *et al.* Field-free switching of a perpendicular magnetic tunnel junction through the interplay of spin–orbit and spin-transfer torques. *Nat. Electron.* **1**, 582–588 (2018).
153. Liu, L., Lee, O. J., Gudmundsen, T. J., Ralph, D. C. & Buhrman, R. A. Current-induced switching of perpendicularly magnetized magnetic layers using spin torque from the spin hall effect. *Phys. Rev. Lett.* **109**, 096602 (2012).
154. Garello, K. *et al.* Ultrafast magnetization switching by spin-orbit torques. *Appl. Phys. Lett.* **105**, 212402 (2014).
155. Yu, G. Two-terminal MRAM with a spin. *Nat. Electron.* **1**, 496–497 (2018).
156. Li, P. *et al.* Spin-orbit torque-assisted switching in magnetic insulator thin films with perpendicular magnetic anisotropy. *Nat. Commun.* **7**, 12688 (2016).
157. Thiery, N. *et al.* Electrical properties of epitaxial yttrium iron garnet ultrathin films at high temperatures. *Phys. Rev. B* **97**, 064422 (2018).
158. Yamahara, H., Mikami, M., Seki, M. & Tabata, H. Epitaxial strain-induced magnetic anisotropy in Sm3Fe 5O12 thin films grown by pulsed laser deposition. *J. Magn. Magn. Mater.* **323**, 3143–3146 (2011).
159. Soumah, L. *et al.* Ultra-low damping insulating magnetic thin films get perpendicular. *Nat. Commun.* **9**, 3355 (2018).
160. Goto, T., Onbaşlò, M. C. & Ross, C. A. Magneto-optical properties of cerium substituted

yttrium iron garnet films with reduced thermal budget for monolithic photonic integrated circuits. *Opt. Express* **20**, 28507–28517 (2012).
161. Gage, T. E., Dulal, P., Solheid, P. A., Flannigan, D. J. & Stadler, B. J. H. Si-integrated ultrathin films of phase-pure Y3Fe5O12(YIG) via novel two-step rapid thermal anneal. *Mater. Res. Lett.* **5**, 379–385 (2017).
162. Dionne, G. F. Molecular field coefficients of substituted yttrium iron garnets. *J. Appl. Phys.* **41**, 4874–4881 (1970).
163. Gomonay, E. V. & Loktev, V. M. Spintronics of antiferromagnetic systems. *Low Temp. Phys.* **40**, 17–35 (2014).
164. Jungwirth, T., Marti, X., Wadley, P. & Wunderlich, J. Antiferromagnetic spintronics. *Nat. Nanotechnol.* **11**, 231–241 (2016).
165. Kimel, A. V., Kirilyuk, A., Tsvetkov, A., Pisarev, R. V. & Rasing, T. Laser-induced ultrafast spin reorientation in the antiferromagnet TmFeO3. *Nature* **429**, 850–853 (2004).
166. Schryer, N. L. & Walker, L. R. The motion of 180° domain walls in uniform dc magnetic fields. *J. Appl. Phys.* **45**, 5406–5421 (1974).
167. Caretta, L. *et al.* Relativistic Kinematics of a Magnetic Soliton. *Science (80-.).* **1442**, 1438–1442 (2020).
168. Douglas, C. B. & Hubler, G. K. *Pulsed Laser Deposition of Thin Films*. (Wiley-Interscience, 1994).
169. Singh, R. K., Holland, O. W. & Narayan, J. Theoretical model for deposition of superconducting thin films using pulsed laser evaporation technique. *J. Appl. Phys.* **68**, 233–247 (1990).
170. Singh, R. K. & Narayan, J. Pulsed-laser evaporation technique for deposition of thin films: Physics and theoretical model. *Phys. Rev. B* **41**, 8843–8859 (1990).
171. Behrisch, R. & Eckstein, W. *Sputtering by Particle Bombardment: Experiments and Computer Calculations from Theshold to MeV energies*. *Topics in Applied Physics* **110**, (2007).
172. Fert, A., Reyren, N. & Cros, V. Magnetic skyrmions: Advances in physics and potential applications. *Nat. Rev. Mater.* **2**, 17031 (2017).
173. Thompson, C. V. & Carel, R. Stress and grain growth in thin films. *J. Mech. Phys. Solids* **44**, 657–673 (1996).
174. Thompson, C. V. Grain growth in thin films. *Annu. Rev. Mater. Sci.* **20**, 245–268 (1990).
175. Pietsch, U., Holy, V. & Baumbach, T. *High Resolution Xray scattering*. (Springer-Verlag, 2004).
176. He, B. B. *Two-dimensional X-ray Diffraction*. (John Wiley & Sons, Inc., 2018).
177. Okada, Y. & Tokumaru, Y. Precise determination of lattice parameter and thermal expansion coefficient of silicon between 300 and 1500 K. *J. Appl. Phys.* **56**, 314–320 (1984).
178. Cullity, B. D. *Elements of X-Ray Diffraction*. (Addison-Wesley Publishing Company, 1978).
179. Orfanidis, S. J. *Electromagnetic Waves and Antennas*. **2**, (2004).
180. Binnig, G., Rohrer, H., Gerber, C. & Weibel, E. Tunneling through a controllable vacuum gap. *Appl. Phys. Lett.* **40**, 178–180 (1982).
181. Binnig, G., Quate, C. F. & Gerber, C. Atomic Force Microscope. *Phys. Rev. Lett.* **56**, 930–933 (1986).
182. Salapaka, S. M. & Salapaka, M. V. Scanning Probe Microscopy. *IEEE Control Syst. Mag.*

65–83 (2008).
183. Sanders, Wesley, C. *Atomic Force Microscopy: Fundamental Concepts and Laboratory Investigations*. *Journal of Materials Processing Technology* **1**, (CRC Press, 2020).
184. Foner, S. Versatile and sensitive vibrating-sample magnetometer. *Rev. Sci. Instrum.* **30**, 548–557 (1959).
185. Nakayama, H. *et al.* Spin Hall Magnetoresistance Induced by a Nonequilibrium Proximity Effect. *Phys. Rev. Lett.* **110**, 206601 (2013).
186. Lu, Y. M. *et al.* Hybrid magnetoresistance in the proximity of a ferromagnet. *Phys. Rev. B - Condens. Matter Mater. Phys.* **87**, 220409(R) (2013).
187. Miao, B. F., Huang, S. Y., Qu, D. & Chien, C. L. Physical origins of the new magnetoresistance in Pt/YIG. *Phys. Rev. Lett.* **112**, 236601 (2014).
188. Majkrzak, C. F. Observation of a Magnetic Antiphase Domain Structure with Long-Range prger in. *Phys. Rev. Lett.* **56**, 2700–2703 (1986).
189. Felcher, G. P. *et al.* Polarized neutron reflectometer: A new instrument to measure magnetic depth profiles. *Rev. Sci. Instrum.* **58**, 609–619 (1987).
190. Ehlers, J. *et al. X-ray and Neutron Reflectivity. Principles and Applications*. (2009).
191. Zabel, H. & Theis-Brohl, K. Polarized neutron reflectivity and scattering studies of magnetic heterostructures. *J. Phys. Condens. Matter* **15**, S505–S517 (2003).
192. Majkrzak, C. F., Donovan, K. V. O. & Berk, N. F. *Polarized Neutron Reflectometry*. (2004).
193. Bauer, J. J. *et al.* Dysprosium Iron Garnet Thin Films with Perpendicular Magnetic Anisotropy on Silicon. *Adv. Electron. Mater.* **6**, 1900820 (2020).
194. Bauer, J. J. *et al.* Magnetic proximity effect in magnetic insulator/heavy metal heterostructures across the compensation temperature. *(in preparation)*.
195. Kirby, B. J. *et al.* Phase-sensitive specular neutron reflectometry for imaging the nanometer scale composition depth profile of thin-film materials. *Curr. Opin. Colloid Interface Sci.* **17**, 44–53 (2012).
196. Kienzle, P. A. *et al.* Reflectometry Software. (2017). Available at: https://www.nist.gov/ncnr/reflectometry-software.
197. Li, M. *et al.* Dirac-electron-mediated magnetic proximity effect in topological insulator/magnetic insulator heterostructures. *Phys. Rev. B* **96**, 201301(R) (2017).
198. Suturin, S. M. *et al.* Role of gallium diffusion in the formation of a magnetically dead layer at the Y3Fe5 O12/Gd3Ga5 O12 epitaxial interface. *Phys. Rev. Mater.* **2**, 1–9 (2018).
199. Cooper, J. F. K. *et al.* Unexpected structural and magnetic depth dependence of YIG thin films. *Phys. Rev. B* **96**, 104404 (2017).
200. Fan, Y. *et al.* Manipulation of Coupling and Magnon Transport in Magnetic Metal-Insulator Hybrid Structures. *Phys. Rev. Appl.* **13**, 061002 (2020).
201. Ankner, J. F. & Felcher, G. P. Polarized-neutron reflectometry. *J. Magn. Magn. Mater.* **200**, 741–754 (1999).
202. Maxwell, J. C. *A Treatise on Electricity and Magnetism*. (Macmillan and Co., 1873).
203. Faraday, M. On the magnetization of light and the illumination of magnetic lines of force. *Phil. Trans. R. Soc.* **136**, (1846).
204. Kerr, J. On rotation of the plane of polarization by reflection from the pole of a magnet. *London, Edinburgh, Dublin Philos. Mag. J. Sci.* **3**, 321–343 (1877).
205. Fakhrul, T. *et al.* Magneto-Optical Bi:YIG Films with High Figure of Merit for Nonreciprocal Photonics. *Adv. Opt. Mater.* **7**, 1900056 (2019).
206. Kobayashi, N. & Muranaka, A. *Circular Dichroism and Magnetic Circular Dichroism*

Spectroscopy for Organic Chemists. (Royal Society of Chemistry, 2012). doi:10.1039/9781849732932
207. de Groot, F. & Kotani, A. *Core Level Spectroscopy of Solids*. (Taylor & Francis Group, LLC, 2008).
208. Mason, W. R. *A Practical Guide to Magnetic Circular Dichroism Spectroscopy*. (2006). doi:10.1002/9780470139233
209. Thole, B. T., Van Der Laan, G. & Sawatzky, G. A. Strong Magnetic Dichroism Predicted in the M4,5 X-Ray Absorption Spectra of Magnetic Rare-Earth Materials. *Phys. Rev. Lett.* **55**, 2086–2088 (1985).
210. Van Der Laan, G. *et al.* Experimental proof of magnetic x-ray dichroism. *Phys. Rev. B* **34**, 6529–6531 (1986).
211. Chen, C. T. *et al.* Experimental confirmation of the x-ray magnetic circular dichroism sum rules for iron and cobalt. *Phys. Rev. Lett.* **75**, 152–155 (1995).
212. Edmonds, K. W. *et al.* Ferromagnetic moment and antiferromagnetic coupling in (Ga,Mn)As thin films. *Phys. Rev. B - Condens. Matter Mater. Phys.* **71**, 064418 (2005).
213. Piamonteze, C., Miedema, P. & De Groot, F. M. F. Accuracy of the spin sum rule in XMCD for the transition-metal L edges from manganese to copper. *Phys. Rev. B - Condens. Matter Mater. Phys.* **80**, 184410 (2009).
214. Singha, A. *et al.* 4 f Occupancy and Magnetism of Rare-Earth Atoms Adsorbed on Metal Substrates. *Phys. Rev. B* **96**, 224418 (2017).
215. Teramura, Y., Tanaka, A., Thole, B. T. & Jo, T. Effect of Coulomb Interaction on the X-Ray Magnetic Circular Dichroism Spin Sum Rule in Rare Earths. *J. Phys. Soc. Japan* **65**, 3056–3059 (1996).
216. Ning, S. *et al.* Voltage Control of Magnetism above Room Temperature in Epitaxial SrCo1-xFexO3-δ. *ACS Nano* **14**, 8949–8957 (2020).
217. Tang, C. *et al.* Anomalous Hall hysteresis in Tm3Fe5O12/Pt with strain-induced perpendicular magnetic anisotropy. *Phys. Rev. B* **94**, 140403 (R) (2016).
218. Sun, Y. *et al.* Damping in yttrium iron garnet nanoscale films capped by platinum. *Phys. Rev. Lett.* **111**, 1–5 (2013).
219. Avci, C. O. *et al.* Fast switching and signature of efficient domain wall motion driven by spin-orbit torques in a perpindicular magnetic insulator/Pt bilayer. *Appl. Phys. Lett.* **111**, 072406 (2017).
220. Büttner, F. *et al.* Dynamics and inertia of skyrmionic spin structures. *Nat. Phys.* **11**, 225–228 (2015).
221. O'Kane, D. F., Sadagopan, V. & Giess, E. A. Crystal Growth and Characterization of Gadolinium Iron Garnet. *J. Electrochem. Soc.* **120**, 1272–1275 (1973).
222. Kim, J. *et al.* Principle of direct van der Waals epitaxy of single-crystalline films on epitaxial graphene. *Nat. Commun.* **5**, 1–7 (2014).
223. Kim, Y. *et al.* Remote epitaxy through graphene enables two-dimensional material-based layer transfer. *Nature* **544**, 340–343 (2017).
224. Kum, H. S. *et al.* Heterogeneous integration of single- crystalline complex-oxide membranes. *Nature* **578**, 75–81 (2020).
225. Sun, X. Y. *et al.* Single-Step Deposition of Cerium-Substituted Yttrium Iron Garnet for Monolithic On-Chip Optical Isolation. *ACS Photonics* **2**, 856–863 (2015).
226. Ortiz, V. H. *et al.* Systematic control of strain-induced perpendicular magnetic anisotropy in epitaxial europium and terbium iron garnet thin films. *APL Mater.* **6**, 121113 (2018).

227. Iida, S. Anomalous Magnetostriction of Tb3Fe5O12 and Eu3Fe5O12. *Phys. Lett.* **6**, 165–167 (1963).
228. Iida, S. Magnetostriction constants of rare earth iron garnets. *J. Phys. Soc. Japan* **22**, 1201–1209 (1967).
229. Hussain, K. A. & Sirdeshmukh, D. B. X-Ray Studies of Some Europium Compounds at Elevated Temperatures **. *Cryst. Res. Technol.* **28**, 1147–1151 (1993).
230. Sutter, J. P. & Yavaş, H. Material properties of alpha-quartz that are relevant for its potential use in X-ray monochromators and analyzers. *arXiv* arXiv:1612.07049 (2016).
231. Popova, E. *et al.* Perpendicular magnetic anisotropy in ultrathin yttrium iron garnet films prepared by pulsed laser deposition technique. *J. Vac. Sci. Technol. A Vacuum, Surfaces, Film.* **19**, 2567–2570 (2001).
232. Yang, Q.-H., Zhang, H.-W., Wen, Q.-Y. & Liu, Y.-L. Effects of off-stoichiometry and density on the magnetic and magneto-optical properties of yttrium iron garnet films by magnetron sputtering method. *J. Appl. Phys.* **108**, 073901 (2010).
233. Bi, L. *et al.* On-chip optical isolation in monolithically integrated non-reciprocal optical resonators. *Nat. Photonics* **5**, 758–762 (2011).
234. Bi, L. *et al.* Magneto-optical thin films for on-chip monolithic integration of non-reciprocal photonic devices. *Materials (Basel).* **6**, 5094–5117 (2013).
235. Balinskiy, M. *et al.* Spin wave excitation in sub-micrometer thick $Y_3Fe_5O_{12}$ films fabricated by pulsed laser deposition on garnet and silicon substrates: A comparative study. *J. Appl. Phys.* **122**, 123904 (2017).
236. Oishi, J. & Kimura, T. Thermal expansion of fused quartz. *Metrologia* **5**, 50–55 (1969).
237. Watanabe, H., Yamada, N. & Okaji, M. Linear Thermal Expansion Coefficient of Silicon from 293 to 1000~{K}. *Int. J. Thermophys.* **25**, 221–236 (2004).
238. Hayashi, H. *et al.* Thermal expansion coefficient of yttria stabilized zirconia for various yttria contents. *Solid State Ionics* **176**, 613–619 (2005).
239. Chen, Y.-T. *et al.* Theory of spin Hall magnetoresistance. *Phys. Rev. B* **87**, 144411 (2013).
240. Chen, Y. T. *et al.* Theory of spin Hall magnetoresistance (SMR) and related phenomena. *J. Phys. Condens. Matter* **28**, (2016).
241. Brataas, A., Nazarov, Y. U. V. & Bauer, G. E. W. Finite-element theory of transport in ferromagnet-normal metal systems. *Phys. Rev. Lett.* **84**, 2481–2484 (2000).
242. Tong, D. *The quantum hall effect*. *TIFR Infosys Lectures* (2016). doi:10.1016/0378-4363(83)90623-X
243. Pearson, R. F. Magnetocrystalline anisotropy of rare-earth iron garnets. *J. Appl. Phys.* **33**, 1236–1242 (1962).
244. Burenkov, Y. A. & Nikanorov, S. P. Temperature effect on the elastic properties of yttrium garnet ferrite Y3Fe5O12. *Phys. Solid State* **44**, 318–323 (2002).
245. Rosenberg, E. R. *et al.* Magnetic Properties and Growth-Induced Anisotropy in Yttrium Thulium Iron Garnet Thin Films. *Prep.* (2021).
246. Tang, C. *et al.* Exquisite growth control and magnetic properties of yttrium iron garnet thin films. *Appl. Phys. Lett.* **108**, 102403 (2016).
247. Liu, Q. B. *et al.* Unusual anomalous Hall effect in perpendicularly magnetized YIG films with a small Gilbert damping constant. *Phys. Rev. B* **101**, 174431 (2020).
248. Mizukami, S., Ando, Y. & Miyazaki, T. Effect of spin diffusion on Gilbert damping for a very thin permalloy layer in Cu/permalloy/Cu/Pt films. *Phys. Rev. B - Condens. Matter Mater. Phys.* **66**, 104413 (2002).

249. Jermain, C. L. *et al.* Low-damping sub-10-nm thin films of lutetium iron garnet grown by molecular-beam epitaxy. *Appl. Phys. Lett.* **109**, 192408 (2016).
250. Crossley, S. *et al.* Ferromagnetic resonance of perpendicularly magnetized Tm3Fe5O12/Pt heterostructures. *Appl. Phys. Lett.* **115**, (2019).
251. Vella-Coleiro, G. P., Smith, D. H. & Van Uitert, L. G. Damping of domain wall motion in rare-earth iron garnets. *Appl. Phys. Lett.* **21**, 36–37 (1972).
252. Mitra, A. *et al.* Interfacial Origin of the Magnetisation Suppression of Thin Film Yttrium Iron Garnet. *Sci. Rep.* **7**, 11774 (2017).
253. Shaposhnikov, A. N. *et al.* Magneto-optical, structural and surface properties of RIB sputtered (Bi,Ga)-substituted DyIG films. *Mater. Res. Bull.* **95**, 115–122 (2017).
254. Zhang, Y. *et al.* Dysprosium substituted Ce:YIG thin films with perpendicular magnetic anisotropy for silicon integrated optical isolator applications. *APL Mater.* **7**, 081119 (2019).
255. Kuila, M., Hussain, Z. & Reddy, V. R. MOKE study of magnetic compensation in polycrystalline gadolinium iron garnet thin film. *J. Magn. Magn. Mater.* **473**, 458–463 (2019).
256. Paoletti, A. *Physics of magnetic garnets*. (Amsterdam; New York: North-Holland Pub. Co., 1979).
257. Geller, S., Espinosa, G. P. & Crandall, P. B. Thermal expansion of yttrium and gadolinium iron, gallium and aluminum garnets. *J. Appl. Crystallogr.* **2**, 86–88 (1969).
258. Bateman, T. B. Elastic moduli of single-crystal europium iron garnet and yttrium iron garnet. *J. Appl. Phys.* **37**, 2194–2195 (1966).
259. Onbasli, M. C. *et al.* Pulsed laser deposition of epitaxial yttrium iron garnet films with low Gilbert damping and bulk-like magnetization. *APL Mater.* **2**, 106102 (2014).
260. Dionne, G. F. Molecular-field coefficients of rare-earth iron garnets. *J. Appl. Phys.* **47**, 4220–4221 (1976).
261. Wilhelm, F. *et al.* Interface magnetism in 3d/5d multilayers probed by X-ray magnetic circular dichroism. *Phys. Status Solidi Appl. Res.* **196**, 33–36 (2003).
262. Katmis, F. *et al.* A high-temperature ferromagnetic topological insulating phase by proximity coupling. *Nature* **533**, 513–516 (2016).
263. Yang, C. Y. *et al.* Direct observation of proximity-induced magnetism and spin reorientation in topological insulator on a ferrimagnetic oxide. *Appl. Phys. Lett.* **114**, 082403 (2019).
264. Lu, Y. M. *et al.* Pt magnetic polarization on Y3Fe5O12 and magnetotransport characteristics. *Phys. Rev. Lett.* **110**, 147207 (2013).
265. Geprägs, S. *et al.* Investigation of induced Pt magnetic polarization in Pt/Y 3Fe5O12 bilayers. *Appl. Phys. Lett.* **101**, (2012).
266. Valvidares, M. *et al.* Absence of magnetic proximity effects in magnetoresistive Pt/CoF e2 O4 hybrid interfaces. *Phys. Rev. B* **93**, 214415 (2016).
267. Zhou, X. *et al.* Tuning magnetotransport in PdPt/Y3Fe5O12: Effects of magnetic proximity and spin-orbit coupling. *Appl. Phys. Lett.* **105**, 012408 (2014).
268. Satapathy, D. K. *et al.* Magnetic proximity effect in YBa 2Cu 3O 7/La 2/3Ca 1/3MnO 3 and YBa 2Cu 3O 7/LaMnO 3+δ superlattices. *Phys. Rev. Lett.* **108**, 197201 (2012).
269. Samant, M. G. *et al.* Induced Spin Polarization in Cu Spacer Layers in Co/Cu Multilayers. *Phys. Rev. Lett.* **72**, 1112–1115 (1994).
270. Figueroa, A. I. *et al.* Breakdown of Hund's third rule in amorphous Co-W nanoparticles and crystalline Co 3W alloys. *Phys. Rev. B* **86**, 064428 (2012).

271. Inyang, O. *et al.* Threshold interface magnetization required to induce magnetic proximity effect. *Phys. Rev. B* **100**, 174418 (2019).
272. Bose, A., Bauer, J., Ross, C. A. & Ralph, D. C. Origin of the transverse thermoelectric signal in TmIG/W and TmIG/Pt bilayers. *(in preparation)*.
273. Hao, Q. & Xiao, G. Giant Spin Hall Effect and Switching Induced by Spin-Transfer Torque in a W/Co40Fe40 B20/MgO Structure with Perpendicular Magnetic Anisotropy. *Phys. Rev. Appl.* **3**, 034009 (2015).
274. Lee, H. R. *et al.* Spin-orbit torque in a bulk perpendicular magnetic anisotropy Pd/FePd/MgO system. *Sci. Rep.* **4**, 3–9 (2014).
275. Aldosary, M. *et al.* Platinum / Yttrium Iron Garnet Inverted Structures for Spin Current Transport. *Appl. Phys. Lett.* **108**, 242401 (2016).
276. Geprägs, S. *et al.* Static magnetic proximity effects and spin Hall magnetoresistance in Pt/ Y3Fe5 O12 and inverted Y3Fe5 O12/Pt bilayers. *Phys. Rev. B* **102**, 214438 (2020).
277. Guo, C. Y. *et al.* Spin-orbit torque switching in perpendicular Y3Fe5O12/Pt bilayer. *Appl. Phys. Lett.* **114**, 192409 (2019).
278. Eschenfelder, A. H. *Magnetic Bubble Technology*. *Springer Series in Solid-State Sciences* **14**, (Springer-Verlag, 1980).
279. Weiss, P. The variation of ferromagnetism with temperature. *Compt. Rend.* **143**, 1136–1139 (1906).
280. Néel, L. Influence des fluctuations du champ moléculaire sur les propriétés magnétiques des corps. *Ann. Phys. (Paris).* **10**, 5–105 (1932).
281. Neel, L. Magnetic Properties of Ferrites: Ferrimagnetism and Antiferromagnetism. *Ann. Phys.* **3**, 137–198 (1948).
282. Kittel, C. Theory of ferromagnetic resonance in rare earth garnets. I. g values. *Phys. Rev.* **115**, 1587–1590 (1959).
283. De Gennes, P. G., Kittel, C. & Portis, A. M. Theory of ferromagnetic resonance in rare earth garnets. II. Line widths. *Phys. Rev.* **116**, 323–330 (1959).
284. Kittel, C. Theory of ferromagnetic resonance in rare earth garnets. III. Giant anisotropy anomalies. *Phys. Rev.* **117**, 681–687 (1960).
285. Anderson, E. E. Molecular Field Model and the Magnetization of YIG. *Phys. Rev.* **134**, A1581–A1585 (1964).
286. Dionne, G. F. *Magnetic Moment Versus Temperature Curves of Rare-Earth Iron Garnets*. (1979).
287. Geller, S., Williams, H. J., Espinosa, G. P. & Sherwood, R. C. Importance of Intrasublattice Magnetic Interactions and of Substitutional Ion Type in the Behavior of Substituted Yttrium Iron Garnets. *Bell Syst. Tech. J.* **XLIII**, 565–624 (1964).
288. Gilleo, M. A. Superexchange interaction in ferrimagnetic garnets and spinels which contain randomly incomplete linkages. *J. Phys. Chem. Solids* **13**, 33–39 (1960).
289. Geller, S., Bozorth, R. M., Miller, C. E. & Davis, D. D. Crystal Chemical and Magnetic Studies of Garnet Systems, Zr or HF. *J. Phys. Chem. Solids* **13**, 28–32 (1960).
290. Geller, S., Williams, H. J., Sherwood, R. C. & Espinosa, G. P. Magnetic and Crystallographic Studies of Substituted Gadolinium Iron Garnets. *J. Appl. Phys.* **36**, 88–100 (1965).
291. Geller, S. Magnetic Behavior of Substituted Ferrimagnetic Garnets. *J. Appl. Phys.* **37**, 1408–1415 (1966).
292. Lahoubi, M. & Guillot, M. Double umbrella structure in terbium iron garnet. *IEEE Trans.*

Magn. **20**, 1518–1520 (1984).
293. Lahoubi, M. & Ouladdiaf, B. Anomalous magnetic reordering in magnetodielectric terbium iron garnet at low temperatures. *J. Magn. Magn. Mater.* **373**, 108–114 (2015).
294. White, R. L. The Magnetostriction of Rare-Earth Garnets Containing Gallium and Europium: Old Theory for New Problems. *IEEE Trans. Magn.* **9**, 606–609 (1973).
295. Chin, Y. Y. *et al.* Local spin moments, valency, and long-range magnetic order in monocrystalline and ultrathin films of Y3Fe5 O12 garnet. *Phys. Rev. B* **99**, 184407 (2019).
296. Rosenberg, E. R., Bauer, J. J. & Ross, C. A. Explanation of the compensation temperature discrepancy in epitaxial terbium iron garnet thin films. (i*n preparation).*
297. Fakhrul, T. *et al.* High figure of merit Magneto-optical Ce and Bi-substituted Terbium Iron Garnet films integrated on Si. *submitted* (2021).
298. Gilleo, M. A. & Geller, S. Magnetic and Crystallographic Properties of Substituted Yttrium-Iron Garnet, 3Y2O3•xM2O3•(5-x)Fe2O3. *Phys. Rev.* **110**, 73–78 (1958).
299. Winkler, G. & Hansen, P. Calcium-Vanadium-Indium Substituted Yttrium-Iron-Garnets with very low linewidths of ferrimagnetic resonance. *Mat. Res. Bull.* **4**, 825–838 (1969).
300. Jungfleisch, M. B., Lauer, V., Neb, R., Chumak, A. V. & Hillebrands, B. Improvement of the yttrium iron garnet / platinum interface for spin pumping-based applications. *Appl. Phys. Lett.* **103**, 0–4 (2013).
301. Khurana, B., Bauer, J. J. & Ross, C. A. Epitaxial Scandium Substituted Terbium Iron Garnet Thin Films for Spintronics. (*in preparation).*
302. Zhang, R. & Willis, R. F. Thickness-dependent curie temperatures of ultrathin magnetic films: Effect of the range of spin-spin interactions. *Phys. Rev. Lett.* **86**, 2665–2668 (2001).

List of Publications

1. **Bauer, J.**, Quarterman P., Grutter, A., Khurana, B., Kundu, S., Mkhoyan, K., Borchers, J., Ross, C. *Magnetic proximity effect in magnetic insulator/heavy metal heterostructures across the compensation temperature.* (in preparation).
2. Khurana, B., **Bauer, J.**, Ross, C. *Epitaxial Scandium Substituted Terbium Iron Garnet Thin Films for Spintronics*. (in preparation).
3. Rosenberg, E., **Bauer, J.**, Ross, C. *Explanation of the compensation temperature discrepancy in epitaxial TbIG thin films.* (in preparation)
4. Bose, A., **Bauer, J.**, Ross, C., Ralph, D. *Origin of the transverse thermoelectric signal in TmIG/W and TmIG/Pt bilayers.* (in preparation).
5. Fakhrul, T., Tazlaru, S., Khurana, B., Beran, L., **Bauer, J.**, Vančik, M., Marchese, A., Tsotsos, E., Kučera, M., Zhang, Y., Veis, M., Ross, C. *Integration of Magneto-optical Ce and Bi-substituted Terbium Iron Garnet films on Si*. (accepted).
6. **Bauer, J.**, Rosenberg, E., Kundu, S., Mkhoyan, K., Quarterman, P., Grutter, A., Kirby, J., Borchers, J., Ross, C. *Dysprosium Iron Garnet Thin Films with Perpendicular Magnetic Anisotropy of Silicon*. Adv. Elec. Mat., 6, 1900820 (2020).
7. Kum, H., Lee, H., Kim, S., Lindemann, S., Kong, W., Qiao, K., Chen, P., Irwin, J., Lee, J., Xie, S., Subramanian, S., Shim, J., Bae, S., Choi, C., Ranno, L., Seo S., Lee, S., **Bauer, J.**, Li, H., Lee, K., Robinson, J., Ross, C., Schlom, D., Rzchowski, M., Eom, C., Kim, J. *Heterogeneous integration of single-crystalline complex-oxide membranes*. Nature, 578, 75-81 (2020).
8. Büttner, F., Mawass, M., **Bauer, J.**, Rosenberg, E., Caretta, L., Avci, C., Gräfe, J., Finizio S., Vaz, C., Novakovic, N., Weigand, M., Litzius, K., Förster, J., Träger, N., Groß, F., Suzuki, D.,

Huang, M., Bartell, J., Kronast, F., Raabe, J., Schütz, G., Ross, C., Beach, G. *Thermal nucleation and high-resolution imaging of submicrometer magnetic bubbles in thin thulium iron garnet films with perpendicular anisotropy*. Phys. Rev. Materials, 4, 011401(R) (2020).

9. Avci, C., Rosenberg, E., Huang, M., **Bauer, J.**, Ross, C., Beach, G. *Nonlocal Detection of Out-of-Plane Magnetization in a Magnetic Insulator by Thermal Spin Drag*. Phys. Rev. Lett., 124, 027701 (2020).
10. **Bauer, J.**, Rosenberg, E., Ross, C. *Perpendicular magnetic anisotropy and spin mixing conductance in polycrystalline europium iron garnet thin films*. Appl. Phys. Lett., 114, 052403 (2019).